High Throughput Synthesis and Discovery of Sustainable Oxygen Reduction Reaction (ORR) and Oxygen Evolution Reaction (OER) Catalysts

Alexandra R. Groves

A thesis submitted to UCL for the degree of *Doctor of Philosophy*

Department of Chemistry

University College London

December 2020

Signed declaration

I, Alexandra Groves confirm that the work presented in this thesis is my own. Where information has been derived from other sources, I confirm that this has been indicated in the thesis.

London, 02nd December 2020

Abstract

Hydrogen as a fuel for electrochemical cells has many benefits. The chemical energy stored in hydrogen is much higher than that found in traditional battery materials and the only emissions produced from hydrogen utilisation devices such as fuel cells are heat and water. However, using hydrogen as a fuel and generating hydrogen from water require opposing reactions, namely the Oxygen Reduction Reaction (ORR) and Oxygen Evolution Reaction (OER). Both reactions have kinetically complex four electron reaction pathways that require expensive noble metal catalysts, reducing the commercial feasibility of hydrogen fuel cells. Low-cost, non-precious-metal catalysts are promising choices to replace traditional noble metal counterparts. However, there are extensive challenges in developing alternative catalysts with comparable performance to noble metals, whilst ensuring sufficient cost reduction.

The primary goal of this thesis was to use Continuous Hydrothermal Flow Synthesis (CHFS) to produce libraries of candidate materials for use as ORR/OER catalysts in aqueous electrolytes. Initially, a library of ATiO$_3$ perovskites (where A = Ba, Ca and Sr) were synthesised and evaluated as ORR catalysts demonstrating a catalytic dependence on the chemical composition. Increased performance was seen in Ba rich areas of the phase space.

A series of AMnO$_3$ perovskites (where A = La, Y, Sm and Ca) were then synthesised with the aim of investigating the effect of A site substitution on ORR catalysis. LaMnO$_3$ was shown to be an excellent candidate material with a low overpotential (0.31 V) and high limiting current density (−6.2 mA cm^{-2}). Further electrocatalytic studies on La$_x$Mn$_y$Ni$_z$O$_3$ showed that enhanced bifunctional activity can be achieved in a region of La sub-stoichiometry with an optimum composition of La$_{0.83}$Mn$_{0.85}$Ni$_{0.32}$O$_3$ with a bifunctional overpotential of 0.69 V. Lastly, a spinel phase diagram consisting of Ni$_x$Mn$_y$Fe$_z$O$_4$ was investigated for bifunctional oxygen activity and enhanced ORR catalysis was seen in a Mn rich Ni/Fe poor region of the phase space.

Impact Statement

Anthropogenic climate change is one of the most significant problems in society today. Fossil fuel emissions have been linked to increasing greenhouse gases in the atmosphere, which has in turn been linked to rising global temperatures. One mitigation route has been the increased implementation of renewable electricity sources such as solar and wind power. However, intermittence in supply versus demand has put research focus on the development of efficient, commercially affordable energy storage devices.

The so called "green hydrogen economy" can be used as an energy storage solution, using green electricity to generate hydrogen from water, which can be stored until needed and then recombined with oxygen to generate water, heat and electricity. Although commercial devices do exist, current catalysts for the two key oxygen reactions are expensive, none earth abundant and can have serious stability issues in-situ. The development of cheaper, more efficient catalysts is necessary to the wide scale adoption of the hydrogen economy. This work developed libraries of oxygen electrocatalysts using cheaper, more sustainable methods and materials and screened them for their oxygen electrocatalytic activity.

The use of Continuous Hydrothermal Flow Synthesis (CHFS) to produce libraries of oxygen electrocatalysts was unreported until this thesis and the work presented within. Libraries of materials were synthesised, physically characterised and then electrochemically characterised allowing for the development of structure-activity relationships. This work has led to the best materials being sent for testing in scaled-up devices.

This work has been presented at conferences both nationally and internationally. Parts of this work have been presented to the JUICED Energy Hub (EP/R023662/1). The work presented in Chapter 3 was presented in 2018 at the Advanced Inorganic Materials conference in Italy. The work presented in Chapter 5 was supposed to be presented at the 2020 MRS spring meet, but due to travel restrictions was instead presented at the 2020 RSC online materials chemistry division symposia. Part of this work has been published or is under review in peer-reviewed journals.

Acknowledgements

Firstly, I would like to thank my supervisor, Prof. Jawwad Darr for giving me the opportunity to study in London and complete this monster. I would also like to thank my secondary supervisor Prof. Andy Beale for his proof-reading skills and invaluable support.

To all the members of the Clean Materials Technologies Group at UCL thank you – for the laughs (and tears), the pub lunches and the games nights. In alphabetical order thanks to Carlos, Charlie, Chris, Dan, Dustin, Ian, Kalyani, Liam, Min, Shutao, Tom, Yiana, Yijie and Zuharia. Also, a special thanks to my one and only masters student, Sabrina, for making my second year great fun!

To Tony in stores for the gossip (and all of his help regarding ordering), Steve for his invaluable help on the TEM and Martin and Jeremy for their help on the PXRD – if we are ever allowed within 2 m of another person, I will buy you all a beer. To Mark at William Blythe, thank you for teaching me that practical chemistry is about resilience (and for making me a better scientific writer through your gratuitous use of memes). To Dr David Pugh in the teaching labs at York, thank you for pushing me to be a better practical chemist. I'd also like to thank Mrs and Mr Conheeney from Tapton Secondary School for inspiring my love of science and encouraging me to follow it.

To Mum and Dad, I couldn't have finished this without your love and support, and to the boys, Tim and David for stealing my degree idea and Matt for having an original idea as to what you want to do with your life. You are the best younger brothers a sister could wish for. To my extended family, thank you for continuing to be a part of my support network.

To various friends from undergrad (Anil, Beth, Charlotte, Churchill, Jenny, Jess, Lorna and Stefan) thanks for not giving up on me even when I moved to London. To Alix, Amy and Imogen, likewise. Also, to the Zumba girls in south London, Emma and Megan, thanks for listening to me rant about chemistry when you both have real grown up jobs. A big thank you to Rosie for being the best London mum a northern girl could wish for.

Finally, to Tom. I couldn't have done it without your support (and without you paying half the rent).

This thesis is dedicated to Diane, without her support I wouldn’t be the person I am today, and I only wish she was around to see me finish this degree.

Table of Contents

Aims & Objectives

In this thesis, the synthesis of nanosized transition metal oxides, which exhibit reversible oxygen catalysis, was explored via a "green" Continuous Hydrothermal Flow Synthesis (CHFS) process. Material and electrochemical characterisation was carried out to evaluate CHFS prepared nanoparticles as electrocatalysts for metal-air batteries and fuel cells. CHFS was chosen as it is a reproducible, scalable technique which offers some control over the size, shape and morphology of materials produced (see Section 1.17).

In Chapter 3, the use of CHFS as a high throughput synthetic method to form libraries of electrocatalysts was explored and a library of $A\text{TiO}_3$ nanomaterials was examined for catalytic performance as oxygen reduction reaction (ORR) catalysts. This was to examine if CHFS was a suitable technique for the synthesis of libraries of oxygen electrocatalysts.

In Chapter 4, having established that CHFS was a suitable synthetic technique, the importance of the *A* site cation in perovskites for the ORR was investigated and four elements examined at the *A* site of $A\text{MnO}_3$ materials. The importance of various synthetic parameters on the catalytic activity was also investigated.

In Chapter 5, CHFS was used in the high-throughput combinatorial study of a library of $\text{La}_x\text{Mn}_y\text{Ni}_z\text{O}_3$ ($x + y + z = 2$) perovskite materials for use as bifunctional oxygen electrocatalysts. The aim was to investigate how changing the *A* and *B* site elements effected the bifunctional oxygen activity. The use of Mn redox peaks as an activity descriptor for bifunctional catalysis was examined.

The aim of Chapter 6 was to investigate the electrochemical activity of an impurity phase seen in Chapter 5, and to explore the electrocatalytic activity of the ternary phase space around this impurity in the $\text{Ni}_x\text{Mn}_y\text{Fe}_z\text{O}_4$ ($x + y + z = 3$) spinel phase diagram. Finally, in Chapter 7 overall conclusions were presented for the work and future directions for research in this area were suggested.

1. Literature Review

1.1. Background

With rising public concern about anthropic effects on the natural environment, there has been renewed interest in climate change mitigating research. CO_2 levels in the atmosphere have been increasing steadily in the past 200 years (see Figure 1.1 a) and have risen from ca. 320 parts per million (ppm) in 1962 to 411 ppm in 2019. Increasing levels of greenhouse gasses in the atmosphere are linked to anthropic climate change[1] and the sudden rise in CO_2 levels in the atmosphere has been linked to an increase in global energy demand.[2]

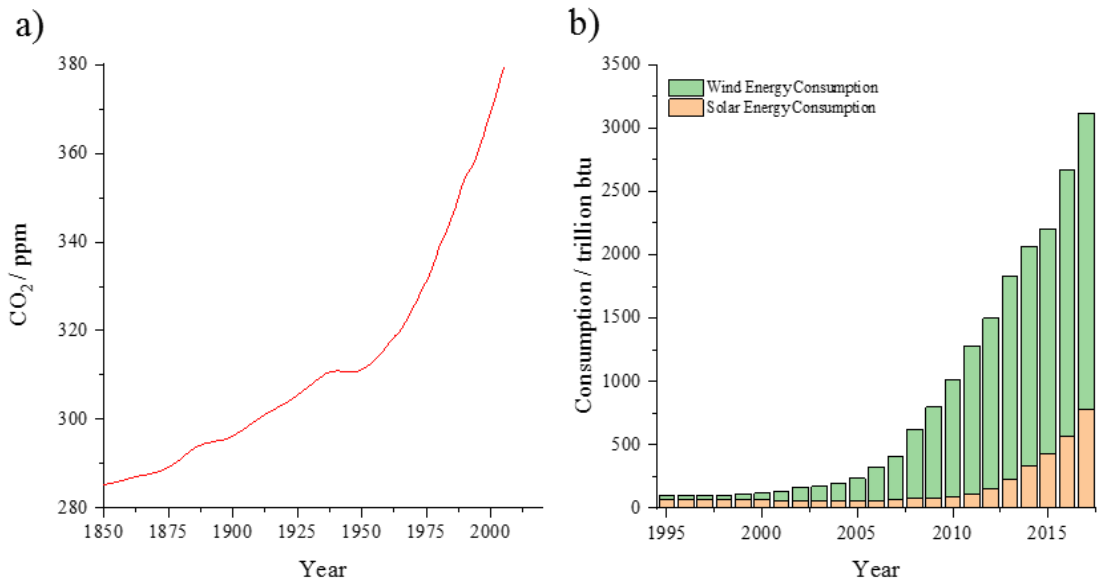

Figure 1.1: a) Graph illustrating the rising CO_2 levels in the atmosphere over the past 200 years, b) increase in consumption of energy generated by solar and wind sources. Data adapted from the National Centers for Environmental imformation.[3]

In the past 30 years, increasing awareness about global warming has led to an increase in the green production of energy. The annual global statistics for solar and wind power can be seen in Figure 1.1 b. However, these energy sources are dependent on the external weather conditions (such as wind speed or light levels) meaning that energy supply to the grid can be intermittent and peak demand does not always match peak supply.[4] Grid-scale energy storage devices smooth delivery to the grid, enabling the use of renewable energy technologies to grow by minimising the problem of intermittent supply.[5]

There are many methods being researched for the smoothing of energy supply vs energy demand on national grid systems and these include using devices such as rechargeable lithium ion batteries which can store excess energy as it is produced and then release this energy as demand increases. For widespread economical acceptance, energy storage devices must demonstrate low cost, high reliability and high energy/power densities.[6] Two promising energy storage devices with the potential to be used as grid smoothing devices are metal-air batteries and fuel cells.[7] Essential to the operation of both devices is the Oxygen Reduction Reaction (ORR) which occurs at the cathode (negative electrode). The sluggish kinetics of the ORR require the use of a catalyst.[8] The current catalysts for the ORR are platinum/platinum oxides which are expensive and unstable in-situ, therefore not economically feasible in the long term.

Research in energy storage has rapidly expanded over the last two decades as the use of fossil fuels derived energy recedes. Although the energy density in a hydrogen electrochemical storage device (such as a fuel cell) is much less than the energy density of fossil fuels,[9] the chemical energy stored in hydrogen is much higher than that found in common battery technologies.[10] As fuel cells don't need recharging (as long as oxidant and fuel are in constant supply) and can use hydrogen as the fuel they are seen as a popular choice for potential energy storage units. If hydrogen is the fuel source, the product from the fuel cell is electricity with water and heat as by-products. This offers a huge advantage over more traditional energy sources which put out polluting gasses into the atmosphere. There are many different examples of fuel cells and these are summarised in Figure 1.2.

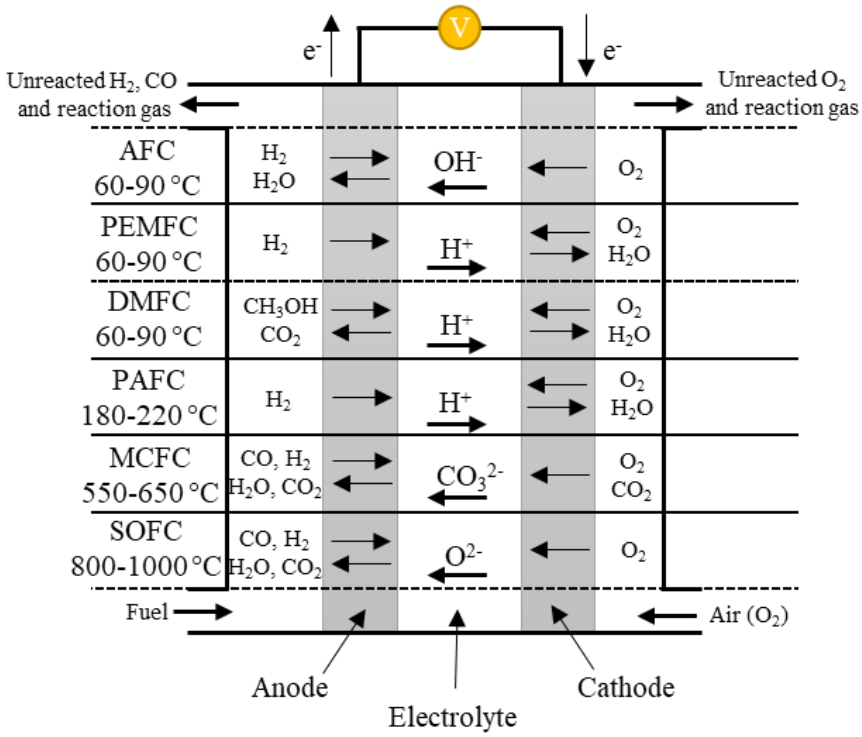

Figure 1.2: Summary of reactions which occur in different fuel cell systems.[11] AFC = alkaline fuel cell, PEMFC = polymer electrolyte membrane fuel cell, DMFC = direct methanol fuel cell, PAFC = phosphoric acid fuel cell, MCFC = molten carbonate fuel cell and SOFC = solid oxide fuel cell.

Metal-air batteries (Figure 1.3) are also promising devices for electrochemical energy storage. They consist of a metal anode and an air breathable electrode capable of using oxygen from the air as the cathode material.[12–14] As the cathode (oxygen) is not stored within the cell, and the anode is a metal which possesses a large number of valence electrons, the theoretical specific energy density of a metal-air battery is much higher than a conventional Li-ion battery (5200 $Wh.kg^{-1}$ for a Li-air battery vs. 200-250 $Wh.Kg^{-1}$ for a Li-ion battery).[15]

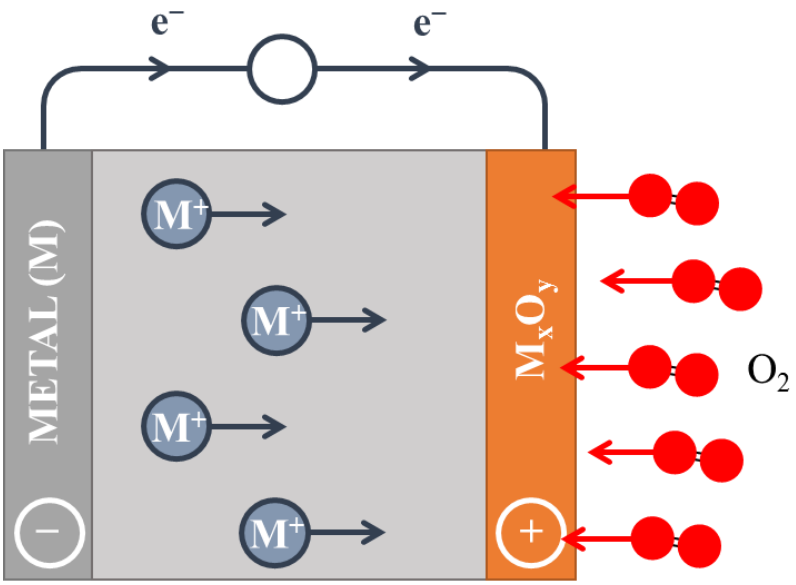

Figure 1.3: Schematic of a metal air battery. The anode is a solid metal and the cathode is porous to air.

Fuel cell, metal-air battery and electrochemical water splitting technologies rely on efficient oxygen evolution and reduction reactions for rechargeable electrochemical energy. Current industrial catalysts for these reactions are Platinum Group Metal (PGM) catalysts including Ru, Ir and Pt. As the earth abundance of these elements is very low (see Figure 1.4), they are expensive making them unsustainable choices for consumer market energy storage devices. The focus of this thesis will be on the replacement of PGM oxygen reduction/evolution catalysts with cheaper, transition metal oxide-based catalysts.

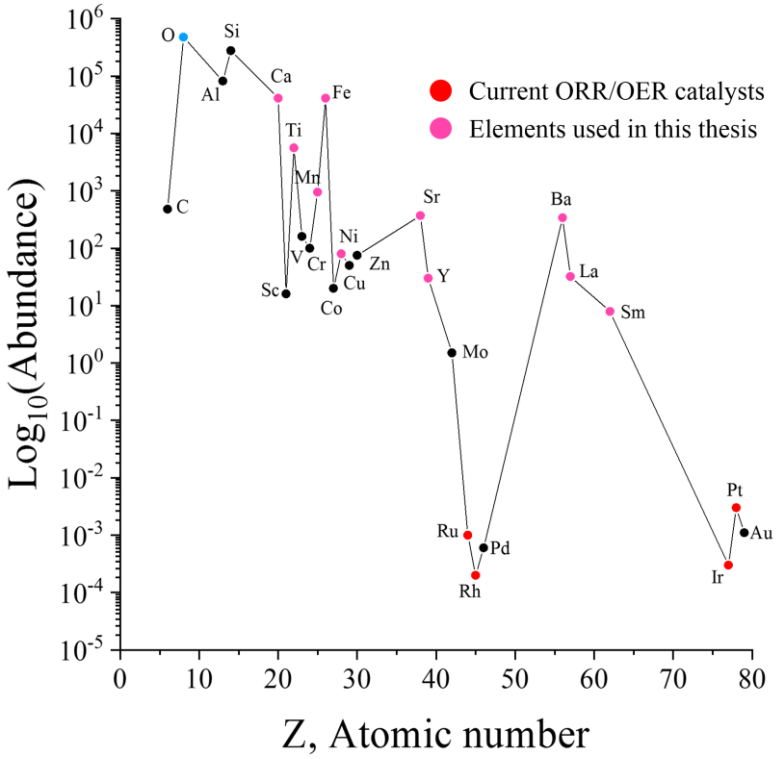

Figure 1.4: Abundance of certain elements in the earth's crust. Elements highlighted in red are current leading catalysts for the OER/ORR. Elements in pink are the focus of this thesis. Data adapted from results collated by K. Barbalace.[16]

1.2. Introduction to Electrochemistry

An electrochemical cell is a device which can store or use electrochemical energy. The simplest cells constitute a positive (cathode) and negative (anode) electrode which are isolated from each other by a separator between the electrodes (preventing short circuits) and an electrolyte. Reduction occurs at the cathode and oxidation at the anode. Essentially, there are two types of electrochemical cell. An electrolytic cell transforms electrical energy into chemical energy. A galvanic cell is effectively an electrolytic cell in reverse. When only reactions occurring at one electrode are of interest, a half-cell can be used to study the electrochemical reactions occurring. A half-cell is constructed of the working electrode (electrode of interest) and a reference electrode with a known potential. A two-electrode cell such as this can only be used if the ohmic droop between the reference and working electrode is small. If it is large (when solution resistance is large) a three-electrode cell may be more appropriate for studying the electrochemistry.[17] In this set-up, the potential of the working electrode is measured relative to the reference electrode (which is in effect a separate working electrode, with

no current flowing through the reference electrode), and the current is passed between the counter electrode and the working electrode.

The potential, under standard conditions, of an electrochemical cell can be calculated using:

$$E_{cell}{}^{o} = E_{cathode}{}^{o} - E_{anode}{}^{o} \quad (1.1)$$

The maximum free energy storable in an electrolytic chemical cell or the energy available from a galvanic cell is equal to the Gibbs free energy change for the cell:

$$\Delta G^{o} = -nFE_{cell}{}^{o} \quad (1.2)$$

where ΔG is the Gibbs free energy change, n is the number of electrons transferred, F is the Faraday constant and E is the potential difference of the cell. A reaction is spontaneous if ΔG is negative, as the most energetically favourable state of the cell has not been achieved. No spontaneous chemical reaction will occur if ΔG is positive.

Under non-standard conditions, the cell potential can be found using the Nernst equation. Under these conditions the standard Gibbs free energy change is related to the actual Gibbs free energy change by the equation:

$$\Delta G = \Delta G^{o} + RT\ lnQ \quad (1.3)$$

where R is the ideal gas constant, T is the temperature in Kelvin and Q is the reaction quotient, given by:

$$Q = \frac{[C]^{c}[D]^{d}}{[A]^{a}[B]^{b}} = \frac{a_{O_x}}{a_{Red}} \quad (1.4)$$

Therefore:

$$-nFE = -nFE^{o} + RTlnQ \quad (1.5)$$

Which can be simplified to the Nernst equation:

$$E = E^{o} - \frac{RT}{nF} ln \frac{a_{O_x}}{a_{Red}} \quad (1.6)$$

where E° is the standard reduction potential, R is the gas constant, T is the temperature in Kelvin, F is the Faraday constant, n is the number of electrons transferred and *a* is the activity of the reduced and oxidized species.

1.2.1. The Oxygen Reduction Reaction (ORR)

Oxygen evolution and reduction in aqueous media are important reactions in many energy storage devices including fuel cells, water electrolyser cells (water-splitting) and metal-air batteries.[18,19] However, owing to their high energy barriers, the reaction kinetics for the oxygen reduction and evolution reactions are very slow under ambient conditions. Platinum group metal catalysts are currently the industry standard for use as catalysts for both oxygen reduction and evolution, iridium oxide is used as an oxygen evolution catalyst and platinum is used as an oxygen reduction catalyst. However, due to the rising cost caused by low earth abundance and the poor stability exhibited by certain precious metal catalysts, other more sustainable materials are being studied as replacements.[20] Oxygen kinetics are generally faster in alkaline rather than acidic electrolytes, showing higher exchange currents and smaller overpotentials. This is primarily due to the reduction of the kinetic barrier as the pH of the electrolyte increases. [21–23] This lowering of the kinetic barrier enables non-precious metal catalysts to reach similar current densities as precious metals, allowing cheaper catalysts to be developed.[22]

The Oxygen Reduction Reaction (ORR) occurs at the cathode of the electrochemical energy storage systems discussed above. It is widely recognised as the kinetically limiting component of devices such as metal-air batteries and fuel cells.[23] This is observed as a large overpotential at the electrode at which the reaction is taking place. In alkaline media, the ORR can occur by one of two pathways. A direct four-electron pathway:[24]

$$O_2 + 2H_2O + 4e^- \rightleftharpoons 4OH^-;\ E^0 = 0.401\ V\ vs\ SHE \quad (1.7)$$

An alternate reduction route is via a two-electron pathway:

$$O_2 + H_2O + 2e^- \rightleftharpoons HO_2^- + OH^-;\ E^0 = -0.076\ V\ vs\ SHE \quad (1.8)$$

This is then followed by a further reduction or by disproportionation:

$$HO_2^- + H_2O + 2e^- \rightleftharpoons 3OH^-;\ E^0 = 0.878\ V\ vs\ SHE \quad (1.9)$$

$$2HO_2^- \rightleftharpoons 2OH^- + O_2$$

The 4 e^- pathway is generally cited as being the preferred pathway[25], as the generation of peroxide can lead to harmful corrosion within the cell as well as affecting the catalyst.[26]

The ORR is a multi-step reaction involving the formation and reaction of intermediates meaning that reaction kinetics are greatly affected by the formation and stability of these reaction intermediates on the catalyst surface.[27] Despite being widely studied for a number of years, the mechanistic aspects of the ORR are still poorly understood due to the transfer of four protons and four electrons to O_2 and the cleaving of the O_2 double bond.[23]

The Nernst equation can be used to find the equilibrium potential of the ORR in non-standard conditions.

$$E = E^0 - \frac{RT}{nF} ln \frac{a_{Ox}}{a_{Red}} \tag{1.10}$$

where E° is the standard reduction potential of O_2 at 298 K, R is the gas constant, T is temperature in Kelvin, n is the number of electrons transferred, F is the Faraday constant, and a is the activity of the oxidised and reduced species.

Due to the sparing solubility of oxygen in aqueous media (1.26×10^{-3} mol L^{-1}), catalytic studies on the ORR must normally involve forced transport of reactants.[28,29] This can be done by utilising a Rotating Disk Electrode (RDE) (Figure 1.5) or Rotating Ring Disk Electrode (RRDE) which make use of a disk electrode mounted on a rotating shaft to force convection within the electrolyte.

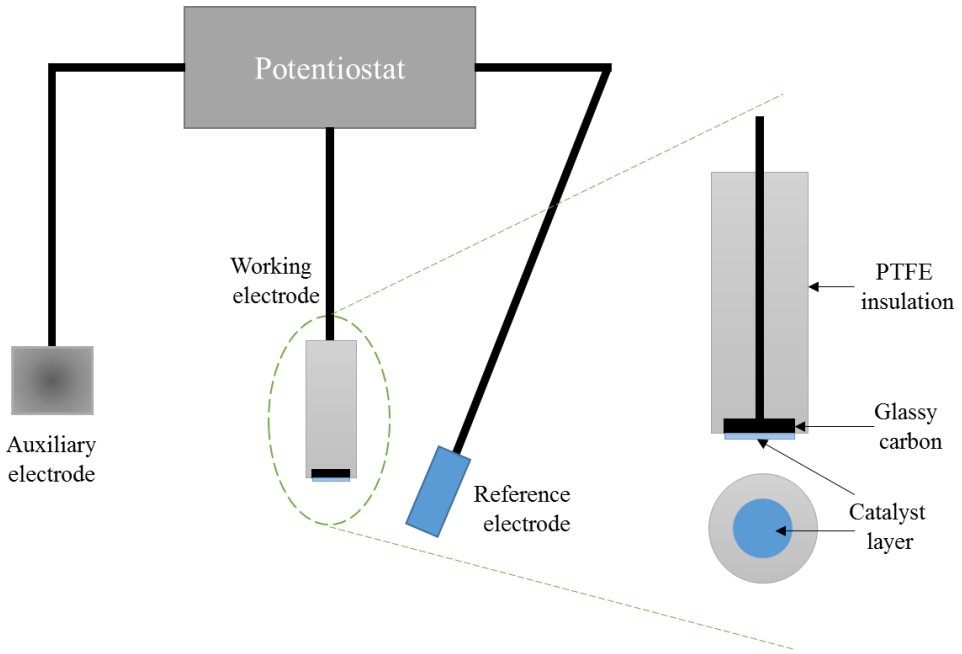

Figure 1.5: A schematic of the typical RDE set up in a three-electrode configuration. The right-hand side shows an expanded diagram of the RDE working electrode.

The most important catalytic markers for the ORR are the onset potential and the limiting current density. The onset potential refers to the point at which the current deviates from the baseline value (i.e. the point at which the catalytic reaction is observed to begin). Tangents can be taken from the slope of the catalysis reaction and the baseline and the intersect is generally reported as the onset potential.[30] By subtracting the onset potential from the standard reduction potential of oxygen, the overpotential for the ORR can be found. The overpotential is therefore defined as the difference between the thermodynamically determined start of reaction and the experimentally observed start of reaction. The observed current is commonly normalised to the mass or surface area of catalyst used giving a current density. The limiting current density gives insight into the practical use of such catalysts at device levels.

1.2.2. The Oxygen Evolution Reaction (OER)

The Oxygen Evolution Reaction (OER) occurs at the anode of water electrolysers and rechargeable fuel cells/metal air batteries.[31] Molecular oxygen is produced via several proton/electron coupled reactions. The reaction is highly dependent on the pH of the electrolyte. The equilibrium half-cell potentials at 1 atm and 25 °C are:

$$4OH^- \leftrightarrow 2H_2O_{(l)} + O_{2(g)} + 4e^- \;\; E^\circ = 0.404\,V\;(alkaline) \tag{1.11}$$

$$2H_2O_{(l)} \leftrightarrow 4H^+ + O_{2(g)} + 4e^- \;\; E^\circ = 1.23\,V\;(acid) \tag{1.12}$$

RDE techniques are also commonly employed to study the OER at catalyst surfaces and several key performance indicators can be taken from the resulting data. It is generally seen that the most significant factor for electrochemical evaluation of OER catalysts is the overpotential. This is the potential difference between the onset potential and reversible oxygen potential of 1.23 V. The convention is to take the potential reached when current is 10 mA cm^{-2}.[32] Generally, if the overpotential is < 400 mV the catalyst is considered a good catalyst for the OER.[32]

1.3. OER/ORR in Practice

The oxygen reduction and evolution reactions are of vital importance in many electrochemical energy devices such as fuel cells, water electrolyser cells and metal-air batteries. In many of these devices the barrier to commercialisation on a large scale is the cost and stability of the anodic and cathodic catalysts, which are necessary due to the slow kinetics of the OER/ORR.[33]

1.3.1. Fuel Cells

Due to the potential for non-fossil fuel energy generation, the hydrogen fuel cell is considered a solution to decarbonise the transport and grid energy sector. One advantage of a fuel cell is the high thermodynamic efficiency in electrochemical energy conversion at low temperatures. It is much higher than that of a conventional heat engine which is limited by Carnot efficiency (the maximum theoretical efficiency when a heat engine is operating between two temperatures) at low temperatures. [34–36]

Fuel cells are often classified according to the electrolyte employed. Alkaline Fuel Cells (AFC, see Figure 1.6) are arguably the most developed and have been used in space applications since the NASA Apollo missions in the 1960s.[37] A schematic of an aqueous electrolyte AFC can be seen in Figure 1.6 a). At the anode, hydrogen is oxidised producing water and electrons. The electrons flow through an external circuit, powering a load, to the cathode, where they reduce oxygen, producing hydroxide ions. Overall, the reaction consumes two hydrogen molecules and one oxygen molecule producing two water molecules. The by-products of this chemical reaction are electricity and heat.

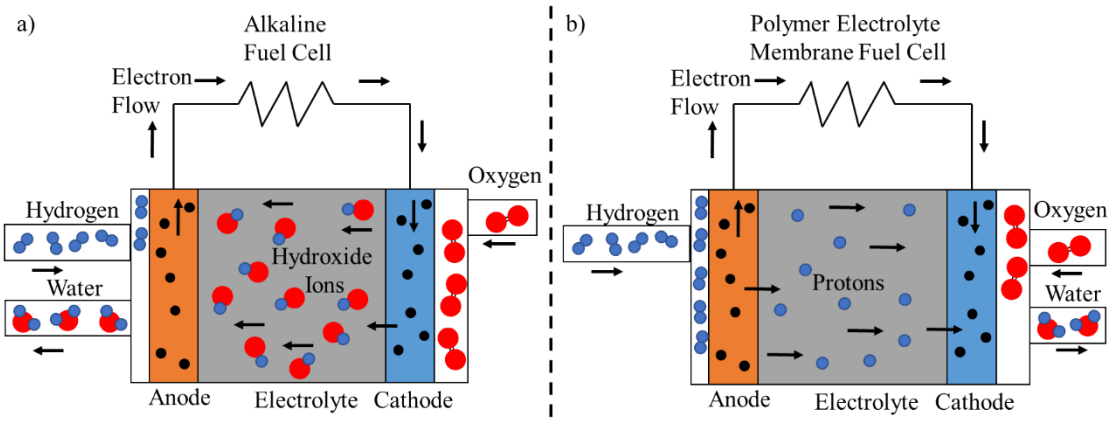

Figure 1.6: a): Diagram of an alkaline fuel cell. The only outputs besides electricity are heat and water. b): Diagram of a polymer electrolyte membrane fuel cell. Red circles represent oxygen atoms and blue circles represent hydrogen atoms.

AFCs offer some advantages over fuel cells with different electrolytes; they have a low operating temperature (typically in the range of 23 to 70 °C) and have higher reaction kinetics due to an alkaline, rather than acidic, electrolyte.[38] They can also possess higher current densities and better electrochemical efficiencies than other fuel cells.[39] This means that lower amounts of precious metal catalyst are needed or that non-

precious metal catalysts can be used.[40] In addition to this, the aqueous electrolyte is much cheaper than its polymer electrolyte companions, as aqueous potassium hydroxide is most commonly used.[41] However, the electrolyte is easily poisoned by carbon dioxide impurities, making it impractical for un-purified air or hydrogen to be used as fuel sources.[39] Carbon dioxide can react with the potassium hydroxide electrolyte, forming potassium carbonate and water. This reduces the number of hydroxyl ions for reaction at the electrodes and can reduce the ionic conductivity of the solution. It may also block the pores in the gas diffusion layer as the potassium carbonate impurity precipitates.[42] To circumnavigate contamination problems, Alkaline Membrane Fuel Cells (AMFCs) were developed. These resemble Polymer Electrolyte Membrane Fuel Cells (PEMFCs), but the membrane transports anions, not cations.[43] The major advantage of using a membrane over a liquid electrolyte is the elimination of the poisoning effect of CO_2, as there are no mobile cations meaning that solid crystals of carbonate can't form on the electrodes.[44] However, the performance of these AMFCs is currently inferior to PEMFCs.

In all current examples of fuel cell technologies, a catalyst is needed to accelerate the rate of oxygen reduction. The catalyst coating on the cathode to a large extent determines not only the energy conversion efficiency but also the cost of a fuel cell.[20,45,46] The costs of current platinum based catalysts are the reason fuel cells are currently so expensive. It has been suggested that platinum loadings would need to be reduced by a factor of 10 to make fuel cells commercially competitive against the internal combustion engine.[47]

1.3.2. PEM Water Electrolysers

Traditionally, the production of hydrogen for fuel cells has come from the steam reforming of hydrocarbons.[48] However, this has produced low quality hydrogen containing carbon species, which may poison the fuel cell as well as producing carbon dioxide as a side product, contributing to the global increase in CO_2 in the atmosphere. An alternative to steam reforming is the electrochemical production of hydrogen and oxygen from water in a process called water electrolysis.[49] Renewable energy from solar cells and wind turbines can be used to produce the necessary electricity, allowing the production of hydrogen from sustainable sources. Proton Exchange Membrane (PEM) water electrolysers are an attractive and efficient way to produce oxygen and hydrogen at low temperatures and pressures.[50] Unfortunately, the cost of precious metal

electrocatalysts and of the membrane are high enough that development of PEMs has been held back. PEM electrolysers offer several advantages over other water electrolysers as they can operate at higher current densities, are compact and produce high purity hydrogen and oxygen gas.[49] Although the primary interest in a water electrolyser has tended to be the production of hydrogen, due to the slower kinetics and higher overpotential for the anodic oxygen evolution reaction, more research has been focused on the development of an efficient catalyst for the OER.[51–54] The current anodic catalyst is IrO_2 as it balances high activity with high stability. However, as with fuel cells and metal-air batteries, the catalyst is expensive and non-abundant, so research is focussed on finding a non-precious metal catalyst with comparative activity and stability.[49]

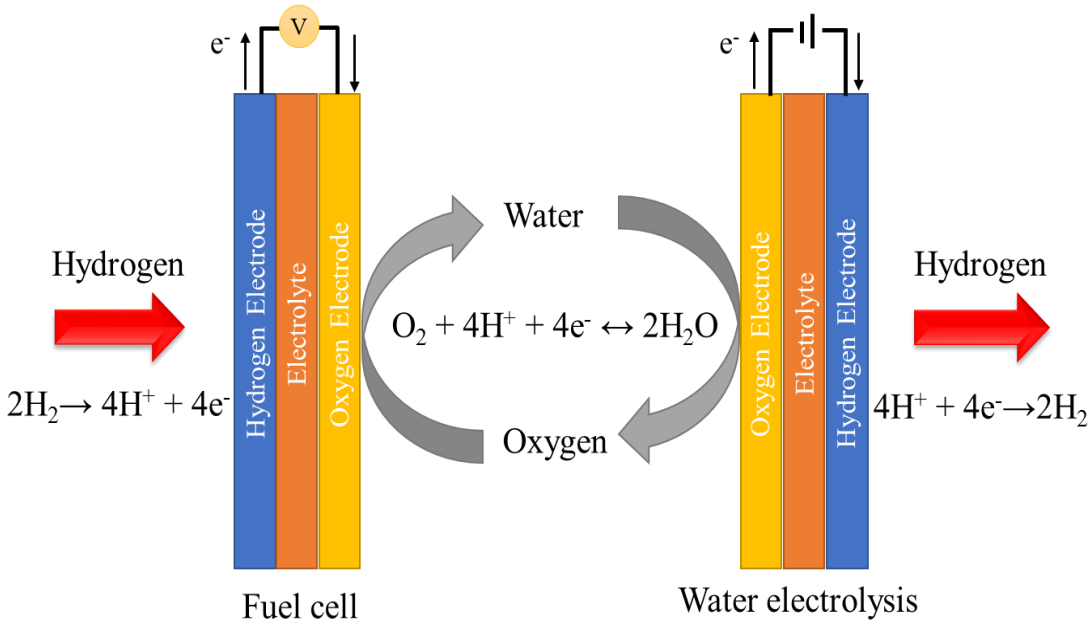

Figure 1.7: Schematic showing a "rechargeable" fuel cell. One half of the cell converts hydrogen to water by combination with oxygen, whilst the other half splits water into H_2 and O_2.

Figure 1.7 shows a "rechargeable" or reversible fuel cell. If a catalyst could be found which catalysed both the ORR and OER reactions, then water splitting could be done in one direction (e.g. using electricity from solar panels or a wind turbine) and O_2 and H_2 could be combined in the other to form water.[55] This is known as a Unitized Regenerative Fuel Cell (URFC).

1.3.3. Metal Air Batteries

Figure 1.8 shows a diagram of a Lithium Ion Battery (LIB). This is a well-established technology with applications from cars to mobile phones and rechargeable LIBs have been investigated as long-term energy storage solutions due to their long-cycling life (>5000 cycles) and high energy efficiency (>90%).[56] However, in comparison to fossil fuels, the theoretical energy density is much lower (approx. 400 W h kg^{-1}) and conventional lithium ion intercalation-based technology is approaching the performance limit.[57] It is estimated that at most there can be a 30% improvement on current cells.[58,59] This poses a problem in certain applications such as battery-operated cars as it limits the drive range to below that of a typical petrol tank (<800 km).[60]

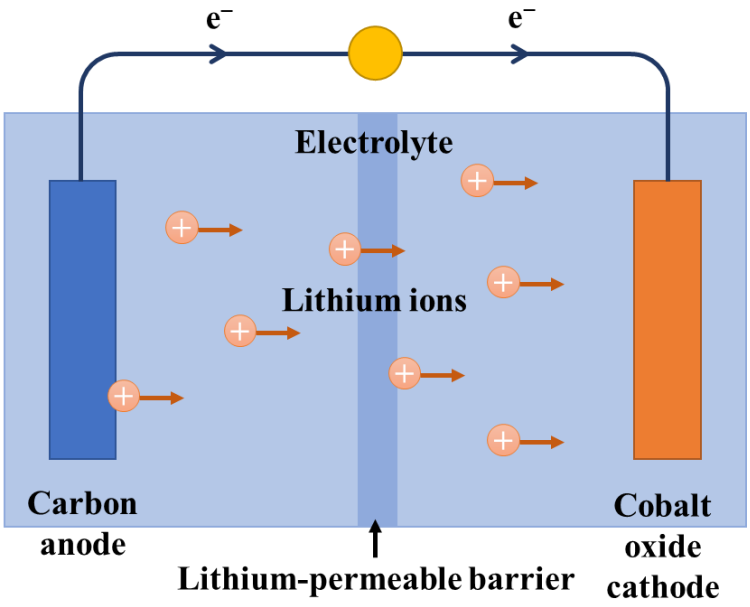

Figure 1.8: A diagram of a discharging lithium ion battery.

One way to circumnavigate the low energy densities found in traditional batteries is to use Metal Air Batteries (MABs), described as those running on oxygen or air as a feedstock.[28] These can be seen as a half-way house between traditional battery technology and fuel cells and replace intercalation reaction chemistry with a catalytic redox reaction of a lightweight metal-oxygen redox couple. MABs (Figure 1.3) consist of a metal anode and an air accessible cathode placed in an appropriate electrolyte with a separator between the two.[61] The breathable air cathode is coated with an electrocatalyst (currently Pt/carbon combinations commercially[62]) which catalyses the slow ORR. On discharging, the metal anode is oxidised, releasing electrons to an external circuit. Concurrently, oxygen accepts electrons from the anode, and is reduced.

Either the charged metal or oxygen reduced species migrates across the electrolyte, combining to form a metal oxide. As the cathode material (oxygen) is not stored within the cell, metal-air batteries have notably higher theoretical energy densities.[28]

Many metals have the potential to be used as commercial metal-air batteries; examples include zinc-air[63], sodium-air[64], lithium-air[65] and aluminium-air.[14] Amongst metal-air batteries, aqueous zinc-air battery (see Figure 1.9) technology is the oldest, and has been investigated since the late 1800s.[13] Zinc-air batteries (ZABs) typically have an aqueous electrolyte and KOH is preferred due to better ionic conductivity, higher oxygen diffusion kinetics and lower viscosity, as well as reaction products with species in the atmosphere being more soluble than in NaOH.[66] Compared to other battery technologies, ZABs are inexpensive, non-polluting, have high specific energy and can offer good safety. They also possess several advantages over other metal-air batteries, including higher safety and lower cost, making them promising candidates for reliable energy storage.[63] The theoretical energy density is 1350 W h kg^{-1} but current practical energy density is ca. 200 W h kg^{-1}.[67]

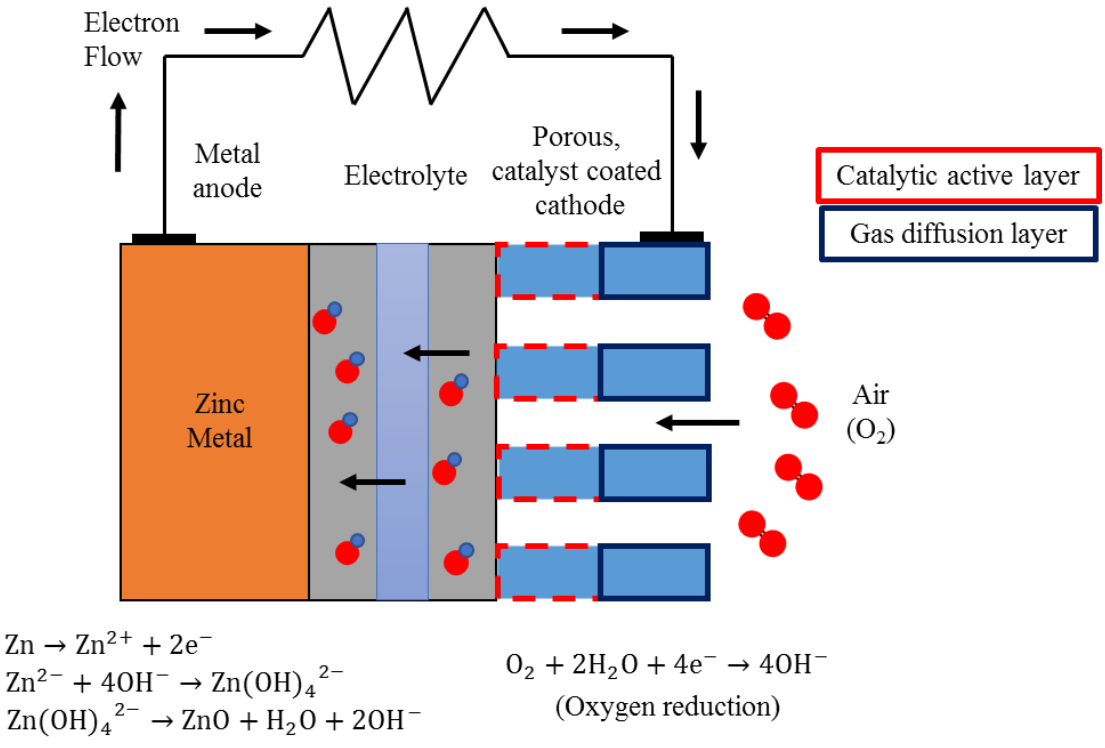

Figure 1.9: Schematic diagram of an aqueous zinc-air battery. At each electrode the chemical reactions occurring are highlighted.

The current major limiting factor in rechargeable zinc-air technology is limited lifetime (typically 200-500 cycles). Zinc chemistry in alkaline electrolytes is readily reversible, but non-uniformity in deposition and dissolution can result in electrode shape change or dendrite formation which is damaging to cycle life and performance.[68]To overcome these various issues, modifications to the electrolyte or electrode have been made, Vatsalarani *et al.* found that by coating a porous zinc electrode with a fibrous network of polyaniline, the movement of hydroxide ions to/from the electrode was allowed but zinc diffusion was restricted.[69] Alternatively, it is well known that the addition of calcium hydroxide to the electrolyte or to the electrode reduces shape change/dendritic growth as an insoluble compound is formed with the zincate ions, meaning that much of the zinc is maintained in a solid form. This increases cell life-time with no apparent determinant to cyclability.[70] This allows the interconversion between Zn and Zn^{2+} at high rates during charge/discharge cycles. A novel way of bypassing cycling stability issues is to use a three-electrode configuration. An additional air electrode is used for OER during charging, with the zinc electrode sandwiched between the two air electrodes.[71] Although this design adds additional weight and complicates the assembly, it has been shown to significantly improve cycle life for the rechargeable ZAB as state of the art OER/ORR catalysts can be used.[72]

Lithium-air batteries have recently been investigated due to their high theoretical energy density of 11680 W h kg^{-1}, which is close to the energy density of gasoline.[73] Due to the inherently violent nature of the Li reaction with water, unlike for Zn-air, the electrolyte for Li-air must be non-aqueous or else the Li anode must be protected from an aqueous environment. Typically, Li-air batteries have a non-aqueous electrolyte due to their potentially higher energy density and rechargeability when compared to a protected Li anode.[74,75] A high-performing, rechargeable Li-air battery must have the following: i) high specific capacity, ii) high round-trip efficiency, iii) good rate capabilities and iv) good cycling performance.[76] The use of a bifunctional electrocatalyst, which is active for the OER/ORR, will facilitate high round-trip efficiency by reducing the overpotential during the charge-discharge process.[77,78] Alongside oxygen diffusion rate, fast OER/ORR reaction rates are also vital for enhancing the cycling rate capabilities of Li-air batteries and therefore highly active catalysts are needed to maximise the rate of Li-air batteries. An efficient electrocatalyst should not only drive the formation of reversible Li_2O_2 as a discharge product but

should limit the formation of undesirable side-products from electrolyte degradation and electrode corrosion. Thus, a stable, porous cathode is necessary to achieve improvements in cyclability.

The main limiting factor on the practical charge density for both Li-air and Zn-air batteries is the sluggish kinetics of the ORR.[38,79] Electrocatalysts for the oxidation and reduction of oxygen play a key role in determining the power, energy density and energy efficiency of metal-air batteries.[80]

1.4. Oxygen Electrocatalysts

Chemical bonds are one of the most efficient ways of storing energy. The electrochemical generation and consumption of fuels is seen in both nature and man-made technologies and remains one of the most efficient energy usage routes. Energy can be stored in chemical bonds by forming H_2 from water splitting and then oxidising the H_2 as needed to release the stored energy. However, the two critical reactions, the ORR and OER have sluggish kinetics as there is a large activation barrier to the reaction occurring, thus a large overpotential must be applied for the reaction to occur. Therefore, oxygen electrocatalysts are needed to realise the potential of using H_2 bonds for electrochemical energy storage and production.[81]

1.4.1. Platinum Group Metals (PGM)

When Platinum Group Metals (PGM) are used as ORR catalysts, the kinetics observed are complex due to the number of electrons transferred ($4e^-$ for the ORR) and also due to the influence of pH and solvation.[82] Pt is generally accepted as the best electrocatalyst for the ORR with good durability in acid, low overpotentials and high mass activity.[83] However, due to the cost of Pt and its scarcity, the focus of research has been reducing its loading at the electrode to less than 0.125 mg cm^{-2} [84] by nanosizing or alloying.[85] Whilst research is moving towards non-PGM catalysts for the ORR, Pt remains the sensible commercial choice for devices such as fuel cells.[86]

PGM have also traditionally been used as OER catalysts.[87] Experimentally, the activity of the metal oxide for ORR has been determined as Au < Pt < Ir < Ru < Os and stability of the catalyst to OER has been determined as Os < Ru < Ir < Pt < Au showing an inverse relationship between activity and stability.[88] Consequently, IrO_2 is often the catalyst of choice for OER, as stability and activity are balanced. Reier *et al.* investigated the difference between bulk and nano-oxides and showed that whilst Ru

and Pt nanoparticulate oxides were highly unstable (meaning activities were lower), Ir nanoparticulate oxides had high activity and stability.[89] Ir nanoparticles and alloys of Ir are currently used as industrial catalysts for the OER.[90]

1.4.2. Carbon Based Catalysts

The majority of research carried out on non-metal-based catalysts for the ORR has been conducted on carbon-based materials. sp^2 hybridised carbons can have delocalised electrons (e.g. graphene-based materials) which can act like metallic electrons, giving the carbon materials unique electronic properties, inducing metallic behaviour.[91] Carbon based materials have an advantage versus PGM catalysts as they are generally more resistant to poisoning by fuels/impurities such as CH_3OH and CO.[92] Doping carbons with heteroatoms such as nitrogen has been shown to increase electrochemical activity of carbon-based materials. In 2009 Dai *et al.* reported N-doped carbon nanotube materials that were electrocatalytically comparable to commercial Pt/C catalysts.[93] Boron-doping has also been widely studied, both due to its atomic radius being close to carbon and due to the availability of an orbital for conjugation with carbon π orbitals.[94] Yang *et al.* showed that by increasing the dopant concentration from 0-2.24 at. % B, the activity of carbon nanotubes towards the ORR could be enhanced.[95]

There has been extensive research carried out on carbon based electrocatalysts for the OER as well as the ORR.[96] Nanostructured carbon materials have emerged as low-cost catalysts with good performance. Doping carbon nanostructures with B or O has been shown to enhance water splitting, and co-doping can increase this activity further. Cheng *et al.* showed that by acidifying commercial carbon cloth, oxidised carbon cloth could be produced that had a low overpotential of 328 mV that maintained catalytic activity over at least 24 hours[97] and Gong *et al.* co-doped a biocarbon with nitrogen and phosphorus to create a metal free catalyst with activity which approached a commercial Pt/C catalyst.[98]

1.5. Transition Metal Oxide Catalysts

Whilst PGM catalysts are highly active, with low overpotentials at high current densities, they are limited in large scale application predominantly by cost as has been discussed before, but also by low stability and poor bifunctionality.[25] Similarly, carbon based materials are often limited by poor activity/stability in low pH and by unoptimized, expensive synthetic routes.[94,96] Transition metal oxides and mixed

transition metal oxides provide an exciting alternative. Not only are they much more abundant (see Figure 1.4) making them significantly cheaper than PGMs (state of the art Pt-alloy catalysts ~\$50 g^{-1}, RuO ~\$2.50 g^{-1}, compared to Fe ~\$0.0001 g^{-1}, Ni ~\$0.002 g^{-1}, La ~\$0.002 g^{-1} and Co ~\$0.003 g^{-1})[81] but they also possess many structural and electrochemical advantages. The ability to easily tune composition, structure and therefore electronic state means that electrocatalysts can be designed with specific uses in mind.[99,100] Metal oxides tend to be corrosion resistant in a wide range of pH's making them ideal for a variety of applications.[101,102]

Mixed metal oxides, once optimised for commercial use, have interest in several applications, particularly in fuel cells and rechargeable metal air batteries. The poor bifunctional activity of PGM catalysts means that separate anodic and cathodic catalysts must be used, whereas the varying oxidation states and structures of mixed metal oxides suggests that bifunctional activity could be tuned into the catalyst.[30]

However, despite the many advantages metal oxides possess, there are still barriers to overcome before they could be considered for commercial applications. Despite decades of research and a rapidly increasing number of publications, there is still much discussion about reaction pathway undertaken on varying metal oxides and the relationship between oxide structure and electrocatalytic activity.[103] The relatively low conductivity of many mixed metal oxides also means that relationships can be further muddied by the addition of conductive carbons to catalysts which can act as co-catalysts.[104]

In a transition metal oxide, the surface cations are not fully coordinated by oxygen anions. This leaves gaps in their coordination sphere allowing other molecules to interact with those elements at the surface. In aqueous solutions this coordination gap is filled by water molecules.[28] The proposed ORR pathways on oxide surfaces in alkaline media has been described as follows;[105]

$$M^{m+} - O^{2-} + H_2O + e^- \rightarrow M^{(m-1)+} - OH^- + OH^- \quad \text{(I)}$$

$$O_2 + e^- \rightarrow {O_2}_{(ads)}^- \quad \text{(II)}$$

$$M^{(m-1)+} - OH^- + {O_2}_{(ads)}^- \rightarrow M^{m+} - O - O^{2-} + OH^- \quad \text{(III)}$$

$$M^{m+} - O - O^{2-} + H_2O + e^- \rightarrow M^{(m-1)+} - O - OH^- + OH^- \quad \text{(IV)}$$

$$M^{(m-1)+} - O - OH^- + e^- \rightarrow M^{m+} - O^{2-} + OH^- \quad \text{(V)}$$

The competition between displacement of O^{2-}/OH^- and OH^- regeneration has been found to be the rate determining step.[23] This is illustrated schematically in Figure 1.10.[106]

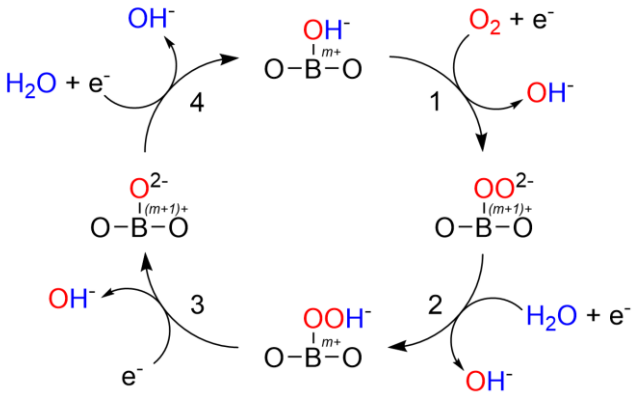

Figure 1.10: Proposed reaction mechanism for the oxygen reaction on transition metal oxide surfaces (*B*) in alkaline media. The proposed mechanism for the ORR has four steps. 1) hydroxide displacement, 2) peroxide formation, 3) oxide formation and 4) hydroxide regeneration.

Electronic structure has been found to have a substantial effect on the performance of transition metal catalysts.[23] In the 1970's reports first appears relating the catalytic activity towards to ORR to the overlap integral between the e_g orbital of the transition metal in doped lanthanum nickel oxides and the sp_σ orbitals of the oxygen.[107] Matsumoto *et al*. reported that the larger the orbital overlap integral, the higher the electrocatalytic activity observed was.[108] In 2011, Sunntivich *et al*. extended this work by suggesting that the ORR activity of metal oxide catalysts could be tuned by tuning the e_g orbital occupancy to be approximately one.[106] They went on to suggest that this was due to the greater covalent contribution to the B-O_2^- species caused by the single occupancy of the e_g orbital, which transferred electron density into the σ* antibonding orbital. This caused increased instability in the bonding to the adsorbate, stabilizing it's displacement.

OER activity is dependent on morphology, oxidation state, composition and number of 3d electrons in the transition metal oxides.[109] Nickel and Cobalt oxides have been widely studied as OER catalysts due to their mixed oxidation states.[110] However, their activity is much lower than that of precious metal oxides. Doping with heteroatoms is

an effective way of tuning the OER activity of homometallic oxides, for example, McCrory *et al.* showed that by doping NiO_x with iron, the overpotential can be reduced from > 0.4 to 0.35 V.[18]

Both ORR and OER catalysts require efficient electron flow through the electrode material to generate a large current response.[111] Although many transition metal oxides have been shown to be active as oxygen electrocatalysts, most TMOs of interest (perovskites and some spinels) possess poor electrical conductivity at room temperatures which limits their effectiveness as oxygen electrocatalysts.[112] To address this issue, most published studies add a secondary phase to the oxide consisting of a highly conductive carbon (e.g carbon black, nanotubes or graphene) or add a conductive carbon support during synthesis.[113] The addition of carbon has been shown to influence the catalytic activity dramatically. Mohamed *et al.* systematically studied the effect of addition of acetylene black on the OER activity of perovskites.[114] They found that the addition of acetylene black significantly enhanced the OER activity of single perovskites, although the activity of double perovskites remained largely unchanged.

1.5.1. Perovskites as Oxygen Electrocatalysts

Perovskites are one set of structural materials which show promise for the replacement of PGM catalysts for the ORR. They have the general formula ABX_3, where *A* is commonly a group II cation, lanthanide cation or a mixture of the two and *B* is commonly a transition metal in the +4 oxidation state. *X* is a negatively charged anion and, in this thesis, will always be oxygen.

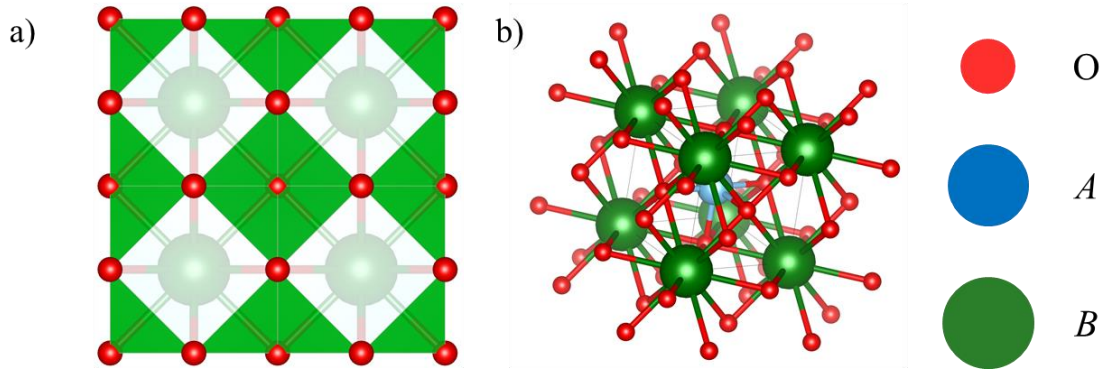

Figure 1.11: a): cubic perovskite oxide structure. b): unit cell of a perfect perovskite oxide.[115]

In a perfect perovskite with no oxygen vacancies (see Figure 1.11), the *A*-site ions are 12 coordinate to the oxygen, whereas the *B*-site ions are octahedrally coordinated to

oxygen. Most *A/B* combinations lead to structural distortion and/or oxygen vacancies, which causes a lowering in the effective coordination number of the cations, meaning that there are very few "perfect" perovskites.[116] This allows for huge structural flexibility within the perovskite family. The degree of deviation from the "perfect" perovskite structure can be calculated using the Goldschmidt tolerance factor:[117]

$$t = \frac{r_A + r_O}{\sqrt{2}(r_B + r_{O)}} \quad (1.13)$$

where r_x is the ionic radii of the species and r_O is the ionic radius of oxygen and is equal to 1.4 Å. However, the perovskite structure is flexible and can withstand mismatch between bong lengths and strain in the structure, allowing for many ions to be accommodated as *A* or *B* site dopants.

Perovskite based catalysts have many advantages over traditional PGM catalysts as they are lighter, more thermally stable and perhaps most importantly cheaper.[118] They are of particular interest as their intrinsic activity can approach that of the current Pt, RuO_2 and IrO_2 industrial catalysts.[90] Since the initial exploration of perovskite catalysts for the ORR and OER in the 1970's, there has been a wealth of literature published examining both new perovskite materials and the activation mechanism on the surface of the perovskites. This is due to the unique structural flexibility which allows for much versatility in the composition of the perovskites studied.

In the 1980s, Bockris *et al*. reported the activity of the ORR on 18 substituted perovskites based on $La_{1-x}Sr_xMO_3$ (*M* = Co, Ni, Mn, V, Cr and Fe).[119] They observed that a higher activity was seen with a high occupancy of the σ* orbital and proposed that a volcano plot could be drawn relating activity to *M*-OH bond strength. They saw that an increase in catalytic activity towards the ORR occurred in parallel with a high orbital occupancy of the antibonding *M*-OH. This work was reiterated by J Suntavich *et al.* in 2011 as shown in Figure 1.10.[106] They showed that an e_g filling of ~1 gave maximum activity. This was rationalised by stating the rate determining step can be affected by the degree of covalency in the *B*-OH^- bond, and by transferring the antibonding electron to the O_2^{2-} adsorbate, the displacement of this absorbate was stabilised, thus increasing the rate of ORR kinetics.

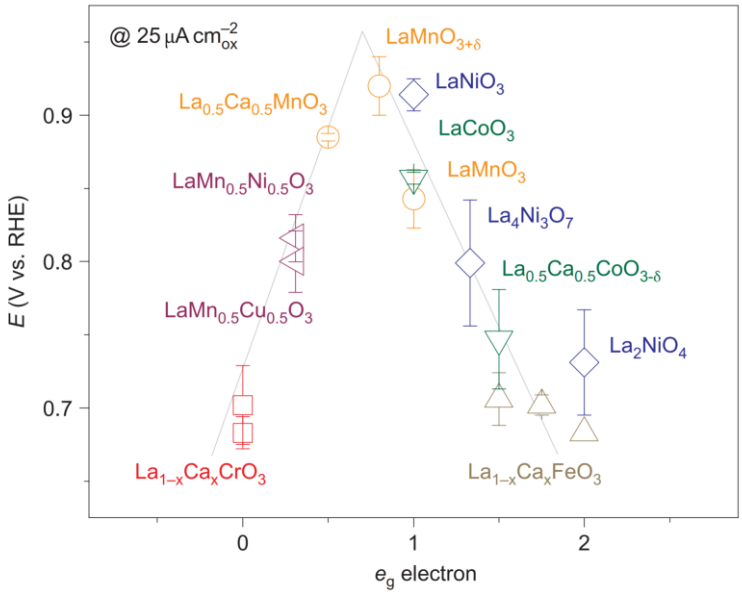

Figure 1.12: A volcano plot showing the relationship between activity of the perovskite for ORR and the filling of the e_g orbital.[106] Reprinted with permission from reference 106. Copyright (2011) Springer Nature.

There have been suggestions in the literature that nanoparticulate perovskites exhibit higher intrinsic ORR activity than their bulk counterparts. Li *et al.* described the synthesis of high surface area $LaMnO_3$ nanoparticles with activity for the ORR on RDE electrodes comparable to a commercial Pt/C catalyst.[120] When evaluated in a Li-air battery the nanoparticles showed improved cycling stability and specific capacities compared to their bulk counterparts. Partially substituting at either the *A* or *B* site of the perovskite has also been shown to dramatically alter the physical and electronic characteristics of perovskites. By substituting at the *A* site, the mean oxidation state at the *B* site can be influenced, and this in turn increases or decreases the e_g orbital filling, directly affecting the catalysis.[121] Xue *et al.* doped $LaMnO_3$ with varying amounts of Ag and examined the mean oxidation state of Mn by XPS. They found that 30% Ag led to an optimum in the interplay between $Mn^{3+}$and Mn^{4+} at the *B* site, giving rise to an onset potential for the ORR close to optimum (0.959 V) and good durability of the electrocatalyst. Zhang *et al.* substituted Ni in the parent $LaNiO_3$ material for Fe and saw an enhancement of the ORR activity, with onset potentials shifting to more positive values for $LaNi_{0.8}Fe_{0.2}O_3$.[122] It was suggested that this was due to the Fe being capable of supressing the formation of Ni^{II} on the perovskite surface, thus forming a stronger Ni-O bond.

Perovskite oxides are also an attractive sub-set of transition metal oxides for the OER due to their structural flexibility.[123] Crystal vacancies are important in catalytic activity for OER.[32] Suntivich *et al.* studied 10 catalysts and found that $Ba_{0.5}Sr_{0.5}Co_{0.8}Fe_{0.2}O_{3-\delta}$ (BSCF) was near the top of the observed activity volcano (see Figure 1.13).[124] They noted that the activity of the catalysts was dependent on the e_g filling of the *B*-site cation at the surface, the σ bonding e_g orbital has a stronger overlap with the absorbed oxygen species than the π-bonding t_{2g} orbital, and therefore can directly influence electrons between the surface of the catalyst and oxygen. The highest activity for OER is expected at orbital occupancy closest to one with high resulting covalency of metal-oxide bonds.

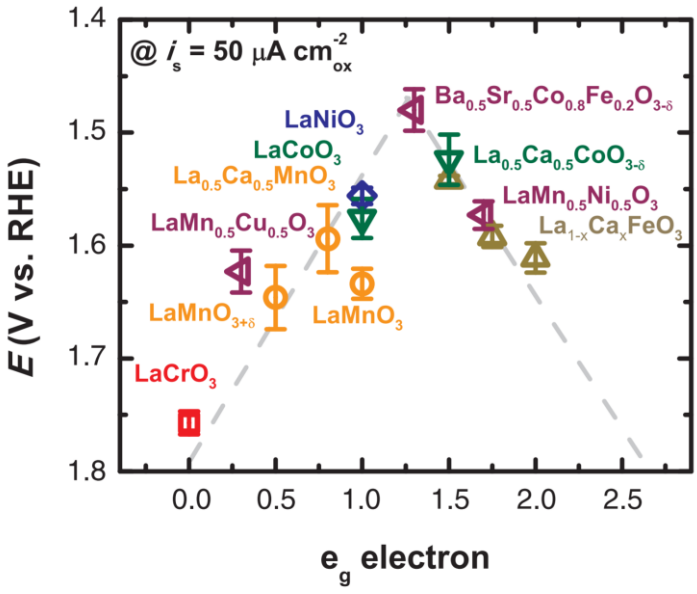

Figure 1.13: Volcano plot showing the activity of metal oxides towards the OER versus the e_g orbital electron occupancy.[124] Reprinted with permission from reference 124. Copyright (2011) American Association for the Advancement of Science.

Nanosizing perovskites has also been shown to influence the OER catalysis. Zhou *et al.* found that by reducing the $LaCoO_3$ perovskite particle size to c.a. 80 nm the e_g filling of the cobalt ions was increased above one, placing the catalyst at the optimum point on the volcano activity plot.[125] They suggested that this was due to a spin-state transition of the Co^{3+} ions originating from the small size and this was observed in both bulk magnetisation techniques and electron energy loss spectroscopy. Substitution at the *A* or *B* site has also been shown to affect the OER catalytic activity. Liu *et al.* found enhanced OER catalytic activity in a $LaMn_{0.7}Co_{0.3}O_3$ material with an overpotential > 200 mV better than the parent $LaMnO_3$.[126] They suggested this was due to cobalt

shortening the lattice spacing, shortening average Mn-Mn distance and therefore promoting the formation of the O-O bond on the surface of the perovskite.

1.5.2. Spinels as Oxygen Electrocatalysts

Another set of interesting transition metal oxide materials are those with the spinel structure, AB_2O_4. Spinels exist generally in two distinct crystalline structures, normal and inverse (see Figure 1.14). The normal spinel oxide structure is a cubic close packed array of O^{2-} ions with *A* cations occupying the tetrahedral interstitial sites and *B* cations occupying the octahedral interstitial sites. Cation *A* can be in either the +2 or +4 oxidation state whereas *B* can be in the +3 or +2 oxidation state. However, if *B* is more stable in the octahedral sites than the tetrahedral sites, then an inverse spinel may form according to a site preference theory.[127] This can be written as $B(AB)O_4$ where half of the *B* site cations are occupying the tetrahedral interstitial sites, with the *A* cations and the other half of the *B* cation occupying the octahedral interstitial sites.

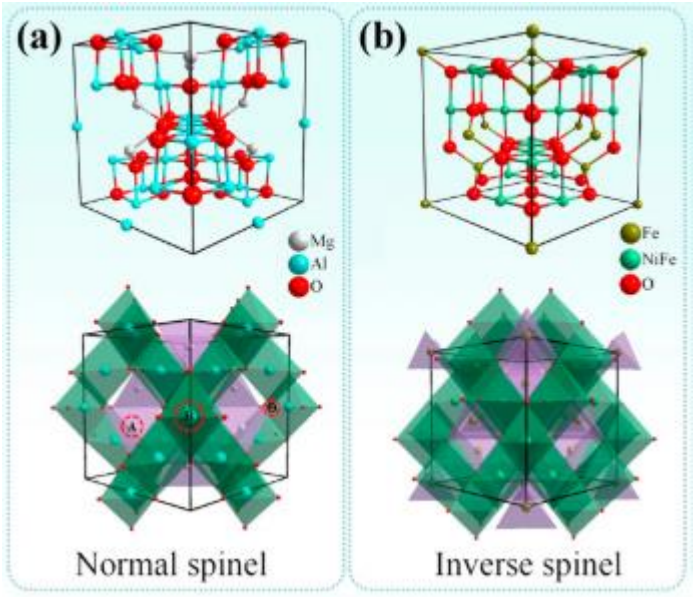

Figure 1.14: a) Crystal structure and unit cell of a normal type spinel. b) Crystal structure and unit cell of an inverse type spinel.[128] Reprinted with permission from reference 128. Copyright (2017) American Chemical Society.

Wei *et al.* provided a rational design approach to a series of $MnCo_2O_4$ spinel materials, where the ORR activity could be tuned by carrying out differing heat-treatments.[129] The activity to the ORR could be described as a function of Mn valence. This work was then applied to other transition metal spinels (see Figure 1.15). As with

perovskites, the activity towards the ORR can be described as a function of octahedral e_g orbital filling.

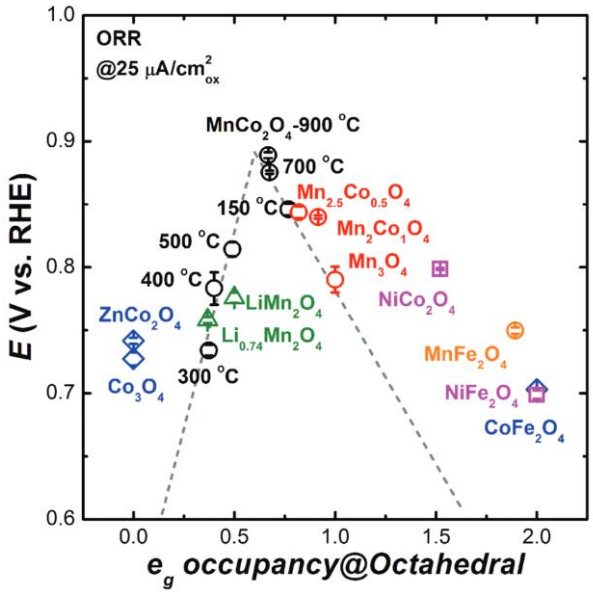

Figure 1.15: A volcano plot showing the relationship between activity of the spinel material for ORR and the filling of the e_g orbital.[129] Reprinted with permission from reference 129. Copyright (2017) John Wiley and Sons.

Du *et al.* successfully synthesised $CaMn_2O_4$ nanorods for oxygen reduction via a low temperature route.[130] They found that the catalytic properties of the materials showed favourable ORR activity, low peroxide formation, with high electron transfer number as well as higher stability than a commercial Pt/C catalyst in alkaline solution. Li *et al.* synthesised ultra-small cobalt manganese spinels at low temperature.[131] When employed as catalysts for the ORR the low temperature materials outperformed the high temperature materials. They discovered that the electrocatalytic activity of the "CoMnO" spinel family corresponded to the crystallographic phase and therefore the surface valence of the Co and Mn. The optimised catalyst had similar activity and greater electrocatalytic stability than that of Pt/C.

Spinels are also an attractive structure group for the OER due to their electronic conductivity and versatile elemental composition.[132] Wei *et al.* performed a systematic study on several Mn containing spinels and found that for the OER, the Mn in the octahedral site could be identified as the active site.[129] They went on to successfully apply this rule to several other spinel materials and discovered an activity descriptor.

As with perovskites, for optimal OER activity an e_g occupancy (at the octahedral site) of slightly greater than one was needed (Figure 1.16).

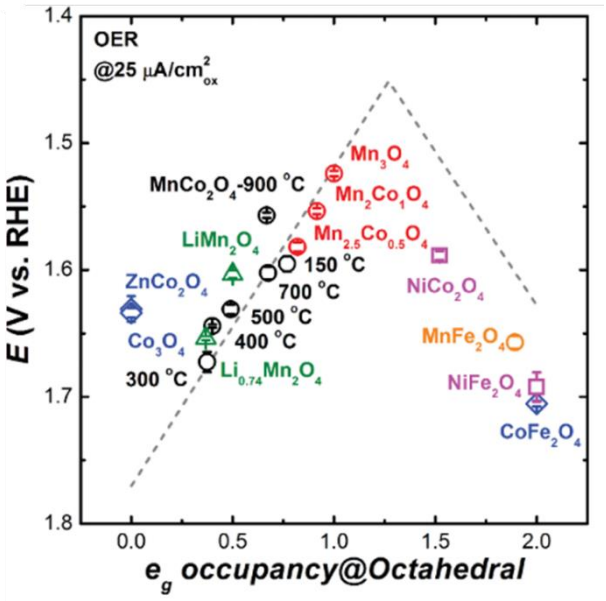

Figure 1.16: A volcano plot showing the relationship between activity of the spinel material for OER and the filling of the e_g orbital.[129] Reprinted with permission from reference 129. Copyright (2017) John Wiley and Sons.

He *et al.* used this rational design to synthesis $NiMnO_3/NiMn_2O_4$ hybrid electrocatalysts.[133] They found that $0.61NiMnO_3.NiMn_2O_4$ had the highest OER activity with an overpotential of 380 mV at 10 $mAcm^{-2}$ and a high mass activity of 291 A g^{-1}_{ox}.

1.6. Nanomaterials

For a material to be classified as a nanomaterial, it must have at least one dimension less than 100 nanometres (1 x 10^{-7} m). Many nanoparticulate shapes have been synthesised including ribbons, sheets, rods and tubes. There is a growing interest in the use of nanomaterials, including nanoparticulate metal oxides, for a variety of applications including catalysis, sensors and optics.[134] This is due to the unique optical, catalytic and electrical properties that are afforded to them by their small size.[135] Therefore, if we can tune size, composition and shape of the nanoparticles, theoretically we can control material properties.[136] Quantum confinement and surface properties dictate the optical, magnetic and catalytic properties of the material. For example, bulk gold is chemically inert but nanoparticulate gold is catalytically active for the oxidation of carbon monoxide.[137] Nanoparticles tend to have higher surface areas than bulk

materials, meaning that a larger number of catalytic sites should theoretically be accessible to reactants and intermediates in a catalytic reaction, which should give a higher catalytic activity. However, as these properties are highly dependent on the size and shape of the nanomaterial, the synthetic method chosen is very important to afford control over nucleation and growth mechanisms. Nanomaterials are being studied for application in a wide range of catalytic reactions such as Fischer-Tropsch catalysis[138], reduction of CO_2[139] and for the ORR and OER reactions.[140]

1.6.1. Synthesis of Nanomaterials

Nanomaterial synthesis can be chiefly divided into two categories: bottom up synthesis and top down synthesis (Figure 1.17). The use of top down synthesis involves having large starting structures (micron sized or larger) and then fracturing these up into smaller, nanostructures. Examples of this include lithography[141], vapour phase infiltration[142] and most typically ball milling[143]. In ball milling, the macroscopic material is placed into a pot with balls (e.g. ceramic or zirconia balls) and then spun. The balls act as a grinding agent, breaking the larger structures up into nanoparticles. This is energy expensive as it is a high intensity process, and it produces a wide size distribution in the final product as it is difficult to control. Lithography involves depositing a thin layer of substrate onto a support material. A beam of radiation is then used to pattern the substrate with nanostructures.[144] As material is often lost as bulk sample, top down synthetic methods are often seen as wasteful. Examples of bottom up synthesis are much more common in the literature. In general, these can be divided into wet chemical processes and other synthetic methods. Wet chemical synthetic techniques include hydrothermal synthesis[145], sol-gel synthesis[146] and precipitation reactions[147]. There are several advantages of wet chemical synthetic techniques. These include the quick synthesis times, the in-expense of many of the techniques and the ease of scalability. A synthetic method that allows for fine control over material properties (e.g. size, shape, electronic properties) would be preferred as nucleation and growth are key to final material properties, Bottom up methods have the advantage here because growth can be controlled by varying a variety of conditions in the synthesis (temperature, pH[148], chemical additives[149], reaction time[150] etc.).

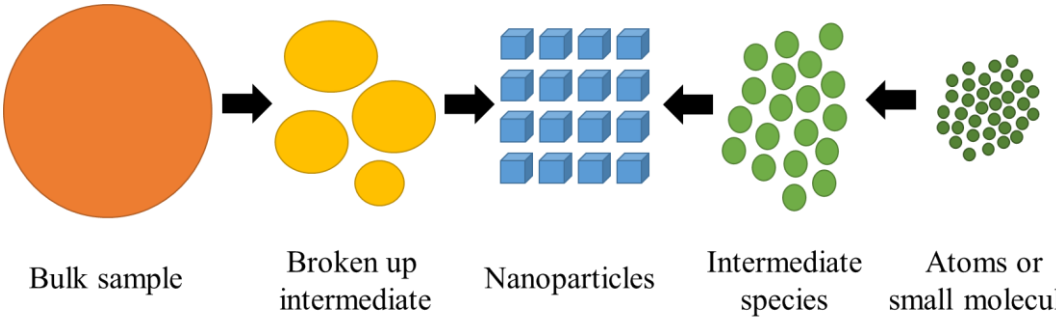

Figure 1.17: Diagram showing the difference between top down synthesis of nanoparticles (left) and bottom up synthesis (right).

The formation of nanoparticles is widely accepted to occur in four steps: I) precursor formation, II) nucleation, III) growth and IV) aging.[151]

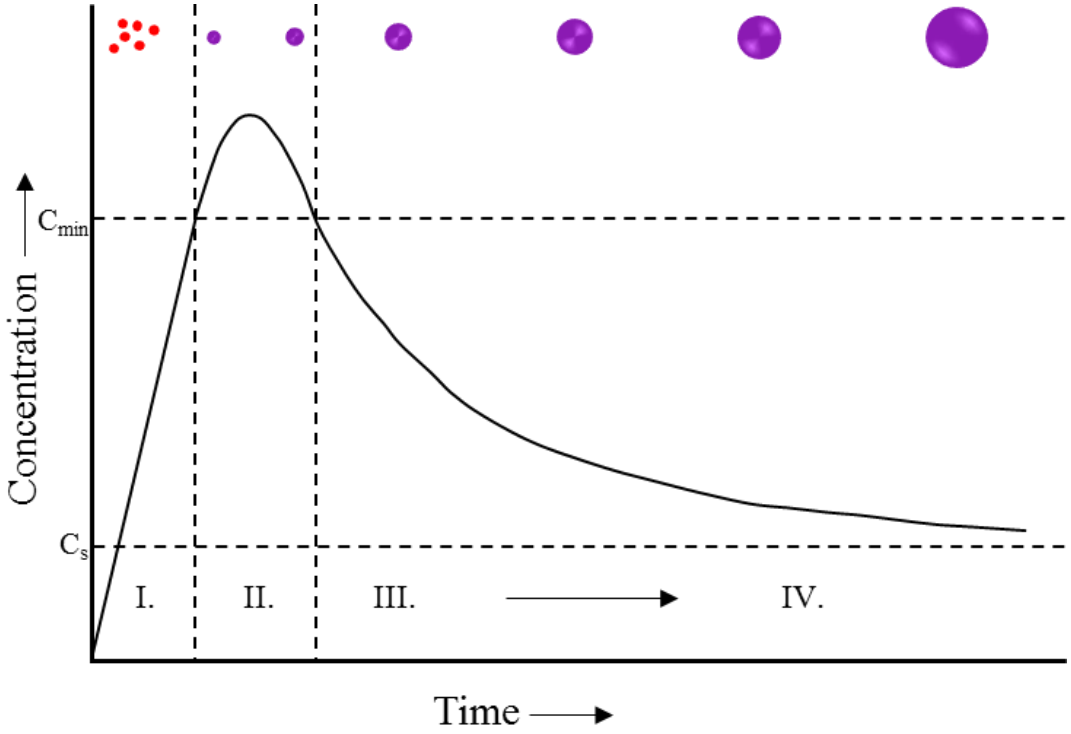

Figure 1.18: Diagram of the La Mer mechanism. I. the concentration of the precursor in solution increases to a critical supersaturation point. II. the energy barrier for nucleation has been reached allowing for the nucleation of nanoparticles, this then causes the decrease in precursor concentration seen (III).

The most widely excepted model for explaining how nanomaterials are formed in solution is the La Mer model of nanoparticle formation.[152] The plot shown in Figure 1.18 can be described as follows: initially (I on Figure 1.18), concentration of some species in solution is increasing by some synthetic mechanism (e.g. acid base

reaction or reduction). A critical supersaturation point is reached where nucleation is possible but "effectively infinite"[153]. The concentration of the species in solution will continue to increase until point C_{min} is reached, at which point the energy barrier for nucleation has been overcome. This allows for rapid nucleation of nanoparticles (II), leading to a rapid decrease in the concentration of the species in solution. This lowers the concentration below the nucleation level (III). At this point nanoparticle growth continues via other mechanisms (IV).

1.6.2. Classical Nucleation

Nucleation is the formation of nuclei (small particulates) which act as seeds for crystal growth. Homogeneous nucleation occurs from solution by molecular driving forces whereas heterogeneous nucleation occurs due to the presence of foreign bodies in the solution.[154] Homogeneous nucleation can be described thermodynamically by considering the total free energy of the nanoparticle in solution:

$$\Delta G = 4\pi r^2\gamma + \frac{4}{3}\pi r^3 \Delta G_v \tag{1.14}$$

where ΔG is total free energy, r is the radius of the particle, γ is the surface energy of the crystal and ΔG_v is the free energy of the bulk crystal, given by:

$$\Delta G_v = \frac{-k_B T ln(S)}{v} \tag{1.15}$$

where k_B is the Boltzmann constant, T is the temperature, S is the supersaturation of the solution and v is the molar volume. Minimising equation 1.14 with respect to the particle radius gives an expression for the crystal free energy. This is due to the fact surface free energy is always positive, and that crystal free energy is always negative.

$$\Delta G_{crit} = \frac{4}{3}\pi\gamma {r_{crit}}^2 = \Delta G_{crit}^{homo} \tag{1.16}$$

The size at which a particle can survive without re-dissolution is described by the critical radius, r_{crit}:

$$r_{crit} = \frac{-2\gamma}{\Delta G_v} = \frac{2\gamma v}{k_B T ln S} \tag{1.17}$$

The rate of nucleation, N, is described by[155]:

$$\frac{dN}{dt} = Aexp\frac{\Delta G_{crit}}{k_B T} = Aexp(\frac{16\pi\gamma^3 v^2}{3{k_B}^3 T^3 (lnS)^2}) \tag{1.18}$$

Therefore, experimental factors can be varied to control the nucleation. These are surface free energy, supersaturation (concentration), and temperature. Surface free energy can be controlled by adding additional species into the solution e.g. surfactants.[156]

1.6.3. Classical Growth

As precursor concentration decreases below the nucleation threshold (Fig 1.18: II-III), the nuclei begin to grow. Growth depends on: 1) The transport of species through bulk solution to the crystal surface and 2) the reaction of the species on the crystal surface. Therefore, the growth of the particles can be controlled by tuning the supersaturation of the solution and other reaction parameters. There are two different pathways by which growth can occur: i) diffusion limited or ii) reaction limited pathways. If growth rate is fast, then the diffusion limited pathway is likely to be dominant whereas if the transfer of reagent to the nuclei is slow, growth will occur by a reaction limited pathway. The growth rate when diffusion is the limiting factor can be described by:

$$\frac{dr}{dt} = \frac{Dv}{r}(C_b - C_s) \tag{1.19}$$

where r is the radius of the particle, D is the diffusion coefficient through the solutions, v is the molar volume, C_b is the concentration of reagent and C_s is the solubility of the sold.

Therefore, the smaller the radius r, the faster the rate of particle growth. When growth is reaction limited, the opposite is true and growth is favoured for larger particles, determined by the rate of the surface reaction.

1.6.4. Ripening and Termination

Ostwald ripening is defined as the dissolution of small crystals into solution and the redeposition of these onto the surfaces of larger crystals.[157] Due to the high surface energy and solubility of these small crystals they re-dissolve allowing for the growth of larger crystals. This can be described by the Gibbs-Thomson equation, where the solubility of C is given as a function of r:

$$C_r = C_b \exp\left(\frac{2\gamma v}{r k_B T}\right) \tag{1.20}$$

Other examples of particle ripening mechanisms are coalescence and orientated attachment. Both occur when two particles attach. However, they differ in the

orientation of the crystal lattice at the grain boundary. Coalescence occurs when there is a random attachment of two particles, leading to a mismatch of lattice planes. Orientation occurs when there is a perfect alignment of particles allowing for continuous crystallographic planes.

Termination of nanoparticle nucleation and growth occurs as reactants are consumed and when the nanoparticle has reached the most stable conformation possible (minimisation of surface energy). Nanoparticles can be stabilised in order to reach termination more quickly and there are two common approaches: i) steric hindrance through the use of capping agents (usually polymers or surfactants) or ii) by using charged species at the surface of a nanoparticle to induce electrostatic repulsion.[152]

1.7. Synthesis of Mixed Metal Oxides

As has been discussed above, the synthetic path and conditions chosen play a large role in the physical and chemical properties of the material synthesised. Traditionally, mixed metal oxides are prepared via a "solid state reaction" where a high temperature is used to combat slow solid diffusion (Figure 1.19).[158] Oxides, carbonates or salts are mechanically mixed and then heat treated, usually above 1000 °C. The properties of the as-prepared materials are related to preparation or sintering conditions.[159] This method often yields large particle size distributions, phase impure materials, is energy intensive and there can be uncontrolled growth of material.[160] Intensive milling of the precursor materials can somewhat overcome this, as can tuning the sintering of materials however these are energy intensive processes.[161] Despite the disadvantages, the solid-state method remains popular with research and industrial scientist alike due to its simplicity.

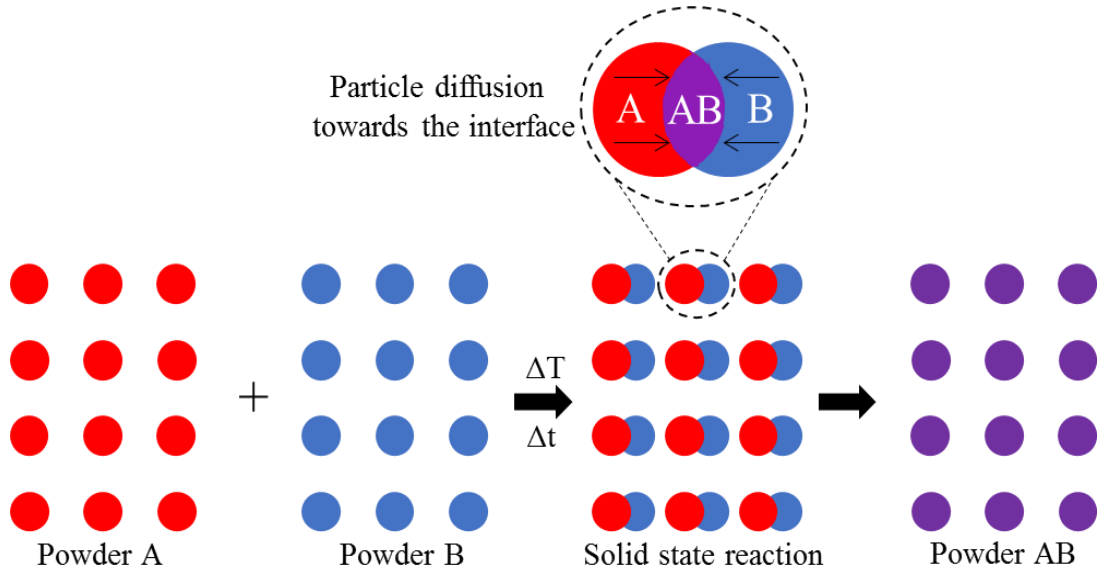

Figure 1.19: Simplified diagram of a solid-state reaction occurring. Powder A and B combine under temperature and time giving the combined powder AB.

Self-combustion reactions are one synthetic method that can overcome the problem of lack of phase purity. The metal salt precursors are mixed with a fuel material (such as urea or sucrose) and then the mixture is ignited, instantaneously obtaining nano-ceramic oxides.[162] Two advantages of pyrolysis (self-combustion reactions) over solid state reactions are that particle size distributions are usually narrow due to the short synthesis time and that crystalline, phase-pure products are usually formed.

Sol-gel synthetic methods (such as the Pechini[163] method) have also been investigated for the synthesis of metal oxides. The Pechini method involves the complexation of ethylene-diaminetetraacetic (EDTA)-Citrate followed by the addition of ethylene glycol. pH is controlled with the addition of NH_3H_2O (ammonia water). This method has several advantages as it produces high purity, homogeneous perovskite materials whilst allowing for accurate control of the composition of the final material.[164,165] The chelating agent (in this case EDTA) is used to prevent the partial segregation of metals in the final compound whilst the ethylene glycol promotes polymerization leading to a homogeneous distribution of ions, minimising segregation of metals during the decomposition of the chelate at heat treatment.[166] Although heat treatment temperatures are still high (800-1000 °C) the sol-gel method is flexible, delivering controlled, homogeneous metal oxides therefore making it attractive as a preparation route to perovskite and spinel materials.[167,168]

Finally, the co-precipitation method can be used. It requires supersaturation conditions where soluble metal ions are mixed with a precipitation agent, usually a base. In this method it is important to control temperature, pH, concentration and mixing rate to reach the desired physical characteristics in the final product (such as particle size and morphology).[165,169] The precipitated product is separated from the liquid, washed, dried and then fired to produce the final material. However, due to differing solubilities of metal cation precursors, the method requires much optimisation. [170]

1.8. Synthesis in Water

The synthetic methods described above use toxic/polluting chemicals in the synthesis or use high temperatures for extended periods of time. The search for "greener" synthetic routes to many materials has begun due to increasing awareness and concerns about the impact of chemistry research on the environment. The interest in the use of water as a solvent has grown in recent years as it is an inexpensive, readily available and most importantly environmentally benign solvent.[171] As water is polar in nature, and can form hydrogen bonds, it is often considered a universal solvent. However, it is poor at solvating non-polar materials (such as long chain hydrocarbons) and due to the ready dissolution of salts, trace impurities can remain in water even after purification.

1.8.1. Supercritical Water

Supercritical water has very different properties to liquid water due to the high pressure and temperature changing the way the water behaves.[172] A supercritical fluid is a substance which has been taken above its critical pressure and temperature, where distinct liquid and gas phases do not exist, but the pressure is lower than that required for compression into a solid. The supercritical point of water occurs at a pressure of 221 bar and a temperature of 374 °C.[173]

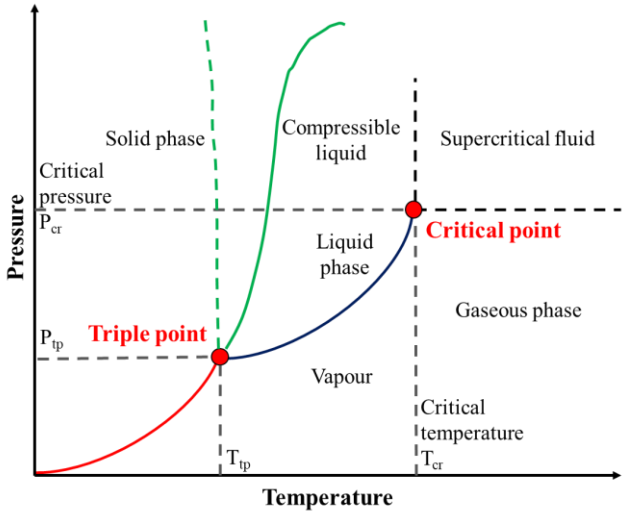

Figure 1.20: Generic phase diagram of materials showing the relationship between pressure and temperature and the phase of the material which is seen. The dotted solid-phase boundary represents an analogous substance whose liquid is denser than the solid, such as water.

At the supercritical point the dielectric constant of water decreases from 78 F m^{-1} to below 10 F m^{-1} which is in the region of polar organic solvents[174]. This has a large effect on the solubility of species and rate of formation of chemical species.[175] The density of water also decreases at the supercritical point, from 0.997 g cm^{-3} to 0.322 g cm^{-3}.[176]

The dissociation constant of water is characterised by the equilibrium constant, Kw, defined as:

$$K_w = [H^+][OH^-] \tag{1.21}$$

where K_w is the ionic product of water, $[H^+]$ is the concentration of protons in solution and $[OH^-]$ is the concentration of hydroxide ions in solution.

Under ambient conditions $[H^+] = [OH^-] = 1 \times 10^{-7}$ mol dm^{-3}. However, K_w depends on the temperature and pressure of the water.[177] A useful quantity to track K_w is pK_w defined as:

$$pK_w = -log_{10}K_w \tag{1.22}$$

At room temperature, pK_w is equal to 14. Under supercritical conditions, this value decreases to 11 which leads to an approximate 30 fold increase in the concentration of both hydroxide ions and protons.[178]

Hydrothermal synthesis is a broad term generally used to encompass the use of supercritical water as a solvent. Although the definition of hydrothermal synthesis is a heterogenous reaction under high pressure and temperature in an aqueous solvent, this has grown to include synthesis in sub-critical pressurised water due to limitations with corrosion in reactors due to the harsh conditions above the supercritical point.[179,180] There are many advantages of hydrothermal synthesis over lower pressure and temperature synthetic techniques. The nanostructures formed can be controlled by varying temperature, time or fill level of the reaction vessel.[181,182] Due to the extreme conditions, reaction temperatures are often lower requiring less energy input, secondary heat-treatment steps are often not necessary and cleaning methods often use water rather than organic solvents, making the work-up process greener.[178] Shape can be controlled by adding surfactants to the reaction mixture which can act as chelating or capping agents.[183] However, because of the use of pressure vessels, cost of reactors can be expensive and it is often impossible to visually observed the reaction occurring.

1.8.2. Continuous Hydrothermal Flow Synthesis

Hydrothermal synthesis of nanomaterials has traditionally been done in batch processes. However, there is now growing interest in the use of Continuous hydrothermal techniques, minimising batch to batch variations and speeding up the production of nanomaterials. Continuous Hydrothermal Flow Synthesis (CHFS) processes share many similarities with hydrothermal vents on ocean beds, where minerals solvated by hot pressurised water under the crust of the Earth are forced out into the ocean forming mineral deposit "chimneys". The CHFS process consists of a stream of supercritical water, meeting a stream of aqueous metal salts in a mixer. This causes the rapid precipitation of nanoparticles. Many different materials have been produced using this technique including sulfides, hydroxides, phosphides, pure metals and metal oxides.[178] Reaction times are in the order of seconds[184] and the process gives superior control of final particle parameters by varying residence time, reaction temperature, pressure, pH, chemical species, mixer design and precursors.[185–187] A simplistic view of processes occurring in the mixer is presented below. A series of hydrolysis and dehydration reactions form the nanoparticles although in reality there will be many other reactions involved in the process including those of the anion and oxyhydroxides.[188]

Hydrolysis: $M(NO_3)_{x(aq)} + xH_2O \rightarrow M(OH)_{x(s)} + xHNO_3$ (1.23)

Dehydration: $M(OH)_{x(s)} \rightarrow M(O)_{\frac{x}{2}(s)} + \frac{x}{2}H_2O$ (1.24)

There are many different designs of CHFS reactor to be found in the literature. The CHFS process was initially developed in the early 1990s in the Japan and the U.S independently.[178] The U.S design involved pumping dissolved metal salt solutions through narrow pipes contained within a heated tube furnace. This allowed for rapid heating of the metal salt solution. Growth of the nanoparticles in the stream was then stopped using a quench step.[189] Although simple, this design was not widely adapted due to the necessity of a quench step and poor control overall of synthetic conditions. The Japanese design involved the use of two High Pressure Liquid Chromatography (HPLC) pumps, one pumping supercritical water and the other pumping dissolved metal salts. The two streams met in a tee-piece and then passed through a heated reactor.[190] This design has been widely adopted and has been used to synthesised many different nanoparticles. Updates to the design have led to a wide variety of CHFS reactors being used globally. Reactor configurations such as pipe diameters and mixing point can be adjusted and additional pumps have been added.[191] The mixer, where supercritical water and dissolved metal salts meet, is a particularly important feature in a CHFS reactor.[192] Studies on similar materials produced via CHFS often report differences in particle sizes or shapes, even though reaction conditions often appear similar or identical. This is because, depending on the mixing point design, the physical mixing of the fluids is different. Essential to the CHFS process is the proper mixing of the supercritical water feed with the ambient temperature metal precursor feed. This can be difficult due to the difference in densities between the supercritical water and the ambient temperature metal salt solution.[193] The design of mixer can cause blockages in the reactor, preheating of metal salt solution, and can affect the thermal history of the nanomaterials produced.[194] Substandard mixing can lead to local hot spots and cold spots, affecting particle homogeneity. Good mixing should prevent blockages from forming in any of the pipes and should ensure a low particle shape and size distribution. Lester *et al.* noted that the mixer design in the CHFS process can affect particle properties and the reproducibility of the reaction.[172] There are several mixer designs in the literature and these include vortex mixers, tee-pieces and counter current mixers.[195]

The simplest mixer design is simply the tee-piece mixer. Kawasaki *et al.* investigated how the direction of flow of the different fluids in the tee-piece mixer affected particle size (Figure 1.21).[196]

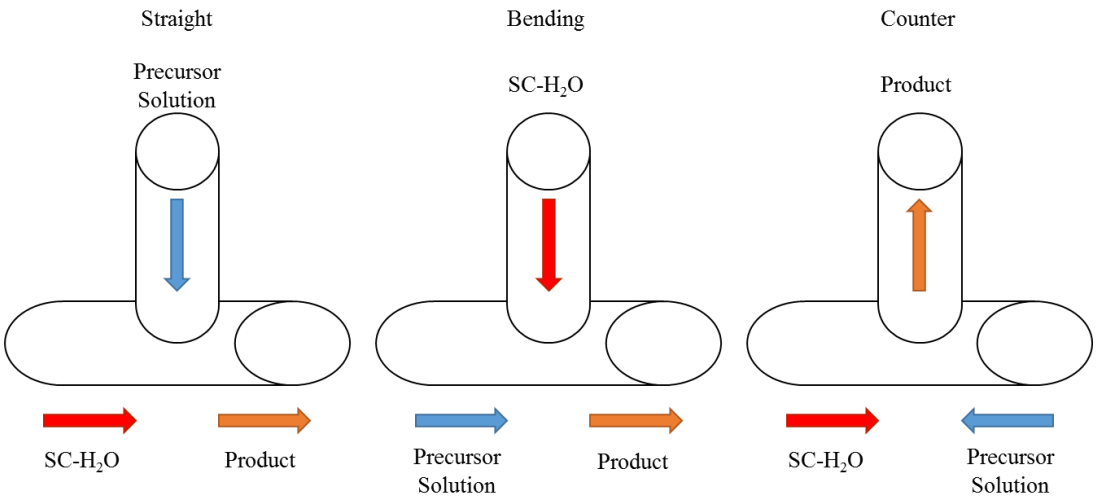

Figure 1.21: From left to right - mixing directions of straight stream, bending stream and counter stream in tee-piece mixers.

Little difference in particle size/shape was seen by the authors when changing the direction of flow of the different fluids in the tee-piece mixer. However, it was discovered that as flow rates decreased, or inner mixing dimeter increased, the particle size of NiO increased. They went on to develop a new mixer design, a swirling micro mixer, and then compared the results to the above study on NiO.[197] In this mixer, the supercritical water stream was split, creating two streams of super critical water, set at a 60˚ angle with respect to the precursor stream. They were displaced by < 1 mm compared to the mixer's central axis. The authors observed that even when the inner mixer diameter was greater than in the previous mixer, smaller particles were produced by the swirling micro mixer.

In 2006, a counter current "nozzle" mixer design was reported by Lester *et al.* It was designed with the intention of giving uniform, instantaneous mixing, with minimal "back-heating" of the precursor stream, a short residence time within the mixer itself and strong downstream flow, preventing blockages. Metal salt solution flowed upwards, through a wide outer pipe, whilst the supercritical water flowed downwards, through a narrower inner pipe fitted with a cone shaped nozzle. Reaction products were therefore forced to flow upwards, around the inner pipe as shown in Figure 1.22. They

reported that the nozzle mixer reduced reaction time and increased the reproducibility of the synthesis.

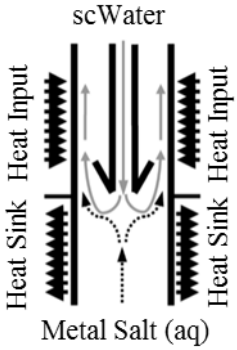

Figure 1.22: A schematic of a nozzle mixer reproduced from a work by Lester *et al.*[172]

Tighe *et al.* studied the counter current mixing occurring using X-ray synchrotron techniques and temperature analysis amongst other techniques.[198] They observed large temperature fluctuations with time below the outlet of the supercritical water pipe and overall a lower temperature was observed at the mixing point than was expected. Subsequently, a new mixer was designed - a Confined Jet Mixer or CJM. This mixer was designed to mix supercritical water with ambient temperature precursors in a co-axial arrangement involving a pipe in pipe configuration.[199] The inlet of the supercritical water flow was confined within the exit of the outlet pipe. This placement avoided blockages of the mixer whist promoting uniform, homogeneous mixing of supercritical and ambient feeds.[178]

There are many advantages to using CHFS as a synthetic method in the production of inorganic nano-materials. When evaluating the commercial viability of the synthesis of nanomaterials for a particular application several points should be considered; i) homogeneous nanomaterials should be produced with desired composition and characteristics, ii) the process should be resource and energy efficient, iii) it should be fast with few steps, iv) there should be no batch to batch variation, v) it should allow for in-line monitoring for quality control and vi) there should be flexibility to allow for tuning of the particles physical properties (i.e. the ability to change certain conditions such as pH and flow rate to effect particle size). Hydrothermal techniques offer significant benefits and meet many of the above criteria as they can operate at lower temperatures, have cleaner processing routes and are easier to scale up than gas-phase or plasma techniques.[200,201]

1.9. Combinatorial Synthesis

Combinatorial materials screening involves the production of large arrays of different materials, followed by the high-through-put measurement of the materials. The technique allows for accelerated materials development, and for the examination of structure activity relationships. CHFS has been previously used to produce combinatorial libraries of materials including $Ce_xZr_yY_zO_2$ materials for various applications. 66 unique nano-oxide materials were synthesised rapidly, and structural characteristics mapped using high-throughput Powder X-ray Diffraction (PXRD) and Raman spectroscopy.[202] Uniform changes in structural characteristics were observed across the studied phase space.[203]

Several different combinatorial synthesis approaches have been examined to produce libraries of oxygen electrocatalysts. Park *et al.* used an impregnation method to prepare a library of 66 ternary Pd-Ir-Ce catalysts on a multielectrode array.[204] They highlighted $Pd_{79}Ir_{12}Ce_9$ as the optimal composition and suggested this was due to decoration of the Pd with IrO_2 and CeO_2. Guerin *et al.* used physical vapour deposition to grow a gradient of Pd-Pt-Ir alloy compositions across a substrate.[205] Electrochemical measurements were taken using a 64-channel current collector and presented as a colour gradient across the ternary space. The study highlighted the power of combinatorial techniques in synthesising and screening large numbers of catalysts (over 800). Serra *et al.* used a sol-gel method to produce 25 catalysts and screened them in a fuel cell.[206] They identified several possible candidate materials, however due to the high temperature annealing required, all materials were ball milled before testing.

CHFS provides many advantages over the mentioned techniques. Reaction conditions are highly reproducible and direct scale-up is simple. When materials are not produced direct in flow, because of the extremely small size of materials produced, heat treatments tend to be less harsh than would be needed otherwise. As mixing is highly controlled, even after heat treatment, uniform size distributions and limited phase separation is usually observed negating the need for intensive ball milling procedures.[178] For these reasons, CHFS was chosen as an exciting synthesis method for the production of libraries of oxygen electrocatalysts.

1.10. Conclusions

This review of the literature surrounding transition metal oxides and their use as electrocatalysts has shown there is much interest in improving the electrocatalytic

performance of transition metal oxide catalysts for use in devices such as fuel-cells and metal air batteries. By carefully choosing elements and structures, transition metal oxides can be synthesised with the aim of competing with current precious metal catalysts. These materials could ultimately make hydrogen technology cheap enough to compete with other electrochemical storage devices such as lithium ion batteries.

The materials and methods used to synthesise and analyse the transition metal oxides for use as electrocatalysts will be discussed in Chapter 2.

2. Materials and Methods

2.1. Continuous Hydrothermal Flow Synthesis

All components of the CHFS reactor used in this report were built from standard Swagelok™ 316 stainless steel seamless pipe and parts (Swagelok Company, Hertfordshire, UK) unless otherwise indicated. A patented confined jet mixer (CJM, US Patent No. 20130136687) was made from standard parts. This mixer design ensured efficient mixing of the ambient temperature aqueous metal salt stream with the supercritical water. The use of this mixer has been described elsewhere.[195]

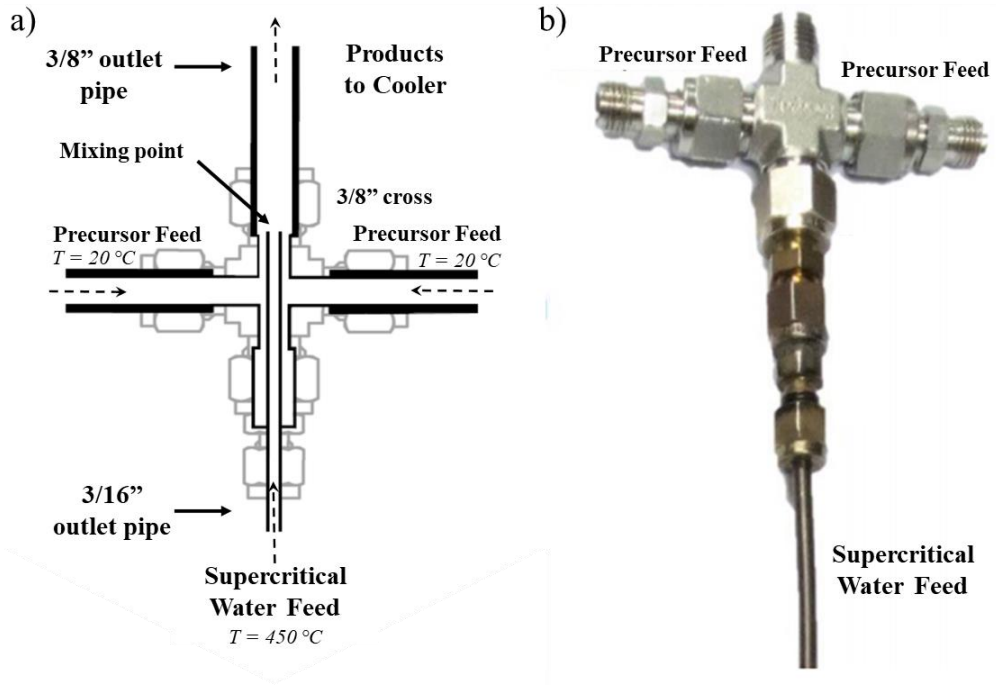

Figure 2.1: a) Diagram of the patented Confined Jet Mixer (CJM). b) Photo of the Swagelok™ CJM used in this thesis.

The CHFS process was pressurised to 240 bar using nitrogen. Pressure was maintained using a back-pressure regulator (BPR) (model EB1HP2 HF, with a 1 mm thick PEEK diaphragm, Equilibar, Fletcher, North Carolina, U.S.A). Up to 4 diaphragm pumps (high pressure Milton Roy Model PrimeRoyal K) were configured, allowing for variable flow rates from each independently. Pump 1 always pumped deionised water, pump 2 typically pumped dissolved metal salts and pump 3 typically pumped aqueous base. The feed from pump 1 was heated to 450 °C by being fed through custom built band heaters. Swagelok stainless steel pipe was wound tightly around an aluminium core allowing for good thermal conductivity. Additionally, 3 × 500 W band heaters

(Mineral Insulated Band Heater MB2J1JN1-E60, Watlow) were placed onto the coiled pipe and a hole was drilled in the aluminium core allowing for a 5/8" diameter, 200 W heater cartridge (Firerod, L8A80-L10j48T, Watlow) to be placed inside. Initially, the feeds from pumps 2 and 3 met in a tee-piece before passing into the CJM and mixing with the supercritical water feed. This gave a mixing temperature of 335 °C. The mixing temperature could be adjusted by changing the temperature of the heaters (and thus of the supercritical water feed) or by changing the flow rates of the pumps. Mixing the metal salt/base feed with the supercritical water feed in the CJM in this way resulted in the rapid precipitation of nanoparticles which were then passed through a pipe-in-pipe heat exchanger, cooling the slurry to < 50 °C. If a 4-pump set up was used, then an addition precursor stream from pump 4 met the precipitated nanoparticles in a second CJM, acting as a quench feed, before the slurry passed through the pipe-in-pipe heat exchanger giving a second mixing temperature of < 150 °C. The product was collected from the exit of the BPR as a nanoparticulate slurry. Once collected, the slurry was left to settle and then the supernatant decanted off. The slurry was then centrifuged (Sigma model 4-15 10730, Sigma Laboratory Centrifuges, Gottingen, Germany) at 4500 rpm until solids were completely settled. The nanoparticle paste was then cleaned in one of two ways. Either by dialysis, where the sample was resuspended into deionised water and placed into a dialysis bag in a tank of water which was replaced approximately once an hour until the conductivity inside the bag was <100 µS. Or it was washed by centrifuge, requiring between 5 and 8 centrifugation steps, with the nanoparticulate paste resuspended in deionised water between each centrifugation step. The clean pastes were then freeze dried (VirTis Genesis 35 XL). Nanoparticulate pastes were frozen to < −40 °C, then slowly heated up to ambient temperature under vacuum (10 to 15 Pa) over approximately 18 hours. This gave a fine powder of the as synthesised product.

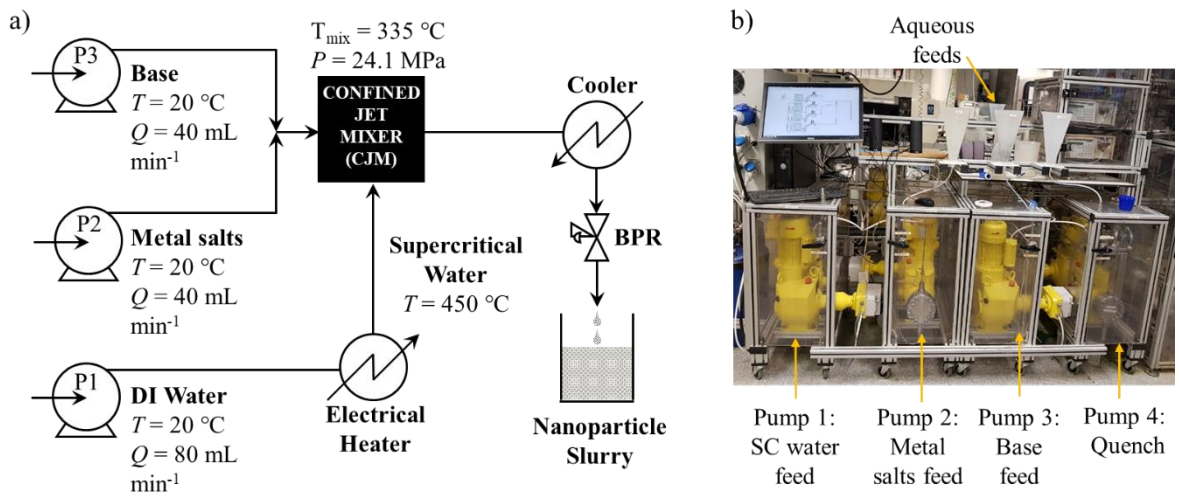

Figure 2.2: a) General diagram of the Continuous Hydrothermal Flow Synthesis (CHFS) set up used. b) Photograph of the CHFS reactor used in this report (lab scale).

2.1.1. Combinatorial Synthesis of Perovskite Titanate Materials

For the synthesis of group 2 titanates, a two-stage synthesis was employed. First, a Ti Sol was synthesised using an additional 5 m pipe heated to 250 °C (residence time approx. 15 s) situated between the mixing point and the pipe-in-pipe chiller. The incoming water temperature was 310 °C and the mixing temperature was < 199 °C. Once the sol was collected, the group two metal salts (barium, strontium and calcium nitrates) were dissolved in the as synthesised Ti sol with no further alterations. The metal ratios used are shown in Table 9.1 in the appendix. The standard three pump set up was then used as described in Section 2.1. A schematic showing the complete synthesis is shown below in Figure 2.3.

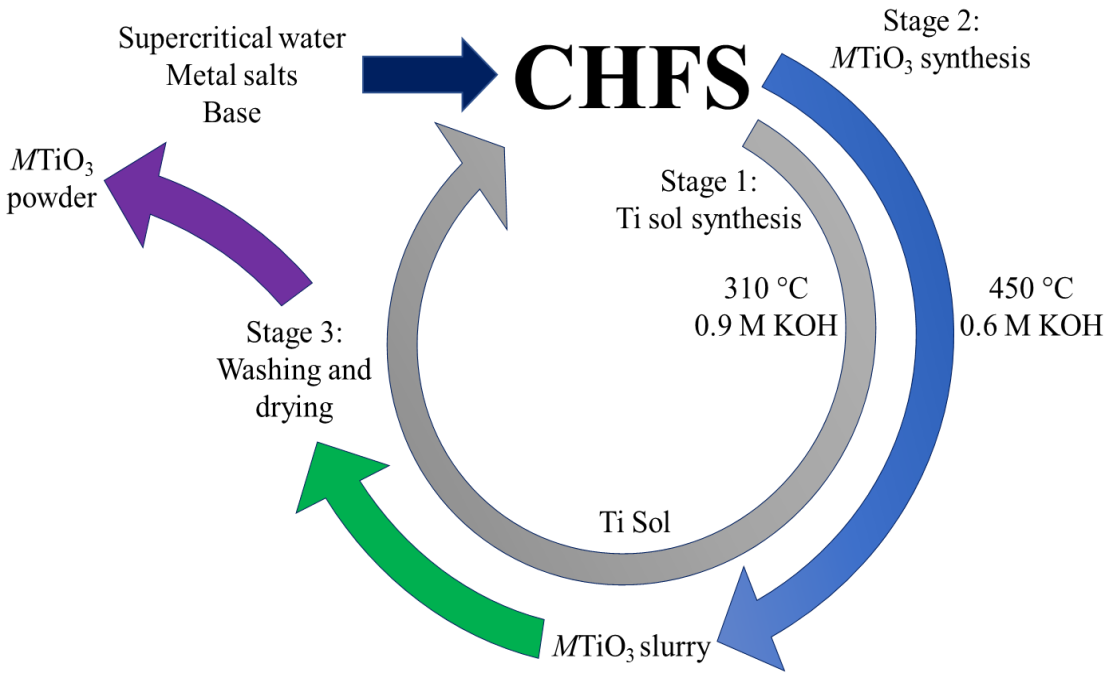

Figure 2.3: Schematic diagram showing the complete synthesis of the titanate materials. The Ti sol is synthesised initially and the passed back through the reactor as a titanium precursor.

Once the slurry had been collected it was washed twice with 1 M acetic acid to remove any trace carbon impurities before being washed by centrifuge. When the conductivity was < 100 µS the samples were freeze dried. Powders were then used with no further treatment.

The precursors used were TiBALD [titanium(IV) bis(ammonium lactate) dihydroxide solution, 50 wt.% in H_2O, Sigma Aldrich, Dorset, UK], $Ca(NO_3)_2{\cdot}4H_2O$ (>99%), $Ba(NO_3)_2$ (>99%) or $Sr(NO_3)_2$ (>99%) (anhydrous unless stated, Sigma Aldrich, Dorset, UK) and KOH (potassium hydroxide, analytical grade, Fisher Scientific).

2.1.2. *A*MnO_3 Materials and their Optimisation:

A range of *A*MnO_3 materials were synthesised using the standard three pump set up described in Section 2.1. For all samples, flow rate ratios (mL min^{-1}) were kept constant at 80:40:40 for Pump 1:2:3. The supercritical water temperature was 450 °C giving a mixing temperature of 335 °C, and the calculated residence time was ca. 7 s. The wet nanoparticles were cleaned by dialysis until the conductivity was < 100 µS before being freeze dried. All nanoparticles required a further heat treatment before being used as oxygen electrocatalysts.

Table 2.1: Synthesis conditions for the *A*MnO_3 samples. HT1 = 1100 °C, 3 hrs, ramp rate 10 °C min^{-1}, in a box furnace. HT2 = 780 °C, 2 hrs, ramp rate 10 °C min^{-1} in a tube furnace.

Material	Pump 2	Pump 3 [KOH] / M	Heat treatment
$YMnO_3$	1:1 Y:Mn 0.1 M total	1	HT1
$SmMnO_3$	1:1 Sm:Mn 0.1 M total	1	HT1
$LaMnO_3$	1:1 La:Mn 0.1 M total	1	HT2
$LaMnO_3$-2.5	1:1 La:Mn 0.1 M total	0.25	No product observed
$LaMnO_3$-5	1:1 La:Mn 0.1 M total	0.5	HT2
$LaMnO_3$-15	1:1 La:Mn 0.1 M total	1.5	HT2
$LaMnO_3$-20	1:1 La:Mn 0.1 M total	2	HT2
0.05-$LaMnO_3$	1:1 La:Mn 0.05 M total	0.5	HT2
0.15-$LaMnO_3$	1:1 La:Mn 0.15 M total	1.5	HT2
0.2-$LaMnO_3$	1:1 La:Mn 0.2 M total	2	HT2
$CaMnO_3$	1:1 Ca:Mn 0.1 M total	1	No product observed
$BaMnO_3$	1:1 Ba:Mn 0.1 M total	1	No product observed
$SrMnO_3$	1:1 Sr:Mn 0.1 M total	1	No product observed
$CaMnO_3$	1.5:1 Ca:Mn 0.125 M total	1	No product observed
$BaMnO_3$	1.5:1 Ba:Mn 0.125 M total	1	No product observed
$SrMnO_3$	1.5:1 Sr:Mn 0.125 M total	1	No product observed

As CHFS of $BaMnO_3$, $SrMnO_3$ and $CaMnO_3$ failed to provide product, a modified sol-gel Pechini method was used to synthesise these materials.[207] $Ca(NO_3)_2 \cdot 4H_2O$,

$Ba(NO_3)_2$ or $Sr(NO_3)_2$ (4 mmol) and $Mn(NO_3)_2{\cdot}4H_2O$ (4 mmol) were dissolved in deionised water (20 mL) with stirring. Citric acid (8 mmol) and ethylene glycol (5 mL) were added under stirring and then the solution was stirred vigorously at 85 °C in a water bath for 6 hours. A yellow-gel was collected and dried in the oven overnight at 80 °C. The obtained precursor was then ground and then further calcined in a box furnace by heating to 180 °C (2 °C min^{-1} ramp rate) for 30 mins then further heated to 900 °C and held for 5 hours in a (5 °C min^{-1} ramp rate) in an air atmosphere. This yielded a grey powder of $SrMnO_3$ and $CaMnO_3$ and a dark green powder of $BaMnO_3$. Samples of $BaMnO_3$ and $SrMnO_3$ were not deemed pure enough to be used further.

A sample of $LaMnO_3$ was flash heat treated to examine the effect of heat treatment on the catalytic performance. 0.5 g CHFS $LaMnO_3$ precursor was weighed into an alumina boat. A tube furnace was pre-heated to 850 °C. The boat containing the $LaMnO_3$ was then placed into the pre-heated furnace for 30 min. It was then taken out of the hot furnace and cooled rapidly in air to room temperature.

The precursors used were $Ca(NO_3)_2{\cdot}4H_2O$, $Ba(NO_3)_2$ or $Sr(NO_3)_2$ (all > 99%, anhydrous unless stated, Sigma Aldrich, Dorset, UK), $Mn(NO_3)_4{\cdot}4H_2O$ (98%, Sigma Aldrich, Dorset, UK), $La(NO_3)_3{\cdot}6H_2O$ (>99%, VWR, Leicestershire, UK), $Sm(NO_3)_3.6H_2O$ (99.9%, Sigma Aldrich, Dorset, UK), $Y(NO_3)_3{\cdot}6H_2O$ (99.8% Sigma Aldrich, Dorset, UK), $C_6H_8O_7$ (99%, citric acid, Sigma Aldrich, Dorset, UK), $(CH_2OH)_2$ (99%, ethylene glycol, Fisher Scientific), and KOH (potassium hydroxide, analytical grade, Fisher Scientific).

2.1.3. Combinatorial Synthesis of $La_xMn_yNi_zO_3$ Materials as Bifunctional Catalysts:

A series of $La_xMn_yNi_zO_3$ samples ($x + y + z = 1$) were synthesised using the standard CHFS lab-scale set up described in Section 2.1. For all samples, flow rates were 80, 40 and 40 mL min^{-1} for pumps 1, 2 and 3 respectively. Pump 1 carried supercritical water, pump 2 carried mixed metal nitrates (0.1 M) and pump 3 carried 1 M KOH. The supercritical water was pressurised to 240 bar and heated to 450 °C giving a mixing temperature of 335 °C. The calculated residence time inside the CJM was ca. 7 s.

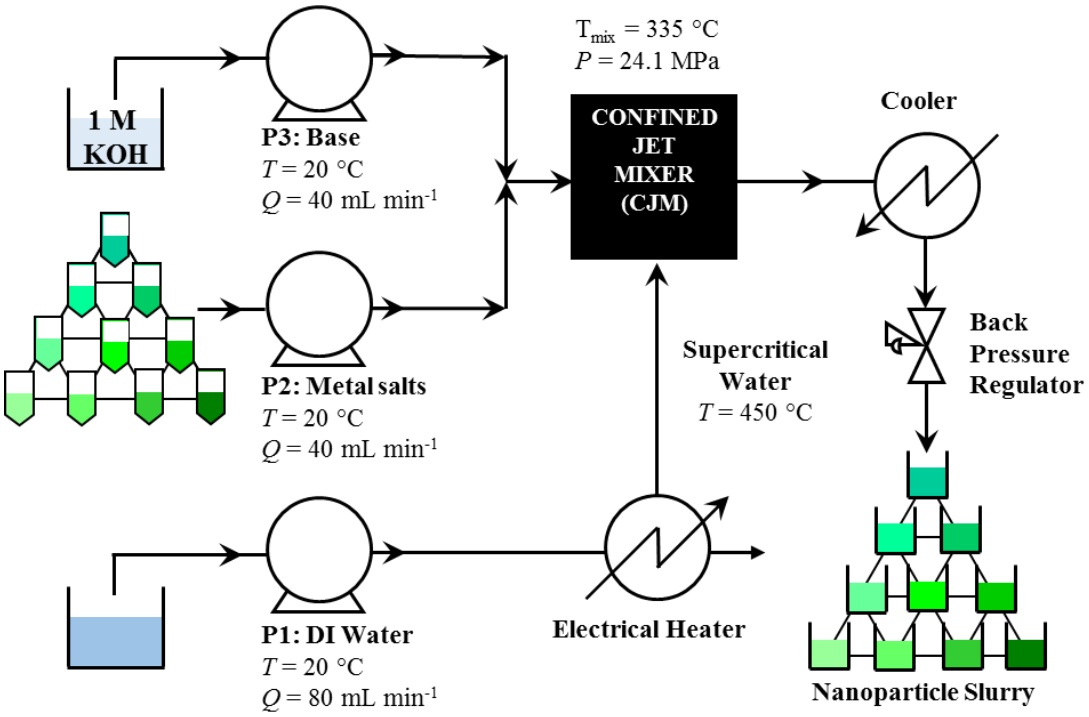

Figure 2.4: Schematic showing combinatorial synthesis via CHFS.

The concentrations of the precursors used are shown in Table 9.3 in the appendix. The ternary phase space studied can be seen below in Figure 2.5. The preparation and synthesis of materials was carried out over 12 hours. The reaction time to synthesise 2 g of all 62 materials was ca. 10 hours.

The nanoparticulate slurries were cleaned by centrifugation until the supernatant conductivity was < 100 µS and then freeze-dried. Once dry, a flash heat-treatment step was carried out at 850 °C for 30 min yielding free flowing, black powders. Approximately 0.5 g of each sample was weighed into an alumina combustion boat. Three samples were placed side-by-side at the same point in the tube furnace each time for 30 min and then removed and cooled rapidly in air to room temperature. Only three samples at a time were heat treated and the placement in the furnace was the same each time to minimise differences in temperature that each sample may encounter.

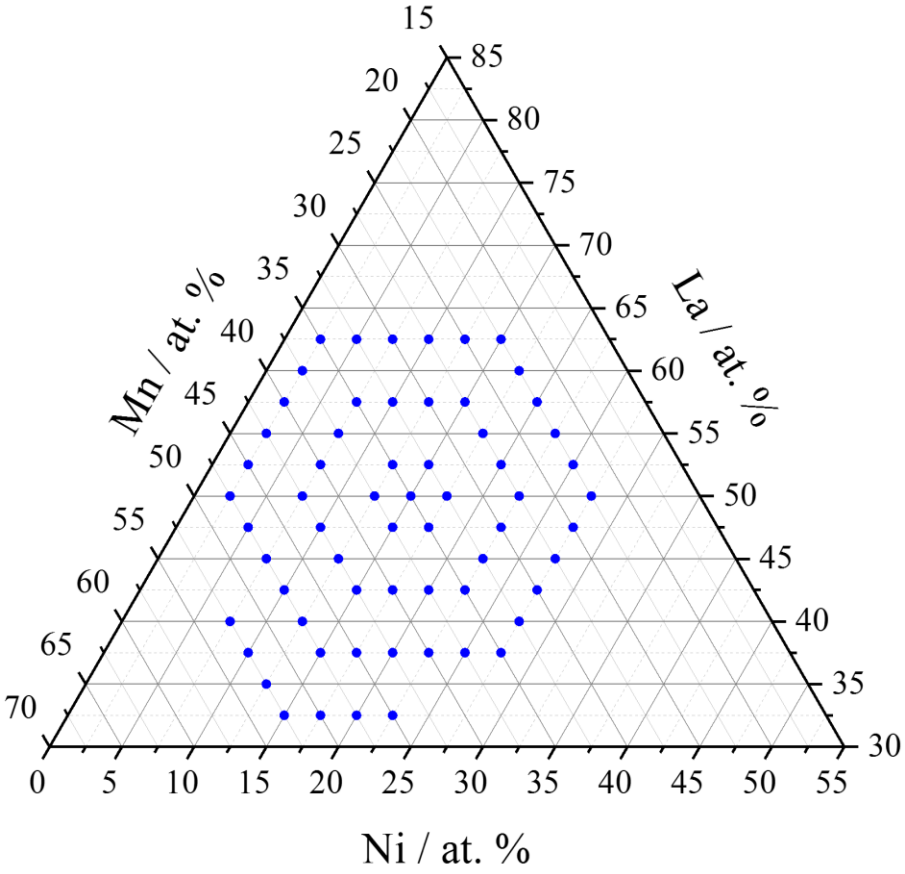

Figure 2.5: Ternary plot showing the nominal composition of the samples synthesised in the $La_xMn_yNi_zO_3$ phase space.

The precursors used were $La(NO_3)_3{\cdot}6H_2O$ (>99%, VWR, Leicestershire, UK), $Mn(NO_3)_2{\cdot}4H_2O$ (98%, Sigma Aldrich, Dorset, UK), $Ni(NO_3)_2{\cdot}6H_2O$ (99%, SLS, Nottingham, UK) and KOH (potassium hydroxide, analytical grade, Fischer Scientific).

2.1.4. Combinatorial Synthesis of $Ni_xMn_yFe_zO_4$ spinel compounds as bifunctional catalysts:

A series of $Ni_xMn_yFe_zO_4$ spinel compounds were made in the phase space between $NiMn_2O_4$, Ni_2MnO_4 and $NiMnFeO_4$. These were synthesised using the standard lab set up (Section 2.1) and the flow rates were 80:40:40 mL min^{-1} for pumps 1, 2 and 3 respectively. Pump 1 pumped supercritical water (240 bar, 450 °C), pump 2 pumped the mixed metal nitrates (0.1 M total, room temperature) and pump 3 pumped NaOH (1 M, room temperature) giving a mixing temperature of 335 °C. The calculated

residence time inside the CJM was ca. 7 s. The molar amount of precursors used can be found in Table 8.5 in the appendix.

The nanoparticulate slurries were cleaned by centrifugation until the supernatant conductivity was < 100 µS and then freeze dried. Once dry, a heat-treatment step was carried out at 850 °C for 30 min yielding free-flowing, black powders. This was carried out in the same way as for the previous set of materials. The ternary phase space studied can be seen below in Figure 2.6.

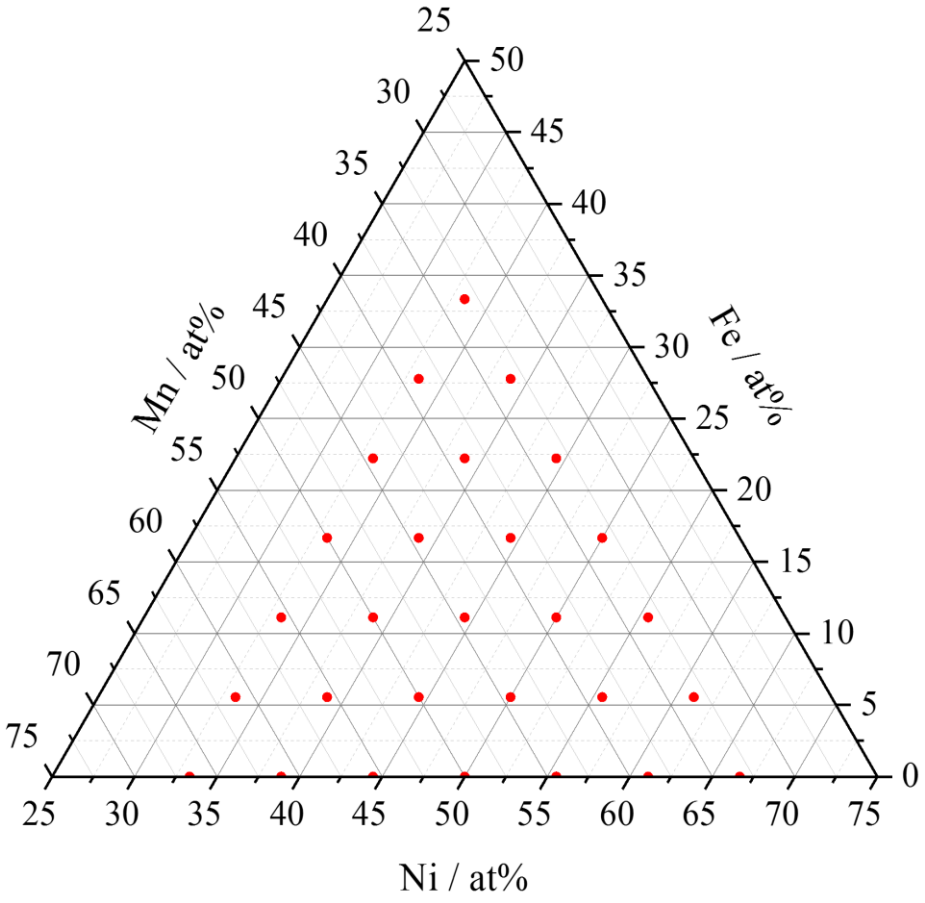

Figure 2.6: Ternary plot showing the nominal composition of the samples synthesised in the $Ni_xMn_yFe_zO_4$ phase space.

In previous synthetic experiments involving the use of manganese nitrate, a small discrepancy between the calculated Mn concentration and the actual Mn concentration was found on elemental analysis of the samples. In the materials here, this discrepancy was exaggerated. This may be due to poor nucleation of both Mn and Ni precursors, meaning that no seeding is occurring. For this reason, Mn concentrations were

increased by a factor of 2 when no Fe was present and a factor of 1.6 when Fe was present to allow for losses during synthesis.

The precursors used were $Fe(NO_3)_3 \cdot 9H_2O$ (>98%, Sigma Aldrich, Dorset, UK), $Mn(NO_3)_2 \cdot 4H_2O$ (98%, Sigma Aldrich, Dorset, UK), $Ni(NO_3)_2 \cdot 6H_2O$ (99%, SLS, Nottingham, UK) and NaOH (sodium hydroxide, analytical grade, Fischer Scientific).

2.1.5. Freeze-drying

At very low pressures (below its triple point), frozen water sublimes at low temperatures. Freeze-drying is the removal of frozen solvents (usually ice) from a material initially through sublimation and then through the removal of bound solvent molecules via desorption. It is used in food processing, the pharmaceutical industry and in the production of nanoparticles.[208] Initially the sample is completely frozen. A high vacuum is then applied keeping the pressure well below the triple point of water. Finally, heat energy is then applied causing the frozen water to sublime.[209] Controlled freeze drying keeps the temperature low enough that there is no change of in the dried materials appearance/physical characteristics making it an ideal drying technique for nanomaterials.[210]

A Virtis Genesis 35XL freeze-drier was used to freeze dry all materials. Wet nanoparticles were frozen to < −40 °C and then a vacuum of 13.3 Pa was applied. The nanoparticles were then heated up to room temperature over the course of ca. 22 hours.

2.2. Physical Characterisation:

This Section details the differing techniques used to identify the materials made via the continuous hydrothermal flow method. It is important to determine the stoichiometry (X-ray fluorescence), crystallinity (Powder X-ray diffraction), redox state of the surface cations (X-ray photoelectron spectroscopy), surface area (BET) and morphology (scanning/transmission electron microscopy).

2.2.1. X-Ray Diffraction

Powder X-ray Diffraction (PXRD) can be used to identify the phase and phase purity of the material which has been synthesised as well as estimation of crystallite size and to determine crystal lattice parameters. X-ray diffraction is a technique based on the constructive interference of monochromatic X-rays with a crystalline sample (represented by Figure 2.7). A cathode ray tube is used to generate X-rays, which are filtered to produce the necessary monochromatic radiation.

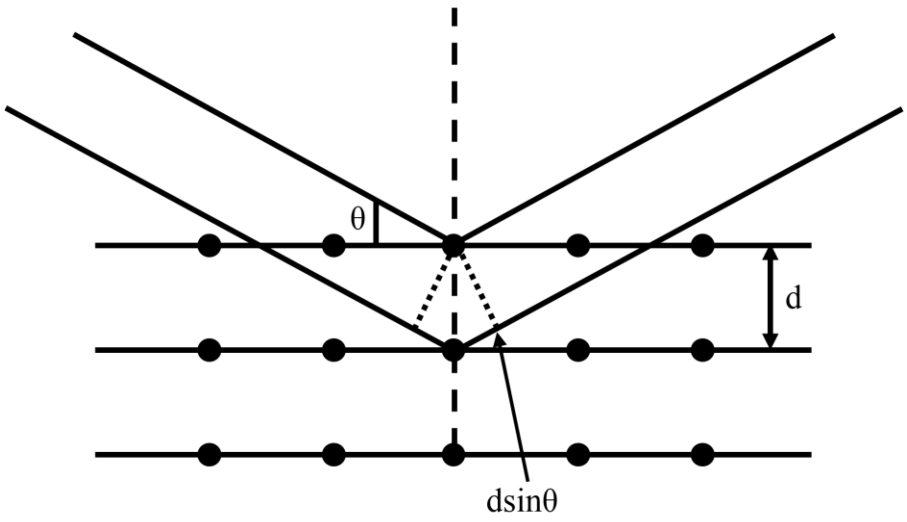

Figure 2.7: Schematic showing the interaction of X-rays with a crystalline material.

The interaction between the X-rays and the sample produces constructive interference only when conditions satisfy Bragg's law[211] (equation 2.1):

$$2dsin\theta = n\lambda \tag{2.1}$$

where d is the spacing between diffraction planes, θ is the incident angle, n is an integer, and λ is the X-ray wavelength. X-rays are used to produce the diffraction pattern as their wavelength is in the same order as the spacing between lattice planes.

Powder X-ray diffraction was performed on a STOE StadiP diffractometer (STOE, Darmstadt, Germany) using Mo-Kα radiation (λ = 0.71 Å). Powders were mounted between two acetate sheets for analysis. A 2θ range of 2 - 40 ° was used with a step size of 0.5 ° and a step time of 15 s. Phase identification was carried out by comparison with reference samples on the Inorganic Crystal Structural Database (ICSD). Peak fitting of reflections was carried out using Fityk (Version 0.9.8). The Scherrer equation (2.2) was used to estimate particulate size in the samples:

$$\tau = \frac{K\lambda}{\beta cos\theta} \tag{2.2}$$

where τ is the mean size of ordered domains, K is a shape factor (0.9 was used in all calculations as it assumes spherical particles), λ is the X-ray wavelength, β is the line broadening at half the maximum intensity and θ is the Bragg angle.

2.2.2. X-ray Fluorescence (XRF)

X-ray Fluorescence (XRF) is a non-destructive technique which can be used to analyse the elemental composition of a sample. The primary X-ray source used is energetic enough to expel electrons from the core orbitals of atoms. This causes electronic instability and electrons from higher energy levels 'fall' down to replace the expelled electrons. When this occurs, a photon is emitted with energy equal to the difference between the two orbitals involved. Thus, the material emits a characteristic radiation which can be used to identify the atoms present.

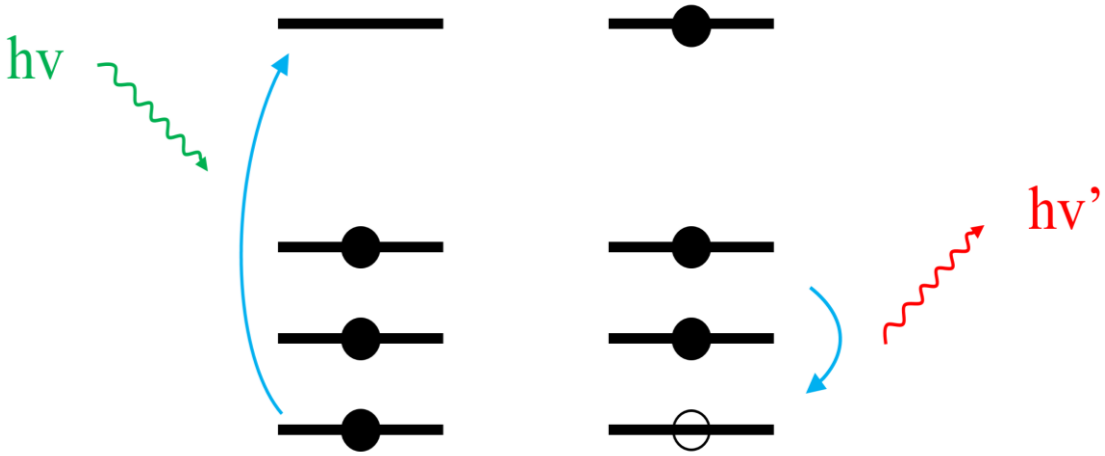

Figure 2.8: Diagram showing the removal of an electron and the subsequent rearrangement of the electrons in the analysis sample leading to the ejection of a photon with characteristic energy.

XRF was carried out on a Panalytical Epsolon 4 XRF spectrometer (Malvern Panalytical, Worcester, UK) on powder samples. Approximately 0.2 g of powder sample was weighed into the XRF pots for analysis. Raw data was converted from weight % into atomic % using equation 2.3.

$$At\%(a) = \frac{Wt\%(a)/m(a)}{\Sigma[Wt\%(a)/m(a)+Wt\%(x)/m(x)+Wt\%(y)/m(y)+\cdots]} \quad (2.3)$$

where At%(a) is the atomic percent of the element of interest, Wt%(a) is the weight percent of the element of interest and m(a) is the atomic mass of the element of interest.

2.2.3. X-ray Photoelectron Spectroscopy (XPS)

X-ray Photoelectron Spectroscopy (XPS) can be used to quantitatively study the surface chemistry of the material being analysed. Chemical and electronic state can be

determined, and surface elemental composition can be determined. The surface of the material is irradiated with X-rays and the kinetic energy and number of electrons that escape from the surface of the material are analysed.

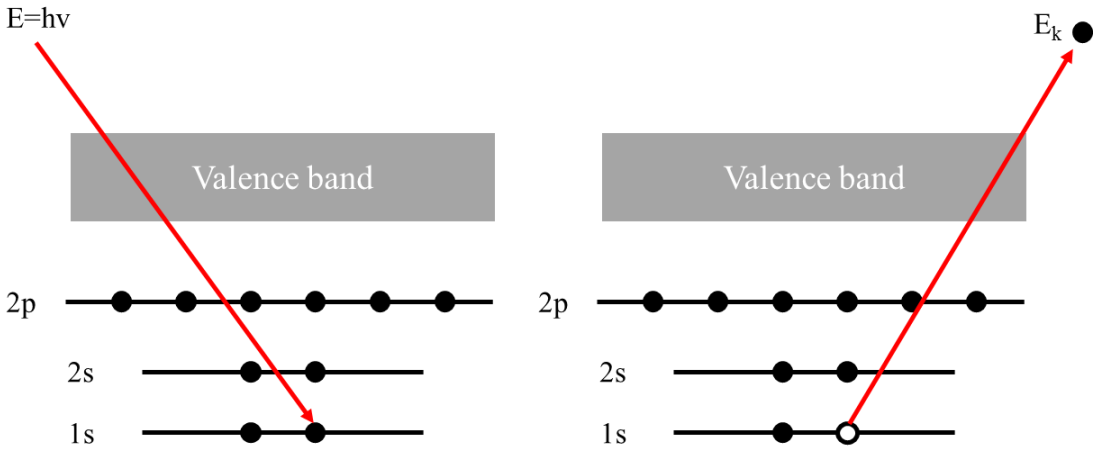

Figure 2.9: Diagram showing the removal of an electron from a core shell during the XPS process.

Only the top 0-10 nm is probed due to it being more probable that electrons will be able to escape from this depth of material than from elements in the bulk of the material. The binding energy ($E_{binding}$) of the collected electrons can be found by using the work function (ϕ), which is the minimum energy required to release an electron from a solid into a vacuum[212], the energy of the incident X-ray used for excitation (E_{photon}, 1486.6 eV for Al-Kα) and the measure kinetic energy of the electron ($E_{kinetic}$).

$$E_{binding} = E_{photon} - E_{kinetic} - \phi \quad (2.4)$$

XPS was carried out using a Thermo Scientific K-alpha spectrometer which used Al-Kα radiation. High resolution regional scans were carried out for the different metal ions presented in this thesis including lanthanum, manganese, nickel and iron at 50 eV. Processing of the XPS data was done using CasaXPS software and by calibrating the C 1s peak at 284.8 eV. Peak fitting allowed for the determination of surface redox states.

2.2.4. BET

Brunauer-Emmett-Teller (BET) theory can be used to determine the specific surface area of a material using gas absorption/desorption (usually nitrogen or argon) at constant temperature (usually 77 K, the boiling point of liquid nitrogen). The technique

requires that gas adsorbs in layers on the surface of the molecule, that there is only interaction between adjacent layers and that each layer is treated discreetly.[213] The BET equation can be written as:

$$\frac{p}{n_a(p_0-p)}S_{total} = \frac{1}{n_m C} + \frac{(C-1)}{n_m C} \times \frac{p}{p_0} \quad (2.5)$$

where p is equilibrium pressure, p_0 is saturation pressure, n_a is absorbed gas quantity, n_m is monolayer capacity and C is the BET constant. C and n_m can be found using the gradient and intercept of the absorption isotherm vs P/P_0 between 0.05-0.35. The total BET surface area can then be found using:

$$S_{total} = \frac{n_m N s}{V} \quad (2.6)$$

where N is Avogadro's number, s the absorption cross Section of the gas used, and V is the molar volume of the absorbing gas.

BET measurements were carried out in a Micrometrics Tristar II (Micrometrics UK Ltd, Hertfordshire, UK) using liquid nitrogen. All samples were degassed for 2 hours at 110 °C using nitrogen gas before measurements were undertaken.

2.2.5. Raman Spectroscopy

Raman spectroscopy is used to determine vibrational modes and can be used as a structural fingerprint to identify molecules. For transition metal oxides, as studied in this thesis, Raman spectroscopy can be used to study the characteristic scattering of light by a crystal lattice. The inelastic scattering of light measured by the Raman technique is a result of the collision of a photon of monochromatic light (emitted by the Raman laser) and a vibrational crystal lattice. The energy difference between the scattered Raman photon and the photon emitted by the monochromatic light source is equal to the difference in the energy levels of a molecular vibration therefore, the shift in energy is material dependant (see Figure 2.10, Stokes and anti-Stokes Raman scattering). However, if the energy of the scattered photon is equal to the energy of the monochromatic photon, the collision between the crystal lattice and the photon is elastic, and this is known as Rayleigh scattering.[214]

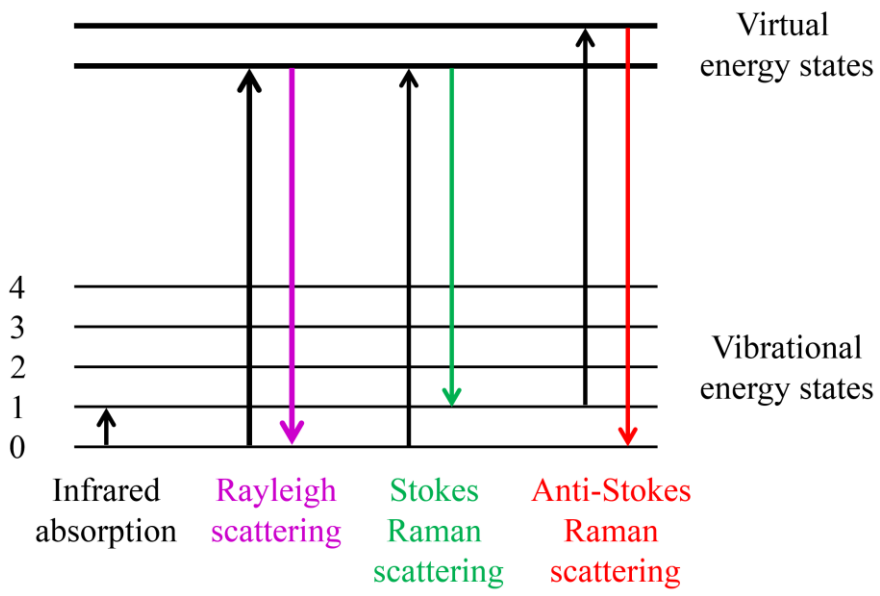

Figure 2.10: Diagram showing the different states involved in a Raman spectrum.

Raman spectroscopy for Chapter 4 was carried out using a Reinshaw InVia Raman microscope at 633 nm nanometer excitation, 10% laser power for 60 s.

Raman spectroscopy for Chapter 5 was carried out using a Reinshaw InVia Raman microscope at 512.5 nm nanometer excitation, 100% laser power for 60 s (three cycles).

2.2.6. Transmission Electron Microscopy (TEM)

Transition Electron Microscopy (TEM) can be used to study morphology, shape and size of nanomaterials. The resolution is limited to 0.5 μm by the wavelength of visible light in an optical microscope as an image can only be resolved at or above the order of magnitude of the wavelength used. The light source of a TEM is an electron beam allowing for resolutions down to 0.2 nm as the wavelength of an electron is much smaller than that of visible light. At one end of a column, an electron source emits electrons, which move down an ultra-high vacuum column to the sample. Electromagnetic lenses are used to focus the electron beam. The focused beam travels through the sample, interacting with it, and then the electrons interact with a detector to form an image.

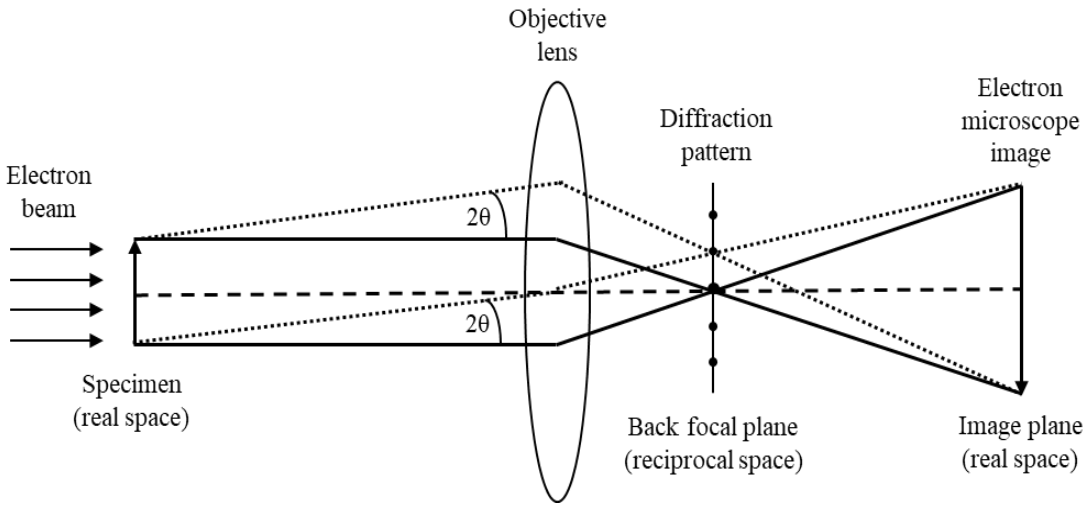

Figure 2.11: Schematic of a TEM column showing the production of an image from the diffraction of electrons.

TEM was carried out using a JEOL JEM 2100 TEM with 200 KeV accelerating voltage and a $LaBF_6$ filament. The TEM was equipped with a GATAN CCD camera allowing digital imaging. Samples were prepared by sonicating a small amount of powder in methanol until dispersed before dropping a small amount of the resulting dispersion onto a copper grid (300 mesh holey copper film).

2.2.7. Scanning Electron Microscopy (SEM)

Scanning Electron Microscopy (SEM) can be used to examine particle size and morphology. An electron source emits primary electrons which are then used to scan the surface of a sample, interacting with atoms on the surface. This interaction causes secondary electrons to be ejected from the K-shell of the atoms, the primary electrons collide with weakly bonded electrons in the outer shells of atoms near the surface of the sample. The secondary electrons are collected by a detector and quantified as electrical intensity. The angle and yield of the secondary electrons is dependent on the smoothness of the samples surface, more electrons are emitted from rough surfaces. A gradient is then employed to visually represent the differences in electrical intensity seen as the sample is scanned, this constructs a 3D image of the sample.

Samples are commonly gold sputtered before imaging. The purpose of this is to coat the sample with a thin layer of conductive material to prevent charging of the surface and promote the emission of secondary electrons.[215] Materials other than gold can be

used (e.g. carbon) but gold does not oxidise and is an excellent conductor so it is most commonly used.

SEM was carried out using a JEOL JSM-6700F microscope. The sample was mounted on a 0.5 cm circular aluminium stub using double-sided adhesive carbon tape and then gold sputtered.

2.3. Electrochemical Characterisation:

This Section details the theory and techniques used to characterise the materials as catalysts for the oxygen reduction or evolution reactions. It is important to examine the redox processes occurring (cyclic voltammetry), overpotentials and current densities (linear sweep voltammetry), electron transfer numbers and peroxide yields (rotating ring disk electrode experiments) and stability (chronoamperometry).

2.3.1. Rotating Electrode Theory:

The activity of the catalysts towards the oxygen reduction reaction was tested using a Rotating Disk Electrode (RDE) or a Rotating Ring Disk Electrode (RRDE).

Figure 2.12: Photograph of the electrochemical cell used in the electrocatalytic testing of all materials.

The RDE set up consists of a rotating shaft with a working electrode attached (usually glassy carbon). This is then inserted into a conventional three electrode electrochemical

cell with a reference and auxiliary electrode. A photograph of the set-up used in this thesis can be seen above in Figure 2.12. The rotator keeps the solution constantly stirred allowing for a well-defined solution flow pattern.[216]

In a static solution, both kinetics and mass transport control the rate of reaction on the electrode surface. However, once an RDE/RRDE working electrode is used, the mass transport of reactants to the electrode surface is controlled by the speed of rotation, allowing of the kinetic component of the current to be isolated. Reactants are moved to the electrode surface, and products are swept outwards (Figure 2.13).

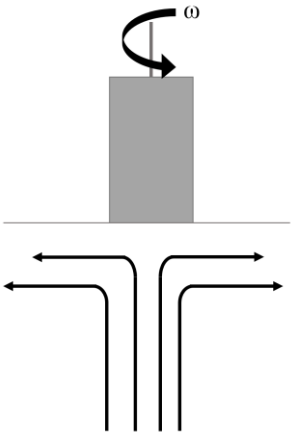

Figure 2.13: Flow pattern close to the rotating disk surface. ω represents the angular momentum.

Several key performance indicators can be determined such as the overpotential and the limiting current density. The overpotential is defined as the difference between the experimentally observed onset of reaction and the thermodynamic potential at which the reaction should occur (in this case, the reversible oxygen potential at 1.23 V vs RHE). The number of electrons being transferred in the reaction can be estimated by using the Koutecky-Levich equation (2.7):

$$\frac{1}{J} = \frac{1}{J_K} + \frac{1}{J_D} \tag{2.7}$$

where j is the current density, J_K is the kinetic current density and J_D is the diffusion limiting current density. J_K and J_D are given by equation 2.8 and equation 2.9 respectively:

$$J_K = nFkC_0 \tag{2.8}$$

$$J_D = 0.62nFC_0{D_0}^{2/3}v^{-1/6}\omega^{1/2} \quad (2.9)$$

where n is the number of electrons transferred, F is the Faraday constant, k is the electron transfer rate constant, C_0 is the bulk concentration of O_2, D_0 is the diffusion coefficient of oxygen in the chosen electrolyte, ν is the kinematic viscosity and ω is angular velocity.

Koutecky-Levich plots can be constructed by plotting the reciprocal of the current density at a set voltage against the square route of the reciprocal of the rotation speed. Figure 2.14 shows a typical K-L plot for a catalyst material. The information that can be extracted from the graph is shown.

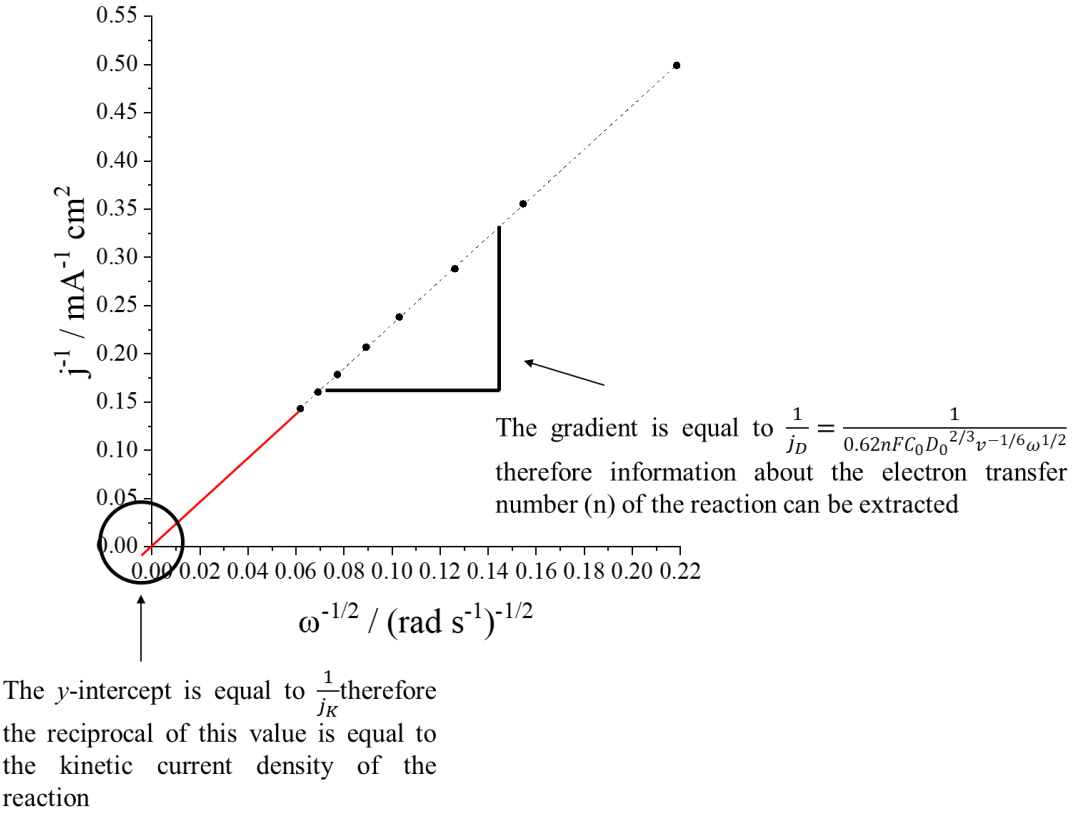

Figure 2.14: Typical Koutecky-Levich plot for an oxygen catalyst material. The *y*-intercept can be used to find the kinetic current density of the reaction whilst the gradient of the plot can be used to infer information about the electron transfer number of the reaction.

The fraction of peroxide produced by the unfavourable 2 e− step during the oxygen reduction, can be measured using a RRDE (Figure 2.15). The ring is capable of detecting products which are generated at the disk electrode. The ring electrode is set to a potential that sits between the onset potential of OH^- to O_2 and the diffusion

limiting value of the oxidation of the intermediate studied (in all cases herein the intermediate is peroxide). The fraction of the current that corresponds to the intermediate is recorded at the ring electrode.

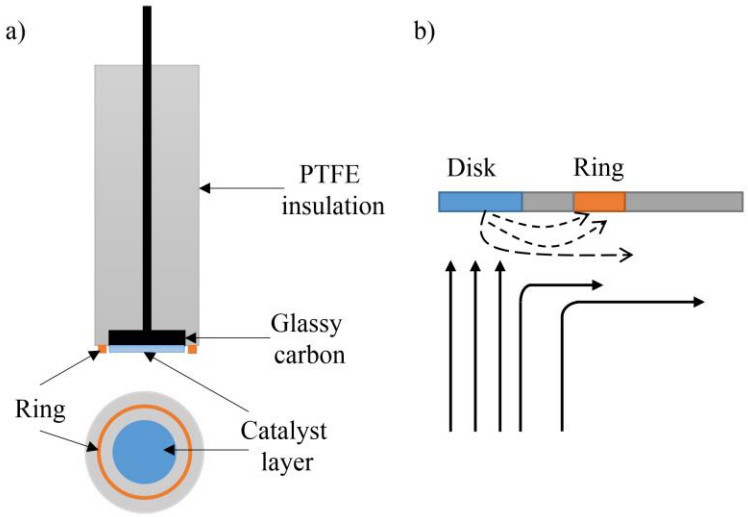

Figure 2.15: a) schematic diagram of the rotating ring disk electrode used for studying intermediates formed at the disk electrode, b) solution flow pattern at the RRDE.

The peroxide yield and electron transfer number can then be calculated by using equations 2.10 and 2.11 respectively:

$$X_{HO_2^-} = 100 \times \frac{2I_R/N}{I_D + I_R/N} \tag{2.10}$$

$$n_e = \frac{4I_D}{I_D + I_R/N} \tag{2.11}$$

where $X_{HO_2^-}$ is the peroxide yield (%), n_e I_R is the ring current, N is the collection efficiency and I_D is the disk current.

The Tafel equation (2.12) can also be used to understand more about the kinetics of the reaction. It relates the rate of a reaction by the current density to the applied potential via a linear relationship between log(current) and the overpotential.

$$\eta = a + b \log i \quad (\eta = U - U_0) \tag{2.12}$$

$$b = 2.3RT/\alpha F \tag{2.13}$$

where η is the overpotential, b is the Tafel slope, i is the current, R is the universal gas constant, T is the temperature, F is the Faraday constant and α is the charge transfer coefficient.

The Tafel slope is an important parameter in electrochemical reactions as it contains information about the charge transfer coefficient. Therefore, if the reaction mechanism is identical, the smaller the Tafel slope, the faster the rate determining step. However, the value of the Tafel slope varies depending on the experimental conditions under which it is measured. The Tafel slope has also been observed to be potential dependant, switching depending on whether the slope is observed at low or high overpotentials. This is assumed to be the result of a change in reaction mechanism.[217]

The mass transport corrected kinetic current density can be found by rearranging the K-L equation to equation 2.14:

$$J_K = \frac{JJ_D}{J_D - J} \tag{2.14}$$

where J_K is the kinetic current density, J_D is the diffusion limited current density and J is the observed current density. By using this, the log of the kinetic current density can be plotted against the potential and a Tafel slope can be found.

The catalysts were tested in a three-electrode electrochemical set up (see Figure 2.13): the reference electrode was an Ag/AgCl electrode (stored in saturated NaCl, BASi, Indiana USA or stored in saturated KCl, Pine Research Instrumentation, North Carolina, USA), the counter electrode was a platinum wire (0.5 mm OD) (Alfa Aesar, Lancashire UK) and the working electrode was a catalyst coated glassy carbon RDE or RRDE. A Gamry potentiostat (Gamry, Pennsylvania USA) was used for all experiments. All electrochemical experiments were conducted at ambient temperature. An RDE cell was used (Adams 7 Chittenden, model no. 946088) as the vessel and the electrodes mentioned before were placed in the appropriate places in the cell. Approximately 120 mL of base (0.1 M NaOH or KOH) was used as the electrolyte. The electrolyte was saturated with oxygen or nitrogen for 30 min before any measurements were taken. The working electrode was screwed into an MSR precision shaft (Pine Research Instrumentation, AFE6MB). A pine modulated speed rotator (PINE Research Instrumentation AFMSRCE) was used to rotate the RDE/RRDE and the shaft.

2.3.2. Ink Preparation and Electrode Coating:

Two ink formulations were used in this work.

1) The as synthesised nanoparticulate perovskite powder was sonicated in a 4:1 mixture of water:IPA with 5 μL Nafion in a bath sonicator for 30 min before being sonicated on a tip sonicator for 30 s. 10 μL of this ink was then spin coated onto a glassy carbon rotating ring disk electrode (AFE7R9GCPT RRDE, Pine Research Instrumentation, North Carolina, USA) with a surface area of 0.25 cm^2 giving a catalytic loading of 0.08 mg cm^2. The electrode was spun at 700 rpm under a heat lamp for 15 min giving an even, dry coating of catalyst across the electrode surface. The electrode was then used with no further modifications.
2) 5 mg catalyst was sonicated with 5 mg acetylene black (Alfa Aesar, Lancashire UK) in 350 μL ethanol with 95 μL Nafion in a bath sonicator for 2 hours giving a homogeneous dispersion of nanoparticles in the liquid. 7 or 9 μL of this ink was then drop coated onto a glassy carbon rotating disk electrode (0.2 cm^2) or a glassy carbon rotating ring disk electrode (0.25 cm^2) (AFE7R9GCPT RRDE, Pine Research Instrumentation, North Carolina, USA) giving a catalytic loading of 0.4 mg cm^2. The electrode was then dried in a vacuum oven at 40 °C for 30 min. The electrode was then used with no further modifications.

Between each catalyst measured the electrode surface was cleaned by polishing on a polish pad using 0.05 μm alumina as a polishing medium. This was done for 5 mins until the surface of the electrode was glassy by visual inspection and then the electrode dried in a vacuum oven at 40 °C for 10 minutes.

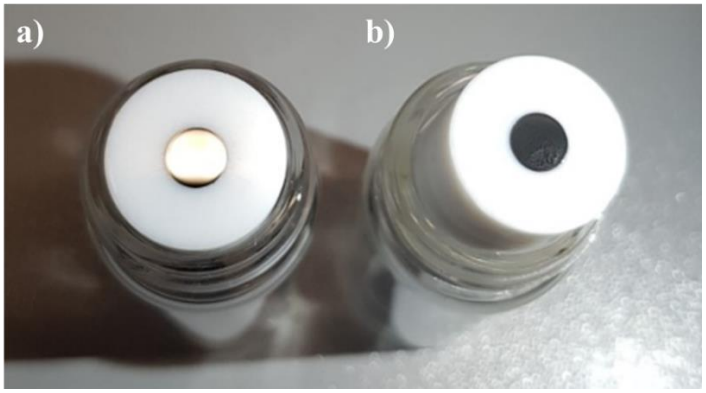

Figure 2.16: a): uncoated glassy carbon rotating disk electrode. b): coated glass carbon rotating disk electrode.

2.3.3. RDE Experiments:

The activity of the catalysts was studied using a rotating disk electrode to minimise the effect of mass transport on the catalytic reaction. A glassy carbon working electrode (0.2 cm^2, Pine) was coated with the catalyst ink as described above and then various electrochemical analyses were carried out as described below.

2.3.4. RRDE Electrochemical Characterisation

The percentage yield of hydrogen peroxide was investigated in a RRDE experiment. The RRDE was coated with the catalyst as above (in Section 2.3.2) and catalytic loading was kept the same. The disk area was 0.25 cm^2, the ring inner diameter was 6.25 mm and the outer diameter was 7.92 mm. Experiments were carried by holding the ring at a potential significant enough to immediately oxidise any H_2O_2 formed at the ring. The collection efficiency was found to be 0.38 previously[218], and this agreed well with literature.[219] The potential vs Ag/AgCl at which the ring was held was material dependent and chosen for each set of materials based on previous studies in the literature.

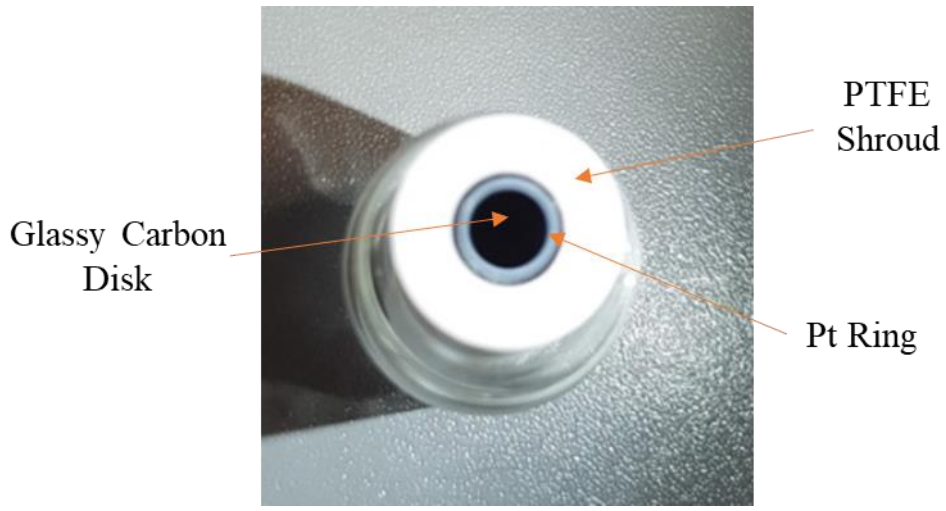

Figure 2.17: Photo of the RRDE electrode used for studying peroxide yields.

2.3.5. Cyclic Voltammetry:

In a cyclic voltammetry experiment, the potential is swept linearly to a predetermined limit before being swept in the opposite direction to return to the initial potential. The current response to the potential over time is measured and plotted against the working potential. These cycles may be repeated as many times as necessary. Cyclic voltammetry can be used to determine the redox processes occurring at the electrode,

the stability of reaction products and the reversibility of a reaction. Scan rates used in the experiments discussed here range from 50 mv s^{-1} to 5 mv s^{-1} over a range of potentials depending on what redox process was being studied.

2.3.6. Linear Sweep Voltammetry:

In linear sweep voltammetry, the current at the working electrode is measured as the potential between the reference and working electrode is swept linearly. A redox process is registered as a peak/trough in the current signal vs the potential where the species begins the redox process.

Linear sweep voltammetry (ORR) was carried out at 10 mV s^{-1} between 0.1 V and −0.6 V (vs Ag/AgCl) unless otherwise stated and at rotation speeds of 200, 400, 600, 900, 1200, 1600, 2000 and 2500 rpm. LSV (OER) was carried out at 10 mV s^{-1} between 0 V and 0.8 V vs Ag/AgCl unless otherwise stated and at 2500 rpm.

2.3.7. Chronoamperometry:

Chronoamperometry can be used to examine the long-term stability of a catalyst. It involves holding the potential of the working electrode at a fixed voltage and examining how the current response changes over time. The potential chosen was sample dependent and will be discussed in the relevant chapters. All chronoamperometry experiments were carried out at 900 rpm in 0.1 M O_2 saturated electrolyte (NaOH or KOH).

2.4. Software:

All electrochemical data were analysed using Gamry EChem Analyst software (Gamry EChem Analyst, Version 7.8, Gamry, Pennsylvania USA). Unless otherwise stated, all data were plotted up using Origin software (Origin(Pro), Version 2019, OriginLab Corporation, Northampton, MA, USA).

2.5. Conclusions:

CHFS was used to synthesise a variety of nanosized perovskite and spinel transition metal oxides. A variety of physical characterisation techniques were used such as PXRD, XRF, XPS, BET, SEM and TEM. The materials were then analysed using a variety of electrochemical techniques including CV, LSV, EIS and chronoamperometry measurements.

The materials synthesised will be discussed in more detail in the following chapter.

3. Synthesis and Testing of a Complete Perovskite Titanate Phase Diagram

3.1. Abstract

CHFS is a powerful synthesis technique for the combinatorial synthesis of phase diagrams of materials. It offers a unique method to quickly synthesise a wide range of materials within the same phase diagram, which show a continuum of physical and electrochemical properties. A ternary nanoparticulate library containing 66 perovskite $Ba_xSr_yCa_zTiO_3$ ($x + y + z = 1$) samples was synthesised in approximately 14 hours yielding 3 g of each material. All samples were analysed via XRD and BET and selected samples were analysed via TEM. Potential trends across the phase diagram were investigated by studying the electrocatalytic performance of the as synthesised powders as active materials for the Oxygen Reduction Reaction (ORR).

3.2. Introduction

Titanium is an inexpensive, earth abundant metal with many applications both on its own and as an alloy or compound.[220] Therefore, materials based on titanium tend to be inexpensive and present interesting properties for use in a wide variety of applications. Barium titanate and its analogues calcium titanate and strontium titanate, have been widely studied due to their ferroelectric properties,[145,221] as well as catalysts for several applications including photocatalytic degradation of organic materials and in the reduction of carbon monoxide.[222,223] $CaTiO_3$ is known as the "first perovskite" and as such, the perovskite class of materials is named after the structure of $CaTiO_3$.[224] The perovskite ABO_3 lends itself to modification as large numbers of differing cations can be supported in the *A* or *B* sites. The ideal unit cell of a perovskite has *A* cations in corner cubic positions, *B* cations in body centred cubic positions and O anions in face centred cubic positions. Therefore, the *A* cation sits in a cuboctahedron of 12 O anions and the *B* cation sits in an octahedron of 6 O anions.[116]

Perovskites have been studied as oxygen electrocatalysts for many years due to the structural and electrical flexibility they exhibit.[100] There are many studies focussing on the partial or full substitution of the *A* site cation for differing elements.[79,225,226] Hyodo *et al.* investigated the effect of substitution of Ca, Ba or Sr into $PrMnO_3$ on the ORR.[227] They discovered that the catalytic performance was in the order of $Pa_{0.8}Ca_{0.2}MnO_3$ > $Pa_{0.8}Sr_{0.2}MnO_3$ > $Pa_{0.8}Ba_{0.2}MnO_3$ > $PrMnO_3$ indicating that ORR catalysis was significantly improved by *A* site substitution. Yang *et al.* found a $Sr_{0.95}Ce_{0.05}CoO_3$

material which was optimised with respect to conductivity by Ce doping.[228] The material was decorated with Cu for additional conductivity and then tested as an oxygen catalyst for Li-air batteries, showing excellent activity and stability.

Chen *et al.* reported the synthesis of an oxygen deficient $BaTiO_{3-x}$ catalyst which was tested for use as a bifunctional oxygen electrocatalyst.[229] They observed that by varying calcination conditions they could induce the appearance of hexagonal $BaTiO_3$ which enhanced the bifunctional electrocatalytic activity observed. However, an energy intensive heat treatment step was needed to synthesise the materials.

The synthetic route chosen for the synthesis of a catalyst is well known to affect the catalyst structure and composition and can therefore influence its activity and stability. Traditionally barium titanate and its group 2 analogues have been synthesised via energy intensive solid state synthetic routes, although more recently batch hydrothermal methods have been preferred due to the one step nature of the synthesis.[145,221] Batch based synthetic routes, however, can lead to poorly controlled growth and variation between batches.[230]

The pharmaceutical industry was the first to invest heavily into combinatorial synthesis and analysis techniques for the acceleration of materials discovery and optimisation.[231] Large numbers of samples are screened for characteristic properties, rather than comprehensive characterisation being carried out on each sample. This allows the mapping of potential hotspots of activity in a series of materials. The limitations in the reproducibility of traditional solid-state synthesis techniques can be a bottleneck in the development of new functional materials via materials synthesis and discovery methods.[230] Several high throughput synthesis techniques have been explored for the production of ORR active material libraries including thin film techniques that produce each composition on a milligram scale.[204,205,232] High throughput CHFS methods can be used to produce large libraries of materials at the gram scale in a matter of hours[188,202,203], making the technique ideal for the synthesis of libraries of materials for screening for a variety of applications.

A complete composition diagram of mixed group 2 metal titanate perovskites was synthesised directly via a one-step CHFS process. Phase identification carried out by PXRD and BET analysis showed that specific surface areas (SSA) were higher than previously reported in the literature.[233–235] Performance indicators for the ORR showed

some catalytic activity, although some additional improvement would be needed before the materials would be able to compete with current industrial standards. However, the promise of CHFS as a high throughput materials discovery technique for oxygen electrocatalysis was displayed.

3.3. Materials and Methods

3.3.1. Synthesis of $Ba_xMn_yNi_zO_3$ Materials

The synthesis of all materials was carried out as described in Section 2.1.1.

3.3.2. Physical Characterisation of $Ba_xMn_yNi_zO_3$ Materials

The physical characterisation of all materials was carried out as detailed in Section 2.2. PXRD, XPS and BET were carried out on all samples with TEM carried out on selected samples.

3.3.3. Electrochemical Characterisation of $Ba_xMn_yNi_zO_3$ Materials

Inks for coating glassy carbon electrodes were prepared according to method 1 in Section 2.3.1.

All electrochemical testing was carried out in 0.1 M NaOH using a Ag/AgCl reference electrode (saturated NaCl) and a platinum wire counter electrode.

Electrochemical screening of the samples for the ORR was carried out by linear sweep voltammetry between 0.1 and −0.6 V (vs Ag/AgCl) at 10 mV s^{-1} at 4 different rotation speeds (400, 900, 1600 and 2500 rpm).

In depth electrochemical analysis was carried out on a selection of samples from the ternary space. RRDE testing was carried out in line with LSV testing but the ink was coated onto a glassy carbon RRDE to give the same catalytic loading as in previous tests. The ring potential was set to 0.2 V vs. Ag/AgCl to ensure complete peroxide decomposition. Chronoamperometry was carried out by holding the potential at −0.5 V vs. Ag/AgCl and measuring the current response over 3600 s. Cyclic voltammetry in N_2 was carried out at 10 mV s^{-1} between −0.8 and 0.2 V vs. Ag/AgCl.

The collection efficiency of the product detection at the ring of a RRDE can be empirically measured using a well-known one electron redox reaction. The collection efficiency refers to the percentage of a material generated at the disk electrode which is detected at the ring electrode. This experiment is caried out to determine the

collection efficiency of the specific rotating ring disk electrode being used in the oxygen reduction/evolution experiments as many factors (such as ring thickness and the gap between the ring and the disk electrodes) can lead to differences in collection efficiencies. It can also be used to check that the electrode is working optimally, as the experimentally determined value can be cross referenced with the value provided by the manufacturer at point of purchase. The ferro/ferricyanide reaction is commonly used to calculate the collection efficiency of an RRDE.[236] As well as being used to determine the collection efficiency, the ferro/ferricyanide reaction can be used to ensure the RRDE is working optimally. There can be cross-talk between the ring and the disk causing incorrect measurements due to uncompensated potential change in one electrode as the current changes in the other.[237]

To determine the collection efficiency, a clean rotating ring disk electrode was placed in a solution of 10 mM of $K_3[Fe(CN)_6]$ in 1 M KNO_3. The RRDE working electrode was rotated at 200, 400, 600, 900, 1200, 1600, 2000 and 2500 rpm. The glassy carbon disk was swept from +0.6 V to −0.2 V vs. Ag/AgCl at 10 mV s^{-1} and the ring was held at such a potential where the product was oxidised (0.94 V vs. Ag/AgCl). The collection efficiency was measured as the ratio of the limiting anodic and cathodic currents at each rotation rate.

Figure 3.1 a) shows the collected RRDE data for the ferri/ferrocyanide reactions. The collection efficiency value of the RRDE is the ratio of the disk and ring limiting currents. This was 39 % at all rotation rates, which agreed well with the theoretical collection efficiency value of 38 %.[238] This test can also be used to evaluate whether the RRDE set up is working optimally. There was a linear dependency of the limiting current as shown by the Koutecky-Levich plot in Figure 3.1 b). The linear plot confirms that the ferri/ferrocyanide reactions were mass transport limited at the limiting current. This further confirms that the electrochemical set up is working optimally.

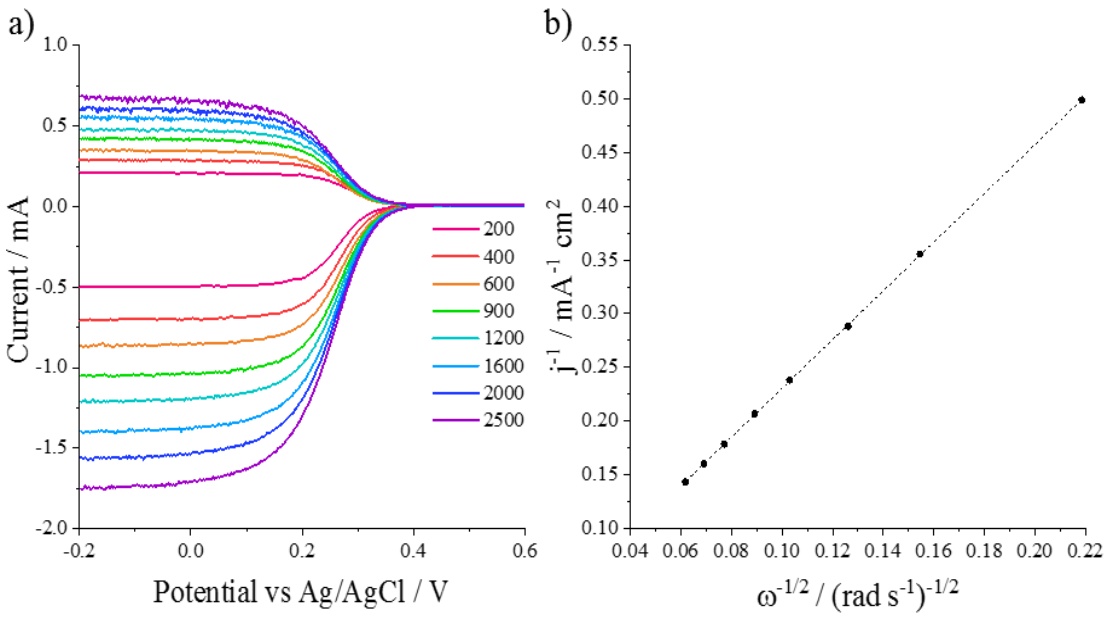

Figure 3.1: a) Linear sweep voltammograms of the ferro/ferricyanide reaction at the ring and disk electrodes of the RRDE, taken in 1 M KNO_3 solution between 200 and 2500 rpm. The scan rate was 10 mV s^{-1} and the disk was swept from 0.6 to −0.2 V vs Ag/AgCl. The ring was held at 0.94 V vs Ag/AgCl. b) Koutecky-Levich plot, plotted using current from the LSVs at −0.2 V vs Ag/AgCl.

3.4. Physical Characterisation

All materials were collected as white or pale-yellow powders after freeze drying with a yield > 90%. Materials were then physically characterised and used in the preparation of inks for use in electrochemical experiments with no further modification. The synthesis was carried out in steps of 10 atomic percent to cover the whole phase space with a reasonable resolution, giving a total of 66 samples.

Powder X-ray diffraction (PXRD) was carried out on all as-prepared materials to identify the phase(s) present in the samples. A selection of the patterns can be seen in Figure 3.2 (full PXRD data can be found in the appendix, Section 8.1). The PXRD data suggested that all binary materials were phase pure (those materials in the corners of the phase diagram). $BaTiO_3$ and $SrTiO_3$ were indexed to the cubic *Pm*-3*m* structure, whereas $CaTiO_3$ was indexed to the orthorhombic *Pbnm* structure. Along the Ba-$SrTiO_3$ and Ca-$SrTiO_3$ binary series lines the PXRD data suggested complete solid solution formation across all compositions. This was expected from relevant literature.[239] Analysis of the (110) peak position revealed that the peak shifted from 12.8 to 13.1 degrees in 2θ for the Sr-$CaTiO_3$ series and from 12.5 to 12.8 degrees in 2θ

for the Ba-$SrTiO_3$ series. These shifts agree well with those expected from the application of Vegards law which states that a linear change in lattice parameters is expected from a change in ionic radii of the metal atom, causing an observed shift in the peak position.[240]

In contrast, the Ba-$CaTiO_3$ system revealed that a single perovskite phase was only observed up to ca. 20 at% Ba dopant in the Ca titanate structure and vice versa for the Ca in the Ba titanate [Figure 3.2 c)]. Above 20 at% dopant levels, a separate $BaTiO_3$ and $CaTiO_3$ like phase co-existed within the solid solution. This is unsurprising as there is a large size mismatch between the Ba^{2+} and Ca^{2+} (ionic radius 1.61 and 1.34 Å, respectively).[241] Durst *et al.* suggested that a continuous solid solution is only formed between elements of identical valency, similar electronegativity, similar crystal structure and only when solvent and solute atoms are not too dissimilar in size.[239] For complete solid solution formation, the percentage difference between the solute and solvent atoms must not exceed 15%.[242] The size factor difference between Ba and Ca is in the order of 20%, thus a continuous solid solution was not seen. Those samples with two observable phases can be seen in Figure 3.3 with a black dashed box around them.

Only a single perovskite phase was observed in the centre of the compositional phase diagram, suggesting that the presence of some Sr^{2+} ions supports the formation and stabilisation of a solid solution, even when significant amounts of Ba^{2+} and Ca^{2+} were present. Overall, the presence of high concentrations of Ba or Ca lead to sharper PXRD peaks which suggested a larger crystalline domain size. Those samples containing large amounts of Sr had a higher signal to noise ratio due to strontium fluorescence in the beam produced by the molybdenum source.

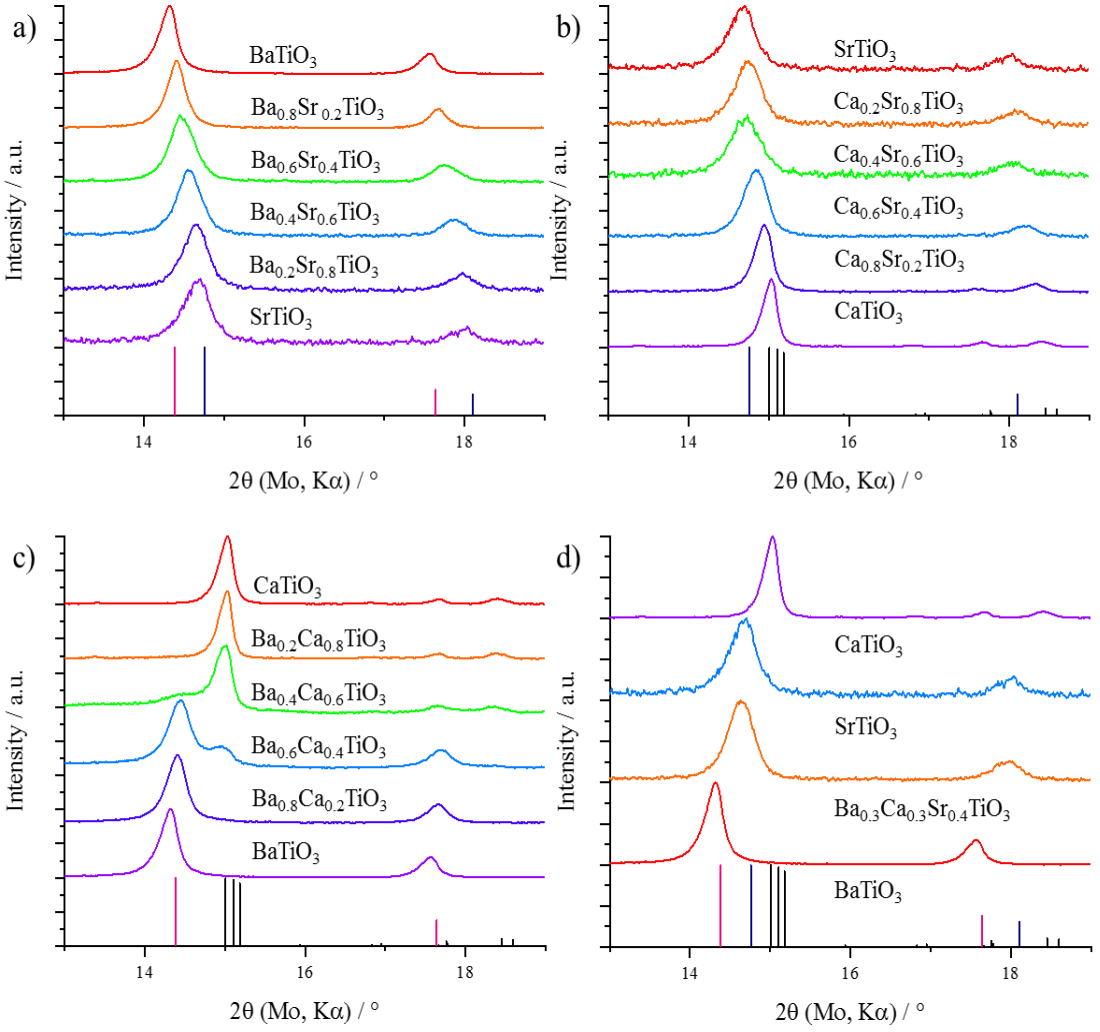

Figure 3.2: PXRD data of as synthesised materials along a) the barium-strontium axis, b) along the strontium-calcium axis and c) along the barium-calcium axis in steps of 20 atomic percent. d) Shows the compositional effects on the PXRD in the centre of the structure diagram ($Ba_{0.3}Ca_{0.3}Sr_{0.4}O_3$) compared to the corners. Standard reference patterns are also given for comparison: $BaTiO_3$ (pink, =ICSD collection code no. 95437[243]), $SrTiO_3$ (navy, =ICSD collection code no. 80871[244]), and $CaTiO_3$ (black, =ICSD collection code no. 71915[245]).

The pink dotted diamond on the diagram below (Figure 3.3) highlights three approximate regions that can be separated by Scherrer size. Those within the diamond itself (low Ba / low Ca) are in the size range of 5 to 11 nm, whereas those in the two triangular areas (high Ba / high Ca) are larger, in the size range of 12 to 16 nm. Only five of the as synthesised materials had more than one phase present according to the PXRD (see the black dashed box in Figure 3.3). This was due to the size mismatch between Ba and Ca in the parent titanate resulting in a miscibility gap (as discussed earlier).

BET surface area measurements were performed on all 66 materials. Specific surface areas (SSA) were found to be in the range of 54 to 116 m^2 g^{-1}. The compositional dependence of SSA can be seen in Figure 3.3. The SSA seen around or at the corners of the compositional phase diagram were consistently higher than group 2 titanate materials reported previously in the literature,[233–235] which is attributed to the low temperature synthesis conditions used herein. The BET data suggests that samples containing high at% Ca had the lowest surface areas and samples containing high at% Sr had the highest surface areas.

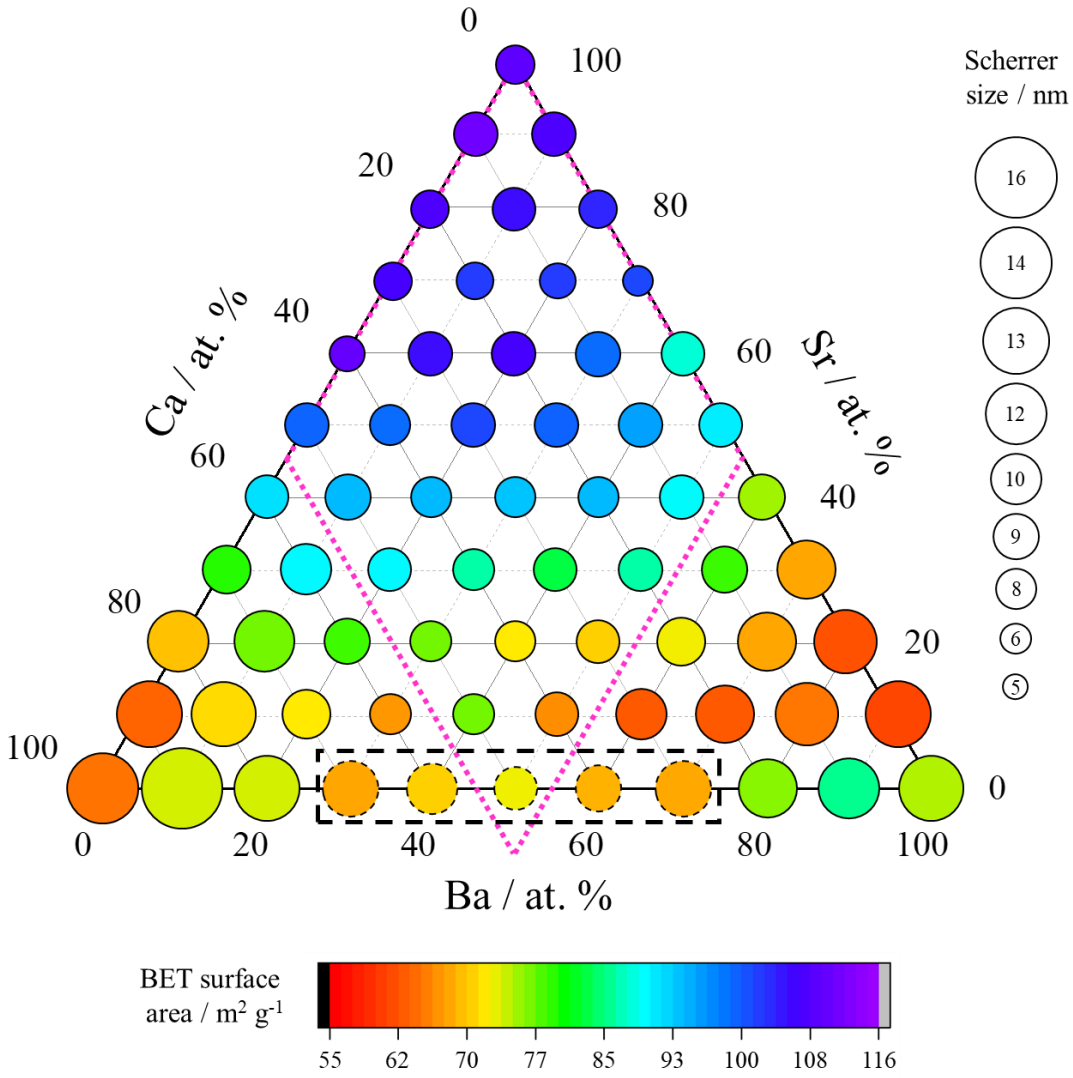

Figure 3.3: Phase analysis, SSA analysis and Scherrer analysis for the full composition diagram. The colour of each ball corresponds to the BET surface area. The size of each ball corresponds to the size calculated from the Scherrer equation. The pink dotted lines split the diagram roughly into three distinct areas of PXRD size. Those balls with a black dashed line represent materials with a phase impurity seen in the XRD along the Ba-Ca titanate system.

Transmission Electron Microscopy (TEM) techniques were used to gain additional information about the structure and morphology of the materials. Images for the three binary compositions are shown below in Figure 3.4.

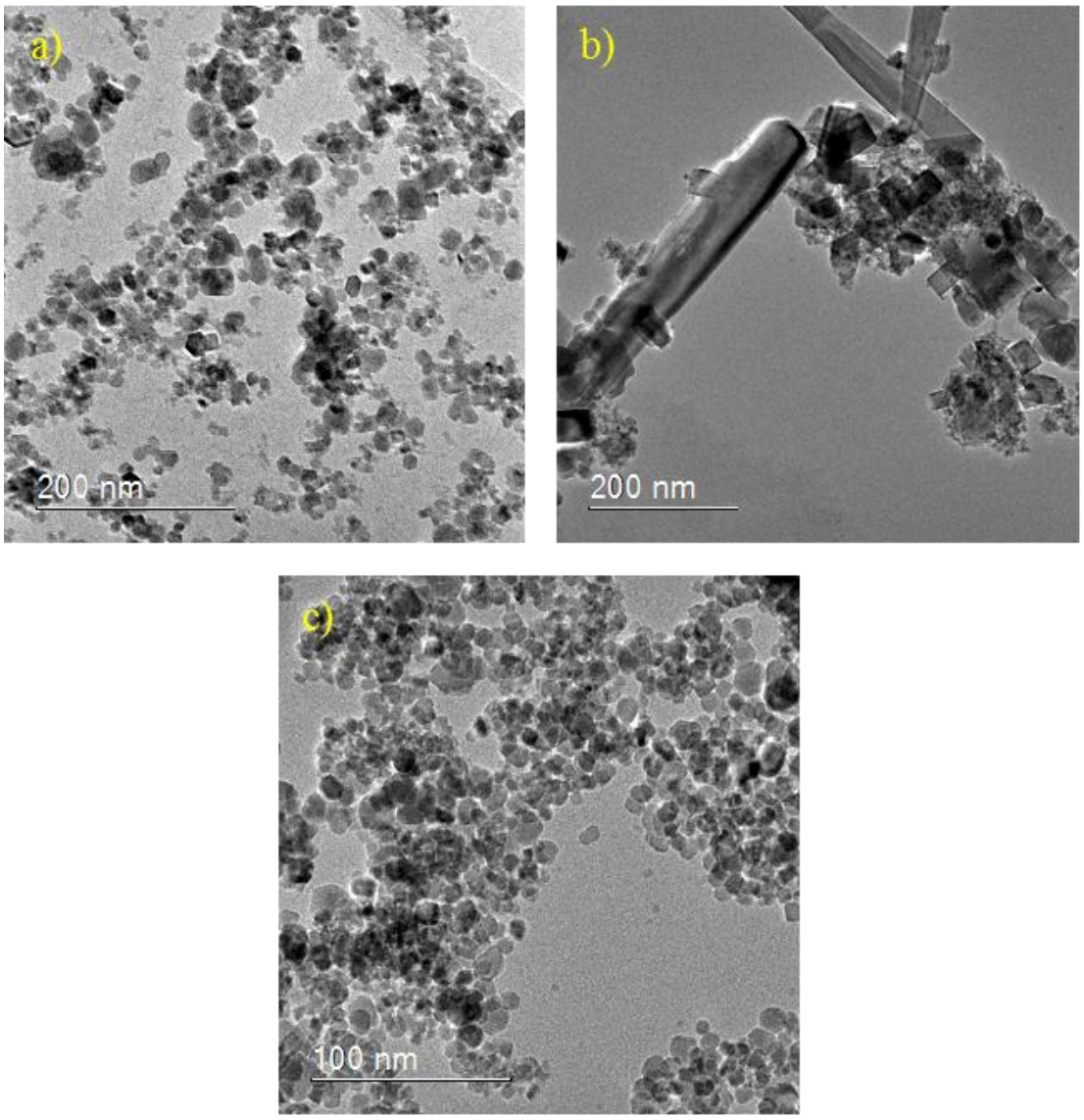

Figure 3.4: Transmission electron microscope images of as synthesised materials: a) $BaTiO_3$, b) $CaTiO_3$, c) $SrTiO_3$.

The TEM images suggest that the discrepancies between SSA and crystallite size are because of differing compositions displaying different particle shapes. The size and shape of the individual titanate perovskites varied greatly depending on composition. $CaTiO_3$ [Figure 3.4 b)] had large variation in particle size and shape with cubes, rods and small irregular particles seen. This suggests Ostwald ripening is occurring to a greater extent. The $BaTiO_3$ [Figure 3.4 a)] and $SrTiO_3$ [Figure 3.4 c)] samples both containing roughly spherical, irregular particles, although the particle size in the $SrTiO_3$

sample was smaller than that of the $BaTiO_3$ sample. There was also a greater variation in size and shape in the $BaTiO_3$ sample.

3.5. Electrochemical Characterisation

3.5.1. High Throughput Electrochemical Characterisation

All samples were screened for their electrocatalytic activity prior to any in-depth analysis being carried out. Samples were formulated into inks according to recipe 1 in Section 2.3.1 and deposited onto glassy carbon rotating disk electrodes with a mass loading of 0.08 mg cm^{-2}. The electrodes were cycled between 0.2 and −0.8 V vs Ag/AgCl in O_2 saturated 0.1 M NaOH at 400 rpm until consecutive CV traces were identical. This was to provide electrode pacification and occurred after approximately 5 cycles. Linear sweep voltammetry was then carried out between 0.2 and −0.6 V vs Ag/AgCl to examine overpotentials and current for the ORR. Well defined reduction curves were seen for all catalysts in the region of 0.0 to −0.6 V vs Ag/AgCl. Currents reached were dependent on the rotation speed of the RDE.

Figure 3.5 shows the typical linear sweep voltammogram response seen by all catalysts. The spacing between the current responses at the differing rotation speeds is related to the square of the rotation speed in line with the Koutecky-Levich (K-L) equation. Well-formed sigmoidal waves can be seen at all rotation rates and were seen for all catalysts although limiting current densities and overpotentials varied significantly.

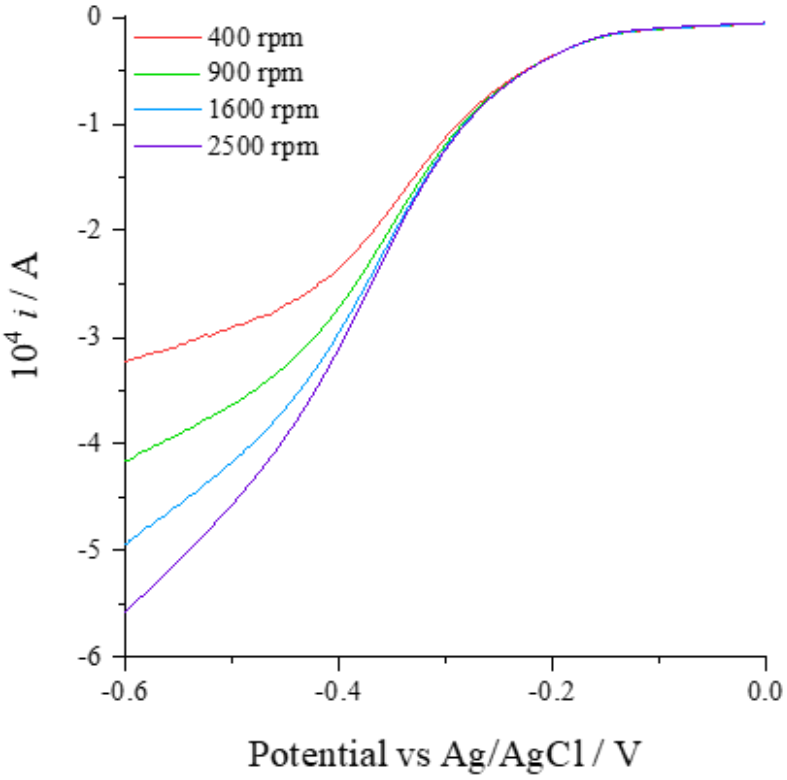

Figure 3.5: Current vs voltage linear sweep voltammetry responses of the $BaTiO_3$ catalyst at four different rotation speeds. Analysis was carried out in 0.1 M NaOH at a scan rate of 10 mV s^{-1} between 0.0 V and −0.6 V vs Ag/AgCl.

Figure 3.6 a) shows the variation seen in the current achieved at −0.5 V vs Ag/AgCl with composition. All plotted data points can be found in the appendix in Table 9.2. The limiting current has some element of compositional dependence; samples with high Ba content had more negative current densities at −0.5 V vs Ag/AgCl than catalysts containing high Ca or high Sr content, making those materials high in Ba better catalyst for the ORR. The best performing catalyst was $Ba_{0.8}Sr_{0.2}TiO_3$ with an observed current density of −1.49 mA cm^{-2} at −0.5 V. The worst performing catalyst was $Ca_{0.9}Sr_{0.1}TiO_3$ with an observed current density of −0.60 mA cm^{-2} at −0.5 V. The observed current may have been limited by the low electrical conductivity of mixed metal oxides. No conductive carbon was used in addition to the catalyst ink in these samples, which could have helped to counteract the lower conductivity.[113]

Figure 3.6 b) shows the onset potential of the ORR and has been taken when the current density reached −0.1 mA cm^{-2}. The onset potential of the samples is more uniform across the phase diagram, with only those samples towards the corners of the phase

diagram showing significant variation. The sample with the most positive onset potential was $BaTiO_3$ with an onset potential of −176 mV vs Ag/AgCl whereas the sample with the the most negative onset potential was $Ca_{0.9}Sr_{0.1}TiO_3$ with an onset potential of −318 mV.

Both onset potential and current density are poor in the left-hand corner, which corresponds to high calcium content in the materials. In comparison, the best performing samples are seen in the right-hand corner for both onset potential, and current density corresponding to high barium content. However, when the catalytic performance indicators are examined over the phase space as a whole, it appears that composition is not the sole reason for the changing activity as the transitions between areas of high and low activity are not smooth. Due to the fairly low resolution of samples examined (samples at every 10 at%) it may be that there are local structure activity relationships that cannot be seen here.

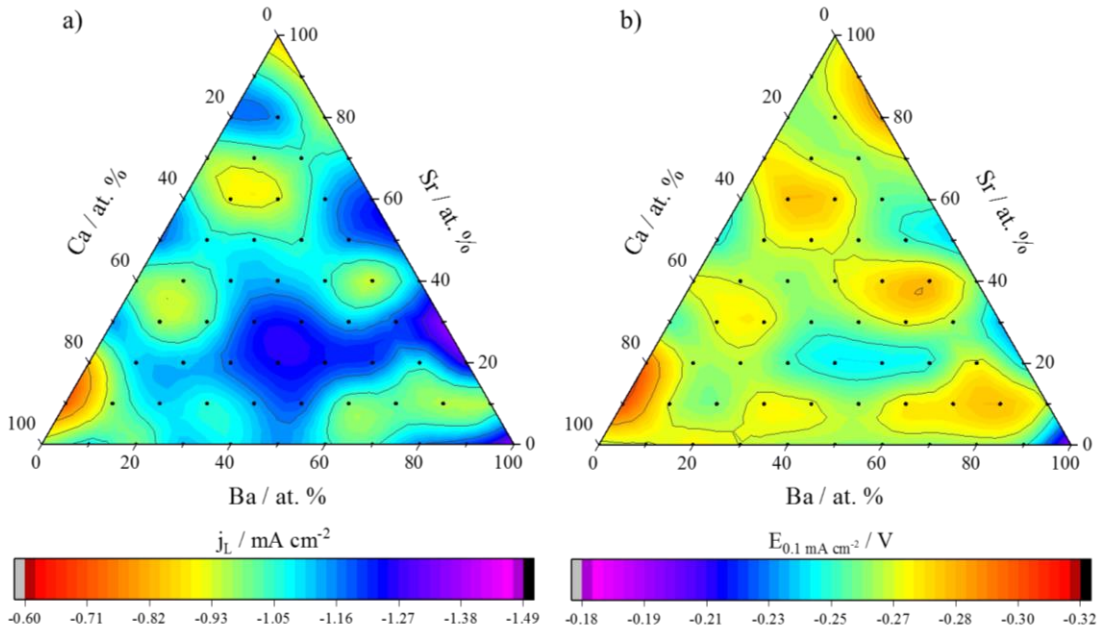

Figure 3.6: a) Current density for the full composition diagram taken at −0.5 V vs Ag/AgCl, b) Onset potential for all compositions taken at a current density of −0.1 mA cm^{-2}. All data was recorded at 900 rpm in O_2 saturated 0.1 M NaOH electrolyte at a scan rate of 10 mV s^{-1}.

The best performing samples had ORR activities that slightly exceeded that of hexagonal $BaTiO_3$ in the work conducted by Chen *et al.* with a more positive onset

potential reported here (an overpotential of 0.85 V vs RHE in this work for $BaTiO_3$ compared to an overpotential of ca. 0.83 V in the referenced work).[229]

TEM images were taken to see if there was a structural reason for the differences in electrochemical activity.

Figure 3.7 shows the TEM images from the best performing sample [Figure 3.7 a)] and worst performing sample [Figure 3.7 b)] by limiting current value reached at −0.5 V vs Ag/AgCl. The TEMs for the best performing sample, $Ba_{0.8}Sr_{0.2}TiO_3$, had an irregular, spherical morphology. However, the TEM for $Sr_{0.1}Ca_{0.9}TiO_3$, which was the worst performing sample, showed a very different morphology and size distribution. Cubes, rods and small particles were seen in the TEM, very similar to the morphology of $CaTiO_3$ seen in Figure 3.4 b). There was a very wide size distribution, with nanoparticles in the < 20 nm region, combined with cubes of 40-50 nm and rods > 200 nm. It may be this wide size distribution and combinations of morphologies that caused the poor catalysis.

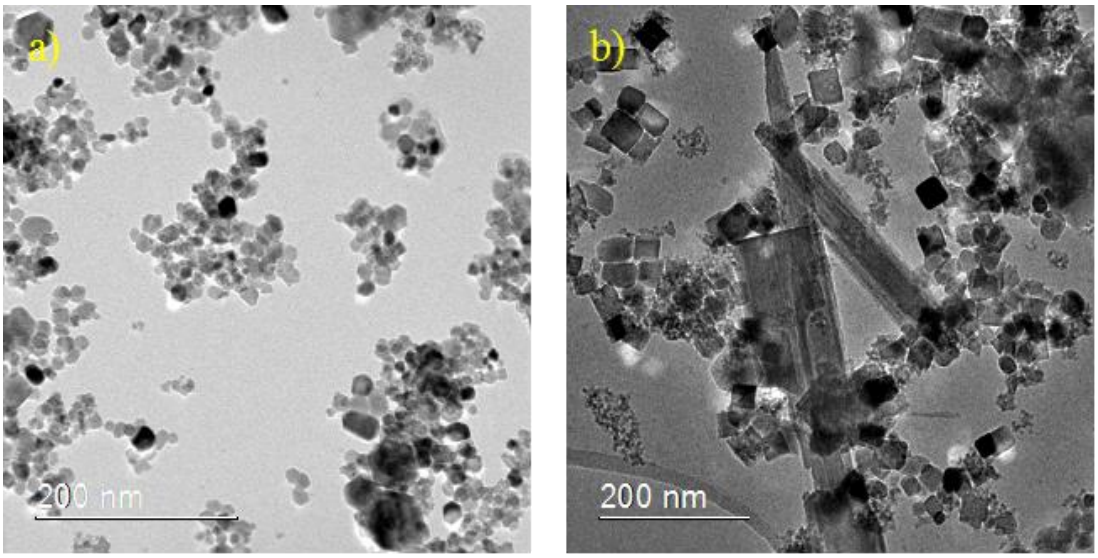

Figure 3.7: TEM images for the best and worst performing electrocatalysts by limiting current value at −0.5 V vs Ag/AgCl: a) $Ba_{0.8}Sr_{0.2}TiO_3$, b) $Sr_{0.1}Ca_{0.9}TiO_3$

3.5.2. In-Depth Electrochemical Characterisation

More in-depth electrochemical characterisaion was carried out on the three best performing samples to gain greater understanding into the catalysis occuring.

The dependence of the voltammogram on the rotation rate was investigated. For all catalysts, well-formed reduction waves were seen at all rotation rates. K-L analysis was

carried out to investigate the electrokinetic information found in the linear sweep voltammograms. The plots for the best performing samples are shown in Figure 3.8 above. All plots show a linear relationship between the rotation rate and the current density at −0.5 V vs Ag/AgCl. The plots for all catalysts show a non-zero intercept on the $1/j_L$ *y*-axis suggesting there was some component of kinetic control to the limiting current as the K-L *y*-intercept is equal to the reciprocal of the kinetic current density.[246]

The intercept of $Ba_{0.8}Sr_{0.2}TiO_3$ is significantly lower than that for the other two catalysts which suggests that the chemical reduction is faster on this catalyst. Only the points for the 400, 900 and 1600 rpm are shown as in all cases the point at 2500 rpm deviated from the line of best fit. This may have been due to a greater contribution from the undesirable $2e^-$ reduction step to the overall reaction at higher rotation rates.[219]

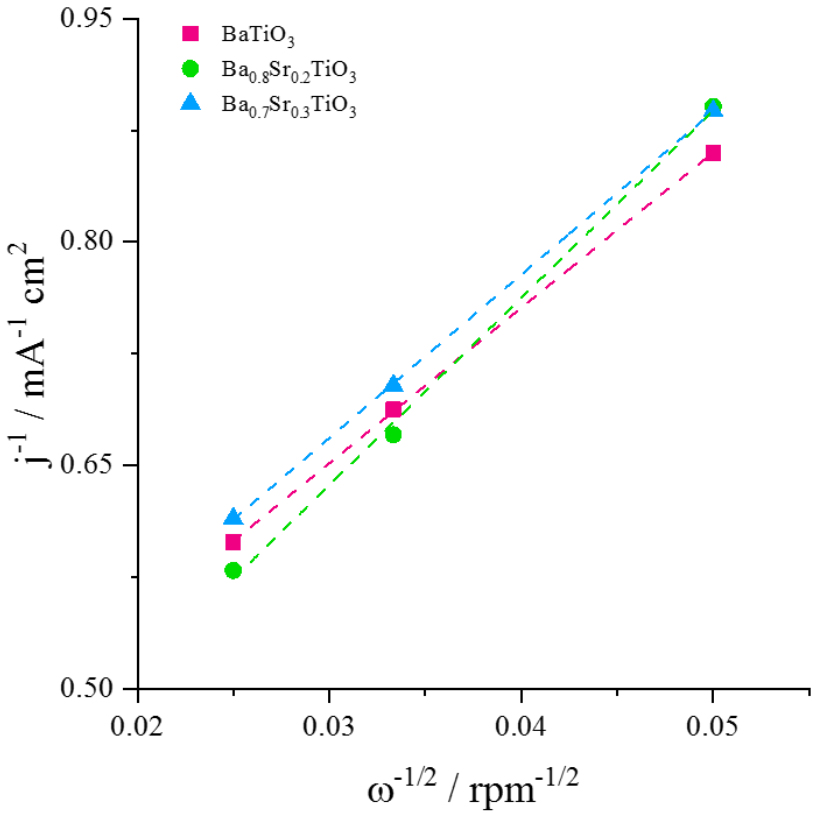

Figure 3.8: Koutecky-Levich plots for O_2 reduction. All measurements were carried out in O_2 saturated 0.1 M NaOH electrolyte with a scan rate of 10 mV s^{-1}. Current densities were taken at −0.5 V vs Ag/AgCl.

To examine in depth the ORR performance on the best performing electrocatalysts, first cyclic voltammogram (CV) measurements were carried out in degassed (N_2 saturated) electrolyte and these are shown in Figure 3.9. All CV curves exhibited small

cathodic reduction peaks near the onset potential of O_2 reduction (around −0.3 V vs Ag/AgCl) even though expeirments were carried out in N_2 saturated electrolyte. The current observed for $BaTiO_3$ and $Ba_{0.8}Sr_{0.2}TiO_3$ was similar, however the current observed for $Ba_{0.7}Sr_{0.3}TiO_3$ was lower. This could not be explained by the BET surface area as $Ba_{0.8}Sr_{0.2}TiO_3$ had a lower Specific Surface Area (SSA) (63.8 m^2 g^{-1}) than $Ba_{0.7}Sr_{0.3}TiO_3$ (68.1 m^2 g^{-1}). Therefore, it is likely that the peaks in the current can be assigned to the reduction and oxidation of oxygen, possibly trapped near the surface of the material (as all experiments were carried out in N_2 saturated electrolyte).

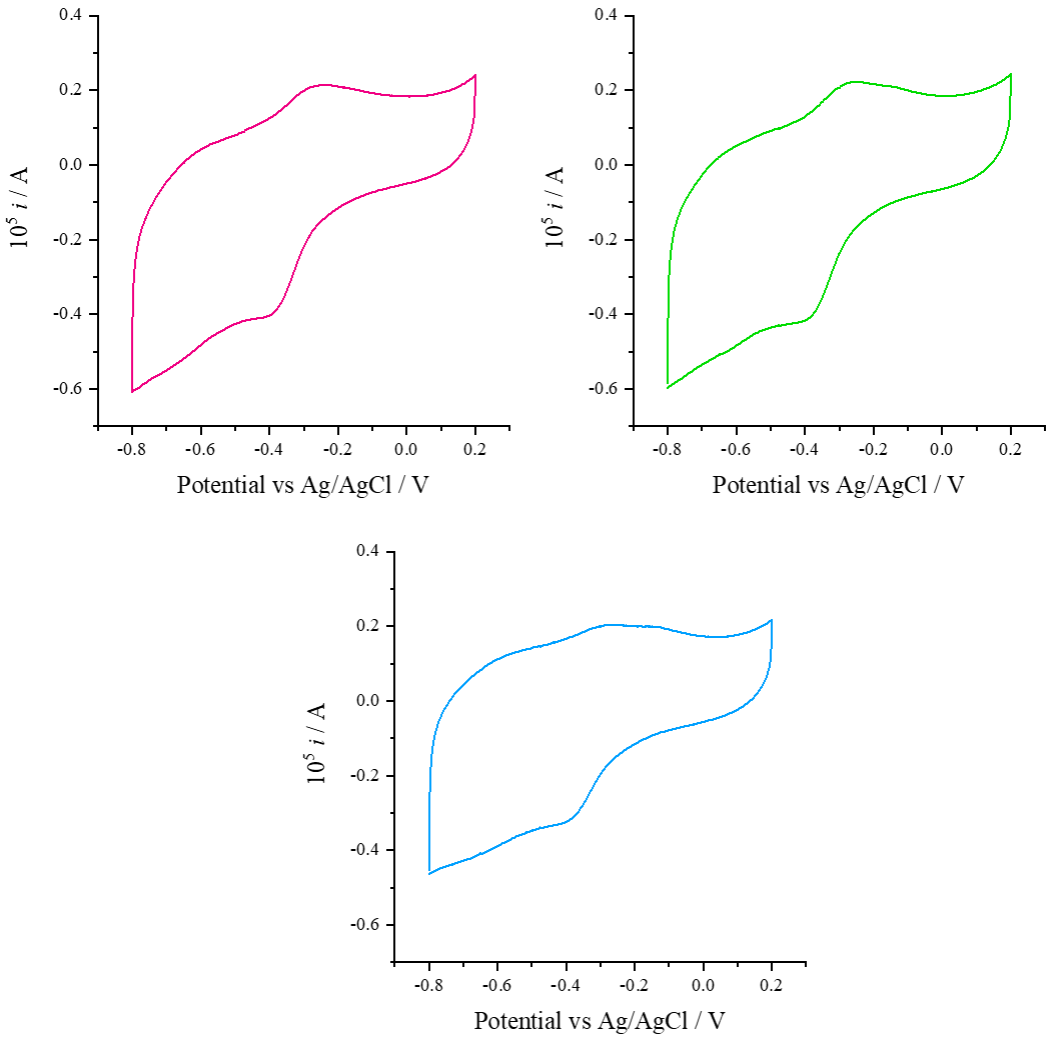

Figure 3.9: Cyclic voltammograms of a) $BaTiO_3$, b) $Ba_{0.8}Sr_{0.2}TiO_3$ and c) $Ba_{0.7}Sr_{0.3}TiO_3$ coated onto a glassy carbon RRDE. Data taken in N_2-saturated 0.1 M NaOH at 10 mV s^{-1} after 5 scans.

The durability of an electrocatalyst is an important factor for evaluating performance for end-use applications. Chronoamperometry was used to examine how the current achieved at a set voltage (−0.5 V vs Ag/AgCl) changed over time. Catalysts were held

at a voltage of −0.5 V vs Ag/AgCl and spun at 900 rpm. The decay in the current response was measured over 1 hour. The responses shown as a percentage of the initial current are shown in Figure 3.10. The best performing catalyst after 3600 s cycling was $Ba_{0.7}Sr_{0.3}TiO_3$ which retained 84 % activity at −0.5 V. The worst performing was $Ba_{0.8}Sr_{0.2}TiO_3$ which only retained 70 % activity. $BaTiO_3$ retained 78 % activity over the cycling time. The trend in stability was not the same as seen for either surface area ($BaTiO_3$ > $Ba_{0.7}Sr_{0.3}TiO_3$ > $Ba_{0.8}Sr_{0.2}TiO_3$) or for Scherrer size ($BaTiO_3$ > $Ba_{0.8}Sr_{0.2}TiO_3$ > $Ba_{0.7}Sr_{0.3}TiO_3$) suggesting that there was a change occurring over the time of the experiment at the surface of the catalyst coated electrode. There have been several discussions in the literature about how degradation occurs at a metal oxide surface and these include H_2O_2 attack, metal dissolution from the catalyst surface and changes in electrolyte concentration over time.[247,248]

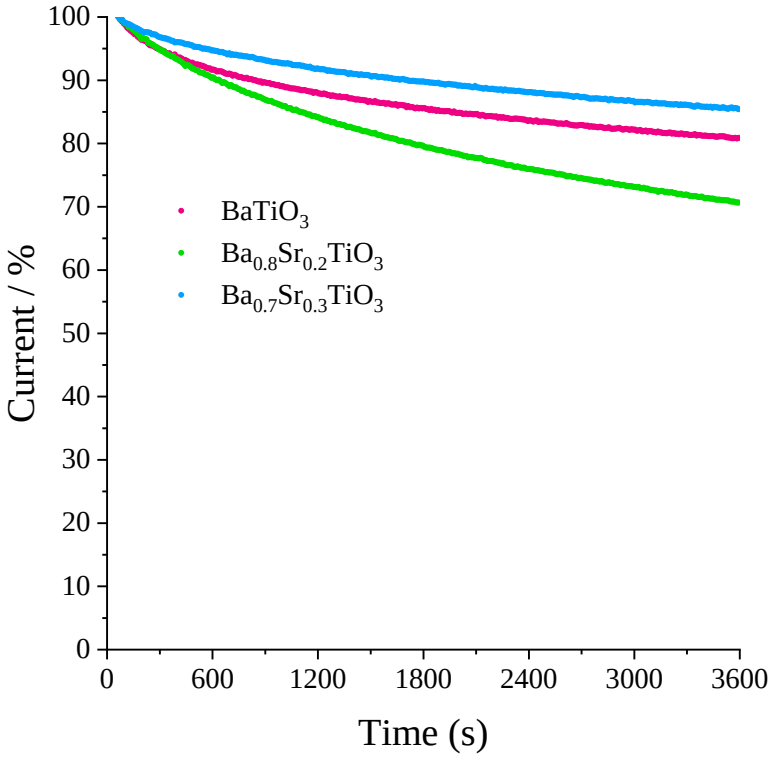

Figure 3.10: Stability data for the three catalysts using the chronoamperometry method. The data are shown as a percentage of the initial current. All measurements were carried out over a period of 1 hour in O_2 saturated 0.1 M NaOH electrolyte with a scan speed of 10 mV s^{-1} and a rotation speed of 900 rpm. The experimental error is ± 2%.

The percentage yield of hydrogen peroxide evolved during the oxygen reduction on the three highlighted catalysts was investigated using a catalyst coated glassy carbon

disk/Pt ring electrode. The potential of the ring was held at 0.2 V vs Ag/AgCl; at this potential the hydrogen peroxide oxidation is mass transport controlled on Pt meaning that the concentration of HO_2^- is effectively zero at the ring surface, the HO_2^- reacts immediately without kinetic barrier.[249] The voltammograms collected at 2500 rpm are shown in Figure 3.11. The peroxide yields and electron transfer numbers calculated from the RRDE experiments at −0.5 V are shown in Table 3.1. These were calculated using the ratio of ring and disk currents alongside the collection efficiency number as described by equations 2.10 and 2.11 in Chapter 2.

The left-hand side of Figure 3.11 shows the calculated electron transfer numbers and peroxide yields once catalytic reduction of oxygen had begun. Initially, at high potentials, peroxide yields were lower and electron transfer numbers were higher although at around −0.4 V a reasonably steady state was reached. This is seen in other RRDE studies.[247] The e^- transfer numbers for $BaTiO_3$ and $Ba_{0.7}Sr_{0.3}TiO_3$ ranged from 2.7-3.3 whereas for $Ba_{0.8}Sr_{0.2}TiO_3$ the e^- transfer number ranged from 3.3-3.8. The peroxide yield followed the same pattern. For reference, industrially used Pt black samples have a peroxide yield of < 1 % and an e^- transfer number that approaches 4.

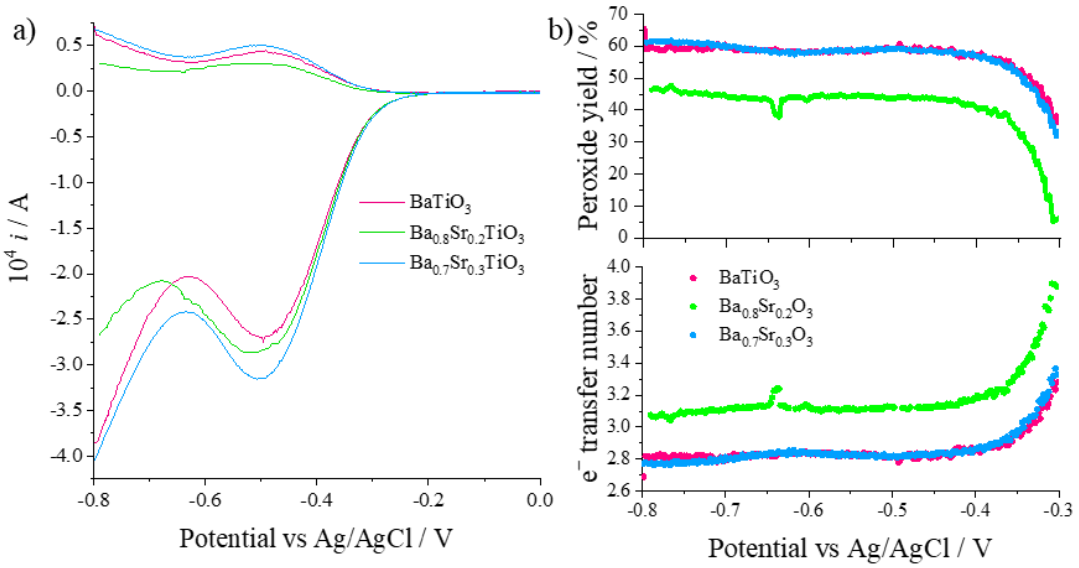

Figure 3.11: a) disk and ring current responses as the disk potential was scanned from 0.2 V to −0.8 V vs Ag/AgCl. The ring was held at 0.2 V vs Ag/AgCl, b) electron transfer numbers and peroxide yields calculated from the RRDE experiment using equations 2.10 and 2.11. All measurements were carried out in O_2 saturated 0.1 M NaOH electrolyte with a scan speed of 10 mV s^{-1}. The experimental error is ± 2%.

Table 3.1: Electrocatalytic data for the three catalysts highlighted above. Onset potential taken at −0.1 mA cm^{-2}. Data for Pt black from reference 220.

Sample	$BaTiO_3$	$Ba_{0.8}Sr_{0.2}TiO_3$	$Ba_{0.7}Sr_{0.3}TiO_3$	Pt Black
K-L Gradient	10.4 ± 0.1	12.6 ± 0.6	10.9 ± 0.01	11.0 ± 0.1
K-L y-intercept	0.34 ± 0.003	0.26 ± 0.02	0.34 ± 0.003	−0.06 ± 0.01
Onset potential / mV	−180	−220	−220	-
$J_{-0.5\ V}$ / mA cm^{-2}	−1.45	−1.49	−1.42	-
n (RRDE)	2.69	3.14	2.9	-
% HO^- (RRDE)	66	43	55	< 1
% Activity loss	22	30	16	-

By comparing the three catalysts above, conclusions about the best performing material could be drawn. $BaTiO_3$ was the poorest catalyst of the three studied, with the lowest electron transfer number, highest peroxide yield and an intermediate stability. However, it had the least negative onset potential by 40 mV. $Ba_{0.8}Sr_{0.2}TiO_3$ had the lowest peroxide yield and therefore had the highest electron transfer number suggesting that the preferred $4e^-$ pathway plays a larger role than the $2e^-$ pathway in this catalyst. However, the stability of this catalyst was much poorer than the other two. This could potentially be improved by changing the ink formulation. The most stable catalyst was $Ba_{0.7}Sr_{0.3}TiO_3$ but this catalyst had a much higher yield of peroxide suggesting that the $2e^-$ reduction pathway was favoured over the $4e^-$ pathway.

3.6. Summary and Conclusions

A ternary phase diagram consisting of group 2 metal titanate perovskites was designed and synthesised by a one-step CHFS method. PXRD was used to confirm that all materials had a perovskite structure ($BaTiO_3$ and $SrTiO_3$-Cubic, $CaTiO_3$ orthorhombic), although those along the $Ba_xCa_{1-x}TiO_3$ line had two distinct perovskite phases above 25 at% dopant. This was due to the large size mismatch between Ba^{2+} and Ca^{2+} ions. The BET specific surface area of all materials was between 54 $m^2\ g^{-1}$ and 115 $m^2\ g^{-1}$; which was higher for all materials than has been previously reported in the literature. It is suggested that this is due to the low temperature synthetic conditions. High at% Sr compositions gave high surface areas and small Scherer sizes whilst high at% Ca compositions gave the reverse. The TEM images revealed that

whilst, $SrTiO_3$ and $BaTiO_3$ had small, spherical particulate morphology, $CaTiO_3$ had an irregular morphology, with large rods and cubes seen as well as smaller spherical particles. This may have been the cause of the lower SSA.

High throughput electrochemical analysis was used to screen all materials for possible activity hot spots. This revealed that materials high in Ba and low in Sr content had high electrochemical activities whereas those high in Ca had low electrochemical activity. Overall, a gradual change in properties was observed for the materials in the library (e.g SSA and PXRD peak positions). This suggested that the conditions for the synthesis of the samples were similar, and that variations in particle properties were largely based on the thermodynamics of the crystallisation for a given composition and not due to variations in the synthetic conditions between samples. Therefore, using CHFS as a synthetic technique has distinct advantages over more conventional or multistep preparation techniques.

The highest performing catalysts were then investigated further using RRDE techniques. Peroxide yields of all catalysts were high, although $Ba_{0.8}Sr_{0.2}TiO_3$ had a considerably lower yield than the other two catalysts. The electron transfer numbers of all three catalysts were between 2 and 4 suggesting some contribution from both the 2 e^- and 4 e^- reduction pathways. The Koutecky-Levich plots had a linear relationship between the rotation speed and the limiting current densities confirming that the reduction was mass transport controlled. The overpotentials of all catalysts were larger than that of platinum although $BaTiO_3$ only by~200 mV.

Whilst the catalysts examined here would not compete with current industrial candidates, this study has successfully demonstrated the potential of using high throughput CHFS synthesis for the creation of candidate libraries of materials for use as oxygen reduction electrocatalysts. Further work may consider the addition of conductive carbon to the catalyst ink to create conductive networks between the perovskite particles. Previous studies have shown that this can decrease overpotentials and increase limiting current densities.[112]

4. Synthesis and Optimisation of *A*MnO_3 Materials as ORR Electrocatalysts

4.1. Abstract

Perovskite manganites (formula *A*MnO_3) have drawn attention as ORR catalysts in the literature since the 1980s. CHFS offers a unique synthesis method to quickly synthesise a variety of *A*MnO_3 materials. Four perovskite manganite materials were initially synthesised and analysed via XRD, BET, XPS, TEM and SEM. Their performance as ORR catalysts was then examined using LSV, CV, and chronoamperometry. $LaMnO_3$ was found to be a superior catalyst for the ORR and was chosen to undergo further optimisation of its synthesis conditions, to examine if the synthesis could be used to control performance.

4.2. Introduction

Manganese oxides are considered to be attractive catalysts for the ORR in comparison to other transition metal oxides due to factors such as their earth abundance, relative low cost and environmentally friendliness.[250] Despite their instability in acidic media, MnO_x materials have been found to be promising catalysts in both metal-air batteries and alkaline fuel cells.[251] For example, Roche *et al.* deposited MnO_x catalysts onto various carbon supports with several catalysts showing exceptional activity towards the ORR, with electron transfer numbers close to four, and onset potentials close to the value of Pt.[252] The best performing catalyst was a Ni doped MnO_x supported on Vulcan XC 72 (carbon black), giving an onset potential of +0.33 V at neutral pH vs SHE. Cheng *et al.* reported that the activity of MnO_2 towards the ORR could be tuned by changing the crystallographic structure and morphology. α-MnO_2 was found to be more active than both β-MnO_2 and γ-MnO_2. α-MnO_2 nanowires proved to be more catalytically active than other structures or bulk microparticles with a reported overpotential of 0.06 V vs Ag/AgCl.[253]

Perovskite manganese oxides have also been extensively studied. As stated in Section 1.7, the physical and chemical flexibility of perovskite oxides is closely related to their *A* or *B* site cations. Therefore, by substituting some or all the *A* site cations a new material with optimised properties may be formed. *A*MnO_3 materials have been the focus of several studies on the effect of the *A* site cation on the observed ORR activity.[254,255] The oxidation state of Mn at the *B* site can be changed by varying the *A* site cation. For example, by substituting La^{3+} for Ca^{2+} at the *A* site, a proportion of

Mn^{3+} is converted to Mn^{4+} on the *B* site which can increase the ORR activity.[256,257] The increase in activity has been proposed to be caused by the redox state of the *B* site (in this case Mn) and its proximity to the reversible oxygen potential.[254,258]

As well as changing the metal cations to affect the physical and catalytic behaviour of the manganite, changing aspects of the synthesis can also lead to different chemical, physical and catalytic properties. Altering precursor concentrations in the CHFS has been shown to have great effects on morphological and size properties.[178] For example, Marchand *et al.* were able to optimise the synthesis of indium tin oxide conductive nanomaterials by varying the base and precursor concentrations.[188] Control over the synthetic conditions meant they were able to maximise the phase purity of the materials and thus control the conductivity. There have been numerous methods employed for the synthesis of nano-manganese oxides including solution based techniques (hydrothermal, sol-gel), solid-state methods and pulsed laser deposition.[259] In 2016 Wang *et al.* reported the synthesis of porous Mn_2O_3 via a solid state method with comparable ORR activity to Pt/C.[260] CHFS has been used as a tool to prepare various Mn_xO_y containing species including Mn_2O_3, MnO_2, $La_{1-x}Sr_xMnO_3$, $LiMn_2O_4$, and $CuMn_2O_4$. [261–263] Lee *et al.* found that by varying precursor concentrations, differing Mn oxides could be formed.[261]

Extensive research has been carried out with the aim of increasing the $LaMnO_3$ surface area due to traditional synthetic methods leading to low surface area and uncontrolled phase impurities which causes low mass activity.[120,264,265] Zhang *et al.* prepared phase pure $LaMnO_3$ via a sol-gel method using citric acid and ethylene glycol with a surface area of 7 $m^2\ g^{-1}$, Hardin *et al.* synthesised a homogeneous, phase pure $LaMnO_3$ perovskite with a surface area of 11 $m^2\ g^{-1}$ via a colloidal synthesis method[264]. Finally, Li *et al*. prepared a high surface area $LaMnO_3$ (21 $m^2\ g^{-1}$) via a sol-gel method using citric acid and EDTA as chelating agents.[120]

An additional way of introducing morphological changes into a material is by varying the heat-treatment, by using different temperatures or techniques. This has been shown to affect the crystal structure present, as well as the degree of sintering and growth in particle size seen. Zhou and Sunarso previously described how temperature shock could be used to enhance the activity of a $LaNiO_3$ material.[266] They discovered that heating to different temperatures followed by rapid quenching in air, led to a family of

crystal structures which had varying activities towards the ORR. This shows that a simple process can be used to adjust the activity of a specific catalyst towards the ORR.

In this chapter, CHFS techniques were used to synthesise various *A*MnO_3 materials (*A* = La, Sm, Y and Ca). The effect of *A* site substitution on the ORR catalytic activity of *A*MnO_3 materials was investigated and compared to materials made by more conventional synthetic routes. The most promising of these materials was then subjected to various pre and post synthetic changes, to optimise it for use as an industrial ORR catalyst.

4.3. Materials and Methods

4.3.1. Synthesis of *A*MnO_3 materials

The synthesis of the materials was carried out as described in Section 2.12.

4.3.2. Physical Characterisation of *A*MnO_3 materials

The physical characterisation of the materials was carried out as described in Section 2.2. PXRD, XRF, XPS, and BET were carried out on all samples with TEM and SEM carried out on selected samples.

4.3.3. Electrochemical Characterisation of *A*MnO_3 materials

Inks for drop casting onto GC electrodes were prepared according to method 2 in Section 2.3.1.

All electrochemical testing was carried out in 0.1 M $KOH_{(aq)}$ electrolyte using a Ag/AgCl reference (saturated KCl) and a platinum wire counter in a 3 electrode setup.

Electrochemical screening of the samples for the ORR was carried out by Linear Sweep Voltammetry between 0.1 and −0.6 V (vs Ag/AgCl) at 10 mV s^{-1} at eight different rotation speeds (200, 400, 600, 900, 1200, 1600, 2000 and 2500 rpm) in oxygenated electrolyte.

RRDE testing was carried out as with LSV testing, but the ink was drop cast onto a rotating ring disk electrode to give the same catalytic loading as in previous tests. The ring potential was set to 0.35 V vs Ag/AgCl to ensure complete peroxide decomposition.[267]

Chronoamperometry was performed by holding the potential at −0.5 V vs Ag/AgCl and measuring the current response over 14400 or 3600 s. Oxygen was bubbled into the electrolyte for the duration of the test.

Cyclic voltammetry was carried out at 5 mV s^{-1} between −1 and 0.65 V vs Ag/AgCl in degassed (N_2 saturated) electrolyte.

4.4. Results and Discussion

Initially, the effect on ORR activity of substituting the *A* site cation in *A*MnO_3 was investigated. Changing the *A* site cation not only affects physical characteristics such as surface area and particle size, but also potentially the surface Mn valence.[268] Here, four cations were substituted onto the *A* site (Ca, La, Sm and Y) and the effect on the oxygen reduction reaction was investigated. Whilst all materials have been studied as ORR catalysts before, there are currently no literature reports on these materials produced via CHFS for use as ORR catalysts, and changing the synthetic method has been shown to have a great effect on the observed catalytic activity.[259]

4.4.1.1. *A* Substitution in *A*MnO_3: Physical Characterisation

After the continuous hydrothermal flow synthesis, cleaning by centrifugation and freeze-drying, the nanoparticulate metal oxides were collected with a >90% yield. Losses can come from freeze drying and washing steps which are not optimised for small scale production. After freeze drying, all materials were free flowing powders. The lanthanum manganites were brown in colour, and the samarium and yttrium manganites were grey/blue in colour. Due to the highly soluble nature of the Ca nitrate precursor, the $CaMnO_3$ material was unsuitable for CHFS. Instead, synthesis was completed via a sol-gel method (see Chapter 2.12) yielding a free flowing, black powder.

All samples were then heat treated to give phase pure materials as shown below in Table 4.1 Heat treatment times and temperatures for $LaMnO_3$, $YMnO_3$ and $SmMnO_3$ were optimised to give phase pure material by PXRD at the lowest time and temperature to minimise growth and sintering of the particles.

Table 4.1: Heat treatment conditions of *A*MnO_3 materials discussed below.

	Temperature	Time	Ramp rate	Appearance
$LaMnO_3$	780 °C	2 hrs	10 °C / min	Black powder
$YMnO_3$	1100 °C	3 hrs	10 °C / min	Black/blue powder
$SmMnO_3$	1100 °C	3 hrs	10 °C / min	Black/grey powder
$CaMnO_3$[269]	900 °C	5 hrs	5 °C / min	Black powder

XRF was used to examine the ratio of elements in the samples. The $LaMnO_3$ sample had a slight La excess, with the stoichiometry measured as $La_{1.06}Mn_{0.94}O_3$. $YMnO_3$ was observed by XRF with no excess of either Y or Mn. $SmMnO_3$ was also observed with no Sm or Mn excess. $CaMnO_3$ was found to have a slight Ca excess (and Mn deficiency), with the stoichiometry measured as $Ca_{1.08}Mn_{0.92}O_3$.

Figure 4.1 shows the XRD patterns of the as synthesised and heat-treated *A*MnO_3 oxide nanoparticles, revealing that all heat-treated materials had *A*MnO_3 as the majority phase and those materials made via CHFS showed a high degree of phase purity. $LaMnO_3$ pre (black) and post (red) heat treatment at 780 °C is shown in Figure 4.1 a). Pre heat treatment there was little or no evidence of $LaMnO_3$, instead a mixture of $La(OH)_3$ and Mn_xO_y species was seen. This was expected as below 410 °C, La_2O_3 was not expected to have formed.[270] Once the precursor mixture made via CHFS was heat treated, phase pure rhombohedral (*R*-3*c*) $LaMnO_3$ was seen, which was a good match for ICSD collection code no. 50041. The peaks observed were very broad which suggested that the crystallite domains were nanosized. $YMnO_3$ pre and post heat treatment is shown in Figure 4.1 b). Unlike $LaMnO_3$, there were some characteristic $YMnO_3$ peaks in the pre heat treatment pattern as well as peaks from other phases such as $Y(OH)_3$ and Mn_xO_y species. However, this was difficult to say with confidence as yttrium fluoresces under Mo radiation, explaining the very high signal to noise ratio in this case. Post heat treatment at 1100 °C, the majority phase of hexagonal $YMnO_3$ was seen (ICSD collection code 181182) with a small impurity phase assigned to Y_2O_3. The peak ratios differ somewhat to the reference pattern which suggested a degree of preferred orientation in the crystal morphology. $SmMnO_3$ pre and post heat treatment is shown in Figure 4.1 c). There was little evidence of $SmMnO_3$ pre heat treatment, instead a mixture of $Sm(OH)_3$ and Mn_xO_y species were identified. Post heat treatment at 1100 °C

the XRD pattern was a good fit for orthorhombic $SmMnO_3$ (ICSD collection code 95491). As with $YMnO_3$, there was a large difference in peak intensities of the reference and as collected patterns which suggested a degree of preferred orientation. Finally, the PXRD pattern for $CaMnO_3$ made using a sol-gel methodology can be seen in Figure 4.1 d). The pattern was a good match for orthorhombic (*Pnma*) $CaMnO_3$ (ICSD collection code no 35218).

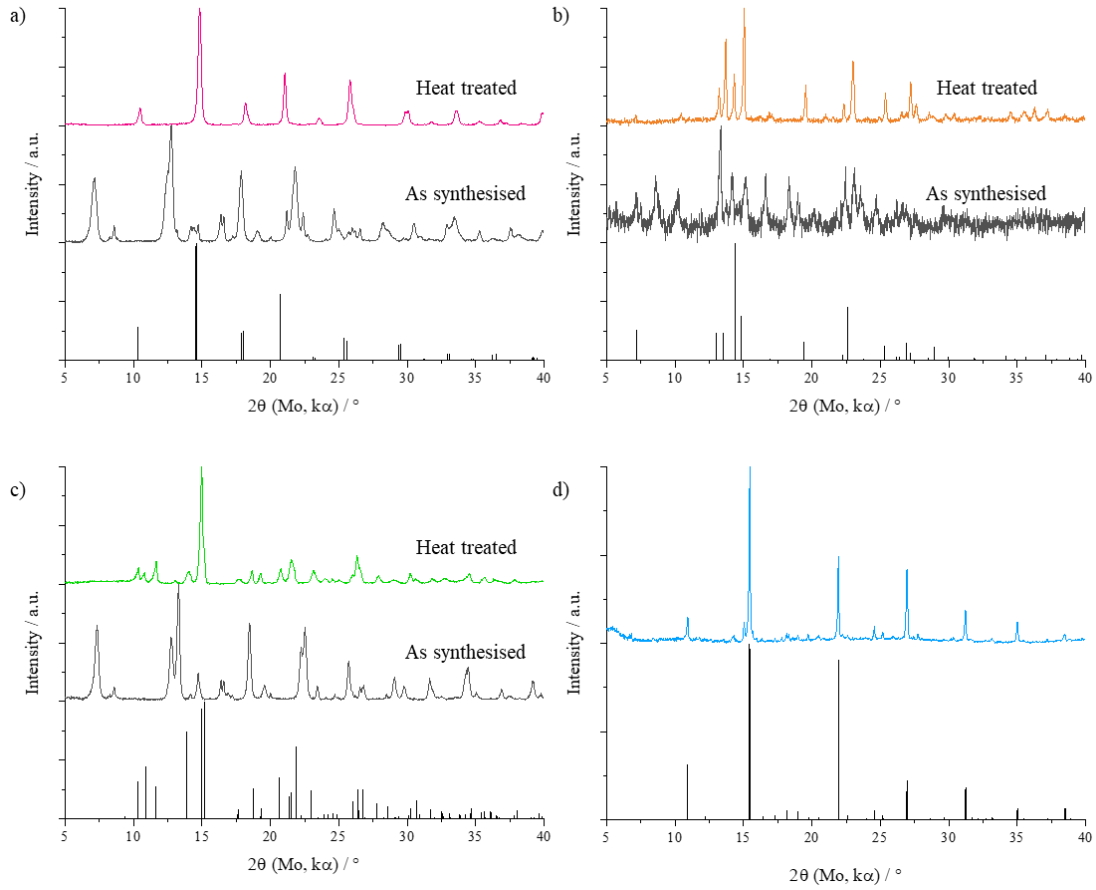

Figure 4.1: PXRD data of a) as synthesised and heat treated $LaMnO_3$, ICSD collection code no. 29119, b) as synthesised and heat treated $YMnO_3$, ICSD collection code no. 181182, c) as synthesised and heat treated $SmMnO_3$, ICSD collection code no. 95491 and d) $CaMnO_3$, ICSD collection code no. 35218.

In comparison to the other three catalysts, a small impurity phase was seen corresponding to α-MnO_2 (ICSD collection code number 9090). This may have been due to the more uncontrollable synthesis method used for this sample. Although there were no obvious additional peaks seen in the $SmMnO_3$ pattern, this was difficult to say for certain due the degree of preferred orientation. The powder diffraction pattern for $LaMnO_3$ had no additional peaks, suggesting that $LaMnO_3$ was the only material

produced in this synthesis, and that $LaMnO_3$ was the only sample certainly made phase pure in this synthesis.

The Scherrer equation was used to determine the primary crystallite size of the materials. These were found to be 16, 21, 26 and 17 nm for $LaMnO_3$, $YMnO_3$, $SmMnO_3$ and $CaMnO_3$ respectively. BET surface area measurements were carried out and found to be 22.7, 2.9, 0.12 and 2.5 $m^2\ g^{-1}$ for $LaMnO_3$, $YMnO_3$, $SmMnO_3$ and $CaMnO_3$ respectively.

XPS was used to study the electronic states of the various manganites. Figure 4.2 shows the XPS spectra of the *A*MnO_3 species investigated. Figure 4.2 a) shows the stacked Mn responses for all materials. Mn can exist in several oxidation states from Mn^{2+} to Mn^{7+}. In Mn based perovskites, the oxidation state is expected to be Mn^{2+}, Mn^{3+} or Mn^{4+}. However, the lack of a satellite peak for Mn^{2+} (648.8 eV) eliminated the possibility of the presence of large percentages of Mn^{2+}.[271] The Mn$p_{5/2}$ signal was observed around 642.0 eV for all samples. This peak contained contributions from Mn^{4+} (642.7 eV) and Mn^{3+} (641.9 eV) states although they are difficult to deconvolute.[254] The peak shifts according to the *A* site cation present, indicating differing amounts of individual manganese species were present. Mn$p_{5/2}$ is observed at 642.3 eV for $LaMnO_3$, 641.8 eV for $CaMnO_3$, 641.7 eV for $YMnO_3$ and 641.4 eV for $SmMnO_3$. The shift to a lower binding energy indicated a shift to a lower Mn valence as the oxygen defect density increased.[269]

Figure 4.2 b) shows the La 3d XPS response. The spectrum shows a doublet splitting which was due to the interaction between the empty La 4f level and an electron from the oxygen valence band.[272] The La $3d_{5/2}$ band was located at 834.45 eV corresponding to La^{3+}. Figure 4.2 c) shows the Y 3d response. Two components could be observed in this spectrum, one at 158.4 eV which was associated with lattice Y in $YMnO_3$ and another at 156.4 eV associated with the formation of Y_2O_3. Figure 4.2 d) shows the Sm 3d line. Due to spin-orbit coupling the 3d state was split into two lines centred at 1108.6 (Sm $2p_{5/2}$) and 1082.4 (Sm $2p_{3/2}$). Both lines confirmed the presence of Sm^{3+}.[273] Figure 4.2 e) shows the Ca 2p line. Two components were observed, the component at lower binding energy confirmed the presence of Ca^{2+} in the perovskite lattice and the component at higher binding energy suggested the presence of other Ca^{2+} species such as CaO.[254,274]

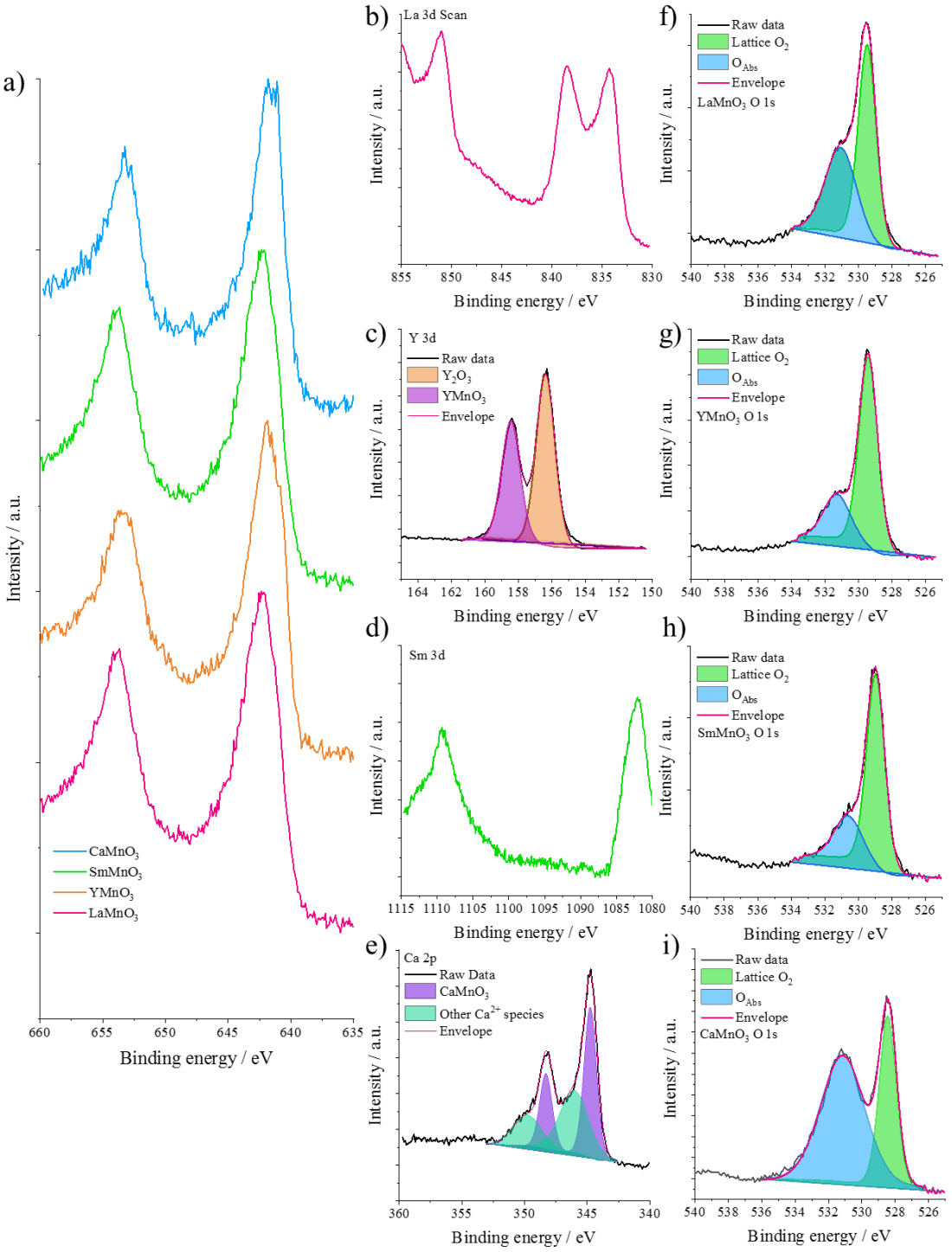

Figure 4.2: XPS data for the *A*MnO_3 materials. a) Mn 2p, b) $LaMnO_3$ La 3d, c) $YMnO_3$ Y 3d, d) $SmMnO_3$ Sm 3d, e) $CaMnO_3$ Ca 2p, f- i) O 1s.

Figure 4.2 f-i) shows the O 1s spectra for all *A*MnO_3 materials. The spectra suggested that there was more than one oxygen species present at the surface of the perovskites. The line at approximately 529.1 eV corresponded to lattice oxygen (e.g. La-O-Mn) and

the line at approximately 531.0 eV corresponded to O_2^-, or coordinated oxygen ions.[275] The presence of O_2^- species on the surface was very important for oxygen reduction, as oxygen in the electrolyte must be coordinated to the catalyst to initiate a reduction reaction.[126] The ratio of lattice to surface oxygen species was calculated from the high resolution region spectra and can be seen in Table 4.2. $CaMnO_3$ had the opposite trend in lattice:surface oxygen species to the other catalysts. This has been previously observed, and may have been due to the presence of additional species such as $CaCO_3$ or $Ca(OH)_2$ on the surface of the material.[274]

Table 4.2: XPS features for *A*MnO_3 catalysts. The surface composition was calculated from the La 3d, Y 3d, Sm 3d, Ca 2p and Mn 2p peak regions considering the corresponding sensitivity factors.

Sample	*A*:Mn	O_L:O_S
$LaMnO_3$	58.8:41.2	79:21
$YMnO_3$	62.1:37.9	88:12
$SmMnO_3$	39.4:60.6	88:12
$CaMnO_3$	61.9:38.1	17:83

The surface ratio of *A* to Mn sites was estimated from the regions of the *A* site cations and the Mn 2p emission and is shown in Table 4.2. A surface-enrichment of *A* site ions was seen in $LaMnO_3$, $CaMnO_3$ and $YMnO_3$ and this was consistent with previous observations.[254] There was an *A* site deficiency at the surface observed for $SmMnO_3$.

Figure 4.3 shows the SEM data at for the materials. $LaMnO_3$ was considerably smaller in size than the other three catalysts. Generally, all catalysts displayed irregular shapes and agglomeration of primary particles, likely due to the heat treatment needed to convert from oxides/hydroxides to perovskites.

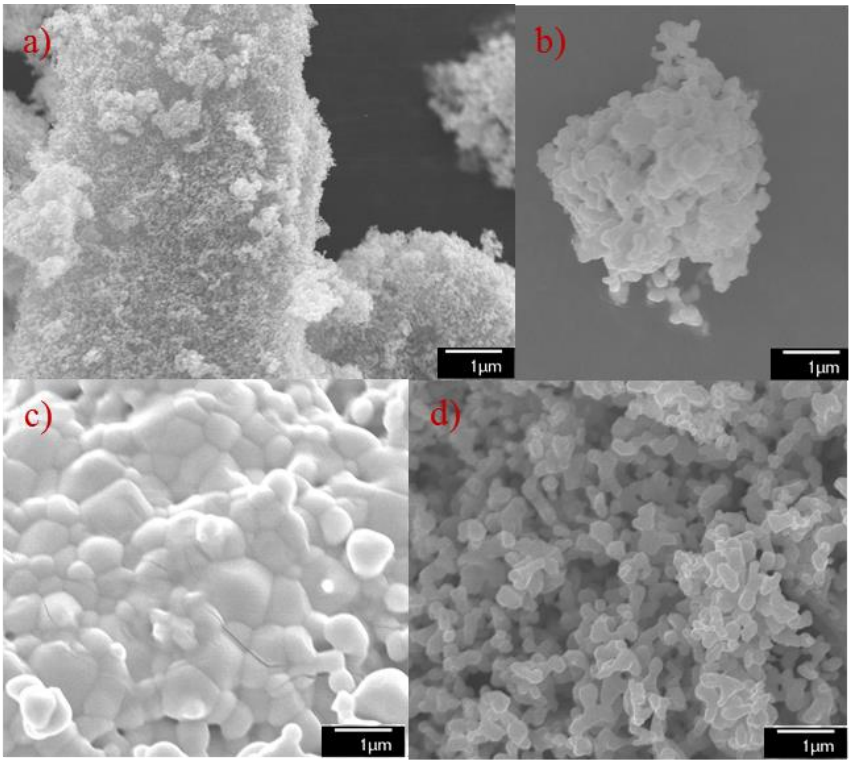

Figure 4.3: SEM images recorded post heat-treatment at × 10000-magnification for a) $LaMnO_3$, b) $YMnO_3$, c) $SmMnO_3$ and d) $CaMnO_3$.

The morphology of the four manganite electrocatalysts was investigated using TEM and selected images were shown in Figure 4.4. The images revealed agglomerated small irregular particles for $LaMnO_3$ (Figure 4.4 a-b) with an average particle size of 32 nm. Large, flake-like, 2-D particles were seen for $YMnO_3$ (Figure 4.4 c-d) and $SmMnO_3$ (Figure 4.4 e-f) with an average particle size of 154 nm and 120 nm for $YMnO_3$ and $SmMnO_3$ respectively. This confirmed the suggestion of preferred orientation in the crystal morphology seen in the PXRD. The larger particle size was attributed to the harsher heat treatment conditions needed to achieve phase pure manganite material. $CaMnO_3$ (Figure 4.4 g-h) also had large irregular cylindrical particles, which look to have some degree of agglomeration with an average particle size of 140 nm. The particle sizes counted in the TEM do not reflect the calculated sizes from the Scherrer equation, although they followed the same trend. There are two reasons for this: 1) the crystallite domain size is not the same as the particle size and 2) the Scherrer equation works only for sub-micron materials and all but $LaMnO_3$ herein were micron sized. Clear interlayer spacings could be identified for all materials; 0.27 nm for $LaMnO_3$ corresponding to the 104 plane, 0.32 nm for $YMnO_3$ corresponding to

the 100 plane, 0.34 nm for $SmMnO_3$ corresponding to the 111 plane and 0.26 nm for $CaMnO_3$ corresponding to the 121 plane.

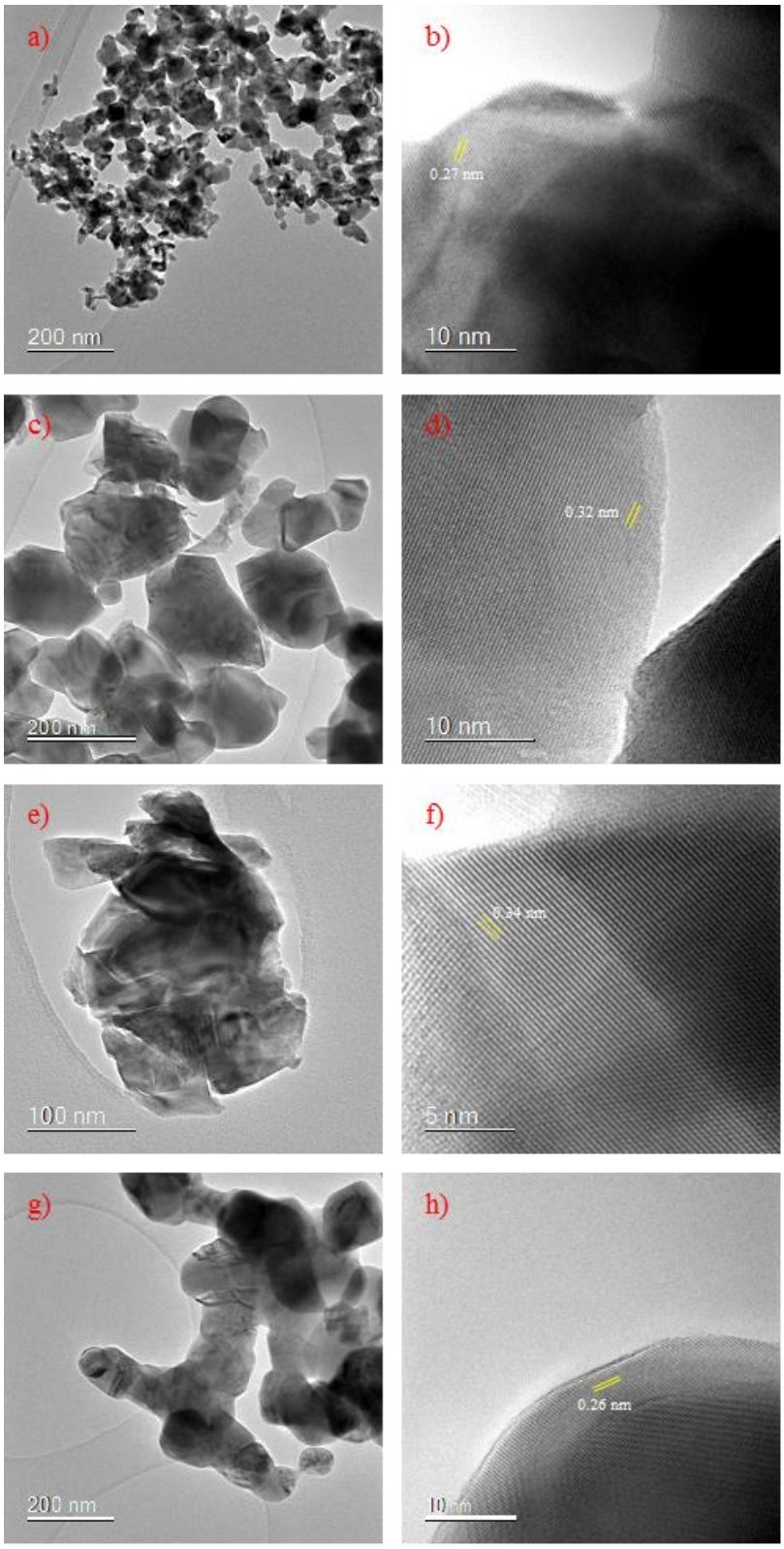

Figure 4.4: TEM images collected post heat-treatment for $LaMnO_3$ a,b), $YMnO_3$ c,d), $SmMnO_3$ e,f), and $CaMnO_3$ g,h).

4.4.1.2. *A* Substitution in *A*MnO_3: Electrochemical Characterisation

A platinum black ink (made to recipe 2 in Chapter 2.3.1), and a pure acetylene black ink (recipe 2 minus the catalyst) were made, deposited onto GC electrodes and the resulting films tested as ORR catalysts to provide industrially relevant benchmarks for comparison. Initially, cyclic voltammetry (CV) was carried out at 5 mV s^{-1} in N_2 degassed electrolyte. The black trace in Figure 4.5 a) shows the Pt black response. The peaks below −0.56 V corresponded to the absorption/desorption of hydrogen from the catalyst surface. The peak centred at −0.9 V corresponded to hydrogen evolution. The peaks above −0.56 V corresponded to the reduction/formation of Pt oxide. The CV values agreed well with literature values for Pt black / Pt black + carbon.[276,277] The red trace in Figure 4.5 a) corresponds the CV trace for Acetylene Black (AB). The response was highly capacitive, as seen by the broad and box like nature of the CV. There were no obvious peaks seen in the CV. The CV closely followed literature results for carbon blacks.[278]

The LSV traces [Figure 4.5 b)] also agreed well with literature values for the two standard catalysts. Pt black had an exceptionally low overpotential, 0.21 V with respect to the reversible oxygen potential of 1.23 V vs RHE (0.28 V vs Ag/AgCl). Acetylene black on the other hand had a large overpotential for the ORR of 0.55 V (−0.27 V vs Ag/AgCl). The limiting current densities seen by both catalysts reflected the maximum diffusion limited current observable. This is changeable depending on many experimental parameters such as the method of oxygen delivery, catalyst loading and electrolyte, illustrating the importance of comparisons carried out under identical electrochemical conditions.[279]

RRDE studies were used to examine the extent of peroxide formation as a by-product of oxygen reduction and can be seen in Figure 4.5 c). The yield of peroxide at carbon black was much greater than that of Pt black at 54.3 % vs 0.82 %. The generation of such a small amount of peroxide at the Pt catalyst showed that overall, the pathway that generated peroxide had a very small contribution to the oxygen reduction. The electron transfer numbers of the two catalysts at 2500 rpm were 2.91 for acetylene black and 4 for platinum black, consistent with literature values.[219]

Koutecky-Levich analysis was carried out and showed a linear trend between current density and rotation speed as was expected from the literature [Figure 4.5 d)]. The

gradient for the Pt black material was shallower than acetylene black due to the higher number of electrons being transferred at the Pt surface. The *y*-intercept for the Pt-black line was smaller than for the carbon black line which is consistent with Pt black having a higher kinetic current than carbon black.[219] The values for both catalysts can be seen in Table 4.3.

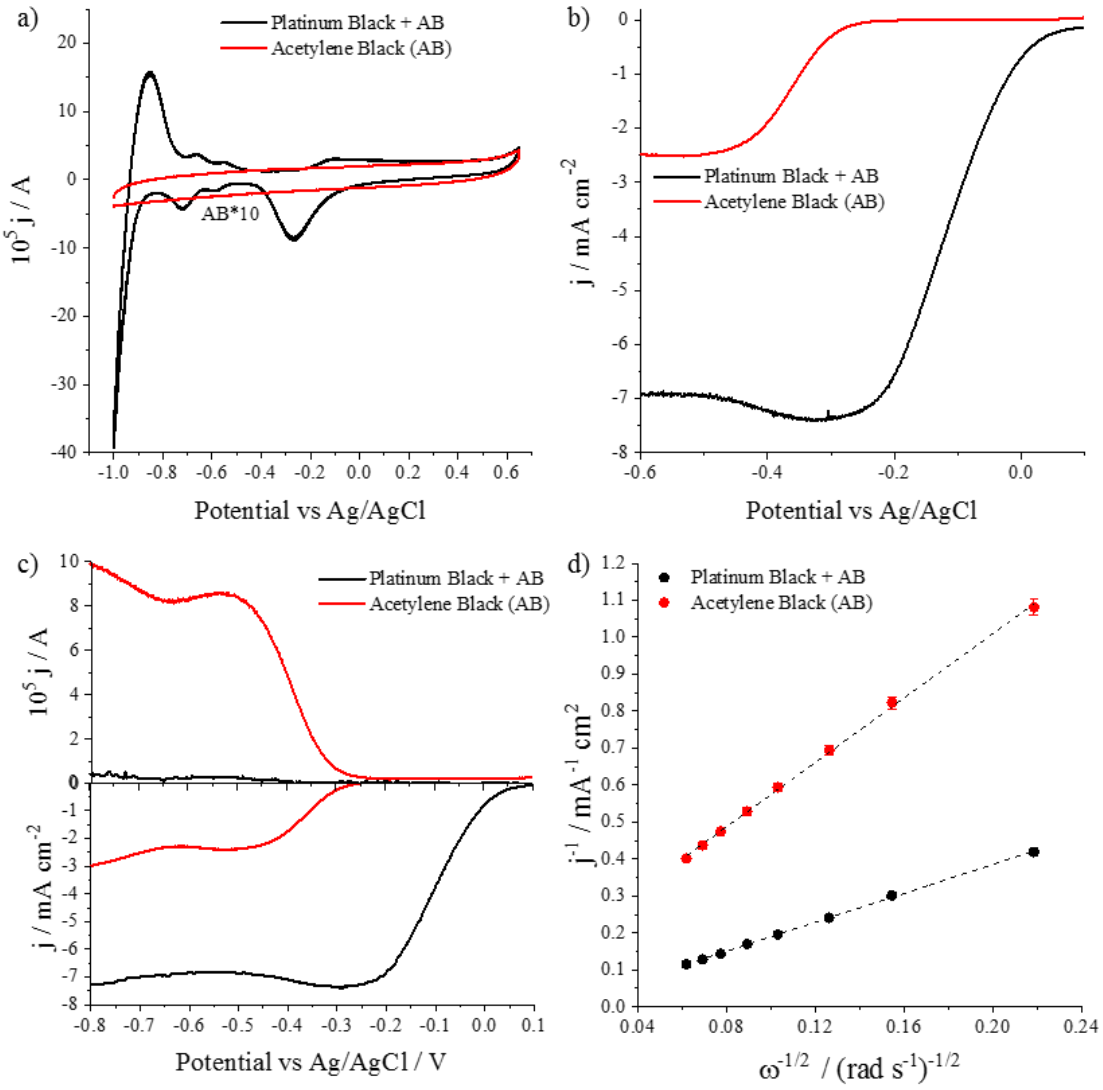

Figure 4.5: a) CVs for Pt Black (black) and acetylene black (red) taken in N_2 saturated 0.1 M KOH at 10 mV s^{-1}. b) LSV trace for Pt Black (black) and acetylene black (red) taken at 10 mV s^{-1} in O_2 saturated 0.1 M KOH at 2500 rpm. c) RRDE results for acetylene black (red) and Pt Black (black) taken at 10 mV s^{-1} in O_2 saturated 0.1 M KOH at 2500 rpm. d) Koutecky-Levich plots for Pt Black (black) and acetylene black (red).

Figure 4.6 shows the cyclic voltammogram responses for the various $AMnO_3$ nanocatalysts studied. The CVs had a complex response, which was expected as there are various redox sites associated with surface Mn surface. $LaMnO_3$ [Figure 4.6 a)] featured two cathodic reduction peaks centered at −191 mV and −532 mV vs Ag/AgCl related to the reduction of Mn from an oxidation state of approximately +3 to +2.[254] Both $YMnO_3$ [Figure 4.6 b)] and $SmMnO_3$ [Figure 4.6 c)] showed no clear redox peaks in the range investigated. $CaMnO_3$ [Figure 4.6 d)] featured a broad reduction peak which was assigned to the reduction of Mn^{4+} to Mn^{2+}. There were large differences in the observed current achieved by each catalyst. This could not simply be rationalised by change in redox state and/or particle size as the specific surface area (SSA) for $LaMnO_3$ was larger than that for $CaMnO_3$ but the current response for $CaMnO_3$ was an order of mangnitude larger than $LaMnO_3$.[254]

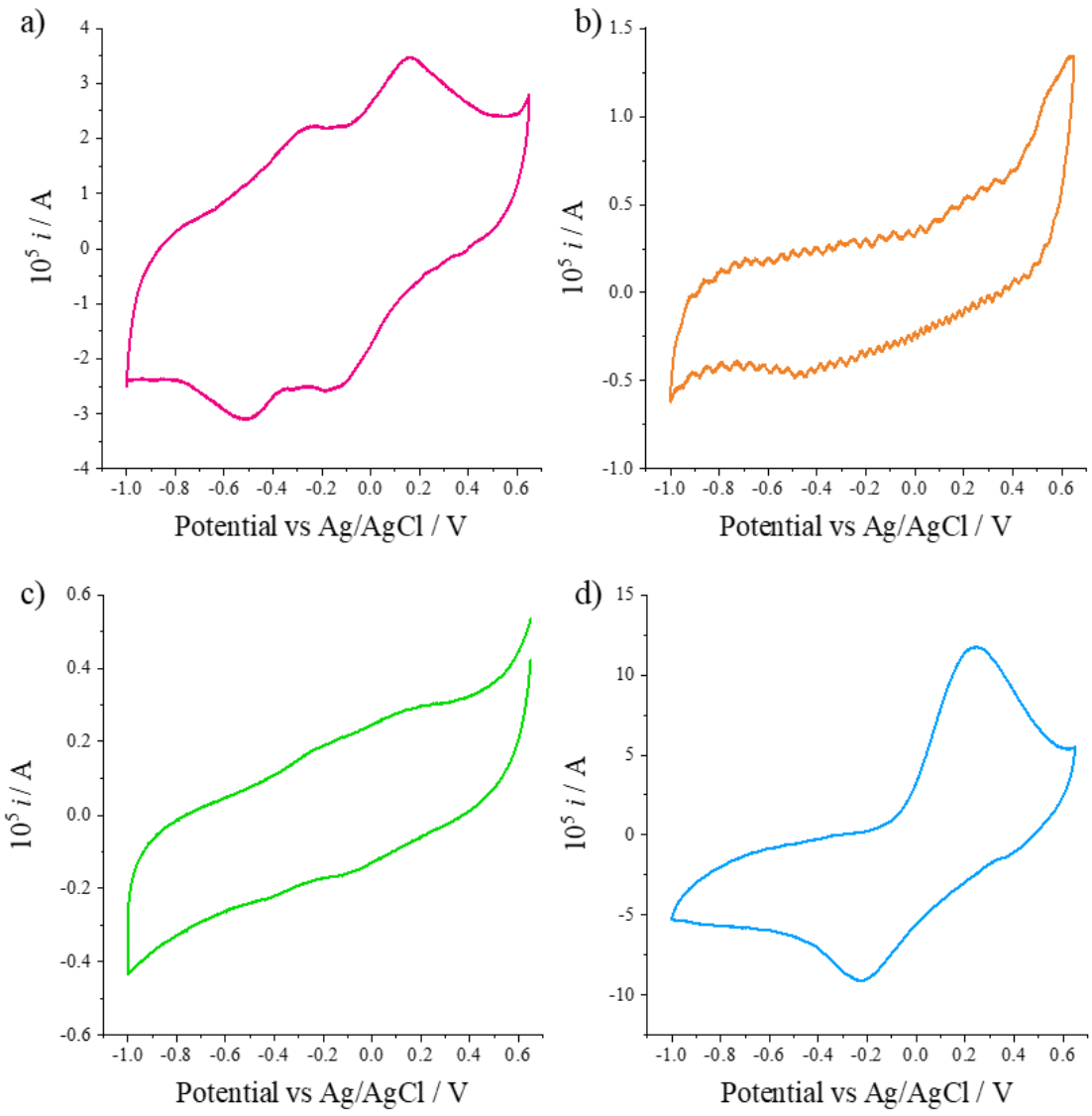

Figure 4.6: Cyclic voltammograms of the *A*MnO$_3$ materials. a) LaMnO$_3$, b) YMnO$_3$, c) SmMnO$_3$ and d) CaMnO$_3$. All measurements were carried out in degassed (N_2 saturated) 0.1 M KOH with a scan speed of 5 mV s^{-1} between 0.60 and −1.0 V vs Ag/AgCl. The experimental error is ± 2%.

The current voltage responses for the LSV of the *A*MnO$_3$ materials are shown below in Figure 4.7. LaMnO$_3$ [Figure 4.7 a)] and CaMnO$_3$ [Figure 4.7 d)] had much more positive onset potentials vs Ag/AgCl (−0.05 and −0.01 V respectively) than YMnO$_3$ [Figure 4.7 b)] and SmMnO$_3$ [Figure 4.7 c)] (−0.30 and −0.29 V respectively). The overpotentials were 0.32, 0.56, 0.56 and 0.28 V for LaMnO$_3$, YMnO$_3$, SmMnO$_3$ and CaMnO$_3$ respectively vs the standard oxygen potential. LaMnO$_3$ and CaMnO$_3$ had overpotentials comparable to Pt black (0.21 V) wheras YMnO$_3$ and SmMnO$_3$ had overpotentials comparable to blank acetylene black (0.55 V). The limiting current

density was highest for $LaMnO_3$ (−6.4 mA cm^{-2}) and lowest for $YMnO_3$ (−2.7 mA cm^{-2}). For $LaMnO_3$ this was a very good result as this approaches the limiting current density observed for Pt black of −6.9 mA cm^{-2} at −0.5 V vs Ag/AgCl.

A large factor in the poor catalysis of the $YMnO_3$ and $SmMnO_3$ catalysts may have been their low surface area (2.9 and 0.12 m^2 g^{-1}) and high levels of agglomoration (as revealed in the TEM), potentially due to the intensive heat treatment required to convert the precursor material to the perovskite. However, this may not be the only cause of poor catalysis. Celorrio *et al.* performed Extended X-ray Absorption Fine Structure (EXAFS) analysis on a series of *A*MnO_3 catalysts and found a volcano trend between rate of conversion of O_2 to OH^- and both the Mn-O mean bond length and the A-site ionic radius.[254] They observed a maximum performance at *A* = La. This would fit the trend in the data seen here as ionic radii increases from Y (1.04 Å) to La (1.17 Å) (Sm = 1.10 Å, Ca = 1.14 Å).

From the LSV plots, $LaMnO_3$ was a candidate for an inexpensive oxygen reduction catalyst exhibiting a low overpotential and high current density. From the volcano plots in Chapter 1 (Figure 1.12), this was to be expected as $LaMnO_3$ sits near the top of the structure activity plot, with an e_g filling of just above unity.[106] Many studies have also highlighted that nanosizing materials can push them further up the volcano.[120,125] The small size of the $LaMnO_3$ synthesised herein may be enhancing its catalytic activity. This has been seen previously in the literature, Li *et al.* synthesised nano-$LaMnO_3$ with a surface area of 21.2 m^2 g^{-1} which outperformed a commercial Pt black benchmark.[120] Nanosizing is generally thought to lead to new catalytic and electronic properties due to the small size effect. Reactivity is enhanced as size decreases due to larger surface-to-bulk ratios and the apperance of surface defects. The larger specific surface area allows more active sites in contact from the catalyst to the electrolyte.[253] In several previous studies it has been reported that the population of additional oxygen species, observed on the surface of the catalyst by XPS, can be correlated to electrochemical activity, as the prescence of surface oxygen is vital to electrochemical reduction.[126,267] This trend is also observed here, with the ratio of O_L:O_{Abs} being higher for $LaMnO_3$ than the other materials (excluding $CaMnO_3$ due to the likely inclusion of other surface species). However, this could also be due to oxygen interacting at different levels with the carbon tape used to support the material. There are a wide range of other factors

that are known to influence the ORR activity such as surface area, e_g orbital occupancy and oxygen vacancies at the surface.[280]

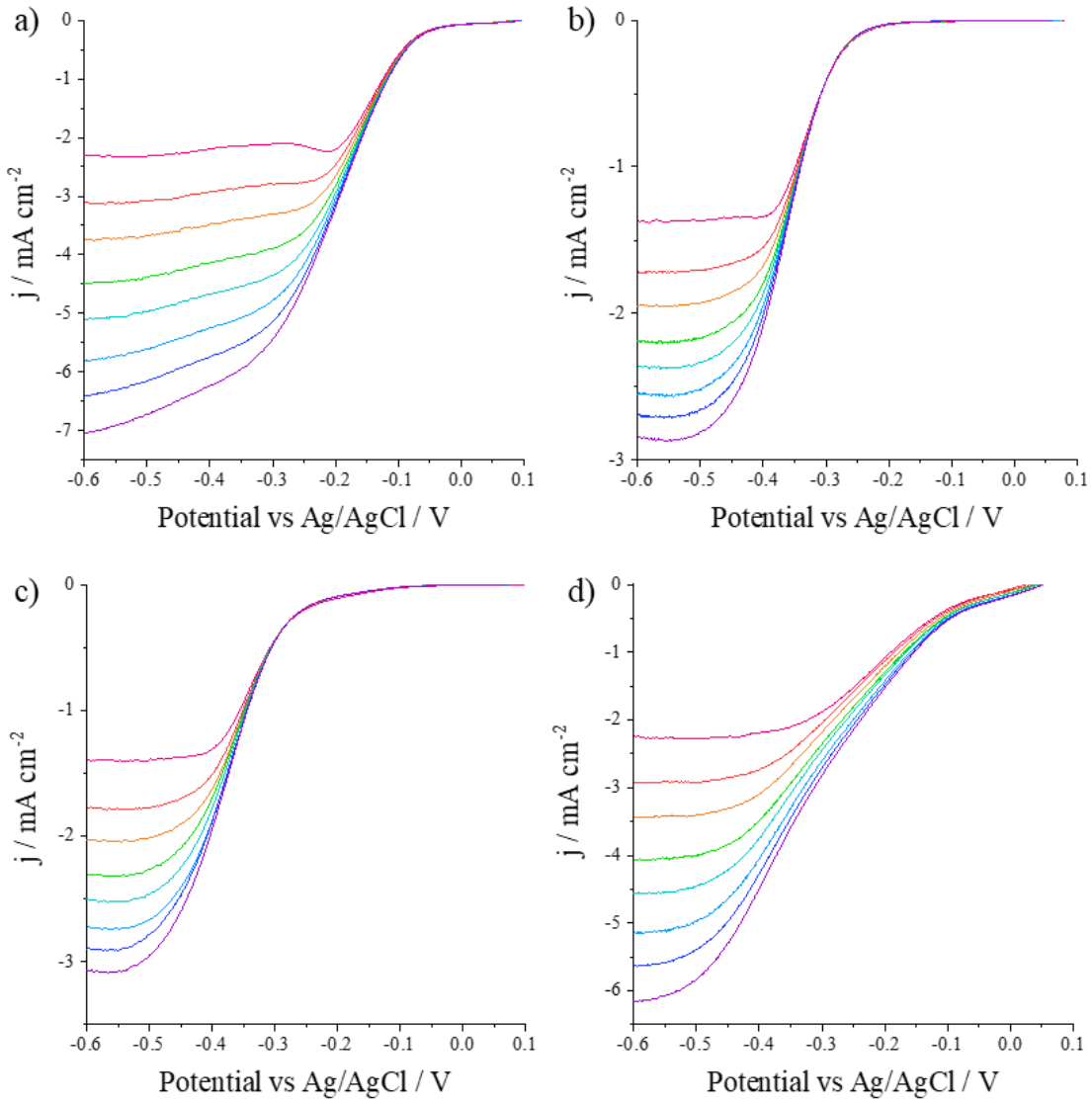

Figure 4.7: Comparison of current voltage responses at 1600 rpm for LSV for *A*MnO$_3$ samples. a) LaMnO$_3$, b) YMnO$_3$, c) SmMnO$_3$ and d) CaMnO$_3$. All measurements were carried out between 0.1 and −0.6 V vs Ag/AgCl in O$_2$ saturated 0.1 M KOH with a scan speed of 10 mV s^{-1}. The experimental error is ± 2 %.

The Koutecky-Levich (K-L) equation (found in Chapter 2, equations 2.8 and 2.9) was used to examine the relationship between rotation rate and current density, as well as the ORR reaction kinetics. The number of electrons transferred could also be calculated. Figure 4.8 shows the K-L plots for the four electrocatalysts. The relationship between current density and rotation speed was linear in all cases. LaMnO$_3$

and $CaMnO_3$ exhibited almost parallel K-L plots suggesting the reaction pathway occurring at these catalysts was very similar. The same can be said about $YMnO_3$ and $SmMnO_3$. Table 4.3 compares the K-L parameters for the four catalysts as well as Pt black and acetylene black.

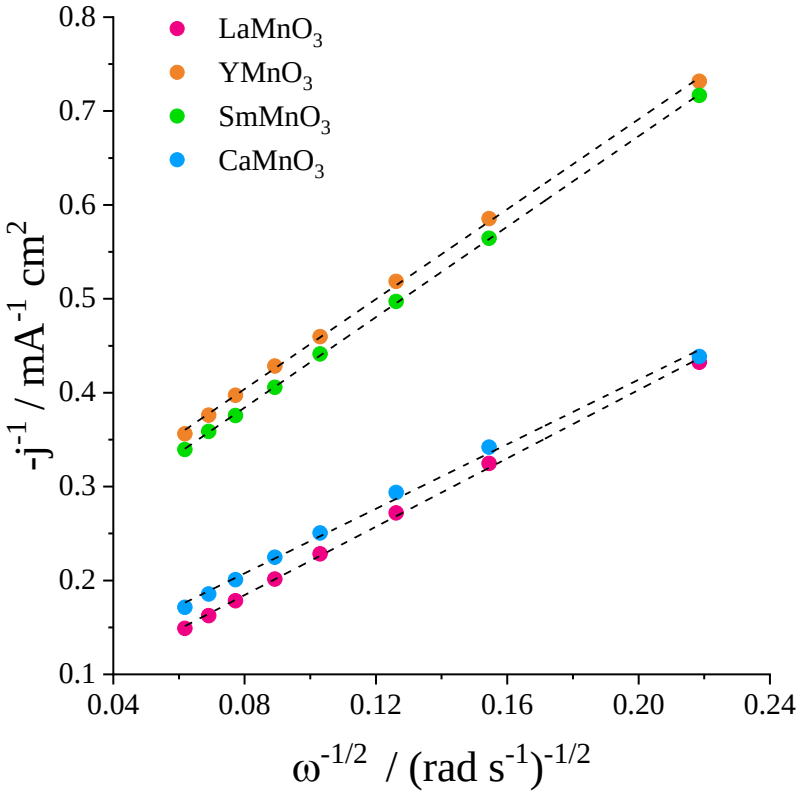

Figure 4.8: Koutecky-Levich plots for O_2 reduction in 0.1 M KOH for $LaMnO_3$, $YMnO_3$, $SmMnO_3$ and $CaMnO_3$. Data taken at −0.5 V vs Ag/AgCl. Scan rate was 10 mV s^{-1}.

Table 4.3: Comparison of K-L parameters for catalyst materials. Data extracted from the K-L plots as presented in Figure 4.8. The K-L gradient gives information about the electron transfer step and the *y*-intercept gives information about the kinetic current density.

Catalyst	K-L Gradient	*y*-intercept
$LaMnO_3$	1.82 ± 0.02	0.037 ± 0.003
$YMnO_3$	2.39 ± 0.02	0.212 ± 0.003
$SmMnO_3$	2.41 ± 0.01	0.191 ± 0.001
$CaMnO_3$	1.72 ± 0.04	0.070 ± 0.005
Pt Black	1.96 ± 0.02	0.005 ± 0.002
Acetylene Black	4.35 ± 0.05	0.140 ± 0.007

The gradients observed for $LaMnO_3$ and $CaMnO_3$ were similar to the observed gradient for Pt black in the same conditions suggesting that reduction occured primarily via a dominant 4 e^- pathway. The observed gradients for $YMnO_3$ and $SmMnO_3$ were steeper and somewhat in-between the gradients for carbon black and Pt black. This suggested a mixed reduction pathway with some contribution from both the 2 e^- and 4 e^- reduction pathways. The *y*-intercept is related to the kinetic current density, the smaller the *y*-intercept the larger the kinetic current density of the catalyst. The order in observed kinetic current density was $LaMnO_3$ > $CaMnO_3$ >> $SmMnO_3$ > $YMnO_3$, with kinetic current density decreasing from 27 mA cm^{-2} for $LaMnO_3$ to 5 mA cm^{-2} for $YMnO_3$.

The Tafel equation can be used to provide insight into the reaction mechanism of the electrochemical processes occurring during an electrochemical reaction. It gives a quantitative relationship between applied potential and the current response seen. In particular, the gradient derived from a Tafel plot can be used to infer information about the charge transfer coefficient of a particular reaction occurring.[217]

The Tafel plots for all materials in the high potential region were calculated using mass transport corrected kinetic current values and are shown above in Figure 4.9. The mass transport corrected kinetic current densities were calculated by performing K-L analysis at all voltages and taking the reciprocal of the K-L *y*-intercept, giving the kinetic current density independent of mass transport limiting factors. There was a shift in the potential at which the Tafel slope was observed. This was due to the large differences in the overpotentials seen for the four catalysts. $SmMnO_3$ had the shallowest Tafel slope of 60 mV dec^{-1}. The Tafel slopes for $LaMnO_3$, and $YMnO_3$ were similar, 89 and 83 mV dec^{-1} respectively. However, the Tafel slope for $CaMnO_3$ was much steeper (202 mV dec^{-1}), suggesting much slower reaction kinetics than the other three catalysts. This was confirmed by examining the half wave potentials of the catalysts in the LSV. $CaMnO_3$ had the most positive onset potential. However, the half wave potential was −255 mV compared to a half wave potential of −172 mV for $LaMnO_3$, indicating a much slower reaction was occurring at the $CaMnO_3$ surface than at the surface of $LaMnO_3$. The Tafel slopes indicated the preference of $LaMnO_3$ over $CaMnO_3$ even though at first glance, the catalysts appeared quite similar.

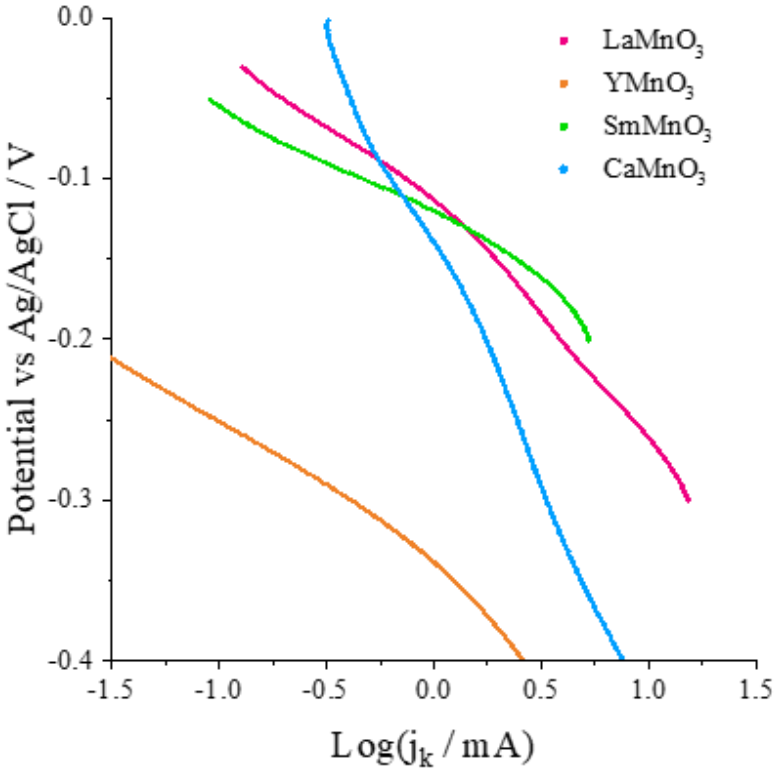

Figure 4.9: Tafel data for the *A*MnO_3 catalysts using mass transport corrected kinetic current densities. The mass transport corrected current densities were calculated using equations 2.7 and 2.8 in Chapter 2.

Figure 4.10 shows the RRDE data for the *A*MnO_3 catalysts. The trend in HO_2^- yield at −0.5 V vs Ag/AgCl was $SmMnO_3$ > $YMnO_3$ > $CaMnO_3$ > $LaMnO_3$ and went from 32% for $SmMnO_3$ to < 1% for $LaMnO_3$. The electron transfer number followed the same trend and went from 3.36 for $SmMnO_3$ to 3.99 for $LaMnO_3$. This suggested that there was a mixed pathway for both $SmMnO_3$ and $YMnO_3$ as the calculated electron transfer number was in between the theoretical 2 or 4 e^- pathways predicted. However, for $LaMnO_3$ and $CaMnO_3$ the calculated electron transfer numbers (3.99 and 3.97, respectively) suggested little to no contribution from the 2 e^- pathway showing the catalysts favoured the preferred 4 e^- pathway.

From the RRDE results, $LaMnO_3$ was found to be the optimal ORR catalyst, with a low HO_2^- yield and a high Electron Transfer Number, ETN. The data here agreed well with literature values[254], with previous reports finding an ETN for $CaMnO_3$ of 3.90[269] and an ETN of between 3.25 and 3.90 for $LaMnO_3$[281], confirming that CHFS can be

used as a synthetic technique to make catalysts comparable to those found in the literature made via other synthetic techniques.

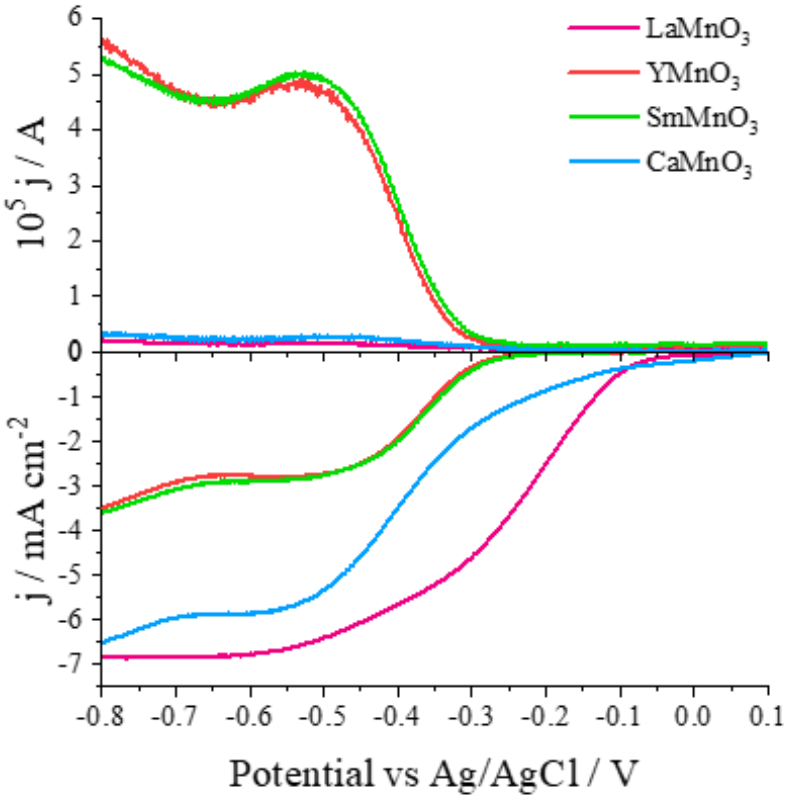

Figure 4.10: RRDE data for the *A*MnO_3 catalysts at 2500 rpm. Disk data is shown on the bottom y-axis, ring data is shown on the top y-axis. All data taken between 0.1 and −0.8 V vs Ag/AgCl in O_2 saturated 0.1 M KOH at 10 mV s^{-1} with an error of ± 2%.

Figure 4.11 shows the stability testing of the four catalysts in the form of a chronoamperometry curve. The selected voltage at which the catalyst was held was −0.5 V as this was sufficiently negative such that all catalysts had reached a limiting current density at 900 rpm. 4 h was chosen as a stability window to examine. There seems to be little consensus in the literature about how long stability testing should be carried out for similar materials. For example, Du *et al* carried out chronoamperometry on a $CaMn_2O_4$ material over 2 hours at −0.5 V and saw a 12.3% loss[130] whereas Lu *et al* carried out chronoamperometry on a hollow spherical $La_{0.8}Sr_{0.2}MnO_3$ materials over 16 hour and saw a 10% stability loss.[247]

The most stable catalyst over the 4 h testing window was $CaMnO_3$ only losing 6% activity in the test period. The least stable catalyst was $SmMnO_3$ losing 22% activity

in the same period. There are many changes that can occur in the catalyst whilst it is running, affecting stability. These include irreversible binding of the active species to the surface of the catalyst, structural changes such as aggregation or agglomeration and change in electrolyte concentration.[247] All samples tested herein were less stable than the Pt-black sample which only lost 5% activity over the same testing period. The synthesis method and possibly heat treatment temperature and time should be optimised to improve on this.

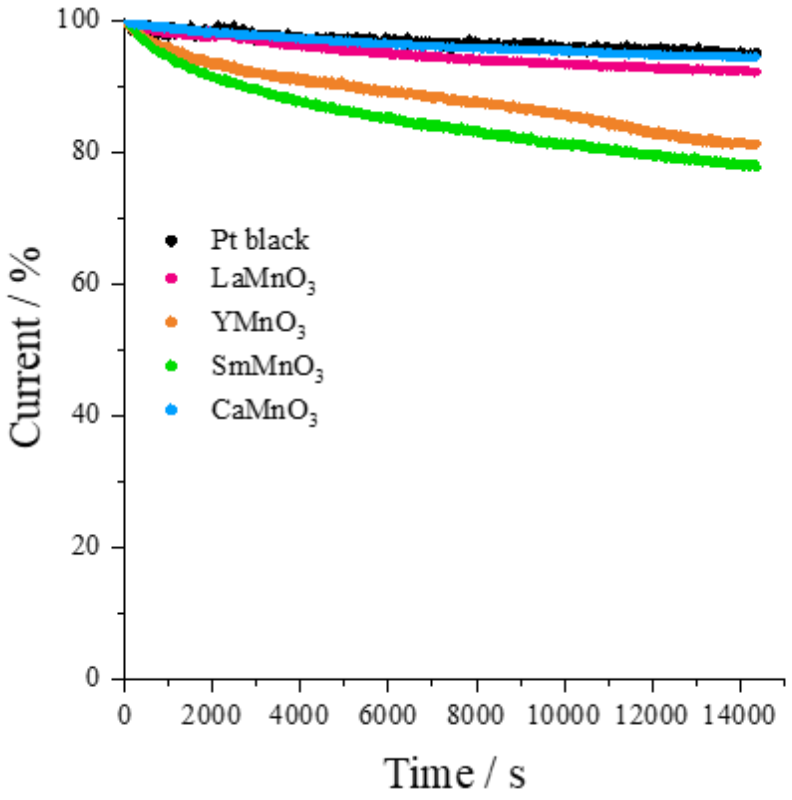

Figure 4.11: Chronoamperometric response for the four catalysts and the commercial Pt black sample taken at −0.5 V vs Ag/AgCl and 900 rpm in oxygenated 0.1 M KOH over a 4 h testing period.

4.4.2. Effect of Precursor Concentrations on *x*-$LaMnO_3$-*y*

Changing precursor concentrations has been shown to change particle size/shape during hydrothermal synthesis. Piticescu *et al.* used batch hydrothermal methods to synthesise barium strontium titanate.[282] By varying the concentration of the precursors and the temperature and time of reaction a controlled product could be produced. Denis *et al.* showed that by changing the precursor concentration, Co_3O_4 nanoparticles could be synthesised via CHFS with a controlled size.[184] They also noted that by changing

the expected flow conditions from laminar to turbulent, the particle size was also effected. By changing metal:base ratios or metal concentration in solution it was predicted that fundamental properties such as particle size would change, leading to a change in catalytic activity observed.

4.4.2.1. Physical Characterisation of *x*-$LaMnO_3$-*y* Materials

To identify the role of KOH concentration in the synthesis, PXRD was carried out on a series of heat treated $LaMnO_3$ samples synthesised with the same total metal concentration (0.1 M) and increasing base concentration (Figure 4.12). The samples are labelled $LaMnO_3$-*y* where *y* is the ratio of [KOH]:[*M*] used in the reaction, with increasing values of *y* corresponding to an increase in [KOH]. Another sample with 2.5 base equivalents was put through the reactor in addition to the four samples below. However, this sample did not precipitate and therefore is not included herein.

After the CHFS, cleaning by centrifugation and freeze-drying, the nanoparticulate metal oxides were collected with a >90% yield. All materials were free flowing, brown powders. After the heat-treatment step, all powders were black.

Pre heat treatment, no $LaMnO_3$ was seen in the PXRD pattern of the material made via CHFS. Instead, as with the $LaMnO_3$ seen in Figure 4.1, a mixture of La_2O_3 and Mn_xO_y species were identified. All samples post heat-treatment were assigned to the rhombohedral (*R*-3*c*) $LaMnO_3$ phase (ICSD collection code: 50041). The PXRD data showed no significant differences, with the (012) peak at approximately 10.5 ° for all materials and the Scherrer size not varying outside of error (18 nm for $LaMnO_3$-5, 16 nm for $LaMnO_3$-10, 14 nm for $LaMnO_3$-15 and 15 nm for $LaMnO_3$-20). BET SSA for the materials were measured and found to be 21.5, 22.7 21.5 and 28.2 for 5, 10, 15 and 20 equivalents of base respectively. Only 20 equivalents of base were found to vary the SSA significantly. The cause of this increase may be due to the precursor solution reaching supersaturation slightly earlier for this sample due to the larger excess of base causing a more alkaline environment. This could mean that as nucleation occurred quicker, and to a greater extent due to the alkalinity of the solution, there was less metal precursor left in solution to cause growth.

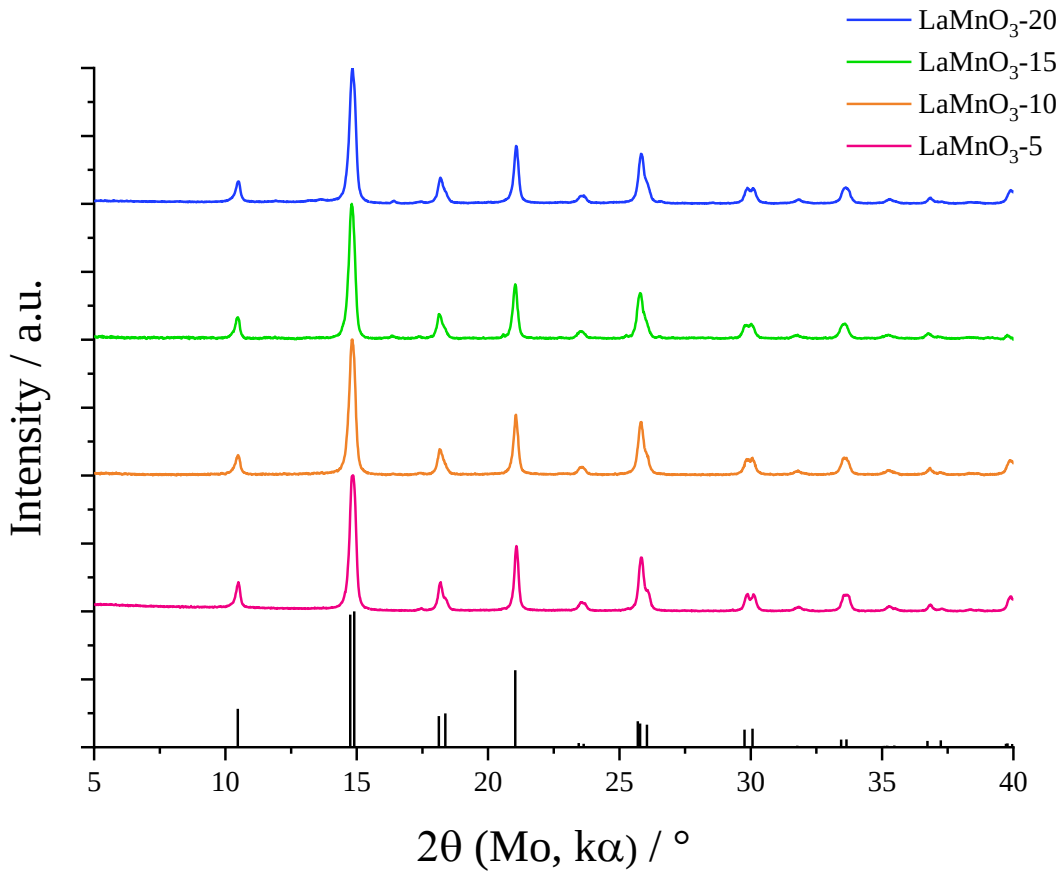

Figure 4.12: PXRD data for $LaMnO_3$ materials where the base:metal has changed but the metal precursor concentration has been kept constant at 0.1 M total metals content. The blue pattern corresponds to a base:metal ration of 20:1, the green pattern corresponds to a base:metal ratio of 15:1, the orange pattern corresponds to a base:metal ratio of 10:1 and the pink pattern corresponds to a base:metal ratio of 5:1.

To identify the role that precursor concentration played on the final catalytic activity of the materials, PXRD was carried out on the series of heat treated $LaMnO_3$ samples synthesised with the same ratio of [KOH]:[*M*] (10:1) but increasing concentration of metal precursors. The samples are labelled *x*-$LaMnO_3$ where *x* corresponds to the total metal concentration used in the reaction, with an increasing value of *x* corresponding to an increase in [*M*]. The PXRD data for all samples were assigned to the rhombohedral (*R*-3*c*) $LaMnO_3$ phase (ICSD collection code: 50041). The PXRD data showed no significant differences, with the (012) peak at approximately 10.5 ° for all materials and the Scherrer size not varying outside of error (15 nm for 0.05-$LaMnO_3$, 16 nm for 0.1-$LaMnO_3$, 16 nm for 0.15-$LaMnO_3$ and 15 nm for 0.2-$LaMnO_3$). At all precursor concentrations the PXRD data reveals majority phase trigonal $LaMnO_3$.

Small impurity phases were seen in 0.05-$LaMnO_3$ which corresponded to $La(OH)_3$ and Mn_xO_y. There was a slight trend seen in the SSA with a slight increase in SSA seen as the base to metal ratio was increased from 20.2 m^2 g^{-1} for 0.05-$LaMnO_3$ to 21.4 m^2 g^{-1} for 0.20-$LaMnO_3$.

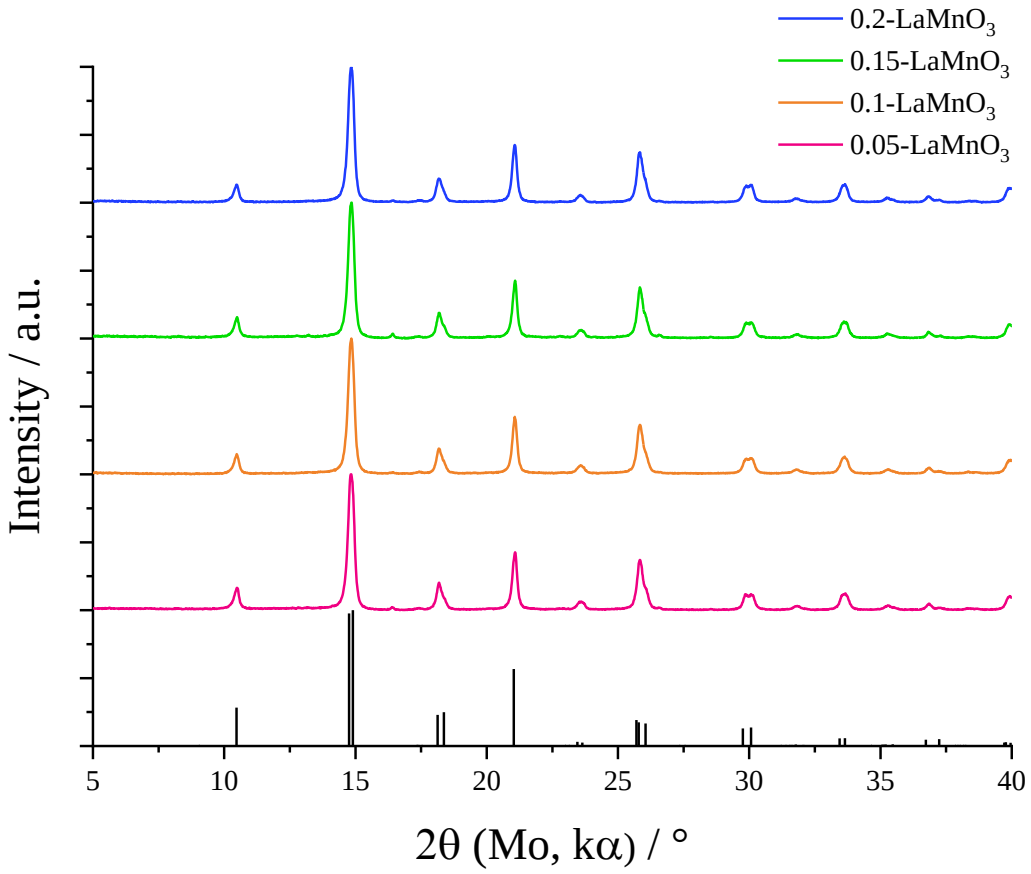

Figure 4.13: PXRD data for $LaMnO_3$ materials where the concentration of precursor materials has changed but the metal:base ratio has been kept constant. The blue pattern corresponds to a total metals concentration in the synthesis of 0.2 M, the green pattern corresponds to a total metals concentration in the synthesis of 0.15 M, the orange pattern corresponds to a total metals concentration in the synthesis of 0.1 M and the pink pattern corresponds to a total metals concentration in the synthesis of 0.05 M. The total concentration of KOH used in the synthesis was 10 × the metal concentration.

4.4.2.2. Electrochemical characterisation of *x*-$LaMnO_3$-*y* materials

All materials were screened using LSV and chronoamperometry to determine differences in activity and stability between the catalysts. 0.1 M O_2 saturated KOH was used as the electrolyte.

Figure 4.14 a) shows the LSV trace at 2500 rpm for the four-differing metal:base ratio samples. The catalyst with the lowest onset potential was $LaMnO_3$-5 with an onset potential of −0.043 V vs Ag/AgCl. The catalyst with the highest onset potential was $LaMnO_3$-20 with an onset potential of −0.055 V vs Ag/AgCl. The data suggested that there was a slight negative influence on the electrocatalytic performance as the metal:base ratio in the CHFS was increased.

Figure 4.14 b) shows the chronoamperometry data for the $LaMnO_3$-*y* materials. This data showed no significant changes between the four catalysts and suggested that in this case, the synthetic conditions of the catalyst made little difference to its stability. However, the data shown were only collected over 3600 s and a greater difference may be expected over a longer test window.

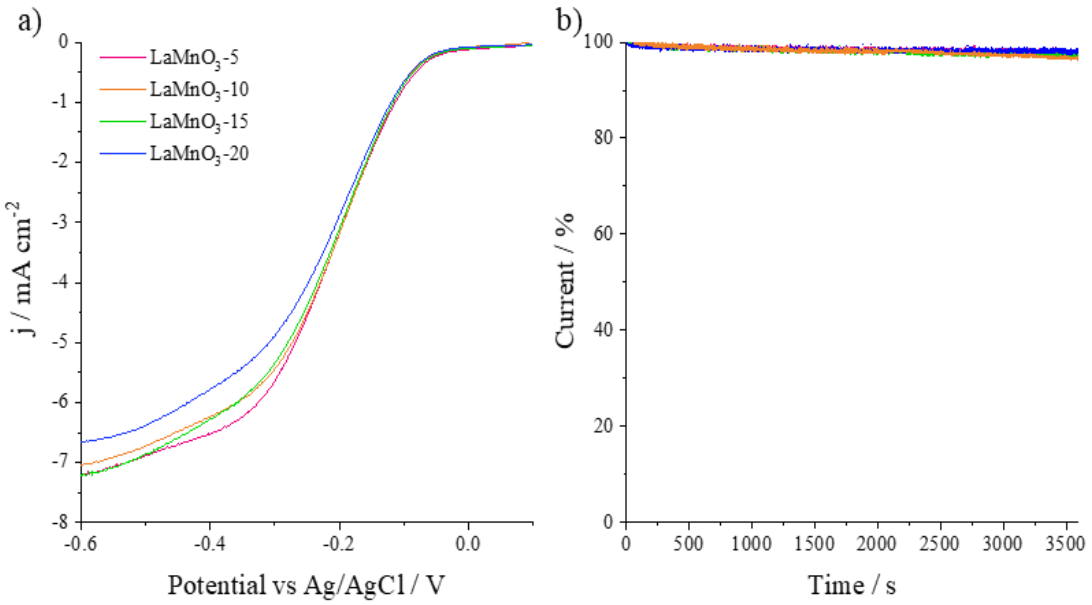

Figure 4.14: a) LSV for the four catalysts taken at 2500 rpm in oxygenated 0.1 M KOH at 10 mV s^{-1}. b) Chronoamperometry data for the four catalysts at −0.5 V vs Ag/AgCl for 3600 s at 900 rpm in oxygenated 0.1 M KOH.

Overall, although there were differences in those data, the catalytic activity was not significantly affected by the base concentration. This would mean that when scaling up, lower concentrations of base could be used, improving safety, reducing reagent requirements and costs whilst maintaining product quality.

Figure 4.15 a) shows the LSV curve from the *x*-$LaMnO_3$ catalysts. 0.2-$LaMnO_3$ had the lowest onset at −0.047 V vs Ag/AgCl and 0.05-$LaMnO_3$ had the highest onset potential at −0.060 V vs Ag/AgCl. 0.2-$LaMnO_3$ also had the highest limiting current density. The slight improvement (approx. 6% compared to $LaMnO_3$) in the catalytic activity of 0.2-$LaMnO_3$ may be due to the higher SSA seen for this sample, this larger surface area allows for a greater quantity of catalytic sites.

As with the previous materials, there were no significant differences in the stability data [shown in Figure 4.15 b)] for the *x*-$LaMnO_3$ catalysts with all catalysts loosing approximately 3% activity over the test period. However, as stated above greater differences in the data may be seen if the test window was extended.

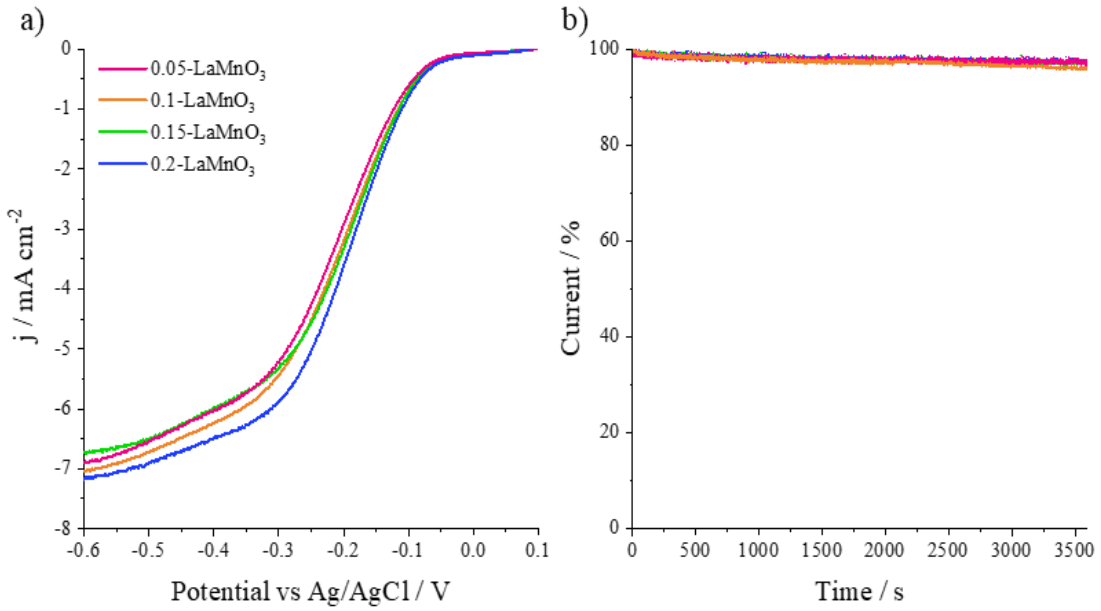

Figure 4.15: a) LSV for the four catalysts taken at 2500 rpm in oxygenated 0.1 M KOH at 10 mV s^{-1}. b) Chronoamperometry data for the four catalysts at −0.5 V vs Ag/AgCl for 3600 s at 900 rpm in oxygenated 0.1 M KOH.

In general, the precursor concentration used did not significantly impact the observed catalytic activity. However, 0.2-$LaMnO_3$ did have a low onset potential and high current density achieved making it an ideal candidate to be taken forward. As well as having superior catalytic merits, this sample was more concentrated in solution, 50 % less water was needed to produce the same mass of catalyst indicating an improved atom economy.

4.4.3. Effect of Heat-Treatment on Performance of $LaMnO_3$

To finish this investigation a trial was conducted where the same CHFS precursor sample was heat treated by a flash heat treatment and compared to the previous method [Batch Heat Treated (BHT)]. It was hypothesised that the Flash Heat Treated (FHT) sample would retain higher SSA and lower particle size, thus making it a better catalyst for the ORR due to the larger availability of active surface sites.

4.4.3.1. Physical Characterisation of Heat-Treated $LaMnO_3$

$LaMnO_3$-BHT denotes the sample that was batch-treated, as in Section 4.4.1. $LaMnO_3$-FHT denotes the sample that was flash heat treated. $LaMnO_3$-FHT was placed into a furnace at 850 °C for 30 mins in air before being removed and quenched in air. Both samples were synthesised at 0.1 M metals concentration with 10 molar equivalents of base.

PXRD was carried out for confirmation of species present and for phase identification, patterns are shown in Figure 4.16. Both batch heat treated (as seen in Section 4.4.1.1.) and flash heat treated $LaMnO_3$ were majority phase rhombohedral (R3-*c*) $LaMnO_3$ (ICSD collection code 50041). In the $LaMnO_3$-FHT sample, a small impurity phase can be seen corresponding to MnO_2 (rutile).

The primary crystallite size as calculated from the Scherrer equation decreased slightly from 16 to 13 nm when changing from batch to flash heat treatment. This was expected as the flash heat treated sample spent only 30 minutes at temperature and was quench cooled by extraction from the furnace into room temperature, whereas the batch heat treated sample spent 90 mins (approx.) ramping to 780 °C where it then spent 2 hours at temperature before being slowly cooled to RT inside the furnace. The longer heat-treatment time would have, theoretically allowed for much greater particle growth and sintering to occur. It also cannot be ruled out that some phase segregation may have occurred as the temperature passed through different thermodynamically stable phases as it cooled. The BET SSA increased from BHT (22.7 $m^2\ g^{-1}$) to FHT (26.2 $m^2\ g^{-1}$), further suggesting that the shorter amount of time spent at temperature allowed for less growth and sintering of the particles.

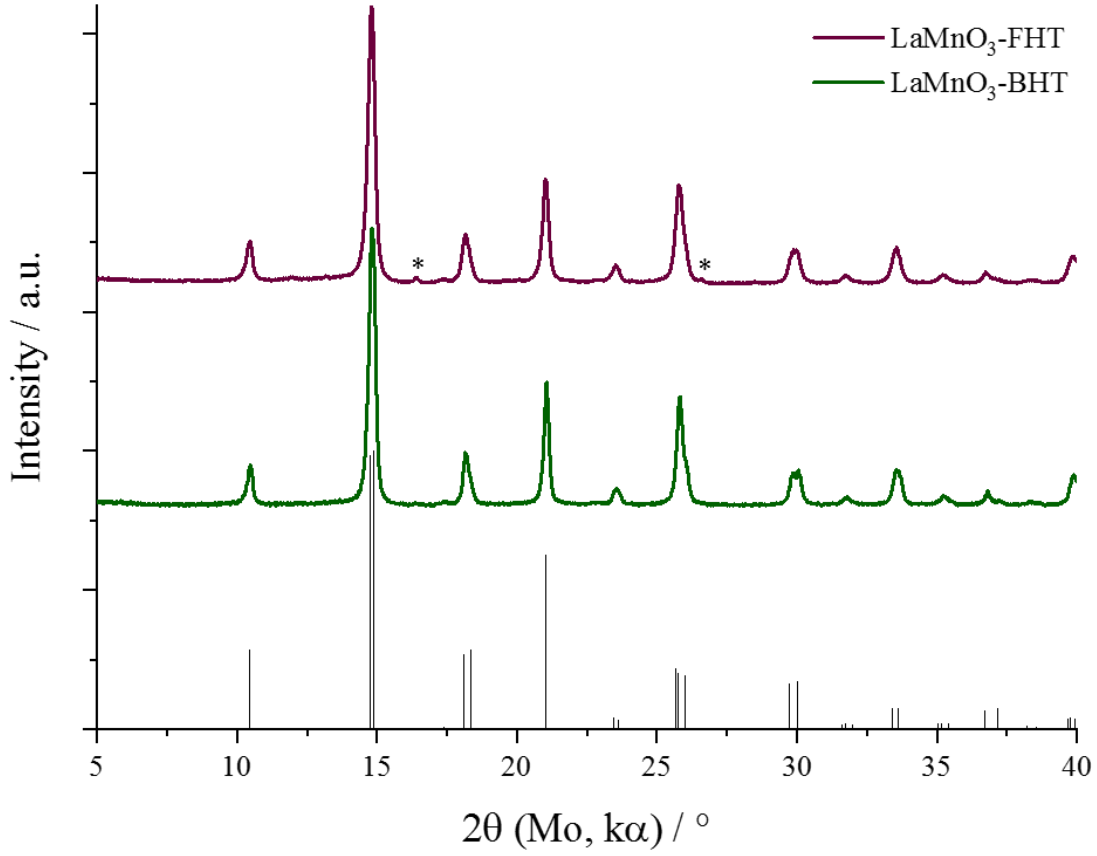

Figure 4.16: PXRD data for batch heat treated and flash heat treated $LaMnO_3$ sample. Impurity phase noted with *.

TEM images of the as synthesised precursor material and flash heat treated sample were taken to compare the size and morphology to the batch heat treated sample. The precursor TEM images [Figure 4.17 a)] clearly showed two different structures or phases. The PXRD of the as synthesised precursor material (shown in Figure 4.1), suggests the co-existence of LaO_3 and MnO_x species and this may be the origin of the two separate structures seen in this image. On heat-treatment more uniform morphology is observed in both the $LaMnO_3$-BHT [Figure 4.17 b)] and $LaMnO_3$-FHT [Figure 4.17 c)] samples. Irregular, spherical particles were observed with some evidence of sintering in both. A slight particle size reduction was seen when swapping from BHT to FHT with $LaMnO_3$-FHT having an average particle size of 27 nm compared to an average particle size of 32 nm for $LaMnO_3$-BHT.

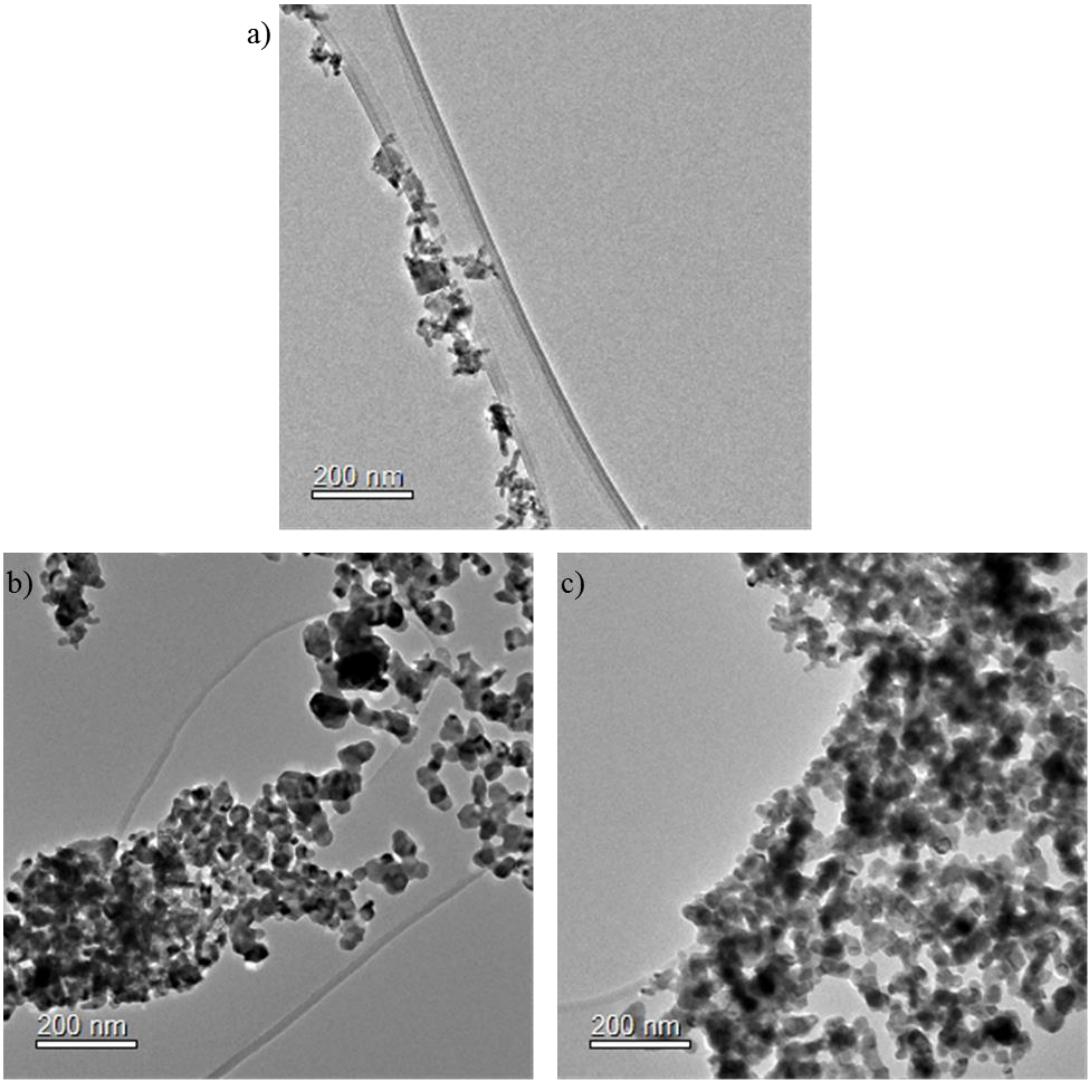

Figure 4.17: TEM data for a) as synthesised material prior to heat treatment, b) $LaMnO_3$-BHT and c) $LaMnO_3$-FHT.

4.4.3.2. Electrochemical Characterisation of Heat-Treated $LaMnO_3$

Figure 4.18 a) shows the CVs taken in degassed 0.1 M KOH. There was no observable peak shift between the BHT and FHT samples. However, there was a large difference in the overall peak magnitudes, with the FHT sample covering a much larger area than the BHT sample. This may be due to the higher surface area of the FHT sample which would therefore be expected to possess more available surface sites for redox reactions (and thus catalysis) to occur.

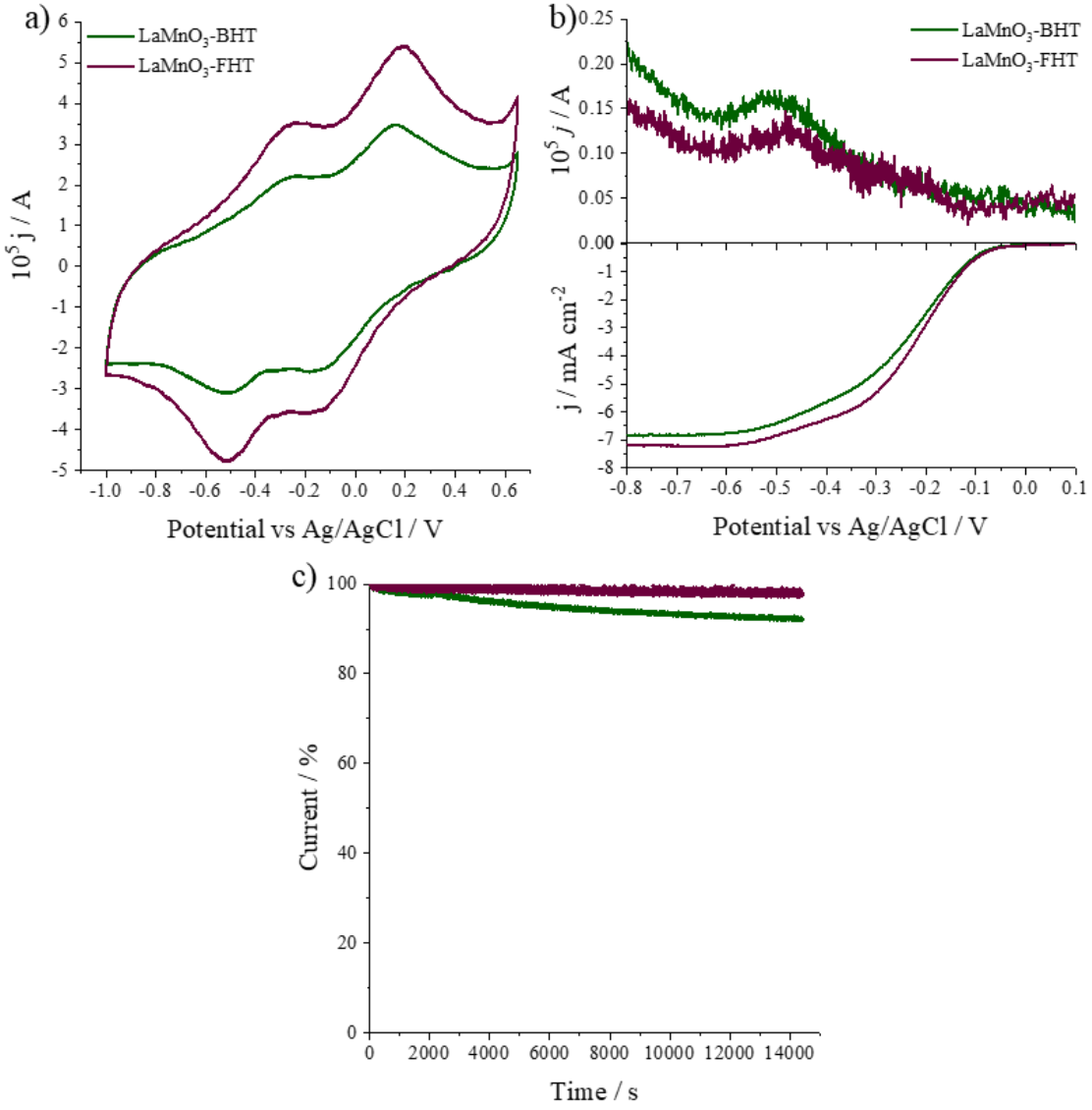

Figure 4.18: a) Cyclic voltammograms of $LaMnO_3$ materials taken in N_2 saturated 0.1 M KOH at 5 mV s^{-1}, b) RRDE data of $LaMnO_3$ materials taken at 2500 rpm and 10 mV s^{-1} in O_2 saturated 0.1 M KOH and c) chronoamperometry data of $LaMnO_3$ materials taken at 900 rpm in oxygenated 0.1 M KOH.

Figure 4.18 b) shows the RRDE curves taken for the BHT and FHT catalysts. $LaMnO_3$-FHT had a lower onset potential at −0.054 V vs Ag/AgCl whereas $LaMnO_3$-BHT had a higher onset potential at −0.072 V. $LaMnO_3$-FHT also had a lower limiting current density of −7.12 mA cm^{-2} at −0.6 V vs −6.76 mA cm^{-2} for $LaMnO_3$-BHT. The curve collected from the platinum ring electrode associated with the production of peroxide has significant noise. This is due to the extremely low currents being collected approaching the limits of the potentiostat's resolution. Both $LaMnO_3$ materials had a

peroxide yield of less than 1% and a calculated electron transfer number of 3.99 making them ideal ORR catalysts as the preferred 4 e^- pathway is dominant in both catalysts. This reported ETN was higher than in some previous reports,[254,281] for example, Xue *et al.* calculated experimentally an electron transfer number of 3.66 for $LaMnO_3$[283], although this may be due to the difference in experimental conditions such as ink formulation, catalytic loading and electrolyte.[284]

Chronoamperometry measurements were taken over 4 h at 900 rpm and −0.5 V and are shown in Figure 4.18 c). The flash heat treated sample was more stable, losing only 2.5% over the test window compared to the batch sample which lost 8% activity over the same time. The FHT $LaMnO_3$ sample was therefore more stable than the commercial PT-black sample which was tested under the same conditions and lost 5% activity.

4.5. Summary and Conclusions

In conclusion, a series of *A*MnO_3 catalysts were synthesised and tested for the electrochemical reduction of oxygen. $LaMnO_3$, $SmMnO_3$ and $YMnO_3$ were successfully synthesised via CHFS followed by a heat treatment step whereas the solubility of Ca^{2+} meant that the corresponding Mn perovskite had to be synthesised via a sol-gel method. The catalytic activity was highly dependent on the *A*-site cation used. $YMnO_3$ and $SmMnO_3$ had very large, sintered particles and poor catalytic activity, $CaMnO_3$ also had large sintered particles but had much higher overall activity. $LaMnO_3$ exhibited the highest overall catalytic activity with a low onset potential of 0.91 V vs RHE and high limiting current density at −0.5 V of −6.4 mA cm^{-2}. The results are similar to those seen in the literature such as $LaMnO_3$ made by combustion synthesis where the onset potential was 0.90 V vs RHE.[285] Whilst electrochemical results could be correlated to XPS results, the use of synchrotron technique such as X-ray absorption spectroscopy (XAS) would allow for a more thorough examination of oxidation states. This is because XAS is a local structure technique (it gives a local average of the bulk material) whereas XPS is surface sensitive technique, meaning it can be unrepresentative of the bulk material.

$LaMnO_3$ was chosen as the most promising candidate for an ORR catalyst. The precursor concentrations were then optimised via CHFS. The PXRD data showed that at all concentrations of precursors and base ratios tried, majority phase $LaMnO_3$ was seen, with no significant peak shifts or change in Scherrer size. The BET data for

changing base ratios showed an increase in SSA of 6.7 $m^2 g^{-1}$ as the base ratio was increased from 5 to 20 equivalents. The BET data for changing metal concentration showed a slight increase in SSA of 1.2 $m^2 g^{-1}$ as the concentration ratio was changed from 0.05 to 0.2. All samples showed similar activity and stability to the initial $LaMnO_3$ sample produced. Small improvements in onset potentials were observed, with lower concentration of precursor metals and higher base ratios giving improvements in activity. The best performing catalyst was $LaMnO_3$-5 with an onset potential of −0.043 V vs Ag/AgCl.

A small study on the effect of heat treatment on the ORR activity was then carried out. A sample of the CHFS precursor material was flash heat treated. Majority phase $LaMnO_3$ was seen in the PXRD and the BET SSA was 26.2 $m^2 g^{-1}$, higher than the SSA of the batch heat-treated sample. The FHT-$LaMnO_3$ sample was more catalytically active than the BHT-$LaMnO_3$, with a higher onset potential (−0.054 V vs −0.072 V), greater limiting current density and greater stability. This suggests that the heat treatment step is the most important step in the synthesis of $LaMnO_3$ for optimisation.

Future work may consider adapting the CHFS reactor to make phase pure $LaMnO_3$ direct in flow. This has been achieved by Wang *et al.* in an adapted CHFS reactor with a band heater set to 550 °C giving a much higher reaction temperature than was used in this thesis.[270] A reheater section could be added to the current CHFS rig to allow the precipitated reaction mixture to reach temperatures > 410 °C allowing for the reaction of $La(OH)_3$. A further way of optimising the overall synthesis may be to do an extended time/temperature study on the precursor material made vis CHFS and optimise the heat-treatment for best ORR activity vs stability. Future work may also consider scaled up testing such as putting the catalyst into a fuel cell setup and examining the activity, as there can be large differences between RDE testing and real cell testing.[286]

5. $La_xMn_yNi_zO_3$ Materials as Highly Active Bifunctional Oxygen Electrocatalysts

5.1. Abstract

As discussed in Chapter 3, CHFS is a valuable technique for the synthesis of libraries of materials which can then be examined as electrocatalysts. A combinatorial library containing 64 different ternary compositions of $La_xMn_yNi_zO_3$ powders was prepared using Continuous Hydrothermal Flow Synthesis (CHFS). The materials were screened using a Rotating Disk Electrode technique (RDE) for their bifunctional activity as oxygen electrocatalysts for the OER/ORR in alkaline electrolyte. The aim of this work was to show that CHFS could be used to scale-up manufacturing of catalysts that had been deposited as thin films and screened as bifunctional electrocatalysts. It was shown that enhanced bifunctional activity was achieved in a region of La sub-stoichiometry with an optimum composition of $La_{0.83}Mn_{0.85}Ni_{0.32}O_3$ yielding a combined "bifunctional" overpotential of 0.69 V. Furthermore, this exceptional activity was correlated with the appearance of the Mn^{3+}/Mn^{4+} redox couple in the cyclic voltammogram. This was associated with the coexistence of Mn^{3+} and Mn^{4+} in the bulk and has been suggested to be due to Ni^{2+} substitution at the A site. This work demonstrated that CHFS can be successfully used as both a high throughput synthesis technique for the synthesis of libraries of reversible oxygen electrocatalysts, and as a successful scale-up synthetic method.

5.2. Introduction

There is growing interest in using transition metal oxides which can catalyse both the OER and ORR.[121,280] This bifunctionality would allow one catalyst to be used in 'rechargeable' fuel cells or rechargeable metal-air batteries, with ORR activity on discharge and OER activity on charge. However, both reactions are multistep, multi-electron transferring reactions leading to sluggish kinetics and complicated mechanisms.[125,264] This limits the practical feasibility of rechargeable electrochemical devices which utilise oxygen. For example, the efficiency of the charge-discharge cycle in a zinc-air battery is usually less than 55-65%.[287] When large overpotentials are needed to drive a reaction in opposite directions, the requirements for catalysis in either direction can be very different. For example, Pt which is an exceptional ORR catalyst, is considered a poor OER catalyst as it often oxidises at the high positive potentials needed for the OER.[30]

When designing a bifunctional oxygen electrocatalyst there are a few key points to consider: the absorption rate of oxygen containing species on the catalyst must be just right to avoid either slow desorption or low probability of adsorption. Secondly, the mass transport between the bulk phase and catalyst surface determines performance therefore tuning the structural features is important. Finally, the catalyst must have high electronic conductivity to facilitate fast electron transfer.[30,288] Designing a bifunctional catalyst can be doubly complex as it is widely accepted that OER/ORR occur on different sites[25,288] and have different requirements at those sites for high catalytic performance. For example: an e_g filling of slightly less than 1 is required for optimal ORR activity, but an e_g filling of slightly greater than 1 is beneficial for optimal OER activity.[106,289] However, there are ways to modify a transition metal oxide catalyst to optimise some, or all of these requirements. For example, Cheng *et al.* found that by engineering the phase of MnO_2 synthesised, the catalytic activity could be changed.[253]

$LaMnO_3$ exhibits high catalytic activity for both the ORR and OER because the Mn valence is between Mn^{3+} and Mn^{4+}. This leads to a moderate bond strength between the catalyst surface and oxygen species giving excellent catalytic activity.[120] Doping $LaMnO_3$ with heteroatoms at the *B* site has been shown to improve catalytic activity. Liu *et al.* doped cobalt into $LaMnO_3$ and saw much improved OER activity in the optimum sample $LaMn_{0.7}Co_{0.3}O_3$ (a shift towards the oxygen reduction potential of 200 mV) whilst maintaining ORR activity.[126]

As mentioned in the previous chapter, tuning the valence of the *A* site can lead to the introduction of both Mn^{3+} and Mn^{4+} at the *B* site. This has been seen as vital for high specific ORR activity in manganese based perovskites.[250] It has been previously shown that a Mn valence slightly above 3+ provides the highest specific ORR activity in basic electrolyte. This valence state can be tuned by partial substitution of Mn for an aliovalent transition metal at the *B* site, substitution of cations at the *A* site, and/or by adjusting the stoichiometry of oxygen.[250] The ability of the presence of Mn^{3+} in catalysing the ORR can be rationalised by considering the rate determining step of the reduction of oxygen at a transition metal surface is the exchange of reduced OH^- with fresh O_2.[118] The oxygen absorption strength at this site is determined by the e_g orbital filling. There are zero e_g electrons in Mn^{4+} but 1 e_g electron in Mn^{3+}. This electron decreases the strength of the O_2 bonding to the transition metal site allowing for faster exchange kinetics, leading to an optimum e_g filling of slightly less than 1.

Nickel based electrocatalysts are well known in the literature. $LaNiO_3$ has been described as one of the most promising bifunctional electrocatalysts for the OER/ORR.[290] It is chemically stable and can be synthesised with a high surface area making it a favourable choice.[291] Many investigations have been carried out with the aim of improving electrochemical activity, such as nanosizing, increasing the SSA and influencing the oxidation state of Ni.[122,267] Effective synthetic strategies include doping the material with heteroatoms or modifying the material with carbon-based materials. Li *et al.* modified $LaNiO_3$ with Ag nanoparticles.[292] They observed enhanced OER/ORR activity in the form of higher current densities and a higher onset potential (0.75 V vs 0.7 V vs RHE) compared to the parent $LaNiO_3$ material.

Recently, Bradley *et al.* reported that by substituting Ni for Mn/La in $LaMnO_3$ thin films the bifunctional activity of the perovskite could be tuned.[293] They showed, that along the pseudo binary line (where $x = 1$ and $y + z = 1$ in $La_xMn_yNi_zO_3$) , there was an anticorrelation in the ORR and OER activities but that in the *A*-site deficient materials, there was a region where both high ORR and high OER activity was observed. This activity was linked to the area of the Mn^{3+}/Mn^{4+} redox peak. However, this work was carried out on thin film electrodes deposited on glass in static conditions. Similar catalysts were synthesised here in powder form, with a focus on the high performing areas of the ternary phase diagram. The catalysts were then examined in rotating conditions, allowing clearer insights into the reaction occurring to be gained, removing the mass transport of O_2 as an issue.

5.3. Materials and Methods

5.3.1. Synthesis of $La_xMn_yNi_zO_3$ materials

The synthesis of the materials was carried out as described in Section 2.1.3.

5.3.2 Physical Characterisation of $La_xMn_yNi_zO_3$ materials

The physical characterisation of the materials was carried out as described in Section 2.2. PXRD, XRF, XPS, BET and Raman spectroscopy were carried out on all samples with TEM, EDX and SEM carried out on selected samples.

5.3.3 Electrochemical Characterisation of $La_xMn_yNi_zO_3$ materials

Inks for drop casting onto GC electrodes were prepared according to method 2 in Section 2.3.1.

All electrochemical testing was carried out in 0.1 M $KOH_{(aq)}$ using a Ag/AgCl reference (saturated KCl) and a platinum wire counter electrode.

Electrochemical screening of the samples for the ORR was carried out by linear sweep voltammetry between 0.1 and −0.6 V (vs Ag/AgCl) at 10 mV s^{-1} at 8 different rotation speeds (200, 400, 600, 900, 1200, 1600, 2000 and 2500 rpm) in O_2 saturated 0.1 M KOH.

Electrochemical screening of the samples for the OER was carried out by linear sweep voltammetry between 0 and 0.8 V (vs Ag/AgCl) at 10 mV s^{-1} and 2500 rpm in O_2 saturated 0.1 M KOH.

In depth electrochemical analysis was carried out on a selection of samples from the grid. RRDE testing was carried out in line with LSV testing but the ink was drop cast onto a rotating ring disk electrode to give the same catalytic loading as in previous tests. The ring potential was set to 0.35 V vs Ag/AgCl to ensure complete peroxide decomposition.[267]

Chronoamperometry was carried out in O_2 saturated 0.1 M KOH by holding the potential at −0.5 V vs Ag/AgCl and measuring the current response over 14400 s.

Cyclic voltammetry in N_2 was carried out at 5 mV s^{-1} between −1 and 0.65 V vs Ag/AgCl in degassed 0.1 M KOH.

5.4. Results and Discussion

5.4.1. Physical Characterisation of $La_xMn_yNi_zO_3$ Materials

After the CHFS step, cleaning by centrifugation and freeze-drying, the nanoparticulate metal oxides were collected with > 80% yield. Losses can come from unoptimized cleaning and freeze-drying steps of small quantities of material. After freeze drying all powders were brown in colour and varied in darkness getting darker for higher nickel content. All samples were then flash heat treated at 850 °C for 30 mins yielding free flowing black powders for all samples.

XRF was used to establish the actual ratios of La:Mn:Ni. A small discrepancy was noticed between nominal and actual composition. Whilst Ni concentration was as expected, the concentrations of La and Mn were higher and lower than expected, respectively. A global shift in composition was observed, with all compositions shifting up and to the right as shown in Figure 5.1. All calculations for elemental ratios were

initially made on the assumption that the Mn precursor had four water molecules of crystallisation. However, it is expected that the actual water of crystallisation was higher resulting in a manganese deficiency. This may have been due to the hygroscopicity of the $Mn(NO_3)_2 \cdot xH_2O$ precursor. Consequently, XRF ratios of elements are used to describe all materials from this point.

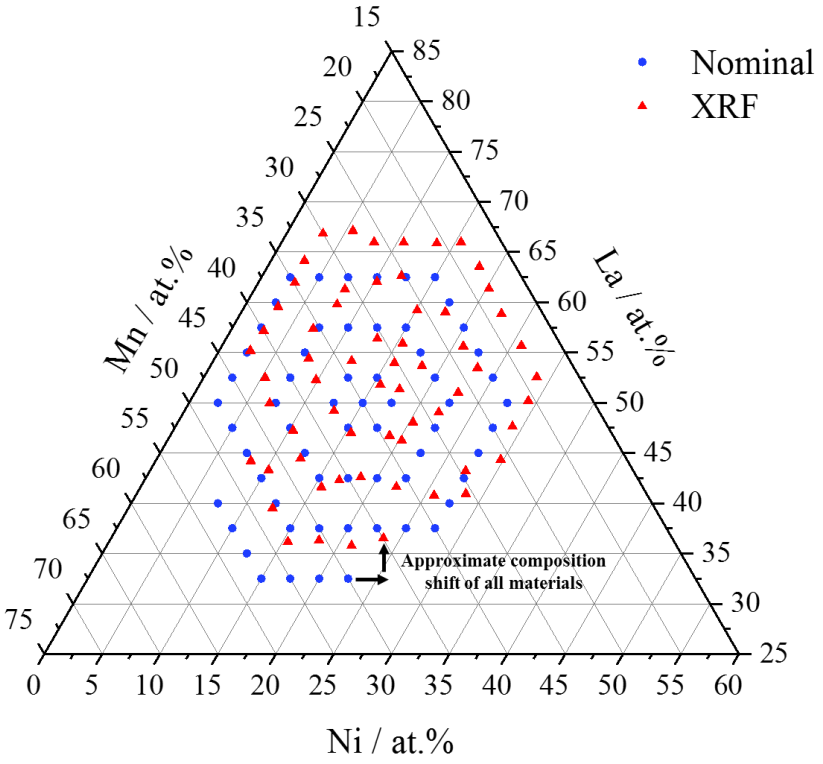

Figure 5.1: Nominal vs actual elemental compositions for the ternary phase series $La_xMn_yNi_zO_3$. Composition shift shown by the black arrows.

To examine the structure of all samples, PXRD and Raman spectroscopy were carried out. The PXRD data shows the formation of crystalline structures indicated by regular peaks at different angles arising from a set of reflections. PXRD patterns for all samples were a good match for ICSD collection code no. 29119 corresponding to cubic (*P*-*m*-3*m*) $LaMnO_3$ (Figure 5.2). Above the pseudo-binary line, a second phase could be seen which was a good match for ICSD collection code no. 167480, corresponding to a hexagonal $La(OH)_3$ impurity phase due to the deficiency in *B* site elements in the perovskite. Below the pseudo-binary line, a secondary phase was observed which was a good match for ICSD collection code no. 185294, corresponding to a cubic $NiMn_2O_3$ spinel impurity, probably due to the lanthanum deficient nature of the materials (*A* site deficiency). The addition of these two impurity phases strongly suggested that only a

small percentage of either *A* site or *B* site elements were crossing to the opposing site. No additional peaks were seen for either Mn_2O_4 or NiO.

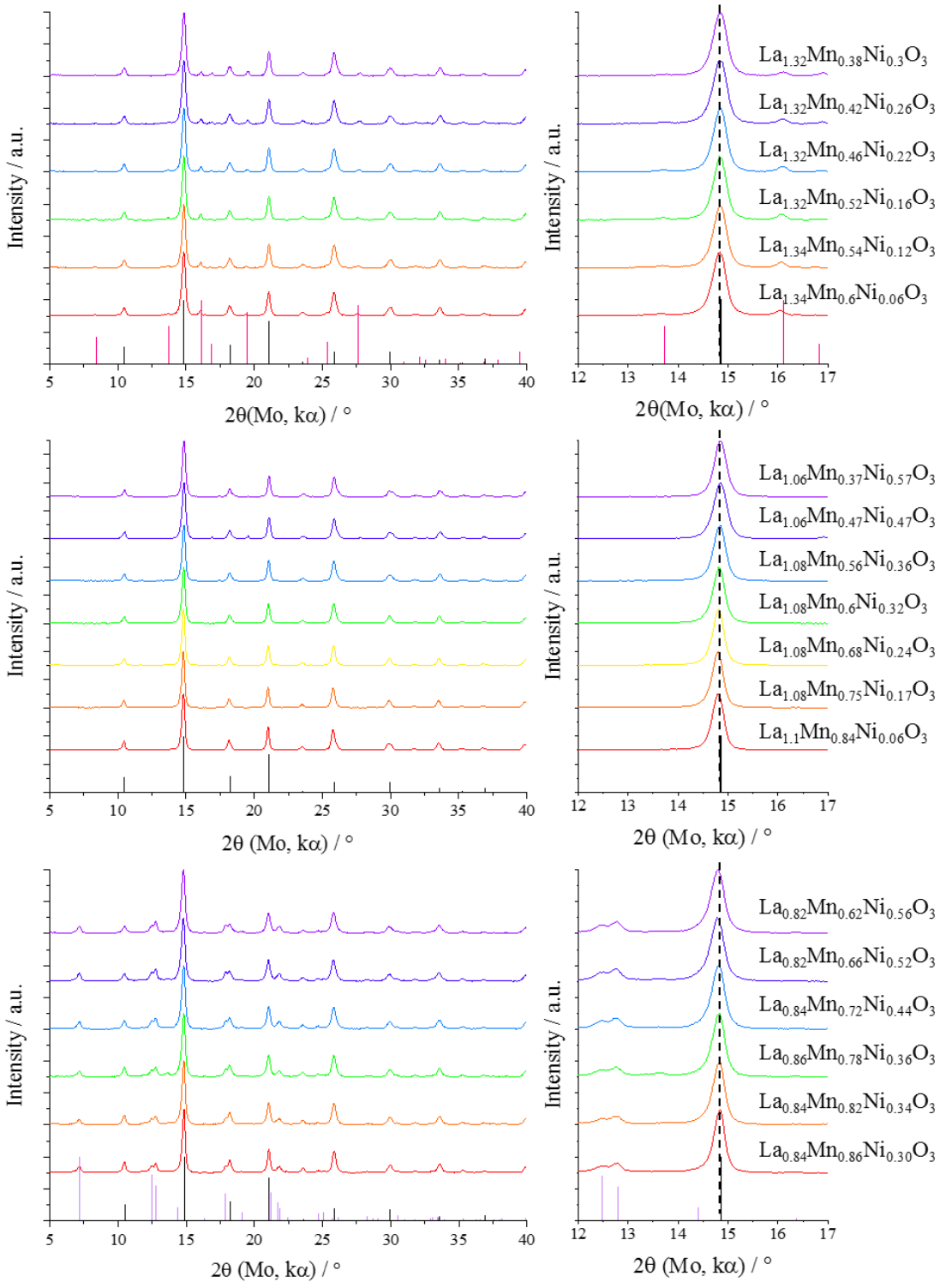

Figure 5.2: PXRD data of heat-treated materials from a selection of the phase diagram, increasing in Lanthanum content up the plot. Black: $LaMnO_3$, ICSD collection code no. 29119, lilac: $La(OH)_3$, ICSD collection code no. 167480, pink: $NiMn_2O_3$, ICSD collection code no. 185294. The dotted line shows the peak shift as the elemental composition is changed.

The XRD peaks were broad, due to the nanosizing of the crystallite domains. This results from the smoothing of the transition between constructive and destructive interference according to Braggs law due to fewer crystal layers diffracting for each plane.[294] A slight shift in 2θ values of the (110) peak (see insert to Figure 5.2) along the pseudo-binary line was observed which corresponded to a gradual change from the cubic $LaMnO_3$ (*Pm*-3*m*) to the trigonal $LaNiO_3$ (*R*-3*c*) lattice, consistent with previous observations.[295,296] It has previously been attributed to lattice contraction on Ni substitution because as Ni (Ni^{3+} low-spin 0.56 Å, high-spin 0.60 Å) replaces Mn (Mn^{3+} low-spin 0.58 Å, high-spin 0.65 Å) the unit cell volume decreases.[271] There were no additional peaks along this line, confirming the presence of a complete solid solution in line with previous reports. There was also an increase in the full-width half maximum of the diffraction peaks on substitution of Mn^{3+} with Ni^{3+} again pointing to structure modification.[296]

Estimation of the crystallite domain size was carried out using the Scherrer equation (equation 2.2) on the (110) peak and the data is represented graphically in Figure 5.3. Scherrer size was found to be in the range of 9-15 nm, which was consistent with observations reported in literature.[271,297] The addition of nickel into the lattice along the pseudo-binary line was found to decrease the Scherrer size, perhaps due to lattice contraction from the addition of nickel, and the deformation, or formation of disorder in the $LaMnO_3$ lattice.[271] Away from the pseudo-binary line, there was a large variation in Scherrer size. Below the line, in La deficient regions, Scherrer sizes were small, between 9 and 11 nm, whereas above the line, in La rich regions, Scherrer sizes were larger. This was particularly the case in areas of high at % Mn, which corresponded to the trend seen in the XRD of lattice contraction on the addition of Ni.

The BET surface area measurements are shown in Figure 5.3. SSA were found to be between 15 and 36 $m^2\ g^{-1}$ which were higher than those for similar materials found in the literature.[271] This could be explained in terms of the amount of lanthanum within the material; materials with less lanthanum showed significantly higher surface areas compared to those with high lanthanum content, possibly due to the presence of a low surface area $La(OH)_3$ impurity. There was also a shift to lower surface areas seen with increasing concentration of Ni along the binary line. $LaMnO_3$ heat treated under the same conditions had an intermediate SSA of 26.2 $m^2\ g^{-1}$ whereas $LaNiO_3$ had an SSA of 12.3 $m^2\ g^{-1}$ confirming the trend along the binary line as the SSA decreases from

pure $LaMnO_3$ to pure $LaNiO_3$. The *A* site deficient materials had much higher SSA than expected, even with increasing concentrations of Ni.

It can be concluded that there was a good correlation between materials with a high surface area and a low Scherrer size which was to be expected.

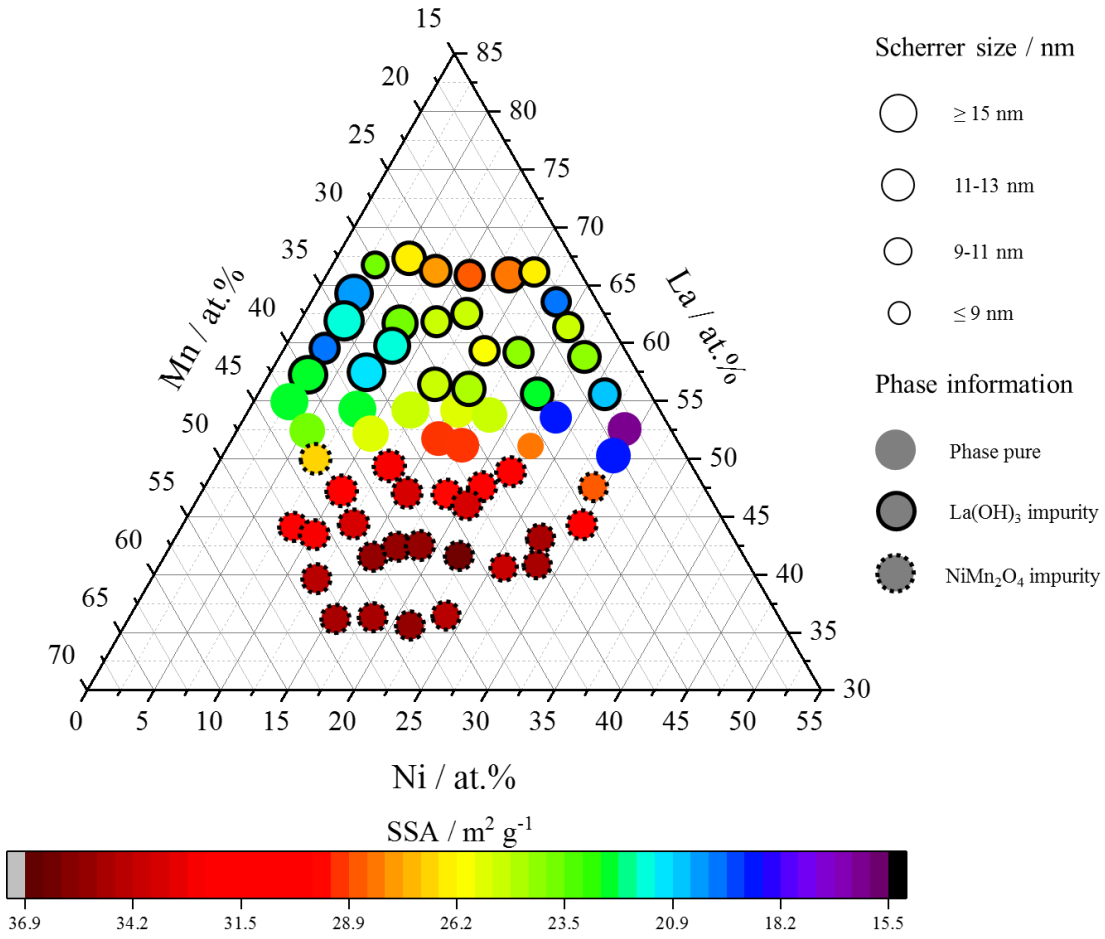

Figure 5.3: Physical characterization data for the full composition diagram. The size of the markers corresponds to the size calculated from the Scherrer equation. The colour of each marker represents the BET surface area. The outline of the marker corresponds to the phase impurities seen in the PXRD data.

SEM analysis on four of the catalysts ($La_{1.10}Mn_{0.84}Ni_{0.06}O_3$, $La_{0.82}Mn_{0.86}Ni_{0.32}O_3$, $La_{1.08}Mn_{0.60}Ni_{0.32}O_3$ and $La_{1.06}Mn_{0.38}Ni_{0.56}O_3$) can be seen in Figure 5.4. Catalysts showed similar morphology, with nanosized, irregular particles partially sintered together. As can be seen in Figure 5.4, samples $La_{1.10}Mn_{0.84}Ni_{0.06}O_3$ and $La_{0.82}Mn_{0.86}Ni_{0.32}O_3$ showed a higher surface area with a more open structure than $La_{1.08}Mn_{0.60}Ni_{0.32}O_3$ and $La_{1.06}Mn_{0.38}Ni_{0.56}O_3$. This would be in line wih the BET data

as SSA decreases along the binary line (a→c→d) and was much greater in La deficient parts of the ternary phase diagram (b). However, due to little change in the morphology, it was not considered as critical when interpreting the activity of various $La_xMn_yNi_zO_3$ catalysts.

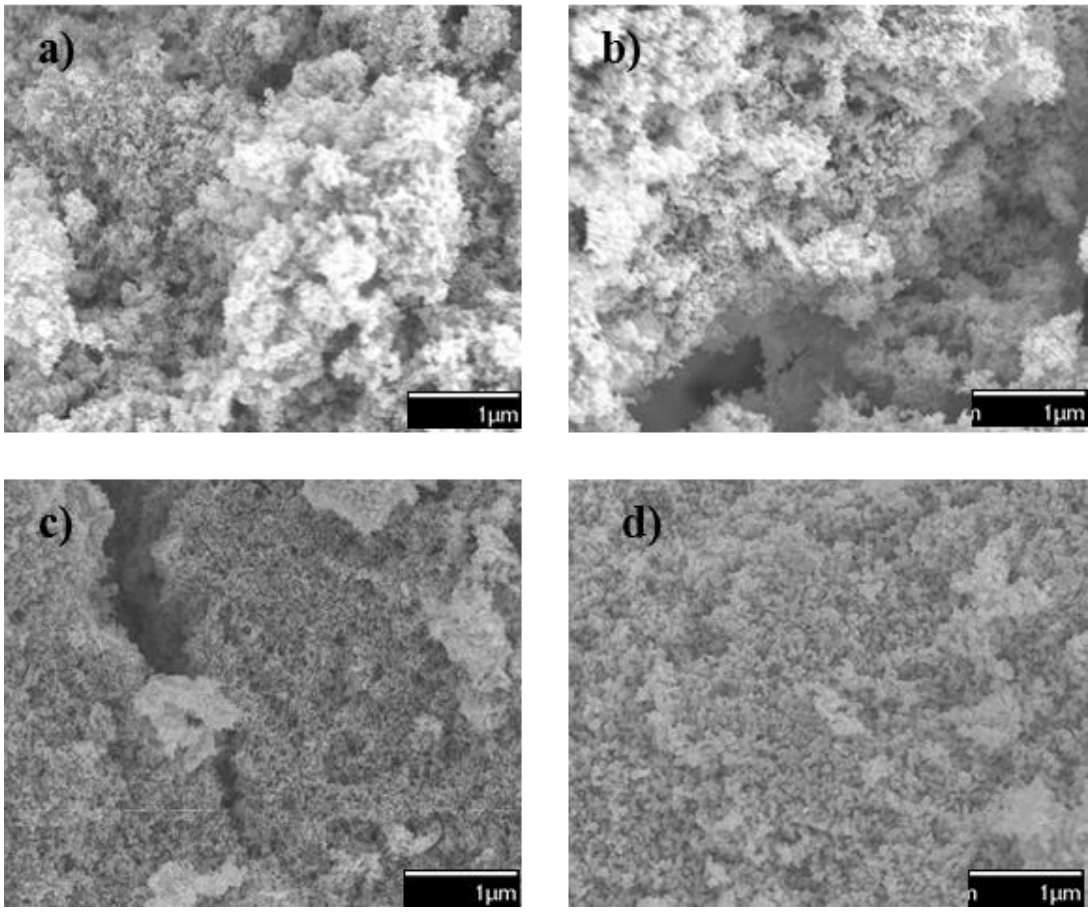

Figure 5.4: SEM data obtained at 15000 magnification for a) $La_{1.10}Mn_{0.84}Ni_{0.06}O_3$, b) $La_{0.82}Mn_{0.86}Ni_{0.32}O_3$, c) $La_{1.08}Mn_{0.60}Ni_{0.32}O_3$ and d) $La_{1.06}Mn_{0.38}Ni_{0.56}O_3$.

The morphology of the four samples was further investigated using TEM and selected images are shown in Figure 5.5. All samples showed similar morphologies of irregular, roughly spherical particles with some evidence of light sintering due to the heat treatment. However, there was some variation in particle size observed, as suggested by the SEM analysis and confirmed by TEM, $La_{0.82}Mn_{0.86}Ni_{0.32}O_3$ [Figure 5.5 c)] was clearly smaller than the other samples. Clear layer interspacing could be seen for all catalysts. For $La_{1.10}Mn_{0.84}Ni_{0.06}O_3$, $La_{0.82}Mn_{0.86}Ni_{0.32}O_3$ $La_{1.06}Mn_{0.38}Ni_{0.56}O_3$ [Figure 5.5 b, d and e)] this spacing was approximately 0.27 nm which corresponded to the 011, 101 and/or 110 planes. For $La_{1.08}Mn_{0.60}Ni_{0.32}O_3$ the spacing was 0.37 nm which corresponded to the 001, 010 and/or 100 planes. 50 nanoparticles were counted to

determine the average particle size and histograms are shown in the supporting information. $La_{1.10}Mn_{0.84}Ni_{0.06}O_3$ had an average particle size of 37 nm. $La_{0.82}Mn_{0.86}Ni_{0.32}O_3$ had an average particle size of 18 nm. $La_{1.08}Mn_{0.60}Ni_{0.32}O_3$ had an average particle size of 22 nm and $La_{1.06}Mn_{0.38}Ni_{0.56}O_3$ had an average particle size of 37 nm. The particle sizes observed via TEM follow the same trend as the Scherrer sizes, though they do not match exactly. This may be due to the crystallite domain size being smaller than the observed (aggregated) particle size.

Energy-Dispersive X-ray spectroscopy (EDX) mapping (Figure 5.6) showed a homogeneous distribution of elements in the case of Figure 5.6 a), c) and d) along the binary Mn-Ni line. However, in Figure 5.6 b) a La deficient region was clearly seen on the map. As this sample was La deficient and Mn, Ni rich this suggested that there was some degree of phase separation, possibly from the impurity phase highlighted in the PXRD, $NiMn_2O_4$.

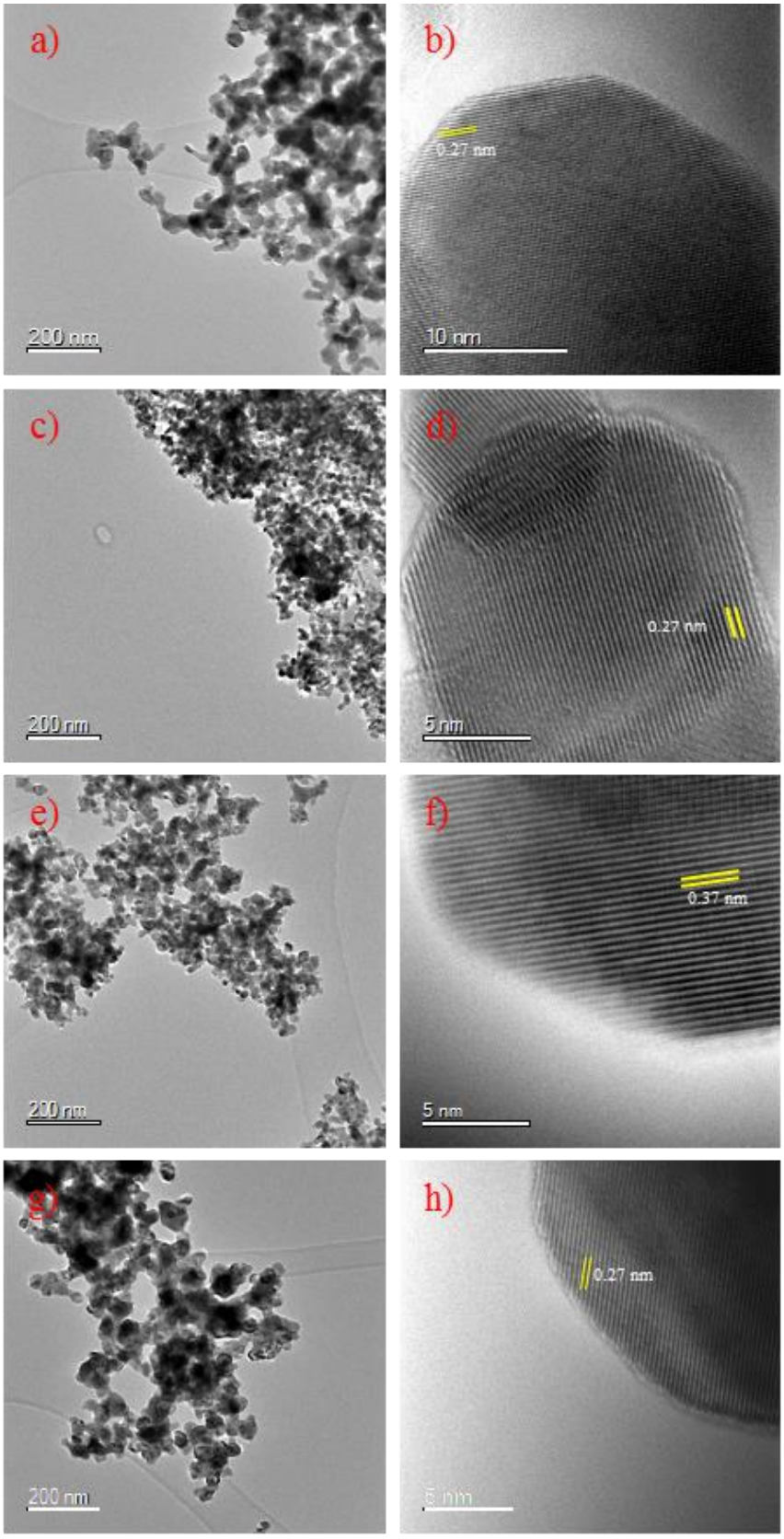

Figure 5.5: Transmission electron micrographs showing an overview of particles and lattice fringes for a,b) $La_{1.10}Mn_{0.84}Ni_{0.06}O_3$, c,d) $La_{0.82}Mn_{0.86}Ni_{0.32}O_3$, e,f) $La_{1.08}Mn_{0.60}Ni_{0.32}O_3$ and g,h) $La_{1.06}Mn_{0.38}Ni_{0.56}O_3$.

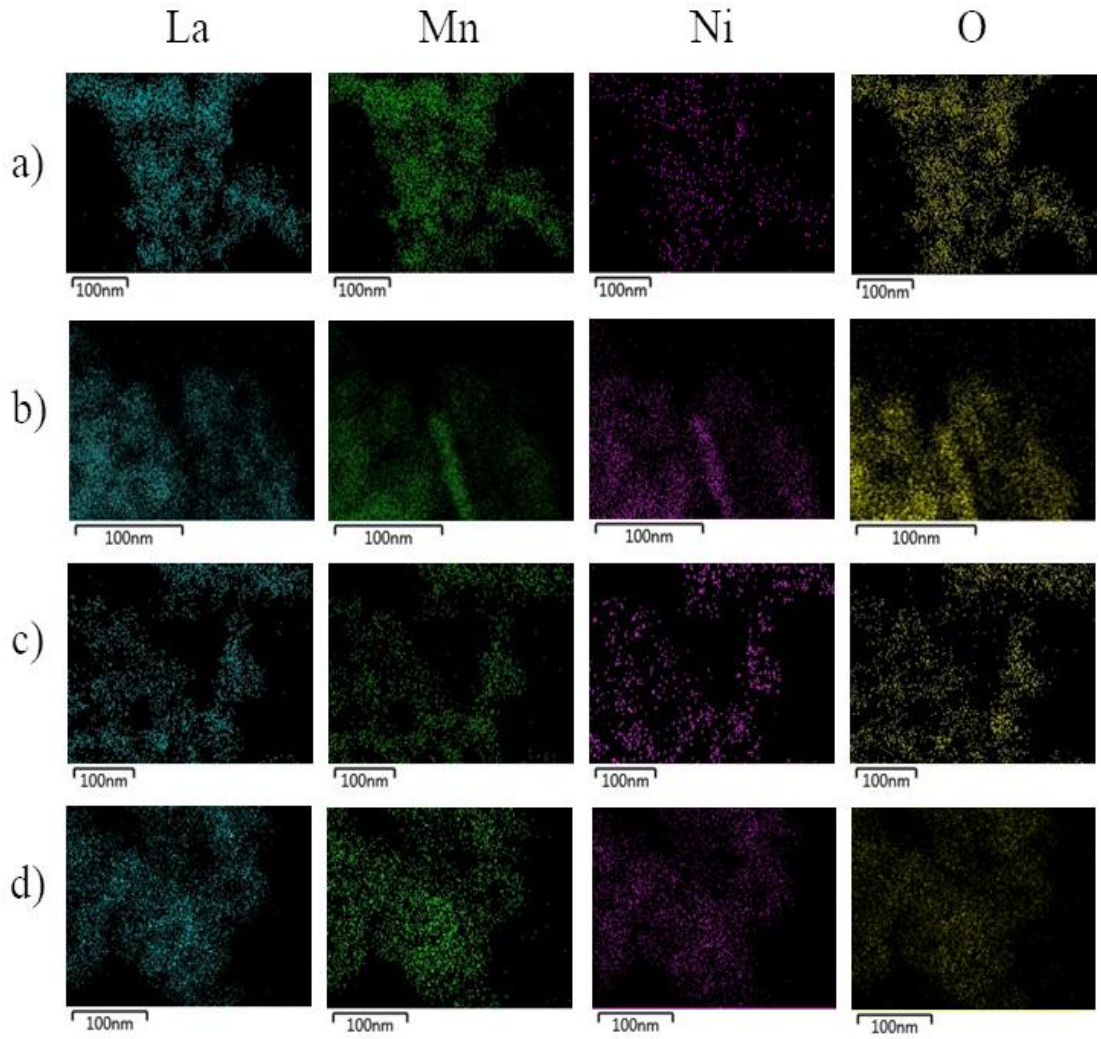

Figure 5.6: EDX data (La, Mn, Ni and O kα) taken using an STEM technique for a) $La_{1.10}Mn_{0.84}Ni_{0.06}O_3$, b) $La_{0.82}Mn_{0.86}Ni_{0.32}O_3$, c) $La_{1.08}Mn_{0.60}Ni_{0.32}O_3$ and d) $La_{1.06}Mn_{0.38}Ni_{0.56}O_3$.

Raman spectroscopy was further used to confirm the presence of a perovskite phase. Raman spectra were taken at room temperature with low laser power to avoid sample decay over the measurement time. There are 24 Raman active modes: $7A_g + 5B_{1g} + 7B_{2g} + 5B_{3g}$. Two clear modes could be seen, located at around 530 and 670 cm^{-1}, with their frequency depending on the temperature and on the Jahn-Teller distortion of the MnO_6 octahedra.[298] At higher Mn concentrations, spectra were difficult to collect due to destruction of the sample by the Raman laser. There was a slight shift to higher frequencies observed in both modes as the concentration of Ni increased. This implied that there was a change in the angles and distances of bonds in the MnO_6 octahedra as Ni content increased, suggesting that Ni was being successfully incorporated into the lattice rather than forming a separate phase.[299]

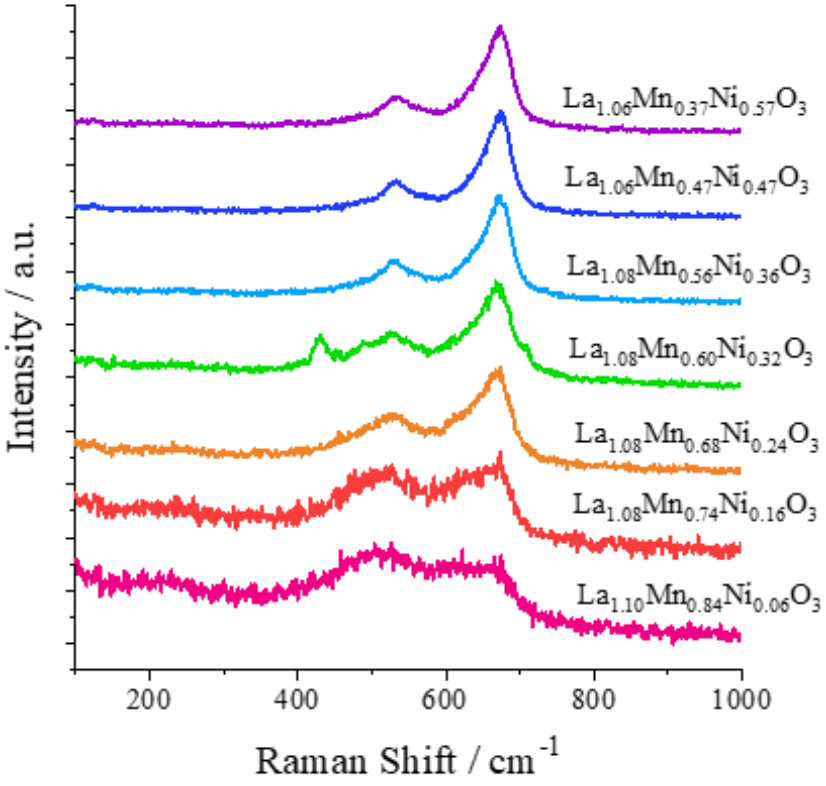

Figure 5.7: Raman spectra across the binary line.

The XPS peaks in the Mn spectra are shown in Figure 5.8 a). They were located at around 642 and 653 eV for all samples, corresponding to the Mn $2p_{3/2}$ and Mn $2p_{1/2}$ spin-orbit doublet, respectively. The Mn $2p_{3/2}$ signal can be separated into two peaks at 641.1 and 642.9 eV which could be assigned to the Mn^{3+} and Mn^{4+} ions respectively. However, the Mn signal is difficult to deconvolute.[254] There was a shift observed in the Mn spectra along the pseudo binary line. The Mn 2p peak was found at 641.3 eV in $La_{1.10}Mn_{0.84}Ni_{0.06}O_3$ but shifted to 642.1 eV in $La_{1.06}Mn_{0.38}Ni_{0.56}O_3$. As the La atomic percentage is roughly constant, this can be ascribed to the addition of Ni or the removal of Mn. When Mn remained constant (along the ternary z axis) the peak shifted from 642.6 eV for $La_{1.34}Mn_{0.60}Ni_{0.06}O_3$ to 642.0 eV for $La_{0.82}Mn_{0.62}Ni_{0.56}O_3$. Therefore it can be concluded that there are differing amounts of Mn^{3+} and Mn^{4+} present depending on the ratios of La and Ni present in the material.[207] No evidence for the presence of Mn^{2+} was found as no satellite peak was present at approximately 648.8 eV.[300]

The O1s peaks (shown in Figure 5.8 b) showed mixed signals from different oxygen species at the material surface. Lattice oxygen (e.g. La-O-Mn at 529.1 eV)[301], hydroxide/carbonate groups (532.3 eV)[302] or low coordinated oxygen ions at special

sites on the surface (531.0 eV) can coexist at the perovskite oxides surface. The ratio of $(O_2)^-$ species to lattice oxygen was seen to be much higher in the materials containing more nickel. This has been seen previously and has been attributed to the fact that La-Ni perovskites are prone to be oxygen deficient, therefore less available lattice oxygen.[271] However, the most noticeable difference in the spectra was that in samples with an excess of La (with an $La(OH)_3$ impurity phase), the peak intensities are almost reversed in comparison to the binary or La deficient systems. This agrees well with the PXRD data in showing that there is a hydroxide impurity in the materials. There may also have been slight influences in the O 1s peak from the uncovered carbon tape.

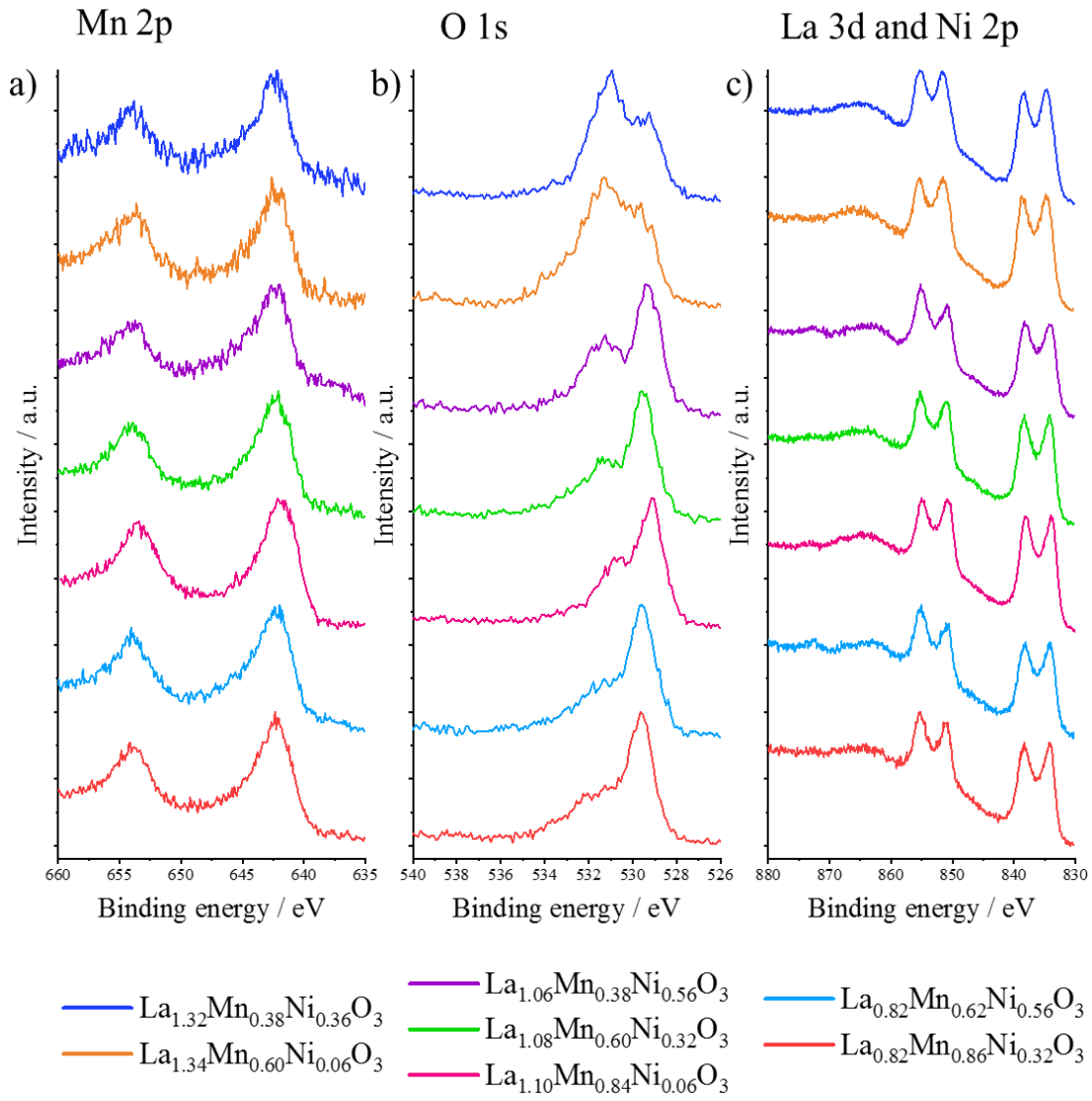

Figure 5.8: XPS spectra for a selection of samples across the ternary space showing a) the 2p Mn spectra, b) the O 1s spectra and c) the La 3d and Ni 2p spectra.

The La 3d spectra [shown in Figure 5.8 c)] showed two doublet peaks at 831 to 841 eV and 848 to 857 eV, which corresponded to the La $3d_{5/2}$ and La $3d_{3/2}$ signals respectively. The Ni $2p_{3/2}$ overlaps with the La $3d_{3/2}$ peak making the contributions difficult to differentiate, however, the $2p_{1/2}$ of the Ni spectra could be seen at approximately 865 eV. The La $3d_{5/2}$ and La $3d_{3/2}$ signals appeared close to the reference peaks for La_2O_3 indicating trivalent La ions.

5.4.2. Electrochemical Characterisation of $La_xMn_yNi_zO_3$ Materials

$LaMnO_3$ and $LaNiO_3$ were synthesised and tested as bifunctional oxygen electrocatalysts to act as benchmarks against which the ternary catalysts could be compared. The PXRD patterns can be seen in the supplementary information, Figure 9.9. Initially, a cyclic voltammogram was carried out at 5 mV s^{-1} in degassed electrolyte. Figure 5.9 a) shows the cyclic voltammetry curves for $LaMnO_3$ and $LaNiO_3$. The $LaMnO_3$ response is shown in blue and several redox peaks can be seen. The cathodic reduction peaks at −0.191 V and −0.532 V vs Ag/AgCl were related to the reduction of Mn oxidation states at the surface of the catalyst. The response was broad and box-like due to the capacitive behaviour seen in $LaMnO_3$ compounds.[303] The response for $LaNiO_3$ can be seen in red. This was less box-like, with clearer redox and catalytic peaks. There were also several redox peaks seen in the curve and these were assigned as the Ni^{2+}/Ni^{3+} redox couple centred at 0.485 V and the Ni^0/Ni^{2+} redox couple centred at −0.565 V vs Ag/AgCl. The peak seen in the most positive Section of the CV was the beginning of the OER reaction, suggesting that $LaNiO_3$ was a much better OER catalyst than $LaMnO_3$ as the intensity of this peak was much greater.

The LSV traces [seen in Figure 5.9 b)] show that whilst $LaMnO_3$ was a much better ORR catalyst, $LaNiO_3$ was a better OER catalyst. The overpotentials for $LaMnO_3$ were −0.036 V for the ORR and 0.685 V for the OER giving a combined overpotential of 0.72 V. The combined overpotential value was lower than previously reported for $LaMnO_3$. For example, Liu *et al.* synthesised $LaMnO_3$ via a sol-gel route and saw a combined overpotential of >1.2 V.[126] The overpotentials for $LaNiO_3$ were −0.155 V for the ORR and 0.623 V for the OER giving a combined overpotential of 0.78 V. This value was similar to those previously reported for $LaNiO_3$ made by typical solid state synthetic routes.[291] Retureto *et al*. synthesised $LaNiO_3$ with a calcination temperature of 1000 °C that had an onset potential for the ORR of −0.14 V vs Ag/AgCl.[267]

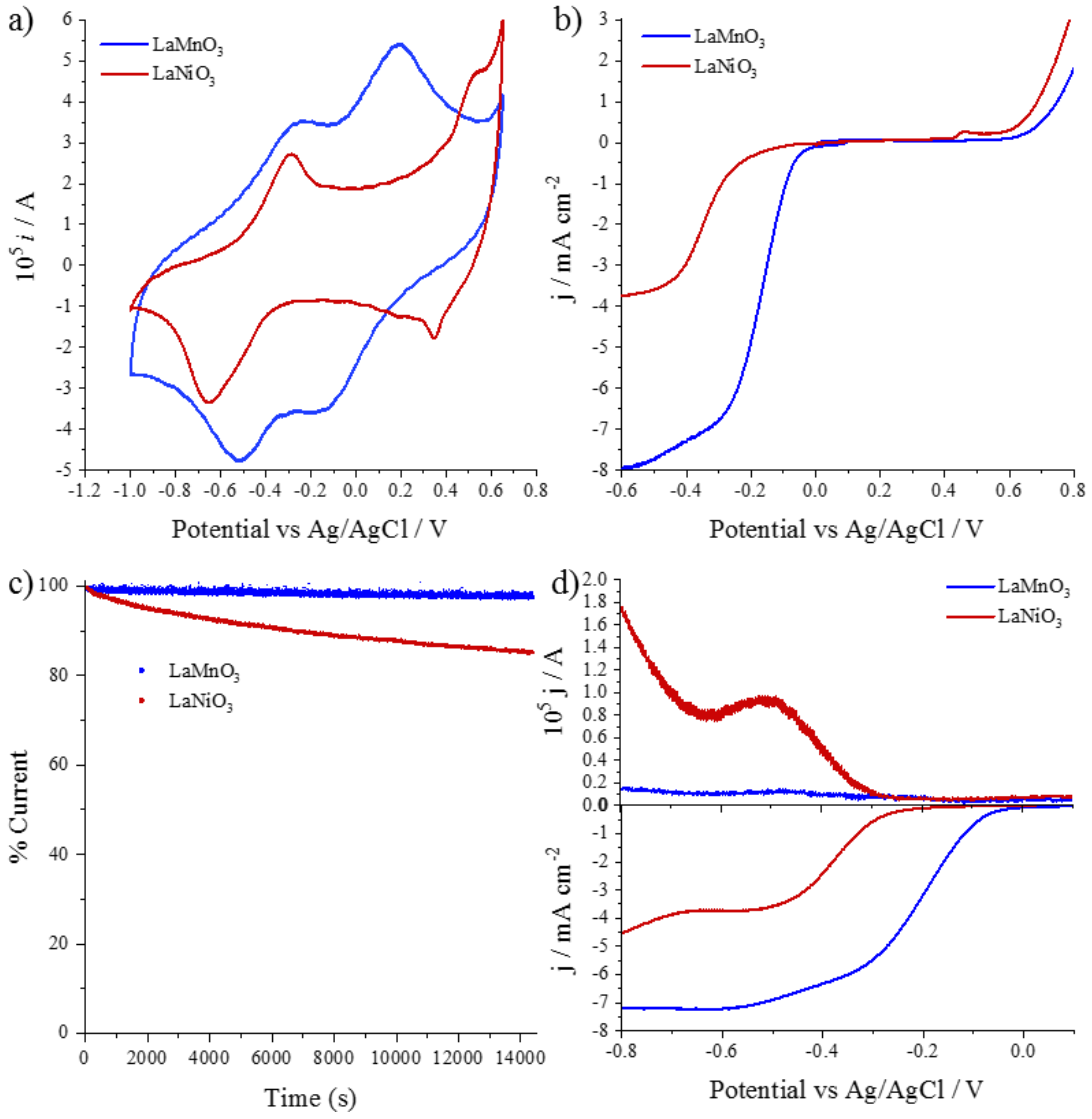

Figure 5.9: Catalytic data for $LaMnO_3$ (blue) and $LaNiO_3$ (red): a) shows the CVs taken in N_2 saturated 0.1 M KOH at 5 mV s^{-1}, b) shows the linear sweep voltammetry curves taken at 10 mV s^{-1} and 2500 rpm in O_2 saturated 0.1 M KOH, c) shows the chronoamperometric response depicted as % of current remaining taken at −0.5 V vs Ag/AgCl and 900 rpm in O_2 saturated 0.1 M KOH over a period of 4 hours and d) shows the RRDE response where the bottom *x*-axis depicts the disk current (the negative traces) and the top depicts the ring current (the positive traces) taken at 10 mV s^{-1} and 2500 rpm in O_2 saturated 0.1 M KOH.

Stability testing at −0.5 V was then carried out and is shown in Figure 5.9 c). $LaMnO_3$ maintained ca. 97.5 % activity over the 4 h testing window whereas $LaNiO_3$ maintained only c.a. 85 % activity. Sakthivel *et al*, also saw significant activity loss on running stability tests on $LaNiO_3$ although their experiment involved long term cycling methods rather than chronoamperometric methods.[290] They saw enhanced evidence of the

Ni^{2+}/Ni^{3+} redox couple in the CV and suggested the parasitic formation of $NiOOH/Ni(OH)_2$ was the cause of this stability loss.

Finally, RRDE studies were conducted to examine the electron transfer numbers for the ORR [Figure 5.9 d)]. There was a much greater yield of peroxide produced at the $LaNiO_3$ catalyst than at the $LaMnO_3$ catalyst, 5.34 % compared to 0.41 %. The calculated electron transfer numbers were 3.89 and 3.99 for $LaNiO_3$ and $LaMnO_3$ respectively. The electron transfer numbers suggested that the preferred $4e^-$ pathway was the dominant pathway for both electrocatalysts although $LaNiO_3$ had a greater contribution from the less desirable $2e^-$ pathway. The same result was seen by Sunarso *et al.* when they examined various La based perovskites, with $LaNiO_3$ generating approximately 5 times more peroxide than $LaMnO_3$.[304]

5.4.2.1. High-throughput Electrochemical Screening of $La_xMn_yNi_zO_3$ Materials

All samples were screened for their electrocatalytic activity towards the ORR and OER prior to any in-depth analysis being carried out. Samples were formulated into inks and deposited onto glassy carbon rotating disk electrodes with a mass loading of approx. 0.4 mg cm^{-2}. The electrodes were cycled between 0.2 and −0.8 V vs Ag/AgCl in O_2 saturated 0.1 M KOH until CV curves were identical to pacify the electrode surface.

Linear sweep voltammetry was then carried out between 0.1 and −0.6 V vs Ag/AgCl to examine overpotentials and current densities for the ORR and between 0 and 0.8 V vs Ag/AgCl to examine the OER. Well defined reduction curves were seen for all catalysts in the region of 0 to −0.6 V vs Ag/AgCl. A limiting current density for the ORR for all catalysts was reached and this was dependent on the rotation speed of the RDE. Examples of ORR and OER linear sweep curves can be seen in Figure 5.10. The ORR activity of $LaNiO_3$ was seen to be poor, and increased with the addition of Mn, with overpotentials moving to more positive values and reduction curves appearing steeper. In contrast to this, $LaMnO_3$ was an excellent ORR catalyst, but performed poorly for the OER. Activity is seen to increase with doping of Ni. However, activity relationships were complex and were studied in relation to the ternary composition below.

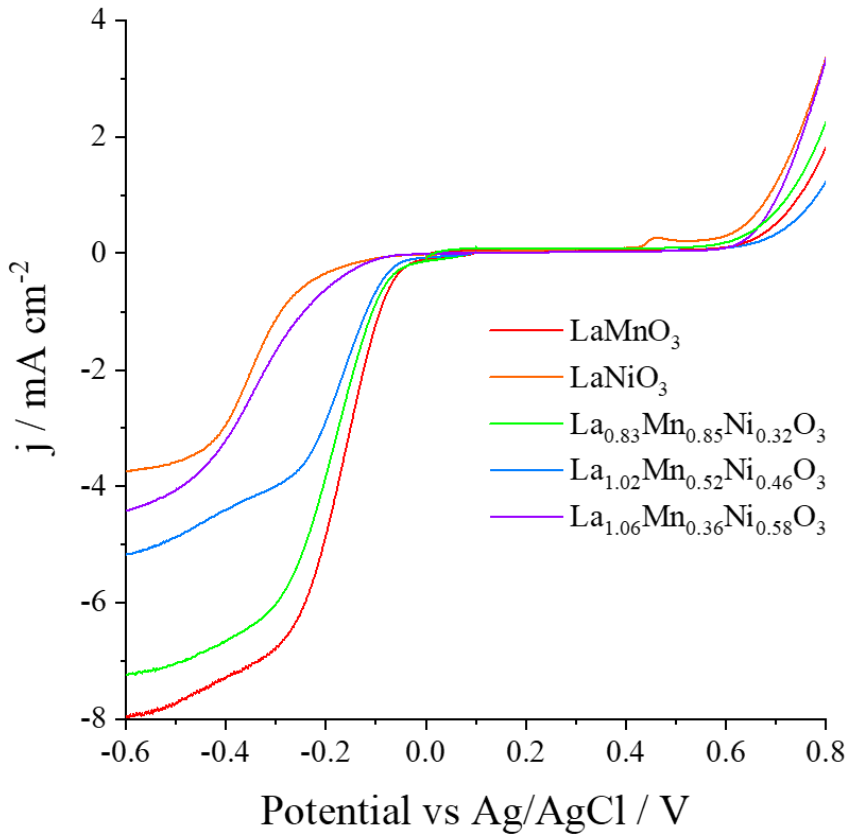

Figure 5.10: Linear sweep voltammograms of the OER and ORR showing selected composition reactions. All measurements were carried out in O_2 saturated 0.1 M KOH with a scan speed of 10 mV s^{-1} and a rotation speed of 2500 rpm. The experimental error is ± 2 %.

Figure 5.11 a) shows the compositional dependence of the overpotential for the ORR (taken at −0.2 mA cm^{-2}). Overpotentials were reported with respect to the reversible oxygen potential of 1.23 V vs RHE. The best performing ORR catalyst in terms of overpotential was $La_{0.83}Mn_{0.85}Ni_{0.32}O_3$ with an overpotential of 0.287 V. This is better than results seen in the literature for similar materials. For example Zhao *et al.* synthesised a $La_{0.4}Sr_{0.6}Co_{0.4}Mn_{0.6}O_3$ perovskite which had an overpotential of 0.492 V for the ORR[305] and Liu et al reported a series of $LaMn_{1-x}Co_xO_3$ materials which had overpotentials of approximately 0.35 V for the ORR.[126] The ternary composition plot shows that ORR activity decreased as lanthanum or nickel concentration increased - those catalysts which performed best for the ORR were on the LHS of the ternary plot (towards the $LaMnO_3$ binary system) and had *A* site sub stoichiometry. The addition of La (keeping Mn concentration constant) appeared to have a greater detrimental effect on the overpotential than increasing Ni concentration. The impurity phase in sub-

stoichiometric regions ($NiMn_2O_4$) is a known oxygen electrocatalyst suggesting that this phase may have been having a positive impact on the activity observed. However, all catalysts had overpotentials below 0.4 V suggesting that all compositions would be suitable as industrial catalysts for the ORR.[32]

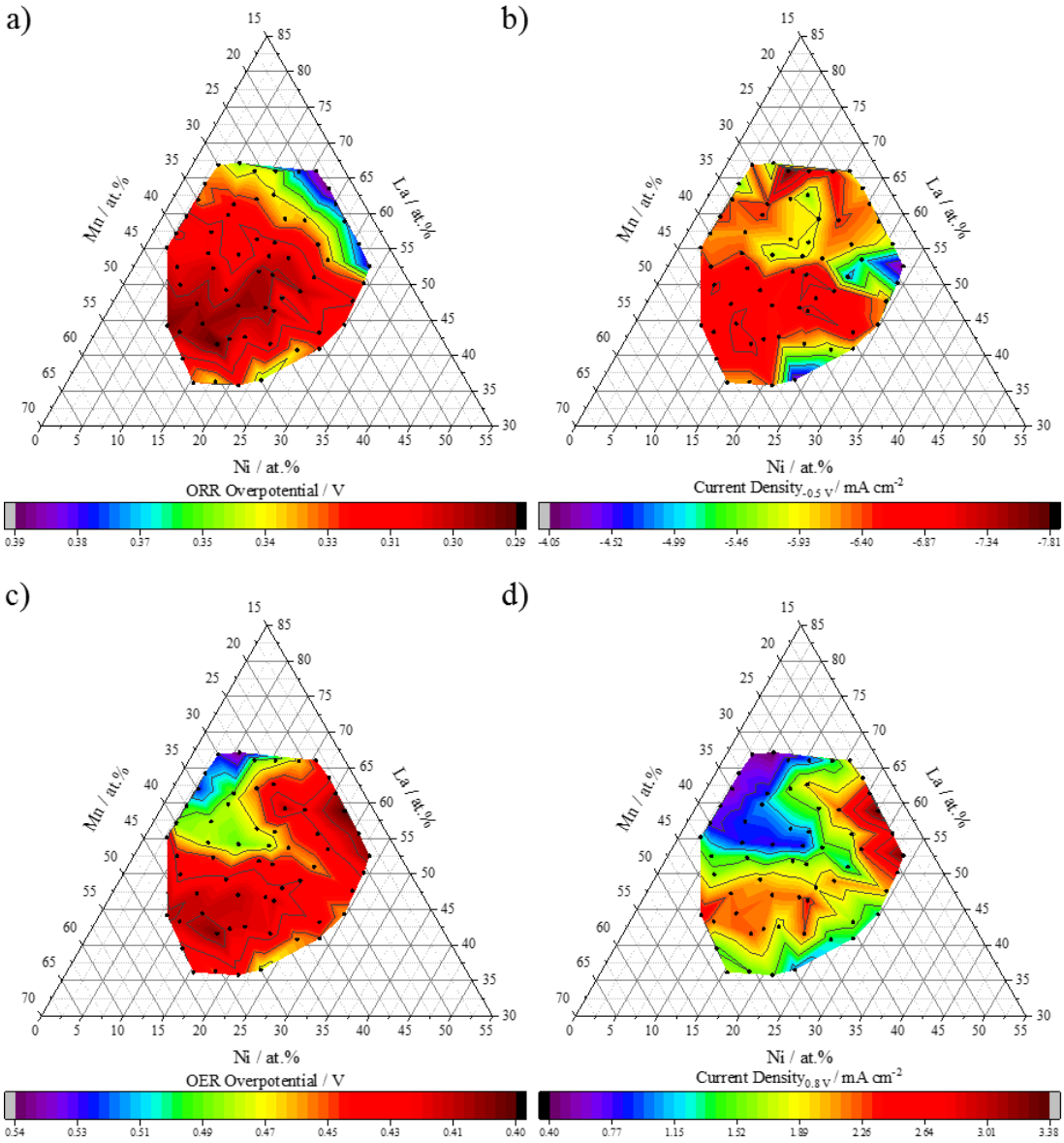

Figure 5.11: Ternary data for catalytic markers for: a) the overpotential for the oxygen reduction reaction (ORR) measured at −0.2 mA cm^{-2}, b) the current density at −0.5 V vs Ag/AgCl, c) the overpotential for the oxygen evolution reaction (OER) measured at 0.4 mA cm^{-2} and d) the current density at 0.8 V vs Ag/AgCl. All measurements were carried out in O_2 saturated 0.1 M KOH with a scan speed of 10 mV s^{-1}. All data points were extracted from LSV data taken at 2500 rpm. The experimental error is ± 2 %.

The current density at −0.5 V vs Ag/AgCl (2500 rpm) was recorded as another indicator of catalytic activity [Figure 5.11 b)]. In general, those catalysts which had low overpotentials had higher limiting current densities. The current densities reported here are similar to the observed current density for Pt/carbon carried out under identical experimental conditions, suggesting that these catalysts could compete with traditional Pt catalysts in terms of current generated. For example, the best performing catalyst $La_{0.83}Mn_{0.85}Ni_{0.32}O_3$ had a current density of −7.03 mA cm^{-2} at −0.5 V vs Ag/AgCl which was the same as the Pt/carbon sample (−6.97 mA cm^{-2}) carried out under identical conditions in Chapter 4 (Figure 4.5). Comparing to literature, the current densities reported here are greater than previously observed in similar materials. Celorrio *et al*. reported current densities of approximately −6 mA cm^{-2} for $LaMnO_3$ and $La_xTe_{1-x}MnO_3$ materials[258] and Zhang *et al*. reported current densities of approximately −4 mA cm^{-2} for $LaNi_{0.8}Fe_{0.2}O_3$.[122]

Figure 5.11 c) shows the compositional dependence for the OER overpotential (taken at 0.4 mA cm^{-2}). The best sample was $La_{1.18}Mn_{0.37}Ni_{0.45}O_3$ with an overpotential of 0.395 V. The OER activity was shown to be greatest in nickel-rich compositions. Samples which contained both high amounts of manganese and lanthanum were shown to be much poorer catalysts. Reading along the *x*-axis (constant Ni concentration), the addition of La has a more negative effect on the overpotential of the OER than the addition of Mn. The $La(OH)_3$ species formed in materials with La excesses has little or no activity for the ORR meaning these materials are in effect "dead weight" and the percentage of the material which could catalyse the OER was reduced. La in the *A* site also only has minor contributions to the catalytic reaction (structural effects on the *B* site). As such, the *B* site species mainly controls the catalytic process.[306] Again, this suggested that the removal of *B* site elements (Mn) for *A* site elements (La) meant the removal of an active species for an inactive one. However, overpotentials for the OER were generally negatively shifted by 100 mV compared to the ORR and all catalysts performed worse for the OER than the ORR. This may be because only Mn rich samples were investigated. The space studied did not exceed 50 % Ni and $LaNiO_3$ is known to be a better OER catalyst than $LaMnO_3$.[293]

The current density at 0.8 V vs Ag/AgCl (2500 rpm) was recorded as another catalytic activity marker for the OER [Figure 5.11 d)]. The difference between highly active and poorly active catalysts was much starker in this comparison than in the overpotential

differences. High activity was seen almost exclusively in the region of Ni-rich samples, with poorest activity being recorded in a region of *A* site excess, Mn-rich materials. There was, in general, a good correlation between those catalysts with the worst overpotentials having the poorest current densities and vice versa. Due to the dissolution of glassy carbon at high potentials in aqueous base, this marker of activity was possibly limited due to the low potential cut off in the test.[307]

The compositional dependence of the ORR and OER overpotentials along the pseudo binary (Mn + Ni = 1) line showed an anti-correlation in the activities of the catalysts. Overpotentials for the ORR were lower when the composition was manganese rich, whereas overpotentials for the OER were lower when the composition was nickel rich. This was also shown by the binary perovskites as $LaMnO_3$ had an overpotential 119 mV lower than $LaNiO_3$ for the ORR whereas $LaNiO_3$ had an overpotential 61 mV lower than $LaMnO_3$ for the OER.

Figure 5.12 shows the combined overpotentials for the ORR and the OER over the compositional space explored. It shows that there was a region of compositional space where the anticorrelation between OER and ORR overpotentials did not hold. Catalysts with high OER and ORR activities were found below the binary line, with less than 50% nickel contribution to the *B* site and were *A* site deficient examples of the series $La_xMn_yNi_zO_3$. The most active reversible catalyst was found to be $La_{0.83}Mn_{0.85}Ni_{0.32}O_3$ with a combined overpotential of 0.69 V. This overpotential for the ORR was even lower than that of $LaMnO_3$, which is a very good transition metal oxide oxygen electrocatalyst.[308]

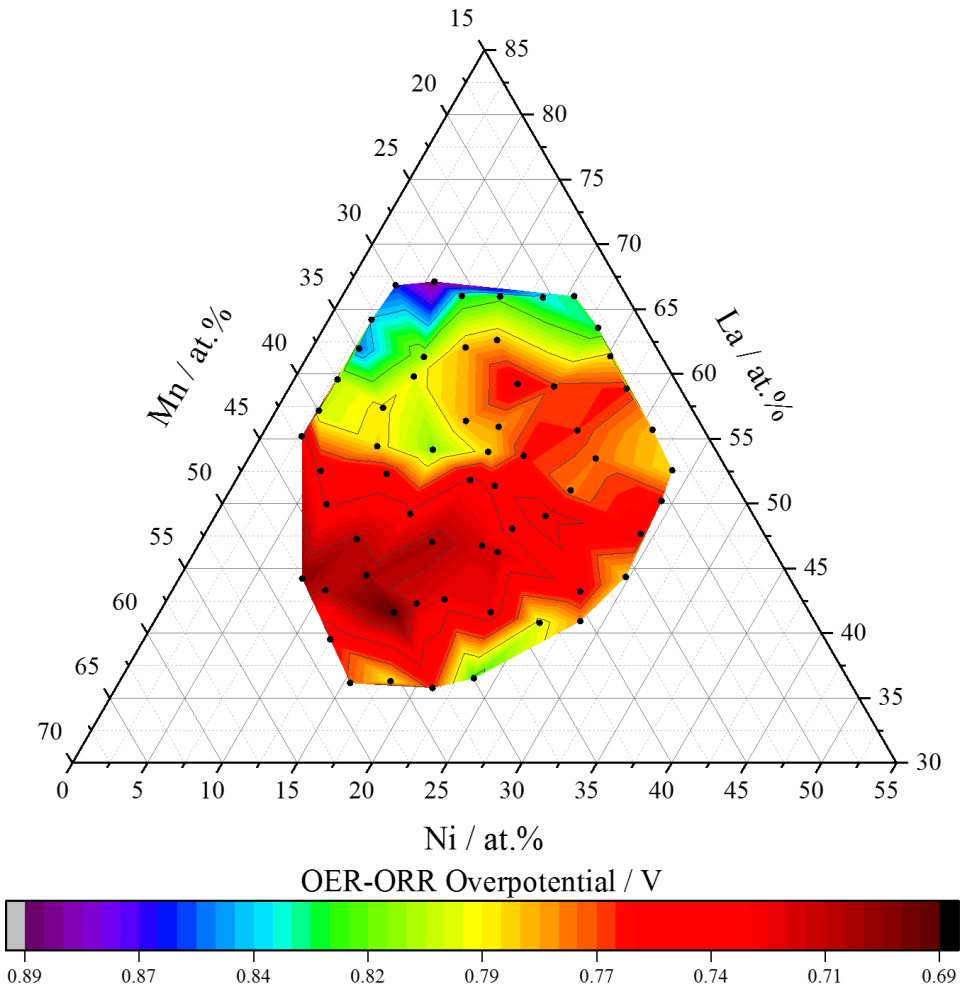

Figure 5.12: The compositional dependence of the reversibility of the ORR/OER on the $La_xMn_yNi_zO_3$ electrocatalysts produced via CHFS reported as the difference between the ORR and OER overpotentials. All measurements were carried out in O_2 saturated 0.1 M KOH with a scan speed of 10 mV s^{-1}. The experimental error is ± 2 %.

The rotation speed dependence of the voltammograms was investigated. With all catalysts, well defined reduction curves were observed at all rotation rates, and the limiting current densities were proportional to the square root of the rotation rates. Koutecky-Levich (K-L) plots were drawn and the limiting current densities observed for all catalysts were found to be mass transport limited as the K-L plots were linear over the whole rotation region studied (see Figure 5.13 b). The limiting current densities at −0.5 V vs Ag/AgCl were examined using the K-L equation:

$$\frac{1}{j_L} = \frac{1}{nFkc_{O_2}} + \frac{1}{0.62nFD^{2/3}\nu^{-1/6}c_{O_2}\omega^{1/2}} \qquad 5.1$$

Where n is the number of electrons, *F* is the Faraday constant, c_{O2} the concentration of dissolved oxygen in the electrolyte, *D* the diffusion coefficient of O_2, *v* the kinematic viscosity of the electrolyte and ω the rotation rate of the disk. *k* is the rate constant for the chemical step involved in the reduction mechanism.

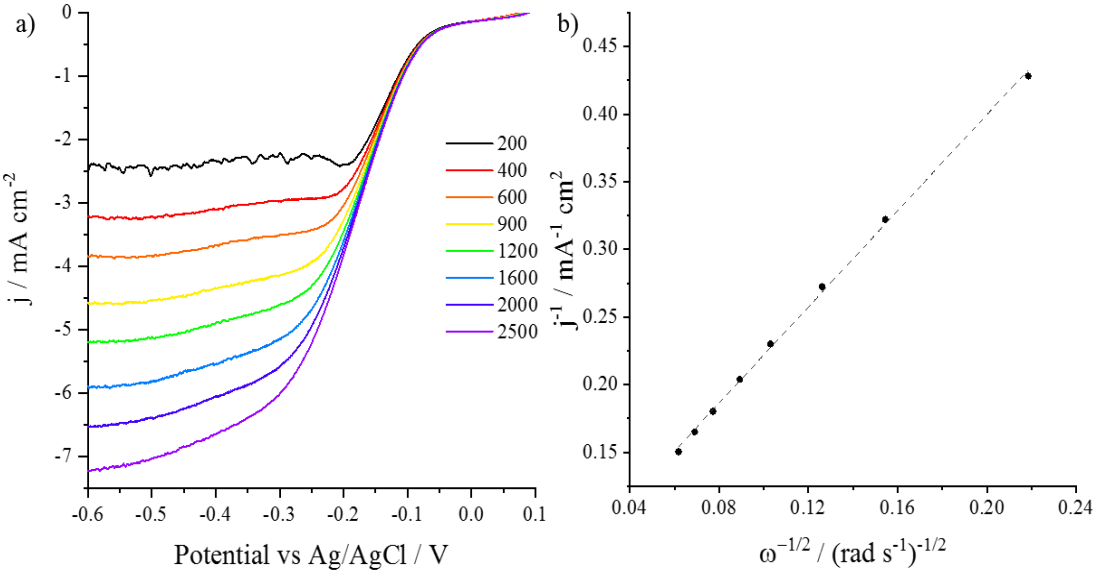

Figure 5.13: a) Example of the typical voltammogram response to the LSV test for $La_{0.83}Mn_{0.85}Ni_{0.32}O_3$ carried out between 0.1 and −0.6 V vs Ag/AgCl, b) Koutecky-Levich plot for the same composition at −0.5 V vs Ag/AgCl showing a linear relationship between rotation speed and current density. All measurements were carried out in O_2 saturated 0.1 M KOH with a scan speed of 10 mV s^{-1}. The experimental error is ± 2 %.

All samples showed a linear relationship between the reciprocal of the current density at −0.5 V and the square root of the rotation speed with all r^2 values > 0.995. Under the same conditions (ink formulation, cell, electrolyte and electrode) as the catalysts above, Pt black had a K-L gradient of 1.72 mA^{-1} cm^2 (rad s^{-1}) $^{-1/2}$ and a y-intercept of 0.0106 mA^{-1} cm^2 (as shown in Chapter 4). The best performing catalysts had slopes similar to that for Pt black [Figure 5.14 a)] suggesting a 4 e^- electron transfer mechanism and complete reduction of O_2 to OH^-. For example, $La_{0.83}Mn_{0.85}Ni_{0.32}O_3$ had a K-L slope of 1.78 mA $^{-1}$ cm^2 (rad s^{-1}) $^{-1/2}$ which was comparable to the calculated slope for Pt/C. The poorer performing catalysts had slopes which were greater than Pt which suggested the reduction mechanism occurred partially via a $2e^-$ process involving the evolution of peroxide as well as OH^-.

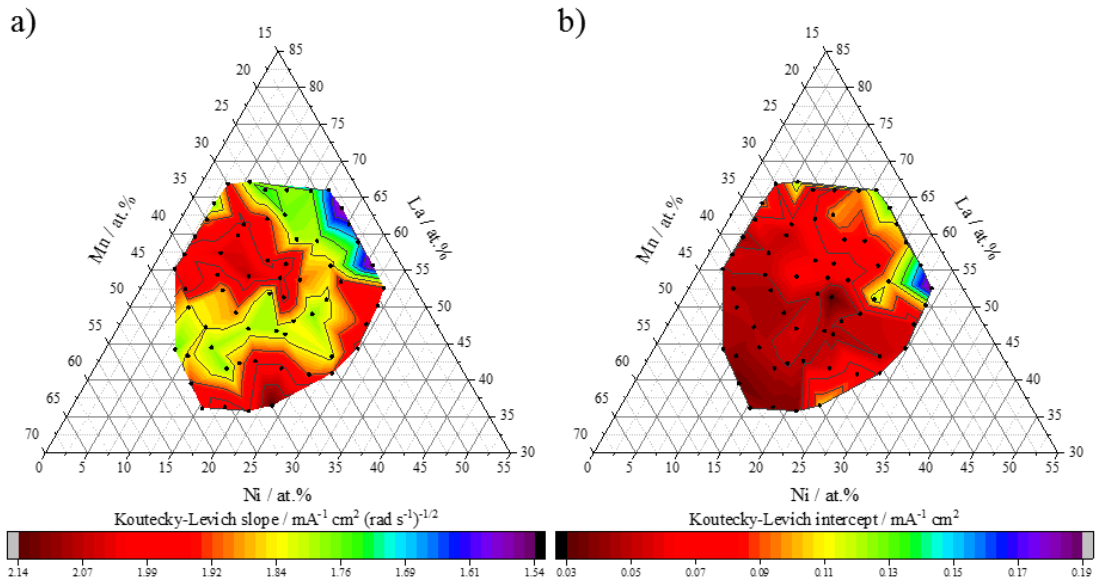

Figure 5.14: a) The compositional dependence of the Koutecky-Levich slope, b) the compositional dependence of the Koutecky-Levich *y*-intercept. Koutecky-Levich plots for all materials were taken at −0.5 V vs Ag/AgCl and were carried out in O_2 saturated 0.1 M KOH with a scan speed of 10 mV s^{-1}. The experimental error is ± 2 %.

As the K-L *y*-intercept is the reciprocal of the kinetic current density, those catalysts with a lower *y*-intercept have a higher kinetic current density and vice-versa. The kinetic current density is the current density in the absence of mass transport restrictions. The *y*-intercepts from the K-L graphs at −5 V are shown in Figure 5.14 b). Kinetic current densities were between 35 and 5 mA cm^{-2}. Catalysts below the pseudo binary line in areas of low Ni had lower *y*-intercepts and therefore higher kinetic current densities than those with greater Ni content. The catalysts with the highest kinetic current densities had higher values than similar materials reported in the literature. For example, Ashok *et al.* reported a kinetic current density of 9.2 mA cm^{-2} for $LaNiO_3$ and 16.1 mA cm^{-2} for $LaMnO_3$.[285] The catalyst with the lowest bifunctional overpotential, $La_{0.83}Mn_{0.85}Ni_{0.32}O_3$ had a y-intercept of 0.0443 mA^{-1} cm^2 giving a kinetic current density of 22.6 mA cm^{-2} and $La_{1.03}Mn_{0.62}Ni_{0.35}O_3$ had a *y*-intercept of 0.0283 mA^{-1} cm^2 giving a kinetic current density of 35.3 mA cm^{-2}. However, these are still much lower than the calculated kinetic current density for Pt/C made to the same ink recipe which was found to be 200 mA cm^{-2}.

5.4.2.2. In-Depth Electrochemical Characterisation of $La_xMn_yNi_zO_3$ Materials

To examine more complex electrochemistry across the whole grid, seven samples were chosen for more in-depth electrochemical analysis of the ORR.

These were chosen to cover the maximum amount of ternary space, and a range of activities. These samples can be seen in Table 5.1 alongside their electrochemical activity markers and can be seen graphically in the ternary phase diagram Figure 5.15. As activity towards the OER was low within safe operating limits of the glassy carbon electrode used, it was not studied any further than the initial screening.

Table 5.1: Selection of materials from across the compositional space chosen for further catalytic examination and their catalytic performance towards the ORR, OER and as bifunctional catalysts.

Sample	ORR overpotential (V)	OER overpotential (V)	Combined overpotential (V)
$La_{1.10}Mn_{0.84}Ni_{0.06}O_3$	0.31	0.42	0.73
$La_{0.82}Mn_{0.86}Ni_{0.32}O_3$	0.29	0.40	0.69
$La_{1.34}Mn_{0.60}Ni_{0.06}O_3$	0.34	0.53	0.86
$La_{1.08}Mn_{0.60}Ni_{0.32}O_3$	0.30	0.48	0.78
$La_{0.82}Mn_{0.62}Ni_{0.56}O_3$	0.32	0.45	0.78
$La_{1.32}Mn_{0.38}Ni_{0.30}O_3$	0.39	0.44	0.83
$La_{1.06}Mn_{0.38}Ni_{0.56}O_3$	0.38	0.41	0.79

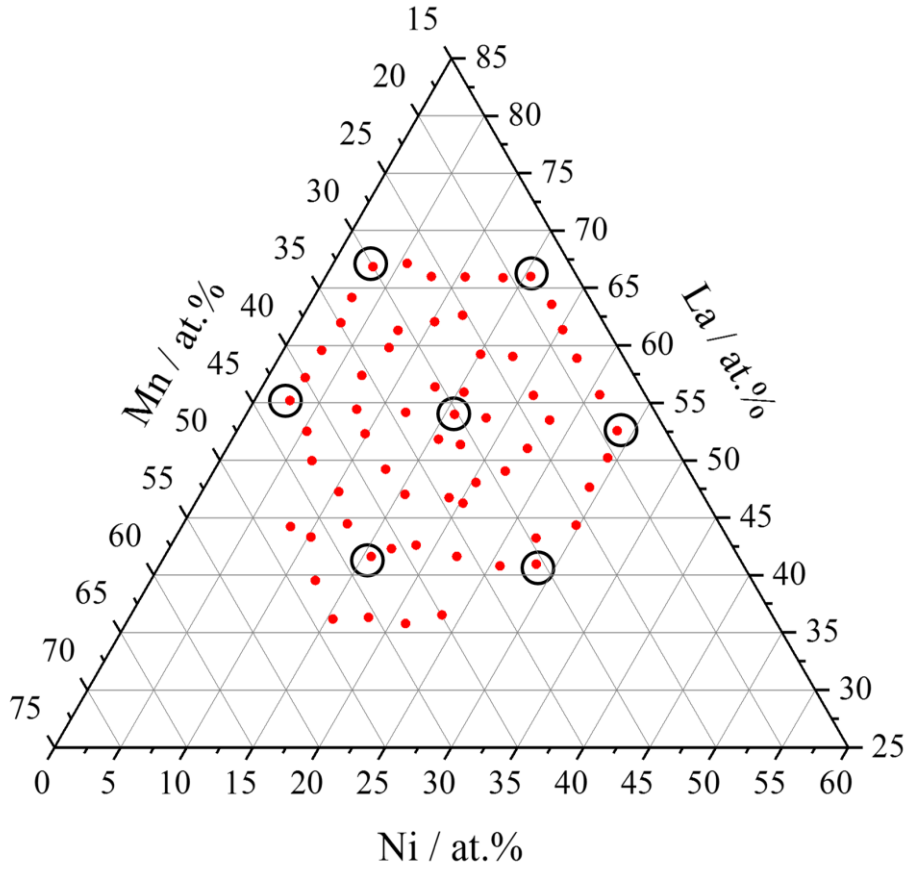

Figure 5.15: Ternary plot showing the phase space examined in this chapter. The samples circled were chosen for extensive electrochemical analysis in order to cover most of the compositional space examined.

Cyclic Voltammetry (CV) experiments were carried out in the absence of oxygen at 5 mV s^{-1} to examine the redox behaviour of the materials and identify the main redox peaks. Figure 5.16 shows the cyclic voltammograms in the absence of O_2.

The CVs in Figure 5.16 showed complex redox behaviour related to the redox properties of surface Mn and Ni sites. All materials showed pseudo-capacitive behaviour, as demonstrated by the box like nature of the CVs. Three of the redox couples observed could be assigned to the Mn^{3+}/Mn^{4+} couple centred at 1.0 V_{RHE}, the Ni^{2+}/Ni^{3+} couple centred at 0.49 V vs Ag/AgCl (1.45 V_{RHE}) and the Ni^{0}/Ni^{2+} couple centred at −0.56 V vs Al/AgCl (0.4 V_{RHE}). The highly irreversible anodic peak feature at the most positive potentials studied could be assigned to the beginning of the oxygen evolution reaction.

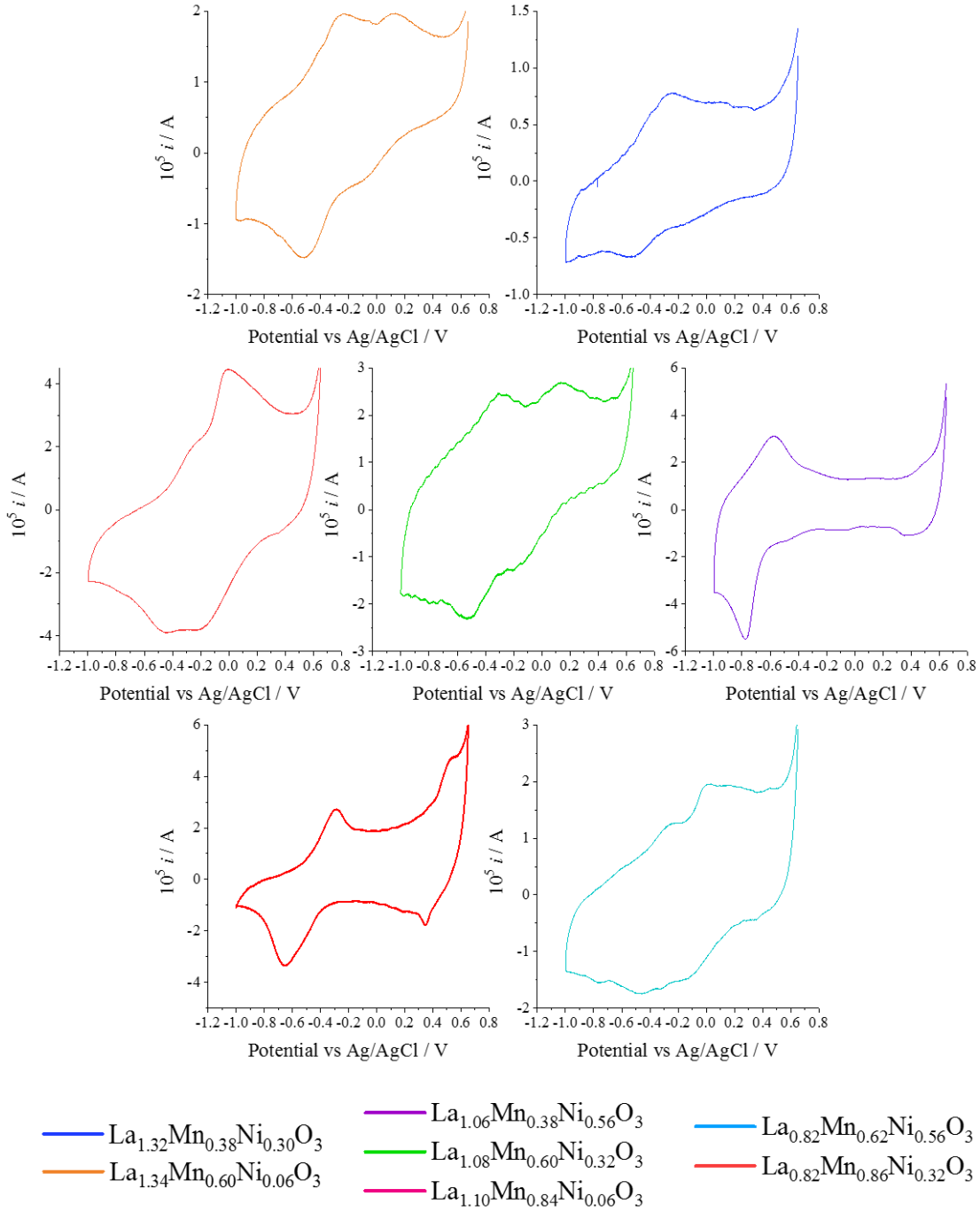

Figure 5.16: N_2 CVs for the 7 samples covering the whole grid. All measurements were carried out in N_2 saturated 0.1 M KOH between +0.8 and −1.0 V vs Ag/AgCl with a scan speed of 5 mV s^{-1}. The experimental error was ± 2%.

Bradley *et al.* observed that the Mn^{3+}/Mn^{4+} redox couple played an important role in catalysing the OER and ORR reactions simultaneously in this region of *A* site substoichiometry.[293] The relationship was examined by integrating the anodic Mn^{3+}/Mn^{4+} in the region between −0.25 V and 0.15 V vs Ag/AgCl. The area decreased

in the order of $La_{0.82}Mn_{0.86}Ni_{0.32}O_3$ > $La_{1.10}Mn_{0.84}Ni_{0.06}O_3$ > $La_{0.82}Mn_{0.62}Ni_{0.56}O_3$ > $La_{1.06}Mn_{0.38}Ni_{0.56}O_3$ > $La_{1.08}Mn_{0.60}Ni_{0.32}O_3$ > $La_{1.32}Mn_{0.38}Ni_{0.36}O_3$ > $La_{1.34}Mn_{0.60}Ni_{0.06}O_3$. This directly correlated to the order of bifunctional activities of the materials, as measured by the reversible overpotentials. It was suggested that the appearance of this redox peak was due to the slight substitution of Ni^{2+} into the *A* site of the perovskite, creating both Mn^{3+} and Mn^{4+} species in the bulk. The appearance of the Mn^{3+}/Mn^{4+} redox couple corresponding to bifunctional activity was consistent with previous observations.[225,309] This suggested that OH was absorbed at the Mn^{3+} site (active site for the ORR in alkaline electrolyte) and that oxygen was absorbed at the Mn^{4+} site giving the catalyst its OER activity.[251,310] It was therefore indicated, that it was the proximity of the Mn^{3+}/Mn^{4+} redox couple to the reversible oxygen potential, alongside the reversible surface redox chemistry which determined the reversibility of the OER/ORR at the bifunctional site.

RRDE experiments can be used to examine the reaction pathway occurring during the ORR. Figure 5.17 shows the disk current and the corresponding ring current as each electrode was swept between 0.2 and −0.8 V vs Ag/AgCl with the ring held at a potential sufficient to fully oxidise peroxide (0.35 V vs Ag/AgCl).

The trend in the OH_2^- yield in the RRDE results shown in Figure 5.17 were $La_{1.32}Mn_{0.38}Ni_{0.36}O_3$ > $La_{1.34}Mn_{0.60}Ni_{0.06}O_3$ > $La_{1.06}Mn_{0.38}Ni_{0.56}O_3$ > $La_{0.82}Mn_{0.62}Ni_{0.56}O_3$ > $La_{0.82}Mn_{0.86}Ni_{0.32}O_3$ > $La_{1.08}Mn_{0.60}Ni_{0.32}O_3$ > $La_{1.10}Mn_{0.84}Ni_{0.06}O_3$. The effective number of electrons transferred ranged from 3.74 for $La_{1.32}Mn_{0.38}Ni_{0.36}O_3$ to 4 for $La_{1.08}Mn_{0.60}Ni_{0.32}O_3$ and $La_{1.10}Mn_{0.84}Ni_{0.06}O_3$ at −0.5 V vs Ag/AgCl. This suggested that for all catalysts the dominant electron transfer pathway was the 4 e^- pathway. Those catalysts containing large *B* site deficiencies had the lowest e^- transfer numbers and the highest peroxide yield. This may have been due to a competing pathway at the $La(OH)_3$ impurity phase or due to poor catalyst support interaction leading to a competing 2 e^- reaction at the carbon black support.[252] Across the pseudo binary line, catalysts containing greater at% Ni generated higher yields of peroxide which was consistent with RRDE results seen for $LaMnO_3$ vs $LaNiO_3$. This was again consistent with Sunarso *et al.* as they carried out an additional study which showed that the removal of 50% Ni for another element at the *B* site dramatically reduced the yield of peroxide seen.[304]

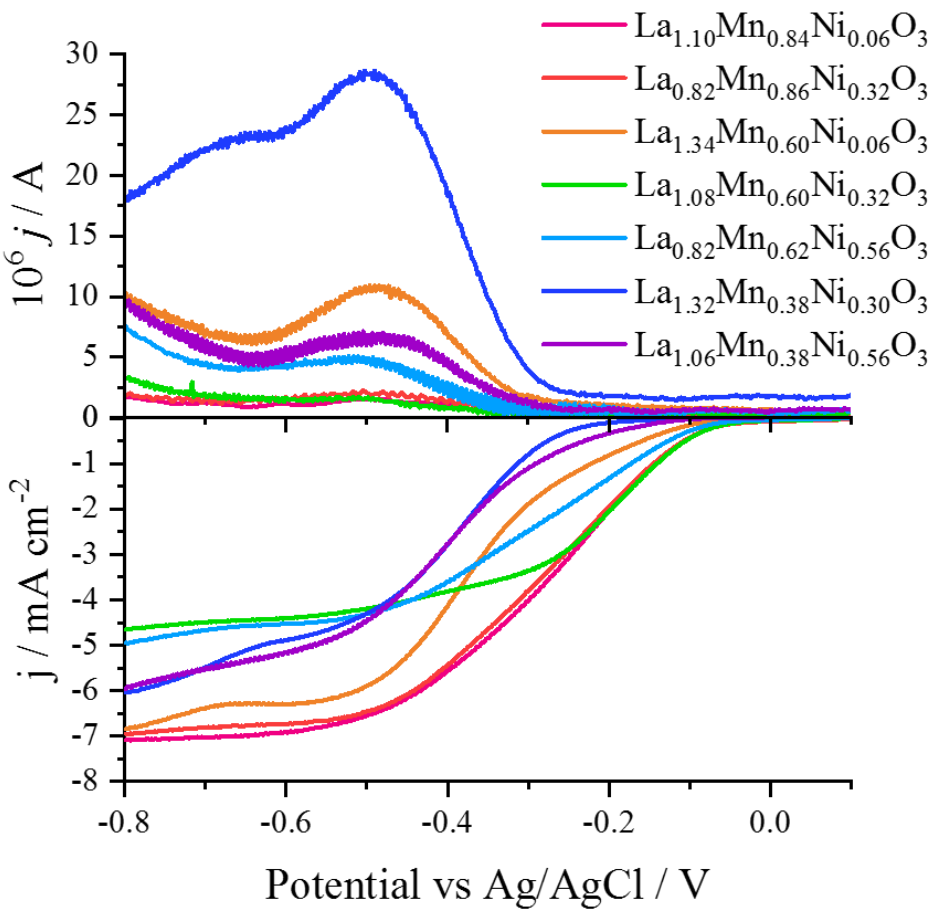

Figure 5.17: Rotating ring disk data for the 7 catalysts over the composition diagram. The bottom response is the disk current response as the disk is swept from 0.2 to −0.8 V vs Ag/AgCl. The top response is the ring response as the disk is swept from 0.2 to −0.8 V vs Ag/AgCl and the ring potential is held at 0.35 V vs Ag/AgCl. All measurements were carried out in O_2 saturated 0.1 M KOH with a scan rate of 10 mV s^{-1}. The experimental error is ± 2%.

Alkaline toxicity and catalytic activity loss over time are two of the main issues which cathodic catalysts face in alkaline media. Stability can also be affected by the deposition of intermediates on the catalyst surface under reducing conditions (e.g. peroxide). Chronoamperometry was used to measure the catalyst stability at −0.5 V vs Ag/AgCl for each catalyst. Each electrode was rotated in oxygenated electrolyte at 900 rpm over 4 hours and the degradation measured as a function of current. The results are shown in Figure 5.18.

The most stable catalyst was $La_{0.82}Mn_{0.86}Ni_{0.32}O_4$ with a loss of 3.5 % over 4 h. The least stable catalyst was $La_{1.32}Mn_{0.38}Ni_{0.30}O_3$ with a loss of 15 % activity over the testing period. This catalyst also generated the most peroxide as seen in Figure 5.18. It

is known that the generation of peroxide at the catalyst surface can destabilise the catalyst.[311] In general, catalysts containing less La were more stable than those with a La excess with the two most stable catalysts having a La and therefore *A* site deficiency (La < (Mn + Ni) therefore *A* < *B*). Along the binary line (*A* = *B*), there was no significant deviation in stability between $La_{1.10}Mn_{0.84}Ni_{0.06}O_3$ and $La_{1.08}Mn_{0.60}Ni_{0.32}O_3$, with both loosing approximately 7% activity over 4 h. However, once $La_{1.06}Mn_{0.38}Ni_{0.56}O_3$ was reached the stability decreased to 8.5% loss in activity. This suggested that the removal of Mn caused a decrease in stability. This was seen in all cases where La concentration remained constant and Mn was replaced by Ni. Only $La_{0.82}Mn_{0.86}Ni_{0.32}O_4$ was more stable than the commercial Pt black catalyst shown in Figure 4.11, which lost 5% activity over the same testing window.

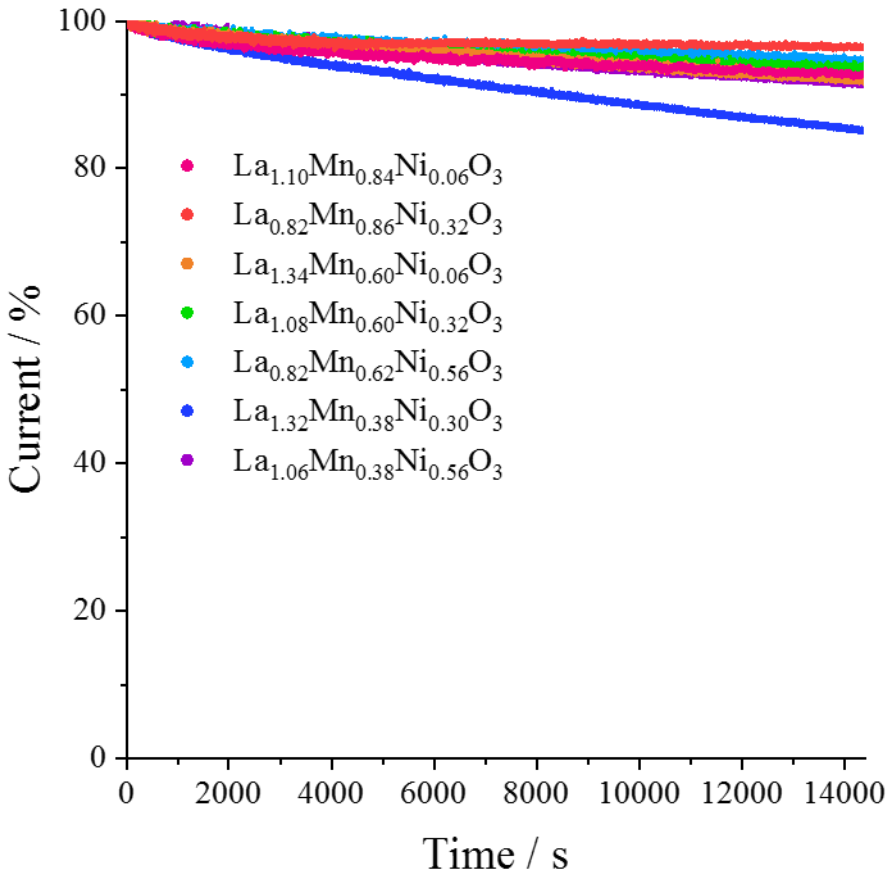

Figure 5.18: Stability data for the 7 catalysts. The data is shown as a percentage of the initial current. All measurements were carried out over 4 hours in O_2 saturated 0.1 M KOH with a scan speed of 10 mV s^{-1}, a potential of −0.5 V and a rotation speed of 900 rpm. The experimental error is ± 2%.

5.5. Summary and Conclusions

In conclusion, a ternary system consisting of 63 $La_xNi_yMn_zO_3$ materials were successfully synthesised via CHFS followed by a flash heat treatment at 850 °C. X-ray diffraction was used to show that in all materials, the majority phase observed was the cubic perovskite phase, although impurities above and below the pseudo binary line were seen corresponding to $La(OH)_3$ and $NiMn_2O_4$ phases respectively. There was a continuous distortion observed across the pseudo binary line of the cubic $LaMnO_3$ lattice as Ni was added. The XPS results confirmed the presence of La, in the +3 oxidation state, mixed Mn valence and the presence of Ni. There was also the suggestion of mixed oxygen valence at the surface of the materials.

High-throughput electrochemical analysis was carried out on all samples to examine them as ORR and OER catalysts. High areas of ORR activity were seen in La deficient, Mn rich samples with the best performing sample, $La_{0.83}Mn_{0.85}Ni_{0.32}O_3$, having an overpotential of 0.287 V with respect to the reversible oxygen potential of 1.23 V. In contrast to this, high OER activity was seen in Ni rich samples with the best performing sample $La_{1.18}Mn_{0.37}Ni_{0.45}O_3$ having an overpotential of 0.395 V. The ORR activity was particularly high with a shift of only 0.07 V in the overpotential compared to the commercial Pt black sample tested in Chapter 4. In general, there was an anticorrelation observed in activities between the ORR and OER. However, a region was identified with La (*A* site) deficiency where relatively high ORR and OER activity was observed. The best bifunctional catalyst was found by the addition of the overpotentials for the ORR/OER and was identified as $La_{0.83}Mn_{0.85}Ni_{0.32}O_3$ with a combined overpotential of 0.69 V. This catalyst was in the same region as the catalysts shown by Bradley *et al.*[293] in thin film measurements highlighting the promise of CHFS as a tool for scaling up synthetic procedures to industrially relevant scales.

Further electrochemical analysis was carried out on seven catalysts. The degassed CVs showed that the catalysts which showed greatest bifunctional activity had a larger redox peak corresponding to the Mn^{3+}/Mn^{4+} redox couple as observed previously.[225,309] RRDE tests were carried out to examine the electron transfer number, and it was seen that samples below or on the pseudo binary line had higher electron transfer numbers (indicated by lower levels of peroxide). An La excess seemed to have a detrimental effect, with large amounts of peroxide detected from samples with *A* site excess. Stability testing suggested that the presence of high at % La caused instability in the

catalysts over 4 h, with $La_{1.32}Mn_{0.38}Ni_{0.36}O_3$ losing 25.03 % current density compared to $La_{1.10}Mn_{0.84}Ni_{0.06}O_3$ with a loss of 3.33 %. Overall, $La_{0.83}Mn_{0.85}Ni_{0.32}O_3$ was found to be an excellent candidate material for a bifunctionally active oxygen electrocatalyst with a low combined overpotential, a RRDE derived electron transfer number of 4 and excellent stability, comparable to Pt black.

Future work may consider further optimisation of the composition as the space studied in this chapter was still wide. Narrowing down the compositional space may allow for a better catalyst, with an even greater bifunctional activity to be found. Making the best performing catalyst at a larger scale (i.e. on a CHFS pilot plant reactor) would also be an important step to demonstrate the scalability of the process as well as the effect of scale on catalytic activity.

In the next chapter, the $NiMn_2O_4$ impurity phase will be synthesised as this was seen in all materials with high bifunctional activity.

6. $NiMn_2O_4$ Spinel Materials as Highly Active Bifunctional Oxygen Electrocatalysts

6.1. Abstract

In the previous chapter (Chapter 5), a $NiMn_2O_4$ spinel impurity phase was seen when the co-precipitated material was made with a lanthanum deficiency and heat treated to 850 °C generating an *A* site deficient perovskite. As those samples below the La(Mn + Ni = 1)O_3 tie line were the most active samples, it was thought that the $NiMn_2O_4$ material may be an active bifunctional oxygen electrocatalyst. Hence, it was decided to investigate similar spinel materials in a systematic way. Herein, a series of 28 spinel materials based on $Ni_xMn_yFe_zO_4$ (where $x + y + z = 3$) were synthesised. The materials were characterised by a range of analytical methods including PXRD, BET and XPS measurements and the materials then screened for catalytic activity towards the ORR/OER. A selection of these materials were then examined in greater depth using RRDE and chronoamperometry techniques to understand the trends in their catalytic properties across the phase diagram.

6.2. Introduction

Spinel oxides are inexpensive, easily synthesised, thermodynamically stable, environmentally friendly and have activity that is generally considered on par with perovskite oxides for the ORR/OER.[312] They have the general formula AB_2O_4 where *A* and *B* are usually metal ions. Metal *A* usually occupies the centres of tetrahedrally coordinated species whereas *B* occupies the centres of octahedrally coordinated positions. The oxygen anion sits at the polyhedral vertices.[128] Tetrahedral interstices are usually smaller than the octahedral therefore the smaller cation tends to occupy the *A* sites. Spinels can have the same cation on the two different sites, and so the *A* and *B* cations distribute in the tetrahedral and octahedral sites in different ratios. Depending on this distribution, spinels are classified as normal, inverse or complex.[128] The multi-valent nature of spinel oxides provides donor-acceptor sites for O_2 adsorption/desorption giving them desirable electrocatalytic activity towards the ORR/OER.[313,314]

Manganese spinels are well known in the literature and have been studied extensively as ORR catalysts.[315–317] Mn can be found at either site in the spinel, with Mn^{2+} preferring the tetrahedral sites and Mn^{3+} the octahedral sites. Liu *et al.* synthesised Mn_3O_4 with differing morphologies and examined the effect on the ORR.[318] The

materials were intentionally synthesised on the 100 nanometre or micrometre scale to negate the effects of surface defects/oxygen vacancies. They discovered a strong link between morphology and ORR activity, with Mn_3O_4 nanoflakes outperforming nanorods and nanoparticles. DFT calculation suggested this was because of the preferentially exposed (001) planes. This conclusion was also drawn by Duan *et al.* who synthesised differing shapes of Mn_3O_4 on N-doped graphene.[319] The ellipsoid Mn_3O_4 showed higher ORR activity and it was concluded that this was likely due to the exposed (001) planes.

One of the most studied Mn containing spinel materials is $CoMn_2O_4$.[320–322] Cheng *et al.* reported a room-temperature synthesis of various spinels from the reduction of MnO_2 in aqueous M^{2+} solution.[132] The prepared $Co_xMn_{3-x}O_4$ nanoparticles had exceptional ORR/OER activity with low overpotentials and high current densities achieved. The cubic spinel outperformed the tetragonal spinel. Wei *et al.* described a study where a series of $MnCo_2O_4$ spinels was synthesised.[129] They identified Mn in octahedral sites as the active site and discovered that the ORR activity could be plotted as a volcano against the nominal Mn valence with the summit at an Mn valence of approximately 3. Therefore, if Mn valence can be tuned using different cations, ORR activity should be designable for the material.

Iron containing spinels have also received much attention as oxygen electrocatalysts.[323–325] Iron is earth abundant and therefore an inexpensive element for inclusion in a catalyst.[326] Xu *et al.* described the synthesis of hollow nanospheres of $CoFe_2O_4$ for the ORR, which outperformed not only solid nanospheres of $CoFe_2O_4$ but also a commercial Pt/C sample.[327] This was attributed to improved oxygen transportation because of the hierarchical porous structure. The work was then taken forward and Ni-doping was introduced into the $CoFe_2O_4$ nanospheres.[328] $Ni_{0.5}Co_{0.5}Fe_2O_4$ had the highest ORR activity with low overpotential and highest limiting current density, however $Ni_{0.75}Co_{0.25}Fe_2O_4$ had the lowest overpotential and highest current density seen for the OER, suggesting that bifunctional activity can be tuned by using various cation ratios.

Whilst Co is a popular choice in spinel compounds for electrocatalysis, its low earth abundance coupled with the environmental hazard it presents makes it an expensive choice for an industrially relevant catalyst.[329] Fe_3O_4 has been extensively studied as an

oxygen electrocatalyst and as with several other spinels, the majority of the literature focusses on synergistic coupling with carbon containing materials.[323,325,330] $NiFe_2O_4$ has been seen to exhibit enhanced catalytic activity due to the presence of multivalent Ni and Fe.[128] $NiFe_2O_4$ is also inexpensive compared to the Co alternative and more environmentally benign.[331]

$NiMn_2O_4$ is an inverse spinel, with Ni^{2+}, Mn^{3+} and Mn^{4+} occupying the octahedral sites and Ni^{2+} and Mn^{2+} occupying the tetrahedral sites. The degree of inversion of the spinel decreases with increasing temperature.[332] It has cubic symmetry, in contrast to a normal spinel which exhibits tetragonal symmetry. Introducing Fe into $NiMn_2O_4$ stabilises the cubic phase as the Fe preferentially enters the tetrahedral sites, stabilising the formation of the partially-inverse/inverse spinel.[333]

Traditionally, the synthesis of spinel compounds has been through high temperature, solid state routes, giving particles of large sizes and small surface areas.[128] However, in the past 20 years the reporting of other low temperature synthetic routes has become much more prevalent. For example, Kutty *et al.* reported the low temperature synthesis of $MgAl_2O_4$ using oxalic acid as an organic template and nitric acid as an oxidising agent.[334] CHFS has been used to make several spinel compounds including $NiMoO_4$, Fe_2CoO_4 and $LiMn_2O_4$[261]. Hydrothermal methods are preferred due to the easily tuneable nature of the synthesis, giving more selectivity over cation ratios, particle size and particle morphology.[178] Herein, CHFS was used to synthesise a series of precursor powders that were heat treated yielding $Ni_xMn_yO_4$ and $Ni_xMn_yFe_zO_4$ materials for use as bifunctional oxygen electrocatalysts.

6.3. Materials and Methods

6.3.1. Synthesis of $NiMn_2O_4$ materials

The synthesis of the materials was carried out as described in Section 2.1.4.

6.3.2. Physical Characterisation of $NiMn_2O_4$ materials

The physical characterisation of the materials was carried out as described in Section 2.2. PXRD, XRF, XPS, BET and Raman spectroscopy were carried out on all samples with TEM, EDX and SEM carried out on selected samples.

6.3.3. Electrochemical Characterisation of $NiMn_2O_4$ materials

Inks from drop casting onto GC electrodes were prepared according to method 2 in Section 2.3.1.

All electrochemical testing was carried out in 0.1 M $KOH_{(aq)}$ using a Ag/AgCl reference (saturated KCl) and a platinum wire counter.

Electrochemical screening of the samples for the ORR was carried out by linear sweep voltammetry between 0.1 and −0.6 V (vs Ag/AgCl) at 10 mV s^{-1} at 8 different rotation speeds (200, 400, 600, 900, 1200, 1600, 2000 and 2500 rpm). Electrochemical screening of the samples for the OER was carried out by linear sweep voltammetry between 0 and 0.8 V (vs Ag/AgCl) at 10 mV s^{-1} and 2500 rpm.

In depth electrochemical analysis was carried out on a selection of samples from the grid. RRDE testing was carried out in line with LSV testing but the ink was drop cast onto a rotating ring disk electrode to give the same catalytic loading as in previous tests. The ring potential was set to 0.35 V vs Ag/AgCl to ensure complete peroxide decomposition.[335] Chronoamperometry was carried out by holding the potential at −0.5 V vs Ag/AgCl and measuring the current response over 4 h. Cyclic voltammetry in N_2 saturated electrolyte was carried out at 5 mV s^{-1} between −1 and 0.65 V vs Ag/AgCl.

6.4. Results and Discussion

6.4.1. Physical Characterisation of $NiMn_2O_4$ Materials

Due to low yields from a variety of base ratios and concentrations tried with KOH, NaOH was chosen as a more suitable base from similar literature preparations and gave a noticeable improvement on yield although this was still < 70%.[336] This may be due to NaOH being a slightly stronger base than KOH, meaning that a greater percentage of metal ions were precipitated out of solution.

After the CHFS step, cleaning by centrifugation and freeze-drying, the nanoparticulate metal oxides were collected with > 66% yield. Loses were mainly from the unoptimized synthesis, cleaning and freeze-drying steps. After freeze drying, all powders were dark brown in colour.

Materials were then flash heat treated at 850 °C for 30 min according to Chapter 2.1.4, yielding free flowing, lustrous black powders for all samples. This heat treatment was

chosen as in the previous chapter, impurities of spinel $NiMn_2O_4$ were seen at this temperature which was the target material in this chapter.

XRF was used to elucidate Ni:Mn:Fe ratios. Due to a precipitation issue discovered in earlier iterations of the synthesis, a large excess of Mn precursor was used in the CHFS step. This resulted in a 10 % Mn excess in binary materials ($Ni_xMn_yO_4$) and a 5 % Mn excess in ternary materials ($Ni_xMn_yFe_zO_4$). The latter materials also contained a 5 % Fe deficiency compared to the nominal compositions. This can be seen in Figure 6.1, below.

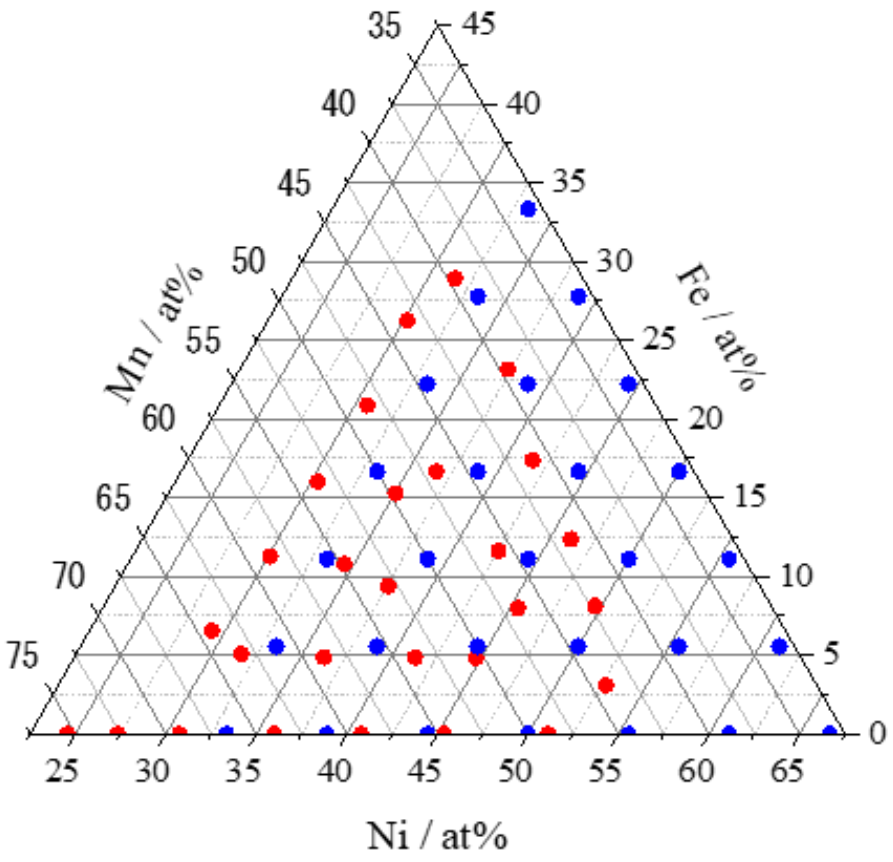

Figure 6.1: Nominal (blue) vs actual (red) elemental compositions of the ternary phase series $Ni_xMn_yFe_zO_4$ ($x + y + z = 3$).

To examine the structure of all samples, PXRD and Raman spectroscopy were carried out. The PXRD data showed the formation of crystalline structures shown by regular peaks at different angles arising from a set of reflections. Peaks were generally broad, suggesting that the crystallite domains in the materials were nanosized as was seen in

previous chapters. A selection of PXRD patterns from across the phase space studied can be seen below in Figure 6.2.

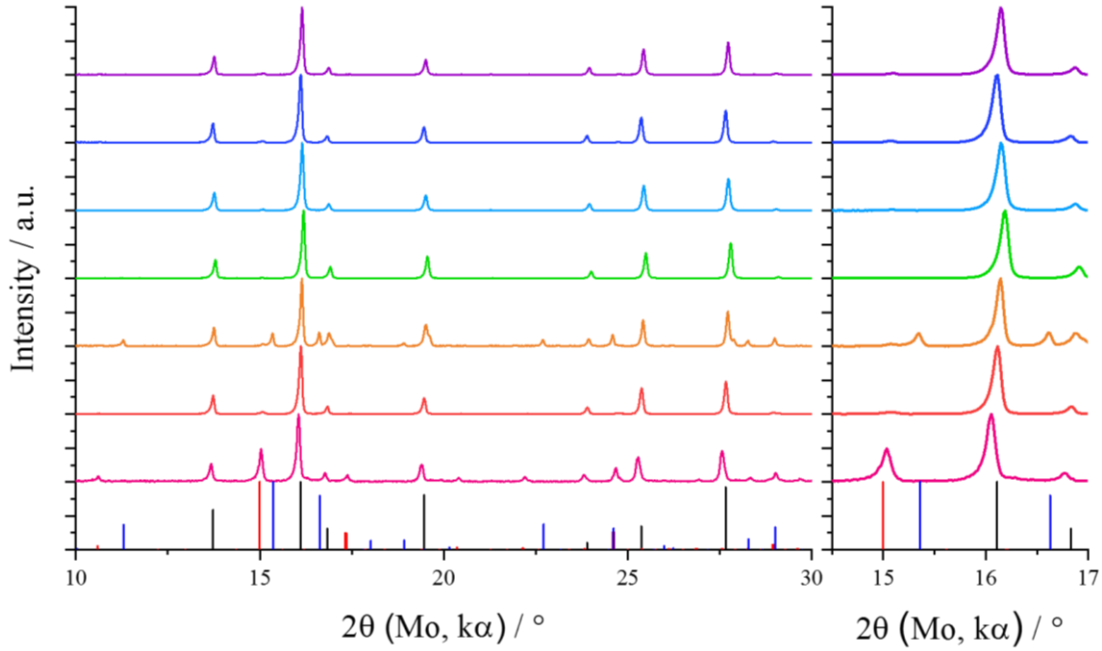

Figure 6.2: PXRD data of heat-treated materials from a selection of the phase diagram. The reference peaks are as follows: the black peak corresponds to cubic $NiMn_2O_4$ (ICSD collection code: 185249), the red peaks correspond to Mn_2O_3 (ICSD. collection code: 9090) and the blue peaks correspond to $NiMnO_3$ (ICSD collection code: 31853).

All patterns were a good match for cubic $NiMn_2O_4$ (ICSD coll. Code 185294). As more Ni was added along the Mn-Ni binary line there was a peak shift from 16.04° to 16.14° which can be seen in Figure 6.3. The shifting to larger diffraction angles in $Ni_xMn_yO_4$ materials has been previously accredited to a change in the degree of inversion in the spinel.[337] The rearrangement of Ni and Mn ions can lead to a change in the lattice parameter, as the degree of inversion increases the lattice constant decreases and this leads to a shifting of diffraction peaks to higher angles. There was a clear compositional dependence on the position of the (311) peak (Figure 5.3) and this was consistent with previous reports.[333] Two impurity phases were also indexed in the diffraction patterns. In the samples with high at% Mn, there was an orthorhombic alpha Mn_2O_3 (*P-b-c-a*) (ICSD collection code: 9090) impurity phase. In the high Ni at% samples there was a trigonal $NiMnO_3$ (ICSD collection code: 31853) impurity phase. These results confirmed that the synthesis approach had the potential to create a spinel with some

Ni^{3+} in the lattice. There was no evidence of any Fe containing impurities (such as Fe_2O_3 or Fe_3O_4) in the PXRD data.

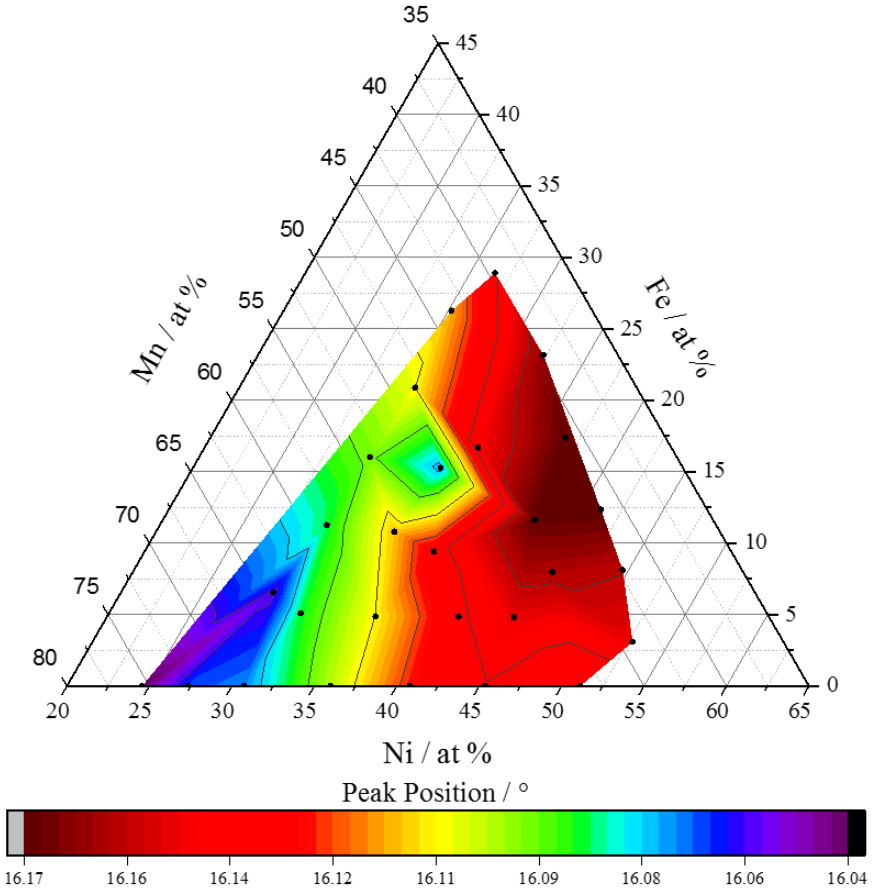

Figure 6.3: PXRD plots peak position of the (311) peak vs composition.

The estimation of the crystallite domain size was carried out using the Scherrer equation on the (311) peak at approximately 16° and the data is shown in Figure 6.4. There was a slight compositional dependence on the Scherrer size, with samples containing large amounts of Ni having a larger crystallite size (36 – 40 nm) than those containing high Mn (30 – 36 nm). The smallest Scherrer sizes (30 nm) were seen in an area with high Fe content and low Mn. Materials containing the $NiMnO_3$ perovskite impurity had a larger Scherrer size on average whereas those materials which were phase pure had a smaller Scherrer size. Samples containing the Mn_2O_3 impurity were of intermediate size.

BET surface area measurements are plotted in Figure 6.4 and were found to be between 2.1 and 6.8 $m^2\ g^{-1}$. The BET surface area was highest in materials with high at% Mn and lowest in materials with high at% Ni. The Specific Surface Area (SSA) of these

spinel materials was much lower than for all other materials reported in this thesis. Due to the precipitation issues with Mn, NaOH was used as the base in the synthesis, and the concentration of metal precursor used in the reaction was doubled. Both changing the base and changing the concentration of metal precursor have been shown to influence the SSA of materials synthesised via both batch and continuous hydrothermal methods.[178] Surface areas of materials synthesised herein are similar to materials prepared by solid state and sol gel methods in the literature (1.3 $m^2\ g^{-1}$)[338], although lower than those prepared by ultrasonic and organic templating routes (22 $m^2\ g^{-1}$).[333] Those materials with smaller crystallite sizes tended to have larger surface areas. However, this was not uniform across all the space explored and it may have been that the presence of an impurity phase was affecting the crystallite size, BET surface area or both.

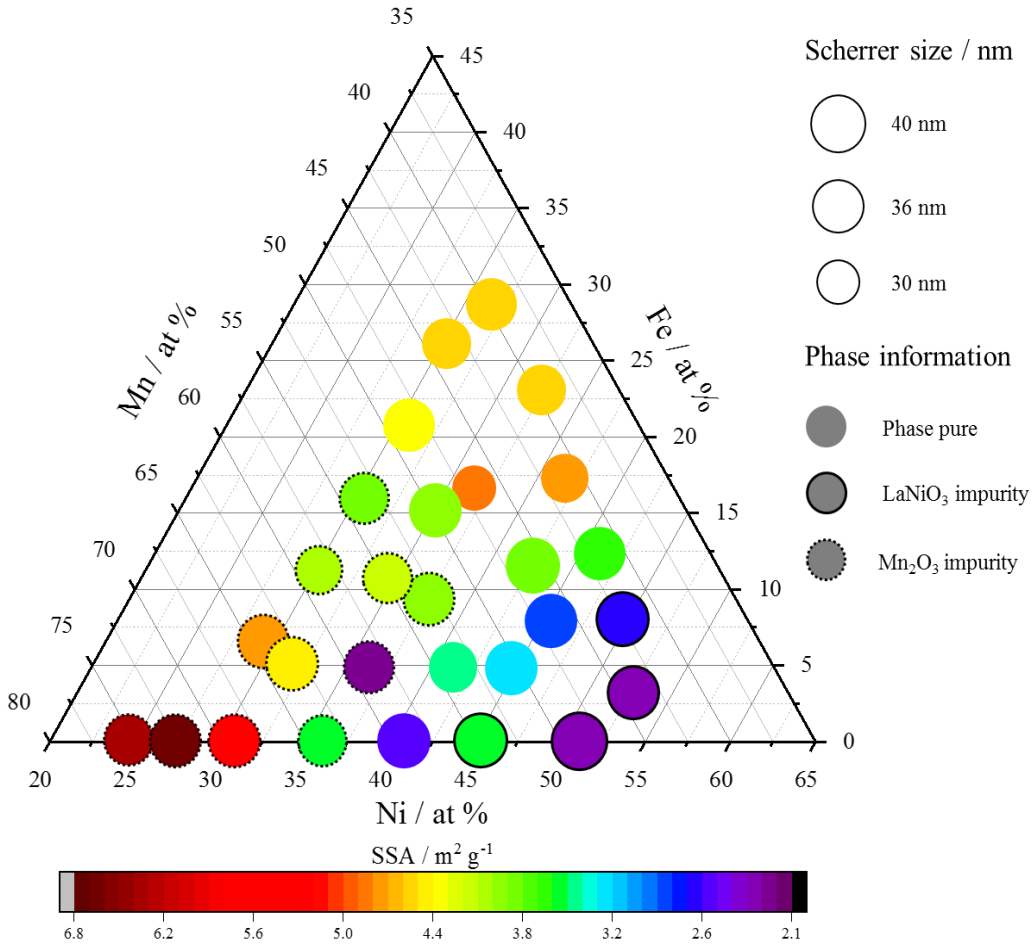

Figure 6.4: Ternary physical characterisation data. The size of the sphere corresponds to the primary crystallite size calculated from the Scherrer equation, the colour of the sphere corresponds to the BET SSA and the outline of the sphere corresponds to impurity phases seen in the PXRD pattern.

Phase impurities were seen in the bottom corners of the ternary plot and in materials with high at% Mn and are mapped in Figure 6.4. The presence of Mn_2O_3 impurities in a large range of samples was attributed to the large excesses of Mn which were necessary in the un-optimised reaction. However, this may also have been due to the low temperature calcination step, as Mn_2O_3 and $NiMn_2O_4$ are known to co-exist at low Ni fractions below 1000 °C.[332] The $NiMnO_3$ impurity seen in Ni rich areas of the phase space studied is also assigned to the unoptimized heat-treatment step.

XPS was used to study the electronic state of the materials and the spectra for the Mn 2p, Ni 2p, Fe 2p and O 1s are shown below in Figure 6.5. As discussed in previous chapters, the Mn 2p spectrum can be difficult to deconvolute due to the presence of multiple oxidation states all coexisting in the same compound. As seen in Figure 6.5 a), two peaks were observed and assigned as the Mn $2p_{3/2}$ (approx. 642.2 eV) and the Mn $2p_{1/2}$ (approx. 653.7 eV). The spin orbit coupling for all materials was around 11.6 eV which was consistent with previous studies.[339] The presence of Mn^{2+} was difficult to assign, as although no clear satellite peak was seen at approximately 648.8 eV, there may have been a low percentage of Mn^{2+} in the material, leading to only a small contribution to the Mn 2p spectrum and there was some degree of asymmetry to the Mn 2p peak towards the higher binging energies.

The Ni 2p XPS spectra shown in Figure 6.5 b) all showed similar features. Peaks were sharper and more defined in compositions containing higher amounts of Ni. The difference in binding energy between the main photoelectron peak at approximately 855.3 eV and the “shakeup” satellite peak at approximately 861.5 eV correlated to the hybridization between cation 3d and ligand p levels as well as the columbic attraction between the 2p/3d electrons.[333] The positioning of these peaks suggested the presence of Ni^{2+}.[338] As with the Mn 2p spectra, direct analysis of the Ni 2p region was complex due to overlapping states and broadening of peaks caused by strongly correlated electron systems.[340]

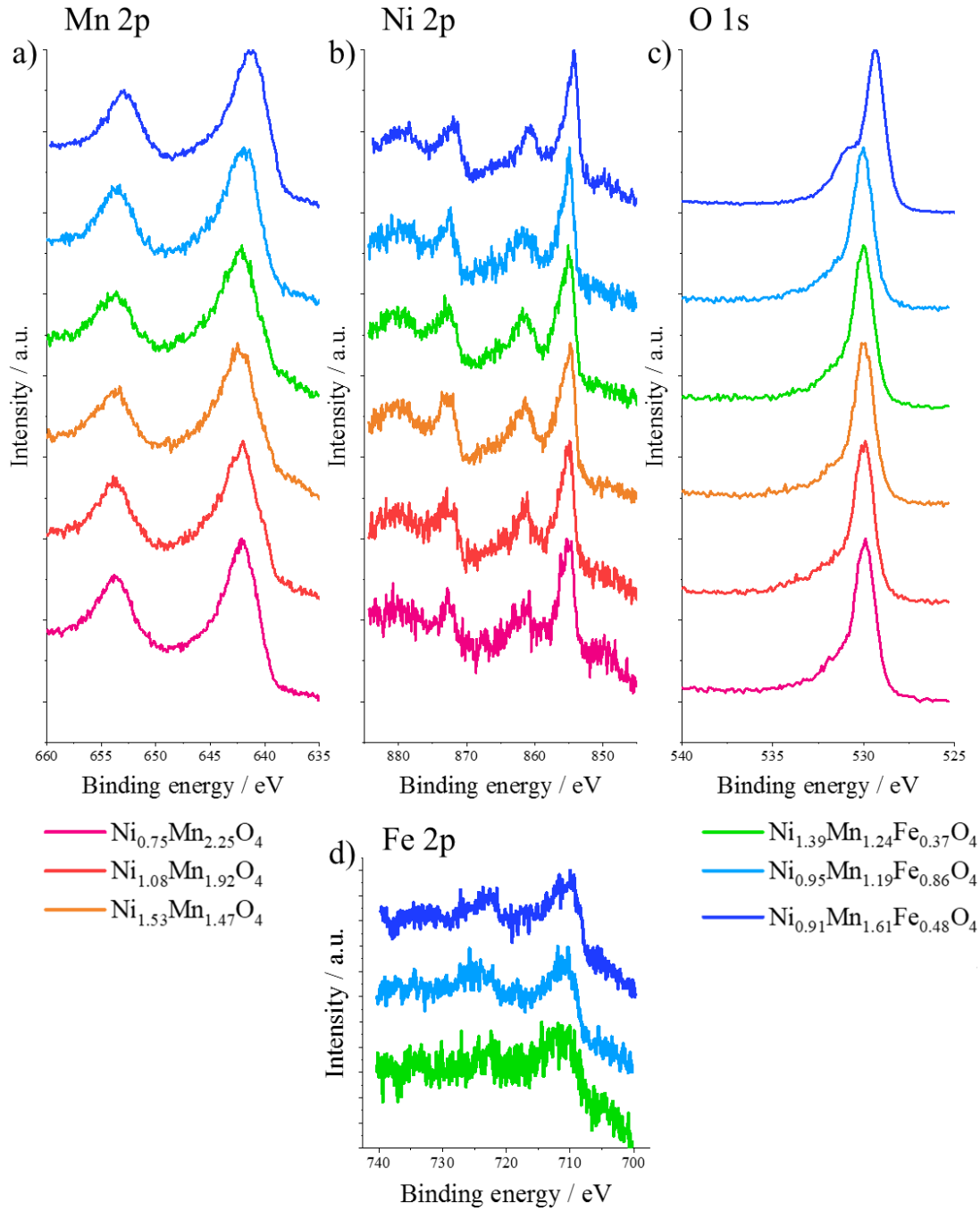

Figure 6.5: a) Mn 2p, b) Ni 2p, c) O 1s and d) Fe 2p XPS spectra of a selection of $Mn_xNi_yFe_zO_4$ materials from around the compositional phase space studied.

Figure 6.5 c) shows the O 1s XPS spectra. The asymmetry in the peak suggested that more than one oxygen species was present at the surface of the spinels. There was no visible peak shift along the binary $Mn_xNi_yO_4$ line, however on the addition of Fe into the spinel the binding energy of the O 1s peak shifted to higher eV. The centre of the two apparent peaks in the O 1s spectra were at approximately 529.9 and 531.2 eV. These corresponded to lattice oxygen and absorbed oxygen species respectively.[313]

The Fe 2p XPS spectra are shown in Figure 6.5 d). The spectra were much less defined than for other elements, due to the lower atomic percentages of iron seen in the samples. As more Fe was added, the peaks became clearer. The Fe $2p^{3/2}$ peak was located at approximately 711 eV for all materials indicating the presence of Fe^{3+}.[341]

Raman spectra were recorded and can be seen in Figure 6.6. Figure 6.6 a) shows the Raman spectra along the *x*-axis in the absence of Fe. The most intense peak at approximately 630 cm^{-1} was assigned to an A_{1g} Raman line corresponding to an asymmetric Mn-O stretching vibration in the octahedral MnO_6 unit cell. The appearance of a shoulder peak at 585 cm^{-1} was assigned to cation mixing between the Ni and Mn at higher Ni concentrations. The less intense peak at approximately 520 cm^{-1} was assigned to the $F_{2g}{}^2$ band corresponding to a Ni-O stretching mode.[342] The low wavenumber peaks (below 300 cm^{-1}) were assigned to Ni-O $F_{2g}{}^1$ band (215 cm^{-1}) and Ni-O F_g band (265 cm^{-1}).[343]

Figures 6.6 b) and c) show the Raman spectra along the y and z-axis respectively. The introduction of Fe into $NiMn_2O_4$ has been shown previously to stabilise the cubic phase, which corresponds to an increase in cation mixing which can be seen in the Raman spectra.[333] It has been previously reported that the bands at approximately 630 and 690 cm^{-1} correspond to the A_{1g} modes reflecting local lattice effects on the tetrahedral site. These peaks were broad and asymmetric, and suggested the contribution of more than one cation occupying the sites. The peak was much broader on the introduction of Fe than it was in Figure 6.6 a). Previous studies have suggested that the higher wavenumber peak corresponds to a Fe^{3+}-O tetrahedral unit cell.[344] This fits the data seen herein as the higher wavenumber peak was only prominent in the samples with the highest Fe concentrations, suggesting a solely Fe containing unit cell.

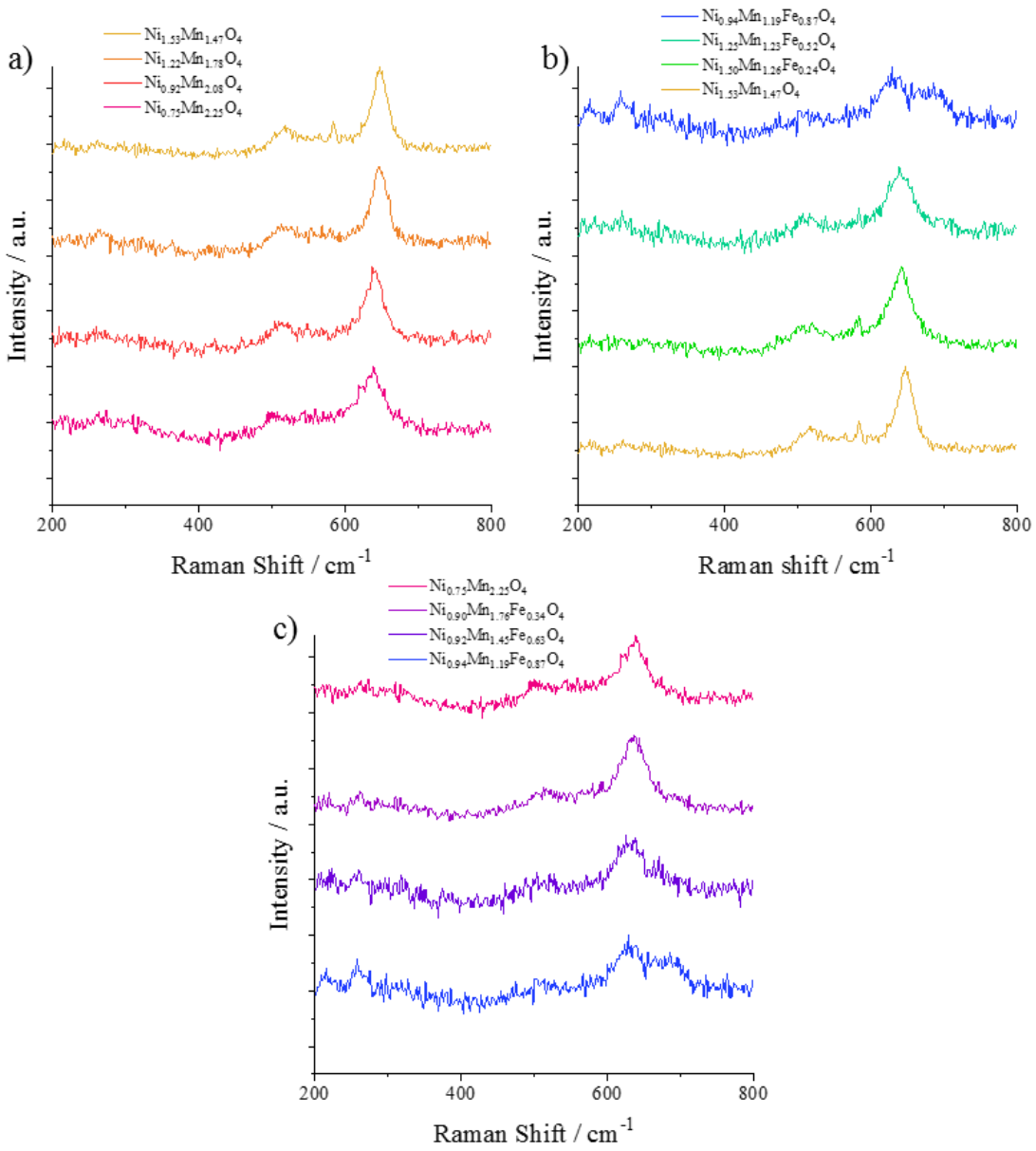

Figure 6.6: Raman spectra for a selection of spinel catalysts: a) along the Mn-Ni binary line (x-axis), b) Mn remaining "constant" (along the y-axis) and c) Ni remaining constant (along the z axis). Spectra were taken with a 512.5 nm laser at 100% power.

All samples were found to possess a degree of magnetic behaviour, which increased with increasing Ni and Fe content. For this reason, SEM, TEM and EDX were not carried out on these samples.

6.4.2. Electrochemical Characterisation of $NiMn_2O_4$ Materials

6.4.2.1. High-throughput Electrochemical Screening of $NiMn_2O_4$ Materials

All samples were screened for their electrocatalytic activity prior to any in-depth analysis being carried out. Samples were formulated into inks and deposited onto glassy carbon rotating disk electrodes with a mass loading of approx. 0.4 mg cm^{-2}. The electrodes were cycled between 0.2 and −0.8 V vs Ag/AgCl in O_2 saturated 0.1 M KOH until repeated CVs were identical.

Linear sweep voltammetry was then carried out between 0.1 and −0.6 V vs Ag/AgCl to examine overpotentials and current densities for the ORR. Well defined reduction curves were seen for all catalysts in the region of 0 to −0.6 V vs Ag/AgCl. A limiting current density for all catalysts was reached for the ORR and this was dependent on the rotation speed of the RDE. LSV was also carried out between 0 and 0.8 V vs Ag/AgCl to examine catalytic activity towards the OER. A selection of voltammograms for the OER and ORR collected for various samples is shown above in Figure 6.7. These responses are typical of the responses seen for all catalysts.

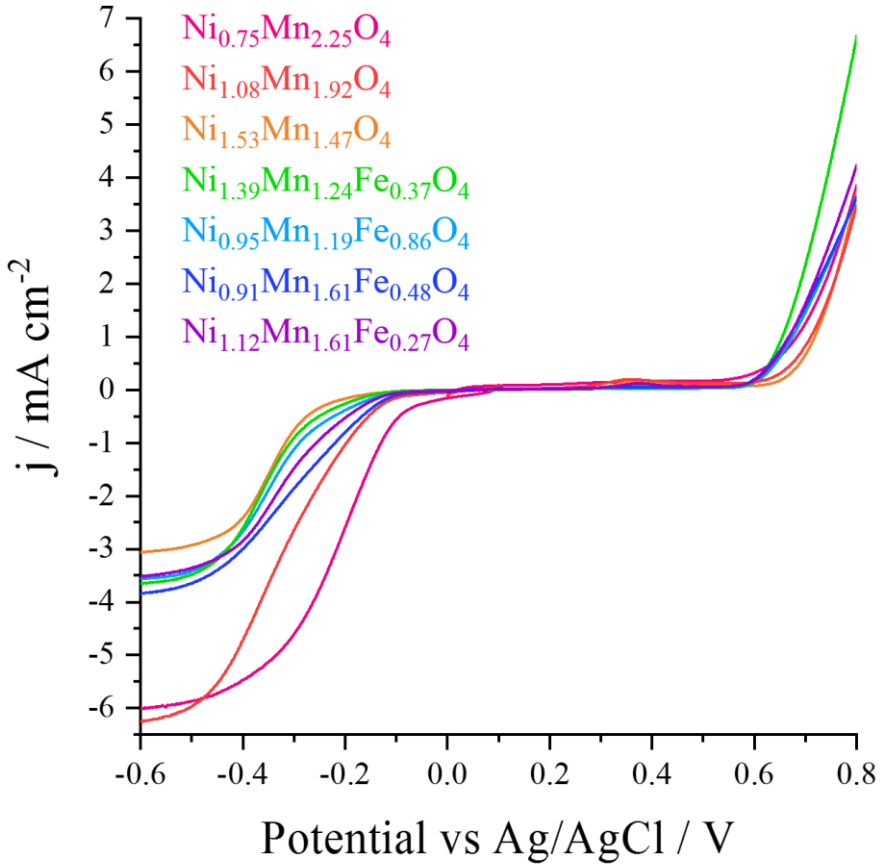

Figure 6.7: Linear sweep voltammograms at 2500 rpm of the OER and ORR showing selected composition reactions. All measurements were carried out in O_2 saturated 0.1 M KOH with a scan speed of 10 mV s^{-1}.

Figure 6.8 a) shows the ORR overpotential at a current density of −0.2 mA cm^{-2} reported with respect to the reversible oxygen potential (1.23 V vs RHE). The best performing catalyst was $Mn_{2.25}Ni_{0.75}O_4$ with an overpotential of 0.28 V. The overpotential seen here is lower than seen in relevant literature. For example, Zhao *et al.* reported an overpotential of 0.42 V for a $Ni_{0.5}Co_{0.5}Fe_2O_4$ catalyst[328] and Zhang *et al.* reported an overpotential of 0.38 V for an Mn_3O_4/CNT hybrid catalyst.[315] The poorest performing catalyst was $Ni_{1.60}Mn_{1.30}Fe_{0.10}O_4$ with an overpotential of 0.47 V. The ternary plot shows that high ORR activity was achieved in a region of Mn rich compounds and that the addition of Ni increased the ORR overpotential along the binary line from 0.28 to 0.47 V. The ternary plot data also suggested that the introduction of Fe into the Mn/Ni spinel did not have any positive impact on the ORR overpotential, when replacing Mn there was an increase in the overpotential leading to poorer catalysis, and when replacing Ni there was little change in the activity. The

bands of colour indicated that activity was roughly aligned along the *z*-axis, which suggested that it was the presence of Mn which was largely dictating the ORR activity. However, due to the presence of Mn_2O_3 in the PXRD, activity was also be seen to be higher in the areas of the phase diagram where this impurity was present. Mn_2O_3 is a well-known, highly active ORR catalyst so there may have been some degree of catalytic activity contributed by this material.[251,260,345]

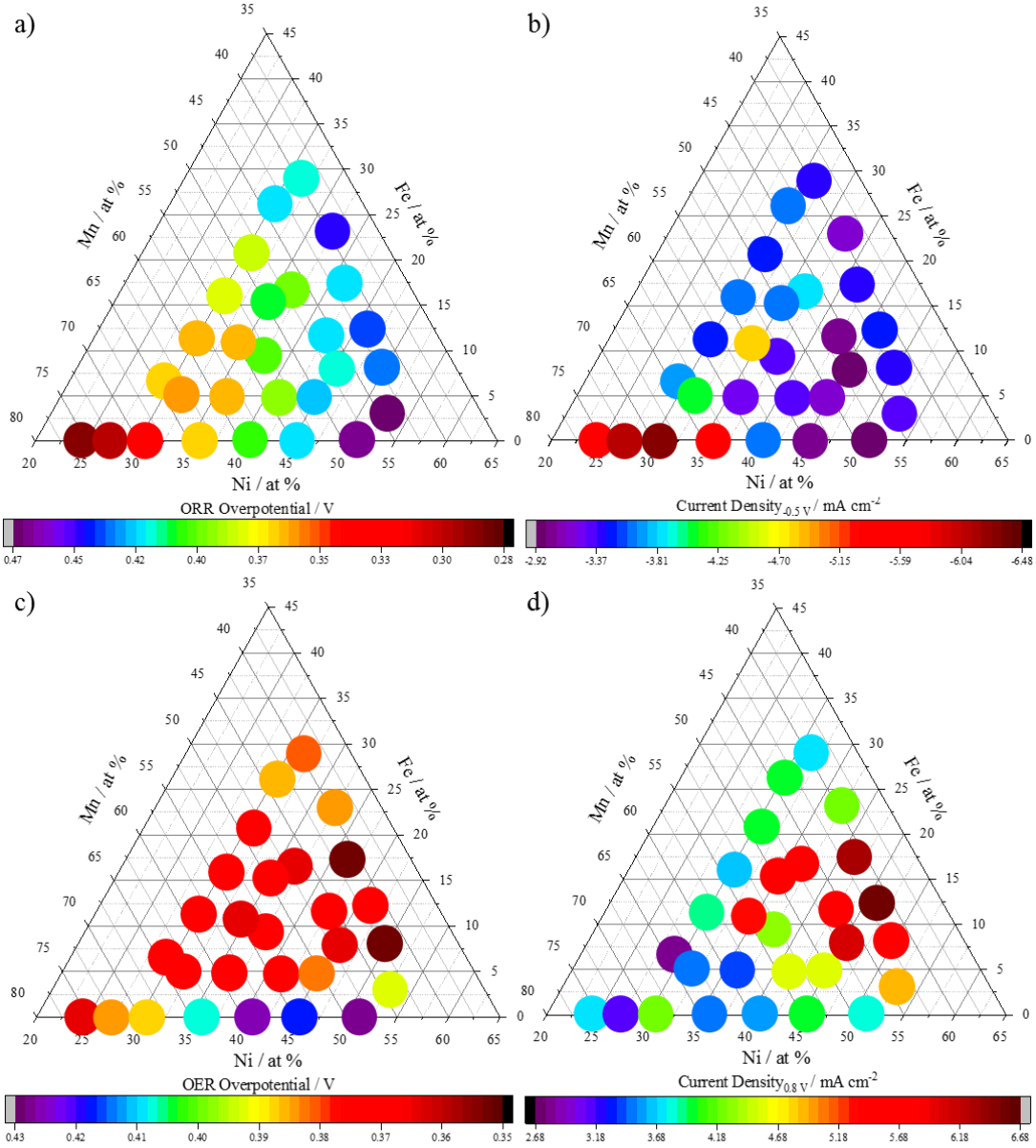

Figure 6.8: Ternary data for catalytic markers for: a) the overpotential for the oxygen reduction reaction (ORR) measured at −0.2 mA cm^2, b) the current density at −0.5 V vs Ag/AgCl c) the overpotential for the oxygen evolution reaction (OER) measured at 0.4 mA cm^2 and d) the current density at 0.8 V vs Ag/AgCl. All measurements were carried out in O_2 saturated 0.1 M KOH with a scan speed of 10 mV s^{-1} and a rotation speed of 2500 rpm.

The current density at −0.5 V vs Ag/AgCl was recorded as another indicator of catalytic activity (Figure 6.8 b). In general, those materials on the binary line containing high Mn concentrations had a much greater current density than all other catalysts. This may have been due to their greater SSA (> 6 $m^2\ g^{-1}$). The catalyst with the highest limiting current density was $Ni_{0.92}Mn_{2.08}O_4$ with a density of −6.48 mA cm^{-2}. The current densities achieved over the rest of the phase space studied was universally low. Overall, the current densities were low compared to the perovskites studied in earlier Chapters. This may also be linked to the much lower SSA seen for these catalysts compared to the perovskites (which had SSA > 10 $m^2\ g^{-1}$) due to the difference in conditions required to achieve the spinel materials via an unoptimized synthetic route.

Figure 6.8 c) shows the compositional dependence on the overpotential for the OER (taken at 0.4 mA cm^{-2}). The OER activity was seen to be greatest at lower concentrations of Mn and moderate concentrations of both Ni and Fe. The best performing sample was $Ni_{1.5}Mn_{1.26}Fe_{0.24}O_4$ with an overpotential of 0.35 V. Ko *et al.* saw similar results, with a reported overpotential of 0.38 V for an $NiFe_2O_4$ nano catalyst.[346] The catalyst with the highest overpotential was $Ni_{1.53}Mn_{1.47}O_4$ with an overpotential of 0.43 V. The activity along the binary line was poor suggesting the presence of Fe supported the OER activity. In general, OER overpotentials were shifted by 50 mV compared to the ORR but there was much less variation in activity across the ternary composition space explored. Moving away from the binary line, the overpotentials were consistent across most of the phase space. There was a slight reduction in activity at the tip of the triangle, where Mn concentration was low and Fe concentration was high (for the phase space studied). It appeared that some percentage of Fe inclusion into the spinel was beneficial for the OER activity. The areas with high activity for the OER were areas with low activity for the ORR and vice versa. However, there were three catalysts on the binary line with moderate activity for the OER and high activity for the ORR.

The current density taken at 0.8 V vs Ag/AgCl was also examined as an indicator of catalytic performance (Figure 6.8 d). There was a group of materials with high activity when Mn concentration was between 45 and 55%, Ni concentration was between 35 and 50% and Fe concentration was between 5 and 20 %. Activity decreased when Mn concentration was increased. This suggested the presence of low concentrations of Fe was increasing the OER activity seen. The areas with the highest current densities

observed for the OER are some of the lowest current densities observed in the ORR and vice versa. Current densities observed for the spinel materials were higher than those seen for the perovskites studied in earlier chapters, possibly due to the greater amounts of Ni and the presence of Fe. Current densities may also appear lower than in the ORR due to the limit on potential of the working electrode. Glassy carbon is not stable at high potentials[307] and so due to the nature of the high throughput experiment, a relatively conservative limit of 0.8 V vs Ag/AgCl was chosen to limit damage to the electrodes.

Figure 6.9 shows the combined overpotentials for the ORR and OER which allowed the evaluation of the bifunctional activity of the catalysts. The catalyst with the lowest observed bifunctional overpotential was $Mn_{2.25}Ni_{0.75}O_4$ with an overpotential of 0.64 V. Activity was highest in the areas with high Mn concentration and low Ni concentration. If the graph is read along the *z*-axis (Mn concentration) it shows that activity was consistently highest when closest to this axis and then decreased as we approached the *x*-axis. This suggested that the addition of Ni into these samples decreased the bifunctional activity of the catalysts. Reading along the *y*-axis (Fe concentration) activity was lowest when Ni concentration was high (and Mn concentration was low) and then increased as the Ni concentration decreased (reading from right to left on Figure 6.9, above). This suggested that the presence of Fe was having little impact on the bifunctional activity of the catalysts. However, catalysts with high concentration of Ni and no Fe performed worse than those catalysts with a slight substitution of Mn for Fe and constant Ni concentration. As the lowest overpotentials for the ORR were approx. 50 mV lower than the lowest for OER, the apparent bifunctional activity may be being driven predominantly by the ORR overpotential.

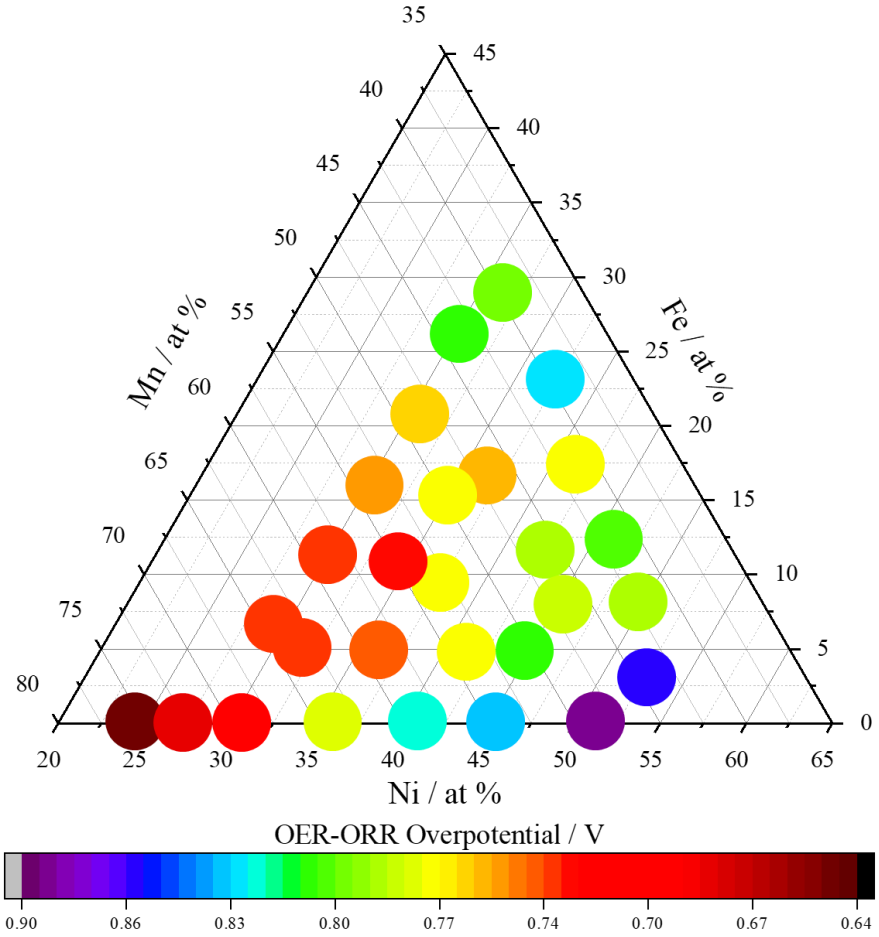

Figure 6.9: Bifunctional overpotential ternary plot for the $Ni_xMn_yFe_zO_4$ space explored. The bifunctional overpotential was found by the addition of the ORR overpotential at −0.2 mA cm^2 and the OER overpotential at 0.4 mA cm^2. All measurements were carried out in O_2 saturated 0.1 M KOH with a scan speed of 10 mV s^{-1}.

The dependence of the voltammograms on rotation speed was investigated using the Koutecky-Levich (K-L) equation. All materials had well defined current response at all rotation rates investigated. An example of this can be seen for $Ni_{0.75}Mn_{2.25}O_4$ in Figure 6.10 a). The current densities at −0.5 V vs Ag/AgCl were used to draw and the K-L plots (an example is shown in Figure 6.10 b). All plots were linear over all rotation speeds, demonstrating that the electron transfer process at the surface of the catalysts in the diffusion-controlled region were fast enough to catch up to the diffusion-convection rate.[246] This meant all limiting current densities were mass-transport controlled.

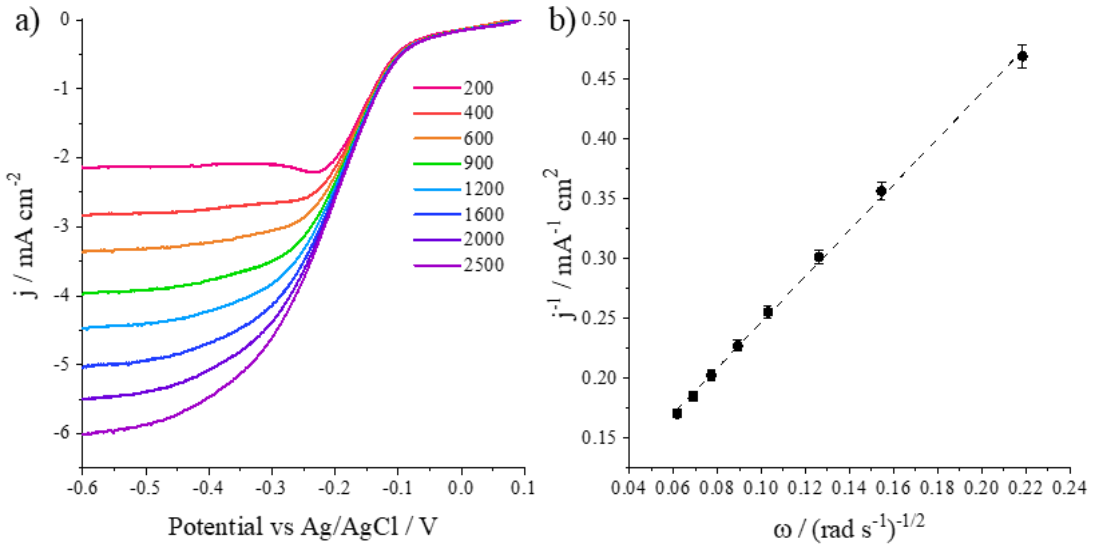

Figure 6.10: a) Variation in curve of LSV traces at differing rotation rates for $Ni_{0.75}Mn_{2.25}O_4$, b) the corresponding K-L plot at −0.5 V for $Ni_{0.75}Mn_{2.25}O_4$. All experiments were carried out in O_2 saturated 0.1 M KOH at 10 mV s^{-1}.

All samples had a linear relationship between the reciprocal of the current density at −0.5 V and the square root of the rotation speed. The K-L gradients and *y*-intercepts were plotted against composition and are shown below in Figure 6.11. All r^2 values for K-L plots were greater than 0.995. The K-L slope is linked to the electron transfer number through the K-L equation. Earlier in this thesis, Pt-black using the same ink formulation as in this piece of work was found to have a gradient of 1.72 mA^{-1} cm^2 $(rad\ s^{-1})^{-1/2}$ and a *y*-intercept of 0.0106 mA^{-1} cm^2 (as shown in Chapter 4, Figure 4.5). The slope of the line reflects the electron transfer path in the oxygen reduction reaction. The K-L gradients for the spinel materials studied in this chapter are shown in Figure 6.11 a). $Mn_{2.25}Ni_{0.75}O_4$ had a K-L gradient of 1.92 mA^{-1} cm^2 $(rad\ s^{-1})^{-1/2}$ which was the lowest observed, closer to that of Pt, which suggested an electron transfer number closer to the ideal value of 4. Whereas, $Mn_{1.37}Ni_{1,28}Fe_{0.35}O_4$ had a K-L gradient of 2.35 mA^{-1} cm^2 $(rad\ s^{-1})^{-1/2}$. Looking at the overall trend across the phase space studied, it appeared that high Mn gave a lower gradient. Steeper slopes were observed with greater concentrations of Ni combined with the introduction of Fe. However, the colour change appeared to correspond to the z axis, which suggested that the removal of Mn, and not necessarily the introduction of Ni/Fe was the cause of the steeper gradient. The impact of Mn on K-L gradient has been observed before with Li *et al.*

reporting that increased concentrations of Mn in $Co_xMn_yO_4$ ($x + y = 4$) lead to a decrease in the K-L gradient and thus an increase in electron transfer number.[131]

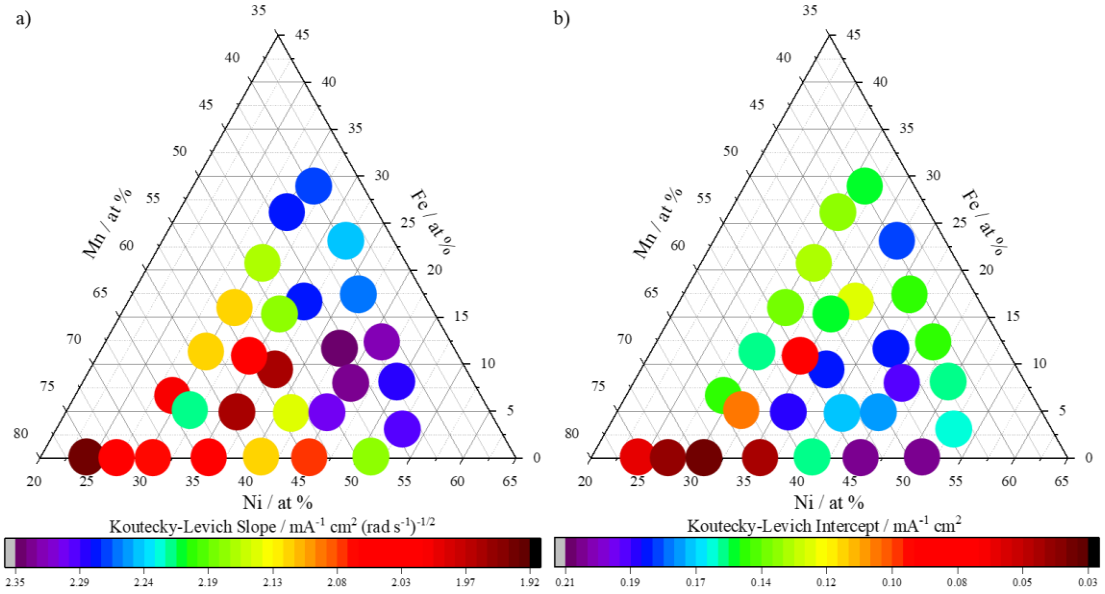

Figure 6.11: Koutecky-Levich plots for the ORR for the spinel phase diagram. a) shows the calculated slope from the plots. b) shows the y-intercept from the plots. All experiments were carried out in O_2 saturated 0.1 M KOH with a scan speed of 10 mV s^{-1}. All plots had an r^2 value of > 0.99.

The K-L *y*-intercept is the reciprocal of the kinetic current density (the current density observed in the absence of mass transport effects) and the values for the spinels studied are shown in Figure 6.11 b). In the left-hand corner, the kinetic current density was higher than at other points in the phase diagram. There was a good correlation between the observed SSA and the value of the kinetic current density. This would make sense as the higher the surface area, the more accessible surface sites for catalysis to occur on. $Ni_{0.93}Mn_{2.07}O_4$ had the lowest y-intercept leading to a diffusion corrected kinetic current density of 33.3 mA cm^{-2}. In contrast, $Ni_{1.53}Mn_{1.47}O_4$ had the highest *y*-intercept leading to an observed kinetic current density of 4.8 mA cm^{-2}. The higher current densities observed here are similar to the better performing catalysts in the literature. Prabu *et al.* reported a calculated kinetic current density of 31.4 mA cm^{-2} for a $CoMn_2O_4$/N-rGO catalyst.[320] However, all kinetic current densities observed were lower than the kinetic current density observed for Pt black in Chapter 4 (200 mA cm^{-2}).

The Tafel slopes for the ORR were calculated from the log of the diffusion corrected kinetic current density and the overpotential. The graph below in Figure 6.12 depicts the Tafel slopes calculated in the high potential range (approx. −0.1 to −0.2 V vs Ag/AgCl).

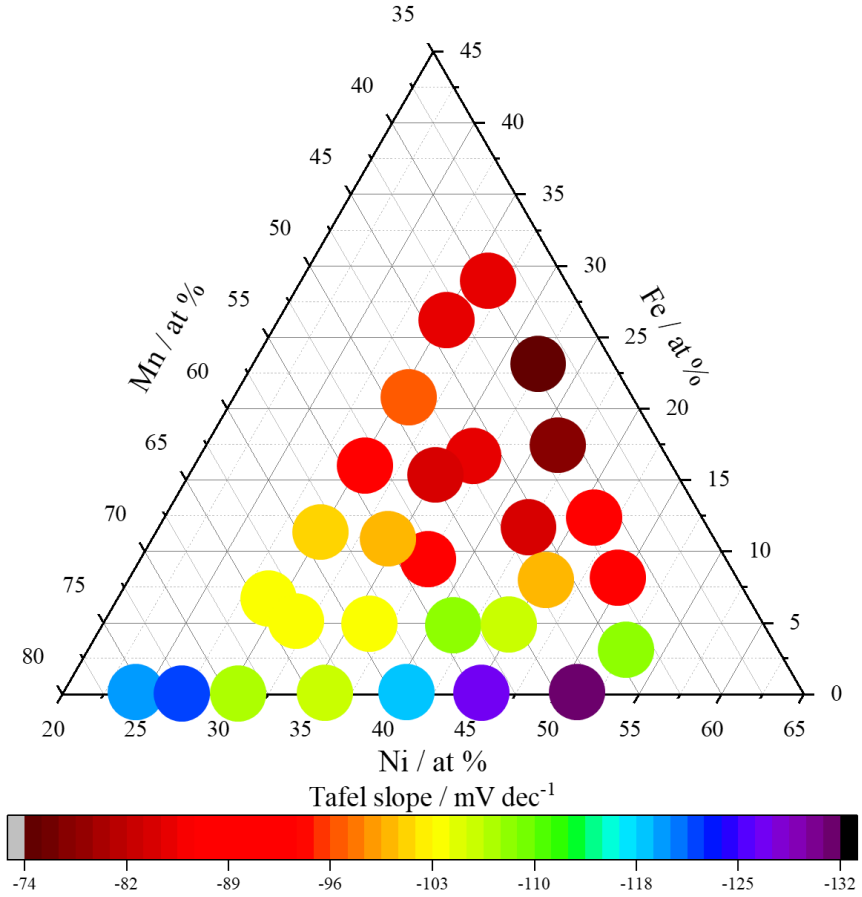

Figure 6.12: Observed Tafel slopes for the catalysts at high potentials (approx. −0.1 to −0.2 V vs Ag/AgCl) calculated by plotting log(J_K) vs E. Kinetic current densities were calculated by using equation 2.14.

Tafel slopes were calculated for all materials and are shown in Figure 6.12. The lowest Tafel slopes were observed in samples with significant iron content. It appeared that the nickel content of the catalysts was having little effect on the Tafel slope in the high potential range. The activity observed from the *z*-axis suggests that high manganese and low iron contents had the largest effect on the observed Tafel slope. The catalyst with the lowest Tafel slope for the ORR was $Ni_{1.11}Mn_{0.69}Fe_{1.20}O_4$ with an observed slope of −74 V dec^{-1}. The catalyst with the highest observed Tafel slope was $Ni_{1.53}Mn_{1.47}O_4$ with a Tafel slope of −132 V dec^{-1}. The lower the Tafel slope, the faster the ORR kinetics (assuming an identical reaction mechanism) so a lower slope was

more desirable.[217] It appeared that the inclusion of iron into the catalysts had a positive impact on the Tafel slope, making the gradient shallower which suggested that the rate of the rate determining step was increasing.

6.4.2.2. In-Depth Electrochemical Analysis of $NiMn_2O_4$ Materials

Seven samples at roughly even intervals within the studied phase space were then taken forward for more in-depth electrochemical analysis on the ORR. The OER was not investigated further.

Table 6.1: Catalytic data for a selection of catalysts chosen from around the phase space for further investigation.

Sample	ORR overpotential (V)	OER overpotential (V)	Combined overpotential (V)
$Ni_{0.75}Mn_{2.25}O_4$	0.278	0.363	0.641
$Ni_{1.08}Mn_{1.92}O_4$	0.368	0.409	0.777
$Ni_{1.53}Mn_{1.47}O_4$	0.468	0.426	0.894
$Ni_{1.38}Mn_{1.24}Fe_{0.38}O_4$	0.438	0.368	0.806
$Ni_{0.94}Mn_{1.19}Fe_{0.87}O_4$	0.413	0.379	0.792
$Ni_{0.91}Mn_{1.61}Fe_{0.48}O_4$	0.380	0.369	0.749
$Ni_{1.13}Mn_{1.59}Fe_{0.28}O_4$	0.400	0.372	0.772

The samples were chosen to cover the maximum phase space possible and to examine a range of activities. Cyclic voltammetry, RRDE experiments and chronoamperometry were used to further understand the electrochemical processes taking place at the surface of the catalysts. Figure 6.13 shows the samples taken graphically.

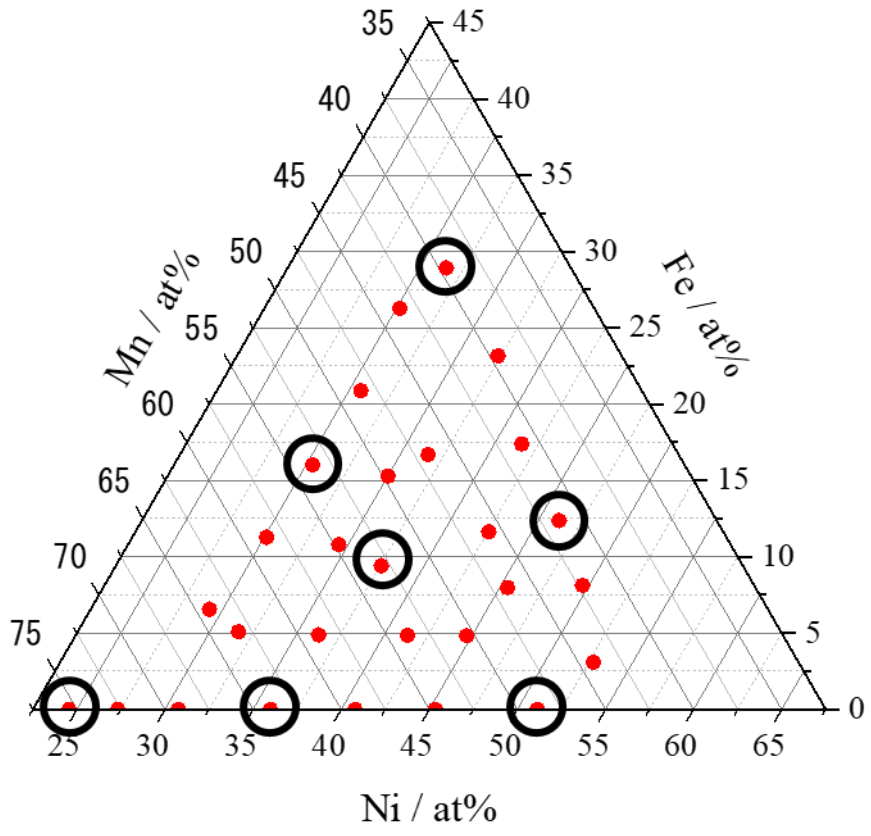

Figure 6.13: Ternary plot identifying the samples chosen for extensive electrochemical analysis from the studied phase space. Those samples circled were taken forward an examined further.

Cyclic voltammetry experiments were carried out in degassed electrolyte at 5 mV s^{-1} to identify key redox behaviour of the materials and identify the main redox peaks. Figure 6.14 shows the cyclic voltammograms for the seven materials studied in the absence of oxygen.

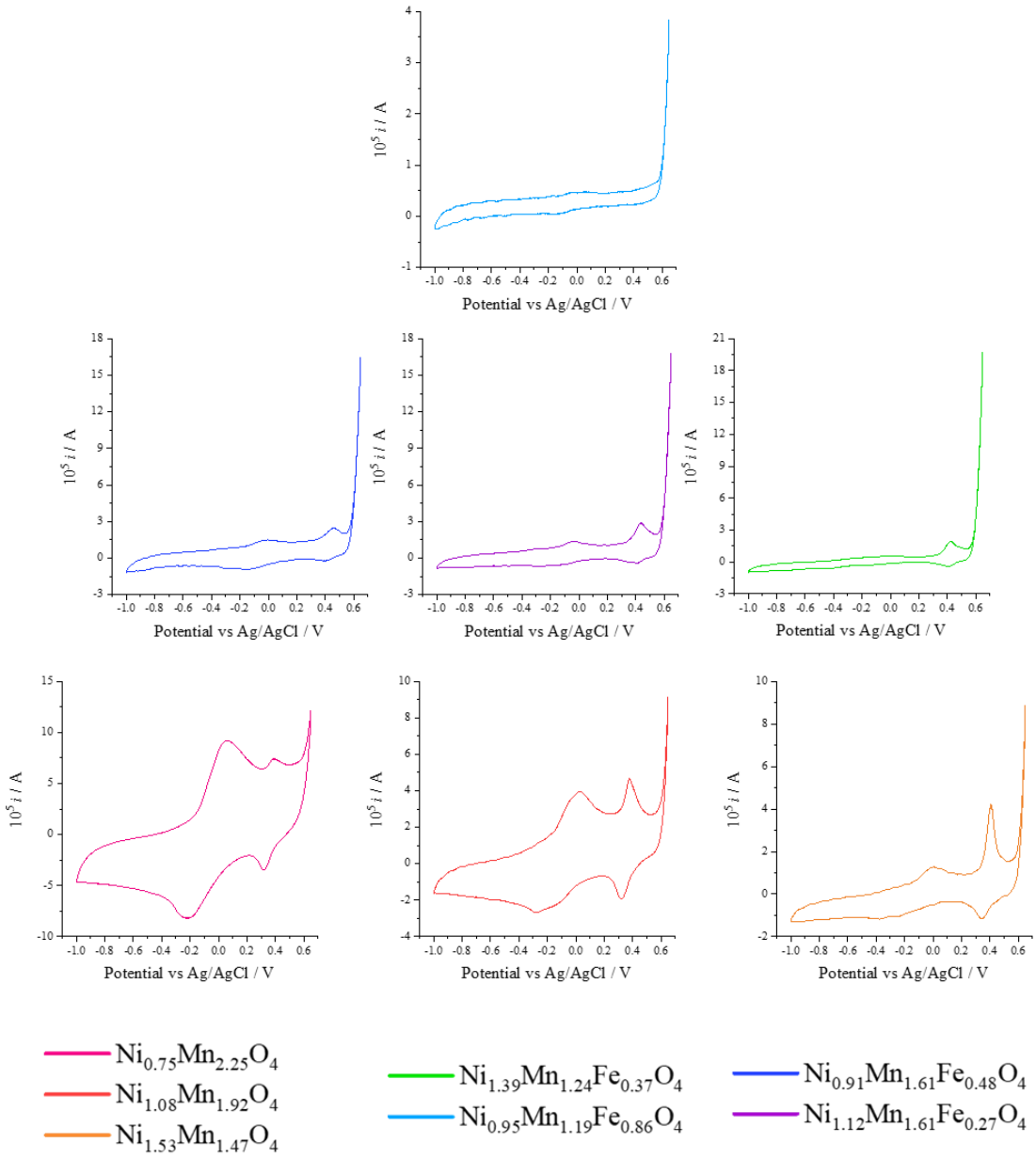

Figure 6.14: Cyclic voltammograms for selected samples from the ternary composition plot. All measurements were carried out in N_2 saturated 0.1 M KOH between +0.8 and −1.0 V vs Ag/AgCl at 5 mV s^{-1}.

Figure 6.14 shows the CVs taken for seven materials taken at even intervals from the ternary space studied in N_2 saturated electrolyte. The catalysts all showed promising redox peaks associated with the reduction and oxidation of Mn and Ni. The redox of Fe in oxides occurs at a more negative potential than the limits applied here.[347] The redox couples associated with the spinels could be assigned with no influence from the ORR due to the lack of oxygen in the electrolyte. The main redox peaks were assigned as follows: the peak centred at approximately 0.95 V vs RHE (–0.015 V vs Ag/AgCl)

was assigned to Mn^{3+}/Mn^{4+}, the peak centred at approximately 1.35 V vs RHE (0.38 V vs Ag/AgCl) was assigned to the Ni^{3+}/Ni^{2+} peak[348] and the large irreversible peak which appears at high potentials in the cathodic current was assigned to the beginning of the OER. This peak had a large variation in intensity, showing the variation in the performance of the materials as OER catalysts. The Mn^{3+}/Mn^{4+} cathodic peak was integrated along the binary line. As the Fe redox couple occurred at more negative potentials and the Ni at more positive potential than the Mn^{3+}/Mn^{4+} cathodic peak we can assume no contribution to their redox chemistry on the Mn peaks. The area decreased from −4.3 mC to −0.5 mC as the composition was changed from $Ni_{0.75}Mn_{2.25}O_4$ to $Ni_{1.53}Mn_{1.47}O_4$. This suggested the inclusion of Ni in majority 2+ form as the area of the peak decreased on increase of Ni.

RRDE experiments were carried out to investigate the reduction pathways across the ternary plot. As can be seen in Figure 6.15 there were a range of peroxide yields across the phase space investigated. The OOH^- evolved can be directly related to the electron transfer number as peroxide is generated through the unfavourable 2+2 e^- reaction as an intermediate. Peroxide yield was greatest for $Ni_{0.95}Mn_{1.19}Fe_{0.86}O_4$ with a yield of 23.2 %, whereas it was lowest for $Ni_{0.75}Mn_{2.25}O_4$ with a yield <1 % at −0.5 V. Both $Ni_{0.75}Mn_{2.25}O_4$ and $Ni_{1.08}Mn_{1.92}O_4$ had electron transfer numbers of approximately 4 suggesting that the favourable direct reduction pathway was dominant in both catalysts with negligible contribution from the indirect 2 electron process. Both electron transfer number and peroxide yield could be correlated with Mn atomic concentration. The higher the concentration of Mn, the lower the peroxide yield and the higher the electron transfer number. Where the Mn concentration remained the same and only Fe/Ni concentrations changed ($Ni_{0.91}Mn_{1.61}Fe_{0.48}O_4$ and $Ni_{1.12}Mn_{1.61}Fe_{0.27}O_4$), the peroxide concentration only changed by 0.5 % which was within the error of the measurement. This further suggested that the concentration of Mn was directly contributing to the observed peroxide yield. The observed electron transfer numbers generally mirrored the shift in overpotential, with higher electron transfer numbers having lower overpotentials. Electron transfer numbers calculated from RRDE data were higher than reported previously for $NiMn_2O_4$[133] (peroxide yield of 35%, electron transfer number of 3.25), although the observed differences may be due to differences in ink formulation and experimental set up. However, many spinel compounds in the literature had similar

peroxide yields and electron numbers as calculated here including 3.79 for $NiCoMnO_4$ and 3.9 for $Ni_{0.5}Co_{0.5}Fe_2O_4$[313,328].

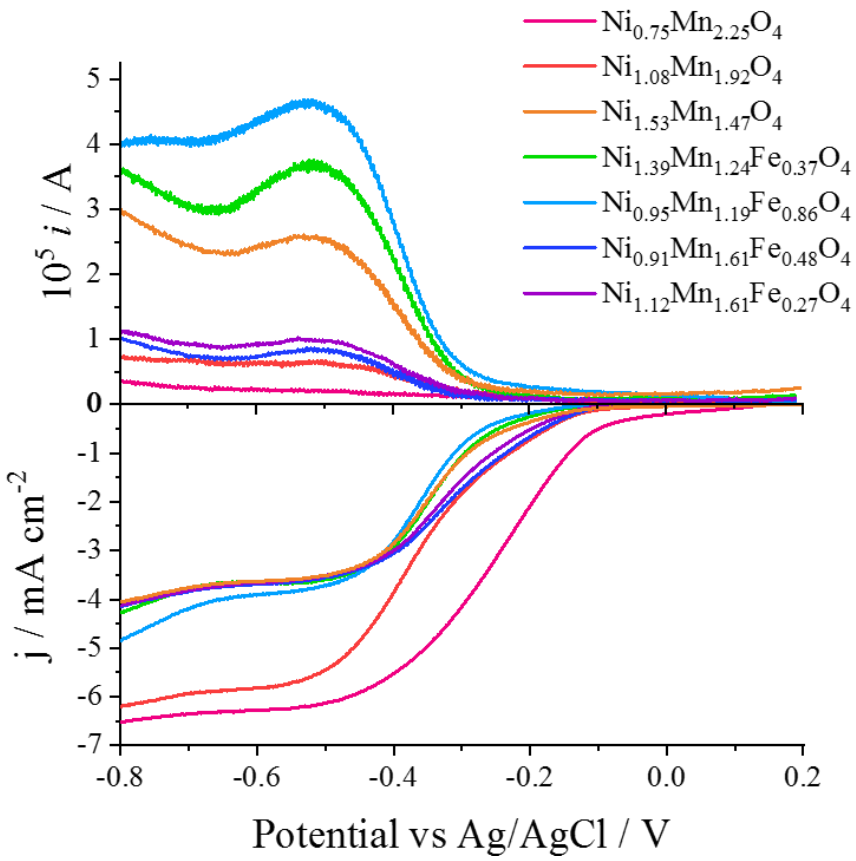

Figure 6.15: Rotating ring disk experimental data for a selection of catalysts from around the ternary plot. The negative response in the disk current response as the disk is swept from 0.2 to −0.8 V vs Ag/AgCl. The positive response is the ring response as the disk is swept from 0.2 to −0.8 V vs Ag/AgCl and the ring potential is held at 0.35 V vs Ag/AgCl. All measurements were carried out in O_2 saturated 0.1 M KOH with a scan speed of 10 mV s^{-1} and a rotation speed of 900 rpm.

The trend followed by the RRDE electron transfer numbers was not the same as the observed trend in K-L gradients. This has been observed previously, and Zhou *et al*. reviewed the current literature and suggested that whilst both methods of determining the observed electron transfer number had advantages and disadvantages, the K-L method is less suitable as some assumptions made in the calculations are found to be false experimentally (as the electron transfer number is significantly dependent on the angular velocity of the RDE).[349]

Figure 6.16 shows the change in e^- transfer number and OOH^- yield over time as the voltage was swept from positive to negative. $Ni_{0.75}Mn_{2.25}O_4$ and $Ni_{1.08}Mn_{1.92}O_4$ both

maintained steady generation of peroxide at below 1 % and thus the e^- transfer number did not vary much as the voltage was swept, maintained at approximately 4. However, the generation of peroxide was much more uneven for $Ni_{0.95}Mn_{1.19}Fe_{0.86}O_4$, $Ni_{1.39}Mn_{1.24}Fe_{0.37}O_4$ and $Ni_{1.53}Mn_{1.47}O_4$. This led to an average e^- transfer numbers of 3.61, 3.71 and 3.77 respectively for the aforementioned catalysts. The variation in peroxide yield is seen in other materials including other manganese containing spinels.[131] This may have been due to a potential dependant reduction mechanism.

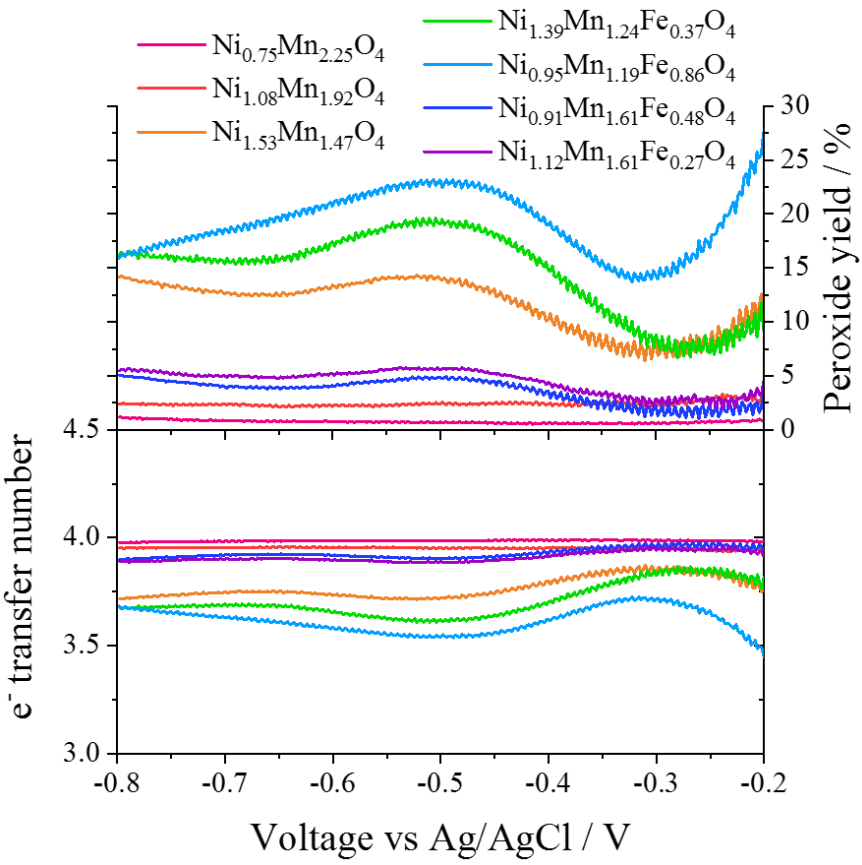

Figure 6.16: Electron transfer numbers (bottom) and peroxide yields (top) for the catalysts over the voltage range −0.2 to −0.8 V vs Ag/AgCl calculated using equations 2.10 and 2.11 in Chapter 2. All measurements were carried out in O_2 saturated 0.1 M KOH with a scan speed of 10 mV s^{-1} and a rotation speed of 900 rpm.

In addition to high activity, a practical catalyst must be active over a long period of time. Chronoamperometry was carried out on the seven selected catalysts. The voltage was held at −0.5 V, which was sufficiently negative so that all catalysts had reached a limiting current density, and the electrode was rotated at 900 rpm. The most stable catalyst was $Ni_{0.75}Mn_{2.25}O_4$ with a loss of 4 % over 4 h. The least stable catalyst was $Ni_{1.39}Mn_{1.24}Fe_{0.37}O_4$ with a loss of 23.7 % over the same time period. $Ni_{0.75}Mn_{2.25}O_4$

was more stable than the commercial Pt sample (Figure 4.11) which lost 5% activity over the same time period. However, this was the only catalyst tested here that was more stable than Pt. The catalysts along the Mn-Ni binary line were the most stable, and catalysts that had lower atomic percentages of Mn were less stable than those with higher at% Mn. These results were similar to those seen in previous studies of similar materials. Pendashteh *et al.* synthesised $NiCoMnO_4$ nanoparticles which retained 90% activity over 10000 s and He *et al*. synthesised a $NiMn_2O_4/NiMnO_3$ hybrid catalyst which retained approximately 95% activity after 14400 s. [133,313] The results collected here compare favourably with the highest stability materials reported in the literature.

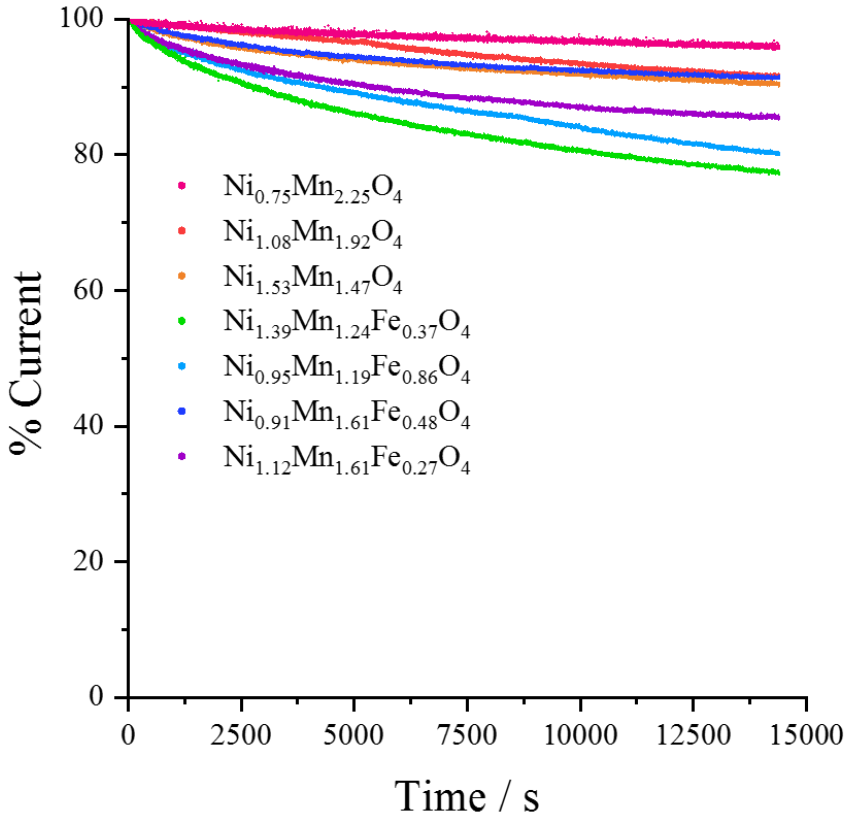

Figure 6.17: Stability data for the 7 catalysts. The data is shown as a percentage of the initial current. All measurements were carried out over 4 hours in O_2 saturated 0.1 M KOH at −0.5 V with a scan speed of 10 mV s^{-1} and a rotation speed of 900 rpm.

Figure 6.18 shows the resistance of two catalyst to methanol poisoning. Methanol poisoning can be a huge problem in mixed fuel/dirty fuel fuel-cells as when methanol reaches the cathode through the polymer electrolyte it can cause loss of activity and permanently damage the catalyst.[260] Pt black is known to be susceptible to methanol poisoning. Shown above is the comparison between the most stable metal oxide spinel

catalyst found in this study and the Pt black commercial sample. The catalysts were tested under identical conditions, with the voltage being held at −0.5 and the electrode rotated at 900 rpm. Methanol was injected after 1200 s of chronoamperometry testing. The Pt black sample lost approximately 40 % activity instantly as the methanol was injected, and activity didn't recover within the testing window of 4000 s, still being only c.a. 80% of the initial activity observed. This is consistent with other literature studies.[350] However, the metal oxide $Ni_{0.75}Mn_{2.25}O_4$ spinel catalyst lost very little activity (c.a. 2%) at the instant the methanol was injected, and the activity was recovered almost instantaneously. Wang *et al.* saw similar results were seen for a $ZnMnCoO_4$ spinel, on the injection of methanol a small interruption in activity was seen but the catalyst swiftly recovered previous activity.[351] This implies that the metal oxide spinel catalysts investigated herein had a degree of methanol resistance making them ideal catalysts for use in methanol containing fuel cells.

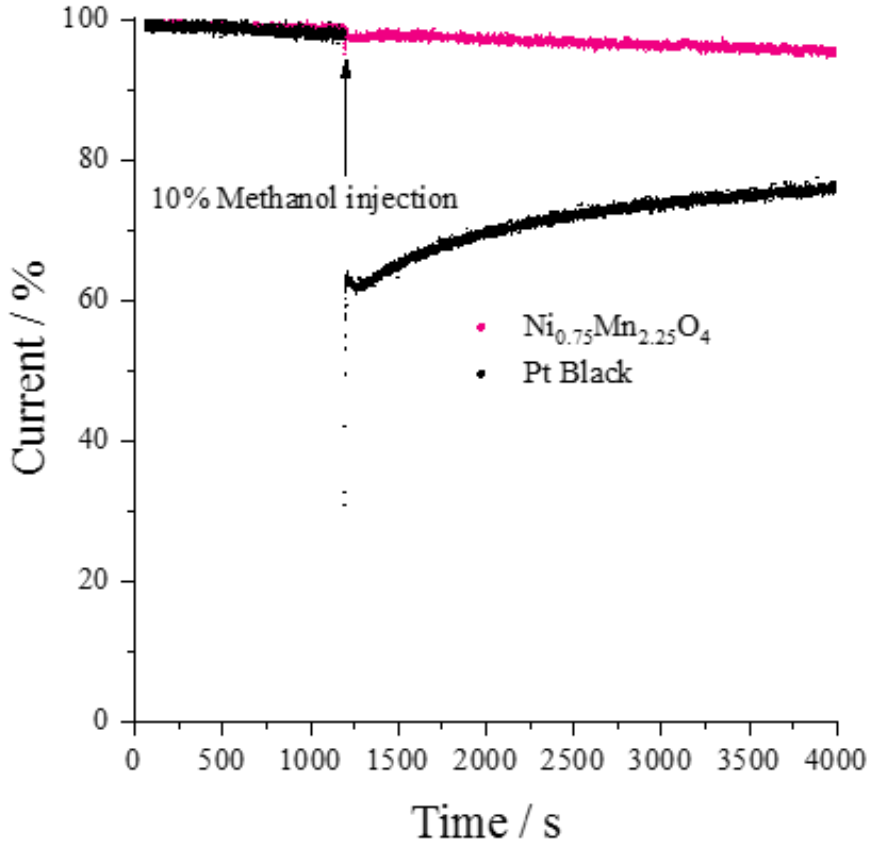

Figure 6.18: The methanol resistance test of $Ni_{0.75}Mn_{2.25}O_4$ vs a commercial Pt Black sample. Measurements were carried out over 4000 s in O_2 saturated 0.1 M KOH at −0.5 V with a scan speed of 10 mV s^{-1} and a rotation speed of 900 rpm. After 1200 s 10 % volume of methanol was injected into the electrolyte.

6.5. Summary and Conclusions

A ternary system of $Ni_xMn_yFe_zO_4$ spinel compounds was successfully synthesised via CHFS followed by a flash heat treatment at 850 °C. XRD confirmed the presence of the cubic spinel phase in all materials but also the presence of an α-Mn_2O_3 phase at high Mn concentration and a $NiMnO_3$ phase at high Ni concentration. Both of these phases were likely due to the unoptimized heat treatment step meaning impurity phases are seen at high concentrations of Ni (*A* site) or Mn (*B* site). BET surface areas were lower than the perovskites previously synthesised in this thesis and this likely lead to a reduction in the current densities observed at −0.5 V vs Ag/AgCl.

Heat maps of the overpotential for the ORR revealed that the presence of Mn was largely dictating the ORR activity, with materials containing higher at % Mn performing better overall. The best performing catalyst was $Mn_{2.25}Ni_{0.75}O_4$ with an overpotential of 0.28 V. However, there may be some contribution to activity from the Mn_2O_3 impurity phase at high at % Mn. The compositional dependence for the OER revealed that high performance correlated with low Mn and moderate Ni/Fe (relative to the space covered in this study). The best performing sample was $Ni_{1.5}Mn_{1.26}Fe_{0.24}O_4$ with an overpotential of 0.35 V. When examining the bifunctional activity by combining overpotentials to create an effective bifunctional overpotential activity was highest in areas with high Mn concentration and low Ni concentration. However, the overpotentials for the ORR were approximately 50 mV lower than for the OER so this observed bifunctional activity may be predominantly driven by the lower ORR overpotentials. The catalyst with the lowest combined bifunctional overpotential was $Mn_{2.25}Ni_{0.75}O_4$ with an overpotential of 0.64 V.

Future work could consider the optimisation of the synthesis for the spinel material. As seen in Chapter 3, it is likely that increasing the SSA of materials would increase their activity (leading to greater current densities achieved and onset potentials closer to the reversible oxygen potential). Therefore, if lower concentrations of precursors could be used and base concentrations optimised for surface area, the activity of the materials may increase. The heat treatment step could also be optimised to improve phase purity although it is likely that both impurity phases are active for the ORR/OER. Whilst this may overall increase catalytic activity, it means that deconvoluting structure/activity relationships is much harder and a phase pure material would allow for this to be done.

7. Overall Conclusions and Future Work

7.1. Summary of Conclusions

The work presented in this thesis examines the synthesis of mixed metal oxide libraries via a Continuous Hydrothermal Flow Synthesis (CHFS) method for use as oxygen reduction and oxygen evolution catalysts in alkaline electrolytes. The materials, which benefited from small particle sizes, high surface areas and a high synthesis rate, exhibited excellent catalytic properties, particularly shown through low overpotentials and high current densities.

In Chapter 3, group 2 perovskite titanates were successfully synthesised and used to prove that CHFS was a suitable synthetic method for the synthesis of libraries of materials for oxygen electrocatalysis. Chapter 4 built on the premise of perovskite synthesis via CHFS. In Chapter 5, CHFS was used to synthesise a library of $La_xMn_yNi_zO_3$ perovskite materials to examine the effect of substitution at the A/B site and the impact of the Mn^{3+}/Mn^{4+} redox couple on bifunctional activity confirmed. Finally, a series of $Ni_xFe_yMn_zO_4$ spinel materials were synthesised based on an impurity phase seen in Chapter 5 and their excellent bifunctional activity reported.

In Chapter 3, it was shown for the first time that CHFS could be successfully used to synthesise a library of perovskite materials for testing as Oxygen Reduction Reaction (ORR) catalysts. 66 perovskite $Ba_xSr_yCa_zTiO_3$ materials were rapidly synthesised and physical properties showed smooth transitions across the ternary space examined. The benefits of CHFS shown including small particle sizes and high Specific Surface Areas (SSA). Materials with high at % Sr were found to be higher surface area than those containing either high at % Ba or Ca. Electrochemical characterisation revealed that materials high in Ba and low in Sr content had high electrochemical activities whereas those high in Ca had low electrochemical activity. Whilst the overpotentials of all catalysts were larger than Pt black, this chapter proved that CHFS could be used to rapidly produce libraries of materials for testing as ORR catalysts.

Chapter 4 discussed the synthesis of *A*MnO_3 perovskite materials as ORR catalysts. Unlike in the previous chapter, these materials were known to be highly active ORR catalysts but their synthesis via CHFS had never been explored. $LaMnO_3$, $YMnO_3$ and $SmMnO_3$ were successfully synthesised but due to the high solubility of $Ca(NO_3)_2$ in solution, $CaMnO_3$ was synthesised via a sol gel route. $LaMnO_3$ outperformed the other

catalyst, exhibiting ideal catalytic characteristics including a low overpotential, high limiting current density and an RRDE observed electron transfer number of 4.

As $LaMnO_3$ was found to possess superior catalytic activity, the synthesis of $LaMnO_3$ via CHFS was explored in more depth. Various precursor concentrations and base: metal ratios were examined; no significant differences were seen in the catalytic markers. However, the catalytic activity increased significantly when a flash heat-treatment method was used to convert the CHFS precursor to $LaMnO_3$ rather than the batch heat-treatment method. The overpotential reduced from 0.34 to 0.32 V and the limiting current density increased from −6.76 to −7.12 mA cm^{-2}. The stability also increased from 8% loss to 2.5% loss over 4 hours. This put the CHFS $LaMnO_3$-FHT material in the ballpark of the industrial standard Pt black catalyst for the ORR.

In Chapter 5, the addition of a third element into the $LaMnO_3$ catalyst was examined and the materials were studied as bifunctional catalysts for both the ORR and the OER. SSA were generally much higher in the $La_xMn_yNi_zO_3$ catalysts than in the parent $LaMnO_3$ material and were higher in La deficient areas of the phase diagram. La deficient, Mn rich areas of the phase diagram had the highest activity for the ORR, with the best sample, $La_{0.83}Mn_{0.85}Ni_{0.32}O_3$, having an overpotential of 0.287 V. An anticorrelation in ORR vs OER activity was seen, with the highest OER activity seen in Ni rich materials. The best performing sample for the OER, $La_{1.18}Mn_{0.37}Ni_{0.45}O_3$, had an observed overpotential of 0.395 V. There was, however, a region in which was observed high ORR and OER activity in La deficient materials containing high at % Mn. The catalyst which performed best bifunctionally was as $La_{0.83}Mn_{0.85}Ni_{0.32}O_3$ with a combined overpotential of 0.69 V.

In Section 5.4.2.2. selected samples underwent further examination. Cyclic voltammetry revealed the presence of several redox active species on the surface. The area under the Mn^{3+}/Mn^{4+} peak was elucidated, and this could be correlated with bifunctional activity. It was therefore indicated that the proximity of the Mn^{3+}/Mn^{4+} redox couple to the reversible oxygen potential determined the bifunctional activity. RRDE results revealed that *B*-site deficient catalysts had the highest peroxide yields (and therefore lowest electron transfer numbers) at ORR potentials and that across the binary line (Mn + Ni = La) peroxide yield increased on the substitution of Mn for Ni. Chronoamperometry revealed that increasing concentrations of La led to a decrease in

the stability of the catalysts for the ORR. $La_{0.82}Mn_{0.86}Ni_{0.32}O_4$ was more stable than the commercial Pt black catalyst and only lost 5% activity over the testing window.

In Chapter 6, a library of $Ni_xMn_yFe_zO_4$ spinel materials were synthesised based of the observation of high activity seen in areas with a $NiMn_2O_4$ spinel impurity phase seen in the PXRD. SSA for these materials were generally low, between 2 and 7 $m^2\ g^{-1}$, potentially due to a change in concentration and base due to the high solubility of precursors. Materials were tested as bifunctional oxygen electrocatalysts. High ORR activity was seen along the Mn-Ni binary line with the best performing catalyst, $Mn_{2.25}Ni_{0.75}O_4$, having an overpotential of 0.28 V. In comparison to this, high OER activity was seen at lower Mn concentrations and moderate Ni and Fe concentrations. The best performing catalyst, $Ni_{1.5}Mn_{1.26}Fe_{0.24}O_4$, had an observed overpotential of 0.35 V. Bifunctional activity was greatest at high Mn concentrations and, whilst the inclusion of Fe seemed to have little effect on overall activity, the inclusion of Ni had a detrimental impact on the bifunctional overpotential. The best performing catalyst was $Mn_{2.25}Ni_{0.75}O_4$ with an overpotential of 0.64 V however, due to the lower overpotentials observed for ORR vs OER, it may be that the observed bifunctional activity is being predominantly driven by the ORR overpotential. Observed current densities for the ORR were lower than the perovskites studied in the previous chapter, but observed currents for the OER were considerably higher, tying in with the lower observed overpotentials.

In Section 6.2.2.2. selected samples underwent further investigation. Redox active peaks were identified at the surface of all materials, close to the reversible oxygen potential. RRDE results revealed that the higher the concentration of Mn in the materials, the lower the peroxide yield and therefore the closer the observed electron transfer number was to 4. When Mn concentration was constant, there was little observed change in peroxide yield, which further suggested that it was the concentration of Mn which directly contributed to the generation of H_2O_2. Chronoamperometry confirmed that the most active catalyst, $Ni_{0.75}Mn_{2.25}O_4$, was also the most stable for the ORR. Further experimentation revealed that, unlike a commercial Pt Black sample, $Ni_{0.75}Mn_{2.25}O_4$ was resistant to methanol poisoning at ORR conditions.

7.2. Future Work

The research presented herein presents a variety of possible opportunities for future studies. The work examined in this thesis shows that mixed metal oxide nanoparticles synthesised via CHFS can be used as highly active catalytic materials for both the oxygen reduction and evolution reactions in aqueous alkaline electrolyte.

Further optimisation of synthetic conditions, with a wider range of parameters could be explored. For example, optimising the base concentration and the base used could potentially increase supersaturation inside the CHFS reactor and allow for faster nucleation, leading to the synthesis of smaller materials. The possibility of adapting the CHFS reactor could be explored, adding a second reheater step allowing for the synthesis of metal oxides containing La direct in flow due to higher reaction temperatures being reached. The heat treatment step could be optimised further, a series of time-temperature studies could be carried out allowing for the exact point at which full conversion of CHFS precursor powder to perovskite/spinel material to be pinpointed. This should lead to higher surface area material being produced which in turn should lead to an increase in the catalytic activity seen.

With the exception of those materials in Chapter 3, all materials in this thesis had a conductive carbon added into the catalyst ink, before deposition of the catalyst onto the working electrode. A study could be carried out, which investigated the addition of carbon precursors into the CHFS step. This not only gives a one-step synthesis of catalysts with support, removing the need for the addition of carbon at a later point, but may allow for greater integration of the catalyst with the carbon support, increasing the catalytic activity seen. Further combinatorial studies could be carried out around the activity hotspots highlighted in this thesis. This would allow for a greater resolution of materials to be explored, possibly discovering localised activity and giving greater insight into the role Mn (in particular) plays in the bifunctional catalysis of oxygen in alkaline aqueous media.

Whilst a rotating disk or ring-disk electrode is an excellent way of gaining initial insights into the performance of an oxygen electrocatalyst, scale up into a full device, such as a reversible fuel cell or rechargeable metal-air battery, would allow for the analysis of catalysts at device scale. As all catalysts here have been tested hydrodynamically, there may be some difference between catalysts that perform well at small scale, and those that perform well at device scale.

8. Bibliography

1 P. Tryjanowski, T. L. Root, C. Rosenzweig, A. Menzel, A. Imeson, N. Estrella, G. Casassa, M. Vicarelli, Q. Wu, D. Karoly, S. Rawlins, C. Liu, P. Neofotis and B. Seguin, *Nature*, 2008, **453**, 353–357.

2 H. T. Pao and C. M. Tsai, *Energy Policy*, 2010, **38**, 7850–7860.

3 NOAA National Centers for Environmental imformation, Climate at a Glance: Global Time Series, https://ncdc.noaa.gov/cag/, (accessed 19 March 2019).

4 R. Wiser and M. Bolinger, 2011 Wind Technologies Market Report, http://www.osti.gov/bridge, (accessed 22 November 2018).

5 National Renewable Energy Laboratory, *U.S. Dep. Energy*, 2012, **1**, 280.

6 K. F. Blurton and A. F. Sammells, *J. Power Sources*, 1979, **4**, 263–279.

7 S. P. S. Badwal, S. S. Giddey, C. Munnings, A. I. Bhatt and A. F. Hollenkamp, *Front. Chem.*, 2014, **2**, 1–28.

8 J. Greeley, I. E. L. Stephens, A. S. Bondarenko, T. P. Johansson, H. A. Hansen, T. F. Jaramillo, J. Rossmeisl, I. Chorkendorff and J. K. Nørskov, *Nat. Chem.*, 2009, **1**, 552–556.

9 M. S. Dresselhaus and I. L. Thomas, *Nature*, 2001, **414**, 332–337.

10 M. A. Pellow, C. J. M. Emmott, C. J. Barnhart and S. M. Benson, *Energy Environ. Sci.*, 2015, **8**, 1938–1952.

11 M. Winter and R. J. Brodd, *Chem. Rev.*, 2004, **104**, 4245–4269.

12 R. E. Williford and J. G. Zhang, *J. Power Sources*, 2009, **194**, 1164–1170.

13 V. Neburchilov, H. Wang, J. J. Martin and W. Qu, *J. Power Sources*, 2010, **195**, 1271–1291.

14 A. Rahman, X. Wang and C. Wen, , DOI:10.1149/2.062310jes.

15 J. S. Lee, S. T. Kim, R. Cao, N. S. Choi, M. Liu, K. T. Lee and J. Cho, *Adv. Energy Mater.*, 2011, **1**, 34–50.

16 K. Barbalace, EnvironmentalChemistry.com 1995-2020, https://environmentalchemistry.com/yogi/periodic/, (accessed 29 January 2020).

17 A. J. Bard and L. R. Faulkner, *Electrochemical methods Fundamentals and Applications*, John Wiley & Sons, Inc, 2nd edn., 2001.

18 C. C. L. McCrory, S. Jung, J. C. Peters and T. F. Jaramillo, *J. Am. Chem. Soc.*, 2013, **135**, 16977–16987.

19 N. Ramaswamy and S. Mukerjee, *Adv. Phys. Chem.*, 2012, 491604.

20 B. C. H. Steele and A. Heinzel, *Nature*, 2001, **414**, 345–352.

21 B. B. Blizanac, P. N. Ross and N. M. Markovic, *Electrochim. Acta*, 2007, **52**, 2264–2271.

22 N. Ramaswamy and S. Mukerjee, *J. Phys. Chem. C*, 2011, **115**, 18015–18026.

23 X. Ge, A. Sumboja, D. Wuu, T. An, B. Li, F. W. T. Goh, T. S. A. Hor, Y. Zong and Z. Liu, *ACS Catal.*, 2015, **5**, 4643–4667.

24 A. Qaseem, F. Chen, X. Wu and R. L. Johnston, *Catal. Sci. Technol.*, 2016, **6**, 3317–3340.

25 K. B. Ibrahim, M. C. Tsai, S. A. Chala, M. K. Berihun, A. W. Kahsay, T. A. Berhe, W. N. Su and B. J. Hwang, *J. Chinese Chem. Soc.*, 2019, **66**, 829–865.

26 C. M. Sánchez-Sánchez and A. J. Bard, *Anal. Chem.*, 2009, **81**, 8094–8100.

27 L. L. J K Nørskov, J Rossmeisl, A Logadottir, *J. Phys. Chem. B*, 2004, **108**, 17886–17892.

28 F. Cheng and J. Chen, *Chem. Soc. Rev.*, 2012, **41**, 2172–2192.

29 K. J. J. Mayrhofer, D. Strmcnik, B. B. Blizanac, V. Stamenkovic, M. Arenz and N. M. Markovic, *Electrochim. Acta*, 2008, **53**, 3181–3188.

30 Z. F. Huang, J. Wang, Y. Peng, C. Y. Jung, A. Fisher and X. Wang, *Adv. Energy Mater.*, 2017, **7**, 1–21.

31 N.-T. Suen, S.-F. Hung, Q. Quan, N. Zhang, Y.-J. Xu and H. M. Chen, *Chem. Soc. Rev.*, 2017, **46**, 337–365.

32 F. Idrees, X. Zhang, M. Tahir, Z. L. Wang, J.-J. Zou, L. Pan and L. Wang, *Nano Energy*, 2017, **37**, 136–157.

33 L. Singh, U. P. Azad, S. P. Singh, V. Ganesan, U. S. Rai and Y. Lee, *Sci. Rep.*, 2017, **7**, 1–10.

34 UK Department for Transport, , DOI:10.1056/NEJMc1503870.

35 Y. Liang, Y. Li, H. Wang and H. Dai, *J. Am. Chem. Soc.*, 2013, **135**, 2013–2036.

36 J. Kunze and U. Stimming, *Angew. Chemie - Int. Ed.*, 2009, **48**, 9230–9237.

37 J. Fitzgerald and N. O'Bryan, Fuel Cells: A Better Energy Source for Earth and Space, https://www.nasa.gov/centers/glenn/technology/fuel_cells.html, (accessed 3 April 2020).

38 S. Park, Y. Shao, J. Liu and Y. Wang, *Energy Environ. Sci.*, 2012, **5**, 9331–9344.

39 A. Tewari, V. Sambhy, M. Urquidi MacDonald and A. Sen, *J. Power Sources*, 2006, **153**, 1–10.

40 G. Merle, M. Wessling and K. Nijmeijer, *J. Memb. Sci.*, 2011, **377**, 1–35.

41 N. Djilali, G. F. Mclean, T. Niet, S. Prince-Richard and N. Djilali, *Artic. Int. J. Hydrog. Energy*, 2002, **27**, 507–526.

42 E. H. Yu, X. Wang, U. Krewer, L. Li and K. Scott, *Energy Environ. Sci.*, 2012, **5**, 5668–5680.

43 E. Agel, J. Bouet and J. F. Fauvarque, *J. Power Sources*, 2001, **101**, 267–274.

44 D. R. Dekel, *J. Power Sources*, 2018, **375**, 158–169.

45 E. Fabbri, D. Pergolesi and E. Traversa, *Chem. Soc. Rev.*, 2010, **39**, 4355–4369.

46 J. Yang, A. Sudik, C. Wolvertonb and D. J. Siegelwa, *Chem. Soc. Rev.*, 2010, **39**, 656–675.

47 F. T. Wagner, B. Lakshmanan and M. F. Mathias, *J. Phys. Chem. Lett.*, 2010, **1**, 2204–2219.

48 P. Millet, A. Ranjbari, F. De Guglielmo, S. A. Grigoriev and F. Auprêtre, *Int. J. Hydrogen Energy*, 2012, **37**, 17478–17487.

49 M. Carmo, D. L. Fritz, J. Mergel and D. Stolten, *Int. J. Hydrogen Energy*, 2013, **38**, 4901–4934.

50 S. Song, H. Zhang, X. Ma, Z. Shao, R. T. Baker and B. Yi, *Int. J. Hydrogen Energy*, 2008, **33**, 4955–4961.

51 J. O. M. Bockris, *Int. J. Hydrogen Energy*, 1999, **24**, 1–15.

52 L. Swette, N. Kackley and S. A. Mccatty, *J. Power Sources*, 1991, **36**, 323–339.

53 G. Chen, D. A. Delafuente, S. Sarangapani and T. E. Mallouk, *Catal. Today*, 2001, **67**, 341–355.

54 Y. Cheng and S. P. Jiang, *Prog. Nat. Sci. Mater. Int.*, 2015, **25**, 545–553.

55 Y. N. Regmi, X. Peng, J. C. Fornaciari, M. Wei, D. J. Myers, A. Z. Weber and N. Danilovic, *Energy Environ. Sci.*, , DOI:10.1039/c9ee03626a.

56 B. Dunn, H. Kamath and J. Tarascon, *Science (80-.).*, 2011, **334**, 928.

57 J. Wang, Y. Li and X. Sun, *Nano Energy*, 2013, **2**, 443–467.

58 R. Van NOORDEN, *Nature*, 2014, 26–28.

59 B. Scrosati and J. Garche, *J. Power Sources*, 2010, **195**, 2419–2430.

60 J. Wu, H. W. Park, A. Yu, D. Higgins and Z. Chen, *J. Phys. Chem. C*, 2012, **116**, 9427–9432.

61 X. Zhang, X. Wang, Z. Xie and Z. Zhou, *Green Energy Environ.*, 2016, **1**, 4–17.

62 J. Zhang, Q. Zhou, Y. Tang, L. Zhang and Y. Li, *Chem. Sci.*, 2019, **10**, 8924–8929.

63 P. Pei, K. Wang and Z. Ma, *Appl. Energy*, 2014, **128**, 315–324.

64 Q. Sun, Y. Yang and Z. W. Fu, *Electrochem. commun.*, 2012, **16**, 22–25.

65 Y. Li and J. Lu, *ACS Energy Lett.*, 2017, **2**, 1370–1377.

66 D. M. See and R. E. White, *J. Chem. Eng. Data*, 1997, **42**, 1266–1268.

67 J. Goldstein, I. Brown and B. Koretz, *J. Power Sources*, 1999, **80**, 171–179.

68 H. Kim, G. Jeong, Y. U. Kim, J. H. Kim, C. M. Park and H. J. Sohn, *Chem. Soc. Rev.*, 2013, **42**, 9011–9034.

69 J. Vatsalarani, D. C. Trivedi, K. Ragavendran and P. C. Warrier, *J. Electrochem. Soc.*, 2005, **152**, A1974.

70 R. Jain, T. C. Adler, F. R. McLarnon and E. J. Cairns, *J. Appl. Electrochem.*, 1992, **22**, 1039–1048.

71 Y. Li, M. Gong, Y. Liang, J. Feng, J. E. Kim, H. Wang, G. Hong, B. Zhang and H. Dai, *Nat. Commun.*, 2013, **4**, 1805–1807.

72 Y. Li and H. Dai, *Chem. Soc. Rev.*, 2014, **43**, 5257–5275.

73 G. Girishkumar, B. McCloskey, A. C. Luntz, S. Swanson and W. Wilcke, *J. Phys. Chem. Lett.*, 2010, **1**, 2193–2203.

74 J. P. Zheng, R. Y. Liang, M. Hendrickson and E. J. Plichta, *J. Electrochem. Soc.*, 2008, **155**, A432.

75 T. Ogasawara, P. G. Bruce, A. Débart, P. Novák and M. Holzapfel, *J. Am. Chem. Soc.*, 2006, **128**, 1390–1393.

76 Z. Ma, X. Yuan, L. Li, Z. Ma, D. P. Wilkinson, L. Zhang and J. Zhang, *Energy Environ. Sci.*, 2015, **8**, 2144–2198.

77 A. Debart, A. J. Paterson, J. Bao and P. G. Bruce, *Angew. Chemie - Int. Ed.*, 2008, **47**, 4521–4524.

78 Y. Lu, H. A. Gasteiger, M. C. Parent, V. Chiloyan and Y. Shao-horn, *Electrochem. Solid-State Lett.*, 2010, **13**, A69–A72.

79 M. M. Natile, G. Eger, P. Batocchi, F. Mauvy and A. Glisenti, *Int. J. Hydrogen Energy*, 2017, **42**, 1724–1735.

80 Z. L. Wang, D. Xu, J. J. Xu and X. B. Zhang, *Chem. Soc. Rev.*, 2014, **43**, 7746–7786.

81 W. T. Hong, M. Risch, K. A. Stoerzinger, A. Grimaud, J. Suntivich and Y. Shao-Horn, *Energy Environ. Sci.*, 2015, **8**, 1404–1427.

82 M. R. Tarasevich and O. V. Korchagin, *Russ. J. Electrochem.*, 2013, **49**, 600–618.

83 X. Ren, Q. Lv, L. Liu, B. Liu, Y. Wang, A. Liu and G. Wu, *Sustain. Energy Fuels*, 2019, **4**, 15–30.

84 M. K. Debe, *Nature*, 2012, **486**, 43–51.

85 R. Loukrakpam, J. Luo, T. He, Y. Chen, Z. Xu, P. N. Njoki, B. N. Wanjala, B. Fang, D. Mott, J. Yin, J. Klar, B. Powell and C. J. Zhong, *J. Phys. Chem. C*, 2011, **115**, 1682–1694.

86 S. Sui, X. Wang, X. Zhou, Y. Su, S. Riffat and C. jun Liu, *J. Mater. Chem. A*, 2017, **5**, 1808–1825.

87 A. Damjanovic, A. Dey and J. O. Bockris, *J. Electrochem. Soc.*, 1966, **113**, 739.

88 N. Danilovic, R. Subbaraman, K. C. Chang, S. H. Chang, Y. J. Kang, J. Snyder, A. P. Paulikas, D. Strmcnik, Y. T. Kim, D. Myers, V. R. Stamenkovic and N. M. Markovic, *J. Phys. Chem. Lett.*, 2014, **5**, 2474–2478.

89 T. Reier, M. Oezaslan and P. Strasser, *ACS Catal.*, 2012, **2**, 1765–1772.

90 Y. Lee, J. Suntivich, K. J. May, E. E. Perry and Y. Shao-Horn, *J. Phys. Chem. Lett.*, 2012, **3**, 399–404.

91 X. Wang, R. Schlögl, A. Thomas, B. Frank, D. S. Su, J. Paraknowitsch and J. Zhang, *ChemSusChem*, 2010, **3**, 169–180.

92 Y. Zheng, Y. Jiao, M. Jaroniec, Y. Jin and S. Z. Qiao, *Small*, 2012, **8**, 3550–3566.

93 L. Dai, K. Gong, F. Du, Z. Xia and M. Durstock, *Science (80-.).*, 2AD, **323**, 760–764.

94 L. Yang, Y. Zhao, S. Chen, Q. Wu, X. Wang and Z. Hu, *Chinese J. Catal.*, 2013, **34**, 1986–1991.

95 L. Yang, S. Jiang, Y. Zhao, L. Zhu, S. Chen, X. Wang, Q. Wu and J. Ma, *Angew. Chemie - Int. Ed.*, 2011, 7132–7135.

96 X. Liu and L. Dai, *Nat. Rev. Mater.*, , DOI:10.1038/natrevmats.2016.64.

97 N. Cheng, Q. Liu, J. Tian, Y. Xue, A. M. Asiri, H. Jiang, Y. He and X. Sun, *Chem. Commun.*, 2015, **51**, 1616–1619.

98 X. Gong, S. Liu, C. Ouyang, P. Strasser and R. Yang, *ACS Catal.*, 2015, **5**, 920–927.

99 C. Goswami, K. K. Hazarika and P. Bharali, *Mater. Sci. Energy Technol.*, 2018, **1**, 117–128.

100 Y. Xue, S. Sun, Q. Wang, Z. Dong and Z. Liu, *J. Mater. Chem. A*, 2018, **6**, 10596–10626.

101 J. K. Cooper, C. Zhu, J. W. Beeman, A. Schwartzberg, C. Kisielowski, L. H. Hess, K. A. Walczak, C. Wang, F. M. Toma, M. Favaro, S. Gul, J. Yano, I. D. Sharp and J. Yang, *Nat. Mater.*, 2016, **16**, 335–341.

102 M. Zhang, M. De Respinis and H. Frei, *Nat. Chem.*, 2014, **6**, 362–367.

103 A. Bonnefont, A. S. Ryabova, T. Schott, G. Kéranguéven, S. Y. Istomin, E. V. Antipov and E. R. Savinova, *Curr. Opin. Electrochem.*, 2019, **14**, 23–31.

104 G. Kéranguéven, C. Ulhaq-Bouillet, V. Papaefthimiou, S. Royer and E. Savinova, *Electrochim. Acta*, 2017, **245**, 156–164.

105 W. Vielstich, A. Lamm and H. A. Gasteiger, *Handbook of Fuel Cells - Fundamentals, Technology and Applications*, Wiley, Chichester, 2003.

106 J. Suntivich, H. A. Gasteiger, N. Yabuuchi, H. Nakanishi, J. B. Goodenough and Y. Shao-Horn, *Nat. Chem.*, 2011, **3**, 546–550.

107 Y. Matsumoto, H. Yoneyama and H. Tamura, *J. Electroanal. Chem.*, 1977, **79**, 319–326.

108 Y. Matsumoto, H. Yoneyama and H. Tamura, *J. Electroanal. Chem.*, 1977, **83**, 237–243.

109 H. Fei, Y. Yang, J. M. Tour, G. Ruan and C. Xiang, *ACS Nano*, 2014, **8**, 9518–9523.

110 L. Han, S. Dong and E. Wang, *Adv. Mater.*, 2016, **28**, 9266–9291.

111 S. Gupta, W. Kellogg, H. Xu, X. Liu, J. Cho and G. Wu, *Chem. - An Asian J.*, 2016, **11**, 10–21.

112 D. Chen, C. Chen, Z. M. Baiyee, Z. Shao and F. Ciucci, *Chem. Rev.*, 2015, **115**, 9869–9921.

113 Y. Zhu, W. Zhou and Z. Shao, *Small*, 2017, **13**, 1–25.

114 R. Mohamed, X. Cheng, E. Fabbri, P. Levecque, R. Kotz, O. Conrad and T. J. Schmidt, *J. Electrochem. Soc.*, 2015, **162**, F579–F586.

115 K. Momma and F. Izumi, *J. Appl. Crystallogr.*, 2011, **44**, 1272–1276.

116 M. Risch, *Catalysts*, 2017, **7**, 154.

117 V. Goldschmidt, *Naturwissenschaften*, 1926, **14**, 477–485.

118 W. T. Hong, M. Risch, K. A. Stoerzinger, A. Grimaud, J. Suntivich and Y. Shao-Horn, *Energy Environ. Sci.*, 2015, **8**, 1404–1427.

119 J. O. Bockris, *J. Electrochem. Soc.*, 1984, **131**, 290.

120 C. Li, Z. Yu, H. Liu and K. Chen, *J. Phys. Chem. Solids*, 2018, **113**, 151–156.

121 N. Kim, Y. J. Sa, T. S. Yoo, S. R. Choi, R. A. Afzal, S. H. Joo and J. Park, *Sci. Adv.*

122 D. Zhang, Y. Song, Z. Du, L. Wang, Y. Li and J. B. Goodenough, *J. Mater. Chem. A*, 2015, **3**, 9421–9426.

123 J. Sunarso, Y. Zhong, Z. Shao, W. Zhou and Y. Zhu, *Adv. Funct. Mater.*, 2016, **26**, 5862–5872.

124 J. Suntivich, K. J. May, H. A. Gasteiger, J. B. Goodenough and Y. Shao-Horn, *Science (80-.).*, 2011, **334**, 1383–1385.

125 S. Zhou, X. Miao, X. Zhao, C. Ma, Y. Qiu, Z. Hu, J. Zhao, L. Shi and J. Zeng, *Nat. Commun.*, 2016, **7**, 1–7.

126 X. Liu, H. Gong, T. Wang, H. Guo, L. Song, W. Xia, B. Gao, Z. Jiang, L. Feng and J. He, *Chem. - An Asian J.*, 2018, **13**, 528–535.

127 J. K. Burdett, S. L. Price and G. D. Price, *J. Am. Chem. Soc.*, 1982, **104**, 92–95.

128 Q. Zhao, Z. Yan, C. Chen and J. Chen, *Chem. Rev.*, 2017, **117**, 10121–10211.

129 C. Wei, Z. Feng, G. G. Scherer, J. Barber, Y. Shao-Horn and Z. J. Xu, *Adv. Mater.*, 2017, **29**, 1–8.

130 J. Du, Y. Pan, T. Zhang, X. Han, F. Cheng and J. Chen, *J. Mater. Chem.*, 2012,

22, 15812–15818.

131 C. Li, X. Han, F. Cheng, Y. Hu, C. Chen and J. Chen, *Nat. Commun.*, 2015, **6**, 1–8.

132 F. Cheng, J. Shen, B. Peng, Y. Pan, Z. Tao and J. Chen, *Nat. Chem.*, 2011, **3**, 79–84.

133 X. He, F. Yin, Y. Li, H. Wang, J. Chen, Y. Wang and B. Chen, *ACS Appl. Mater. Interfaces*, 2016, **8**, 26740–26757.

134 G. Oskam, *J. Sol-Gel Sci. Technol.*, 2006, **37**, 161–164.

135 C. R. Kagan and C. B. Murray, *Nat. Nanotechnol.*, 2015, **10**, 1013–1026.

136 N. Sharma, H. Ojha, A. Bharadwaj, D. P. Pathak and R. K. Sharma, *RSC Adv.*, 2015, **5**, 53381–53403.

137 N. Lopez, T. V. W. Janssens, B. S. Clausen, Y. Xu, M. Mavrikakis, T. Bligaard and J. K. Nørskov, *J. Catal.*, 2004, **223**, 232–235.

138 Y. Lu, Q. Yan, J. Han, B. Cao, J. Street and F. Yu, *Fuel*, 2017, **193**, 369–384.

139 G. Melaet, W. T. Ralston, C. S. Li, S. Alayoglu, K. An, N. Musselwhite, B. Kalkan and G. A. Somorjai, *J. Am. Chem. Soc.*, 2014, **136**, 2260–2263.

140 S. Schauermann, N. Nilius, S. Shaikhutdinov and H. J. Freund, *Acc. Chem. Res.*, 2013, **46**, 1673–1681.

141 A. Biswas, I. S. Bayer, A. S. Biris, T. Wang, E. Dervishi and F. Faupel, *Adv. Colloid Interface Sci.*, 2012, **170**, 2–27.

142 K. Gregorczyk and M. Knez, *Prog. Mater. Sci.*, 2016, **75**, 1–37.

143 T. Prasad Yadav, R. Manohar Yadav and D. Pratap Singh, *Nanosci. Nanotechnol.*, 2012, **2**, 22–48.

144 S. P. Li, D. Peyrade, M. Natali, A. Lebib, Y. Chen, U. Ebels, L. D. Buda and K. Ounadjela, *Phys. Rev. Lett.*, 2001, **86**, 1102–1105.

145 Y. Zhang, L. Zhong and D. Duan, *Ceram. Int.*, 2015, **41**, 13516–13524.

146 M. Breedon, P. Spizzirri, M. Taylor, J. Du Plessis, D. McCulloch, J. Zhu, L. Yu, Z. Hu, C. Rix, W. Wlodarski and K. Kalantar-zadeh, *Cryst. Growth Des.*, 2010, **10**, 430–439.

147 D. Bonvin, H. Hofmann and M. Mionic Ebersold, *J. Nanoparticle Res.*, , DOI:10.1007/s11051-016-3695-4.

148 J. E. Evans, K. L. Jungjohann, N. D. Browning and I. Arslan, *Nano Lett.*, 2011, **11**, 2809–2813.

149 S. S. and and H. Zeng, *J. Am. Chem. Soc.*, 2002, 8204–8205.

150 E. M. Chan, R. A. Mathies and A. P. Alivisatos, *Nano Lett.*, 2003, **3**, 199–201.

151 J. Polte, T. T. Ahner, F. Delissen, S. Sokolov, F. Emmerling, A. F. Thünemann and R. Kraehnert, *J. Am. Chem. Soc.*, 2010, **132**, 1296–1301.

152 J. Polte, *CrystEngComm*, 2015, **17**, 6809–6830.

153 V. K. La Mer, *Ind. Eng. Chem.*, 1952, **44**, 1270–1277.

154 A. D. Randolph and M. D. Cise, *AIChE J.*, 1972, **18**, 798–807.

155 N. T. K. Thanh, N. Maclean and S. Mahiddine, *Chem. Rev.*, 2014, **114**, 7610–7630.

156 S. G. Kwon and T. Hyeon, *Small*, 2011, **7**, 2685–2702.

157 T. Tadros, *Encycl. Colloid Interface Sci.*, 2013, **1801**, 820–820.

158 H. Fukuoka, T. Isami and S. Yamanaka, *Chem. Lett.*, 1997, 703–704.

159 A. Waindich, A. Möbius and M. Müller, *J. Memb. Sci.*, 2009, **337**, 182–187.

160 R. A. Richardson, R. M. Ormerod and J. W. Cotton, *Ionics (Kiel).*, 2003, **9**, 77–82.

161 M. Naito, S. Ohara, K. Sato, A. Kondo, H. Abe and H. Shimoda, *Mater. Lett.*, 2008, **62**, 2957–2959.

162 L. Da Conceião, A. M. Silva, N. F. P. Ribeiro and M. M. V. M. Souza, *Mater. Res. Bull.*, 2011, **46**, 308–314.

163 A. M. Huízar-Félix, T. Hernández, S. de la Parra, J. Ibarra and B. Kharisov, *Powder Technol.*, 2012, **229**, 290–293.

164 S. Komarneni, I. R. Abothu and A. V. Prasada Rao, *J. Sol-Gel Sci. Technol.*, 1999, **15**, 263–270.

165 P. Cousin and R. A. Ross, *Mater. Sci. Eng. A*, 1990, **130**, 119–125.

166 M. Kakihana, M. Arima, M. Yoshimura, N. Ikeda and Y. Sugitani, *J. Alloys Compd.*, 1999, **283**, 102–105.

167 M. James, D. Cassidy, K. F. Wilson, J. Horvat and R. L. Withers, *Solid State Sci.*, 2004, **6**, 655–662.

168 X. Ding, Y. Liu, L. Gao and L. Guo, *J. Alloys Compd.*, 2008, **458**, 346–350.

169 J. Sunarso, S. Baumann, J. M. Serra, W. A. Meulenberg, S. Liu, Y. S. Lin and J. C. Diniz da Costa, *J. Memb. Sci.*, 2008, **320**, 13–41.

170 D. D. Athayde, D. F. Souza, A. M. A. Silva, D. Vasconcelos, E. H. M. Nunes, J. C. D. Da Costa and W. L. Vasconcelos, *Ceram. Int.*, 2016, **42**, 6555–6571.

171 R. A. Sheldon, *Green Chem.*, 2005, **7**, 267–278.

172 E. Lester, P. Blood, J. Denyer, D. Giddings, B. Azzopardi and M. Poliakoff, *J. Supercrit. Fluids*, 2006, **37**, 209–214.

173 P. Pollet, C. A. Eckert and C. L. Liotta, *WIT Trans. Ecol. Environ.*, 2011, **154**, 21–31.

174 K. Sue, T. Adschiri and K. Arai, *Ind. Eng. Chem. Res.*, 2002, **41**, 3298–3306.

175 T. Adschiri, Y. W. Lee, M. Goto and S. Takami, *Green Chem.*, 2011, **13**, 1380–1390.

176 H. Weingärtner and E. U. Franck, *Angew. Chemie - Int. Ed.*, 2005, **44**, 2672–2692.

177 A. V. Bandura and S. N. Lvov, *J. Phys. Chem. Ref. Data*, 2006, **35**, 15–30.

178 J. A. Darr, J. Zhang, N. M. Makwana and X. Weng, *Chem. Rev.*, 2017, **117**, 11125–11238.

179 H. Hayashi and Y. Hakuta, *Materials (Basel).*, 2010, **3**, 3794–3817.

180 K. Byrappa and T. Adschiri, *Prog. Cryst. Growth Charact. Mater.*, 2007, **53**, 117–166.

181 V. Subramanian, H. Zhu, R. Vajtai, P. M. Ajayan and B. Wei, *J. Phys. Chem. B*, 2005, **109**, 20207–20214.

182 J. S. Lee and S. C. Choi, *Mater. Lett.*, 2004, **58**, 390–393.

183 Y. Chen, F. Li, T. Li and W. Cao, *CrystEngComm*, 2016, **18**, 3585–3593.

184 C. J. Denis, C. J. Tighe, R. I. Gruar, N. M. Makwana and J. A. Darr, *Cryst. Growth Des.*, 2015, **15**, 4256–4265.

185 E. Lester, G. Aksomaityte, J. Li, S. Gomez, J. Gonzalez-Gonzalez and M. Poliakoff, *Prog. Cryst. Growth Charact. Mater.*, 2012, **58**, 3–13.

186 R. I. Gruar, C. J. Tighe, P. Southern, Q. A. Pankhurst and J. A. Darr, *Ind. Eng. Chem. Res.*, 2015, **54**, 7436–7451.

187 G. P. Evans, M. J. Powell, I. D. Johnson, D. P. Howard, D. Bauer, J. A. Darr and I. P. Parkin, *Sensors Actuators, B Chem.*, 2018, **255**, 1119–1129.

188 P. Marchand, N. M. Makwana, C. J. Tighe, R. I. Gruar, I. P. Parkin, C. J. Carmalt and J. A. Darr, *ACS Comb. Sci.*, 2016, **18**, 130–137.

189 D. W. Matson, J. C. Linehan, J. G. Darab and M. F. Buehler, *Energy and Fuels*, 1994, **8**, 10–18.

190 T. Adschiri, K. Kanazawa and K. Arai, *J. Am. Ceram. Soc.*, 1992, **75**, 1019–1022.

191 Y. Hakuta, K. Scino, H. Ura, T. Adschiri, H. Takizawa and K. Aral, *J. Mater. Chem.*, 1999, **9**, 2671–2674.

192 E. Lester, P. J. Blood, J. P. Denyer, B. J. Azzopardi, J. Li and M. Poliakoff, *Mater. Res. Innov.*, 2010, **14**, 19–26.

193 D. Housley, T. Huddle, E. Lester and M. Poliakoff, *Chem. Eng. J.*, 2016, **287**, 350–358.

194 L. L. Toft, D. F. Aarup, M. Bremholm, P. Hald and B. B. Iversen, *J. Solid State Chem.*, 2009, **182**, 491–495.

195 R. I. Gruar, C. J. Tighe and J. A. Darr, *Ind. Eng. Chem. Res.*, 2013, **52**, 5270–5281.

196 S. I. Kawasaki, K. Sue, R. Ookawara, Y. Wakashima, A. Suzuki, Y. Hakuta and K. Arai, *J. Supercrit. Fluids*, 2010, **54**, 96–102.

197 S. A. S Kawasaki, Sue K, Ookawara R, Wakashima Y, *Oleo Sci.*, 2010, **59**, 557–562.

198 C. J. Tighe, R. I. Gruar, C. Y. Ma, T. Mahmud, X. Z. Wang and J. A. Darr, *J. Supercrit. Fluids*, 2012, **62**, 165–172.

199 C. Y. Ma, M. Chen and X. Z. Wang, *Chem. Eng. Sci.*, 2014, **109**, 26–37.

200 J. Sánchez-Oneto, J. R. Portela, E. Nebot and E. Martínez de la Ossa, *J. Hazard. Mater.*, 2007, **144**, 639–644.

201 K. Minami, T. Arita, T. Adschiri, K. Moriya and T. Naka, *Chem. Lett.*, 2010, **39**, 961–963.

202 X. Weng, J. K. Cockcroft, G. Hyett, M. Vickers, P. Boldrin, C. C. Tang, S. P. Thompson, J. E. Parker, J. C. Knowles, I. Rehman, I. Parkin, J. R. G. Evans and J. A. Darr, *J. Comb. Chem.*, 2009, **11**, 829–834.

203 R. Quesada-Cabrera, X. Weng, G. Hyett, R. J. H. Clark, X. Z. Wang and J. A. Darr, *ACS Comb. Sci.*, 2013, **15**, 458–463.

204 S. H. Park, C. H. Choi, J. K. Koh, C. Pak, S. A. Jin and S. I. Woo, *ACS Comb. Sci.*, 2013, **15**, 572–579.

205 S. Guerin, B. E. Hayden, C. E. Lee, C. Mormiche and A. E. Russell, *J. Phys. Chem. B*, 2006, **110**, 14355–14362.

206 J. M. Serra and V. B. Vert, *ChemSusChem*, 2009, **2**, 957–961.

207 J. Du, T. Zhang, F. Cheng, W. Chu, Z. Wu and J. Chen, *Inorg. Chem.*, 2014, **53**, 9106–9114.

208 A. Ciurzyńska and A. Lenart, *Polish J. Food Nutr. Sci.*, 2011, **61**, 165–171.

209 J. Barely, Basic Principles of Freeze Drying, https://www.spscientific.com/freeze-drying-lyophilization-basics/, (accessed 19 February 2020).

210 W. Abdelwahed, G. Degobert, S. Stainmesse and H. Fessi, *Adv. Drug Deliv. Rev.*, 2006, **58**, 1688–1713.

211 P. W. H. Bragg and W. L. Bragg, *Proc. R. Soc. A*, 1913, **88**, 428–438.

212 A. Jablonski, *Surf. interface Anal.*, 1993, **20**, 317–321.

213 K. S. W. Sing, *Adv. Colloid Interface Sci.*, 1998, **76**–**77**, 3–11.

214 L. Dixit, D. L. Gerrard and H. J. Bowley, *Laser raman spectra of transition metal oxides and catalysts*, 1986, vol. 22.

215 S. A. Leslie and J. C. Mitchell, *Palaeontology*, 2007, **50**, 1459–1461.

216 J. Nikolic, E. Expósito, J. Iniesta, J. González-Garcia and V. Montiel, *J. Chem. Educ.*, 2000, **77**, 1191.

217 Y. H. Fang and Z. P. Liu, *ACS Catal.*, 2014, **4**, 4364–4376.

218 K. S. Gupta, University College London, 2018.

219 T. Sönmez, S. J. Thompson, S. W. T. Price, D. Pletcher and A. E. Russell, *J. Electrochem. Soc.*, 2016, **163**, H884–H890.

220 M. A. Tarselli, *Nat. Chem.*, 2013, **5**, 546.

221 C. Y. Su, Y. Otsuka, C. Y. Huang, D. F. Hennings, C. Pithan, F. T. Shiao and R. Waser, *Ceram. Int.*, 2013, **39**, 6673–6680.

222 W. William, W. Chung, W. Huang, W. Lin, W. Lin, Y. Jiang and C. Chen, *J. Taiwan Inst. Chem. Eng.*, 2013, **44**, 660–669.

223 H. Yoshida, L. Zhang, M. Sato, T. Morikawa and T. Kajino, *Catal. Today*, 2015, **251**, 132–139.

224 E. A. R. Assirey, *Saudi Pharm. J.*, 2019, **27**, 817–829.

225 Y. Zhao, Y. Hang, Y. Zhang, Z. Wang, Y. Yao, X. He, C. Zhang and D. Zhang, *Electrochim. Acta*, 2017, **232**, 296–302.

226 J. T. Mefford, X. Rong, A. M. Abakumov, W. G. Hardin, S. Dai, A. M. Kolpak, K. P. Johnston and K. J. Stevenson, *Nat. Commun.*, , DOI:10.1038/ncomms11053.

227 T. Hyodo, M. Hayashi, S. Mitsutake, N. Miura and N. Yamazoe, *J. Appl. Electrochem.*, 1997, **27**, 745.

228 W. Yang, J. Salim, S. Li, C. Sun, L. Chen, J. B. Goodenough and Y. Kim, *J. Mater. Chem.*, 2012, **22**, 18902–18907.

229 C. F. Chen, G. King, R. M. Dickerson, P. A. Papin, S. Gupta, W. R. Kellogg and G. Wu, *Nano Energy*, 2015, **13**, 423–432.

230 E. C. Vreeland, J. Watt, G. B. Schober, B. G. Hance, M. J. Austin, A. D. Price, B. D. Fellows, T. C. Monson, N. S. Hudak, L. Maldonado-Camargo, A. C. Bohorquez, C. Rinaldi and D. L. Huber, *Chem. Mater.*, 2015, **27**, 6059–6066.

231 A. Chighine, G. Sechi and M. Bradley, *Drug Discov. Today*, 2007, **12**, 459–464.

232 D. Schäfer, C. Mardare, A. Savan, M. D. Sanchez, B. Mei, W. Xia, M. Muhler, A. Ludwig and W. Schuhmann, *Anal. Chem.*, 2011, **83**, 1916–1923.

233 G. Pfaff, *Chem. Mater.*, 1994, **6**, 58–62.

234 K. Uchino, E. Sadanaga and T. Hirose, *J. Am. Ceram. Soc.*, 1989, **72**, 1555–1558.

235 S. Burnside, J.-E. Moser, K. Brooks, M. Grätzel and D. Cahen, *J. Phys. Chem. B*, 1999, **103**, 9328–9332.

236 G. Panomsuwan, N. Saito and T. Ishizaki, *J. Mater. Chem. A*, 2015, **3**, 9972-9981A.

237 S. Vesztergom, N. Barankai, N. Kovács, M. Ujvári, P. Broekmann, H. Siegenthaler and G. G. Láng, *Electrochem. commun.*, 2016, **68**, 54–58.

238 P. Research, No Title, https://pineresearch.com/shop/product-category/electrodes/rrde/, (accessed 27 August 2020).

239 G. Durst, M. Grotenhuis and A. G. Barkow, *J. Am. Ceram. Soc.*, 1950, **33**, 133–139.

240 von L. Vegard, *Zeitschrift für Phys.*, 1921, **5**, 17–26.

241 R. D. Shannon, *Acta Cryst. A*, 1976, **32**, 751–767.

242 A. W. Hume-rothery, G. W. Mabbott and K. M. C. Evans, *Philos. Trans. A. Math. Phys. Eng. Sci.*, 1934, **233**, 1–97.

243 S. Aoyagi, Y. Kuroiwa, A. Sawada, I. Yamashita and T. Atake, *J. Phys. Soc. Japan*.

244 Y. A. Abramov, V. G. Tsirelson, V. E. Zavodnik, S. A. Ivanov and I. D. Brown, *Acta Crystallogr. Sect. B*, 1995, **51**, 942–951.

245 R. H. Buttner and E. N. Maslen, *Acta Crystallogr. Sect. B*, 1992, **48**, 644–649.

246 S. Treimer, A. Tang and D. C. Johnson, *Electroanalysis*, 2002, **14**, 165–171.

247 F. Lu, J. Sui, J. Su, C. Jin, M. Shen and R. Yang, *J. Power Sources*, 2014, **271**, 55–59.

248 Z. Chen, D. Higgins, A. Yu, L. Zhang and J. Zhang, *Energy Environ. Sci.*, 2011, **4**, 3167–3192.

249 N. M. Marković, H. A. Gasteiger and P. N. Ross, *J. Phys. Chem.*, 1996, **100**, 6715–6721.

250 K. A. Stoerzinger, M. Risch, B. Han and Y. Shao-Horn, *ACS Catal.*, 2015, **5**, 6021–6031.

251 A. S. Ryabova, F. S. Napolskiy, T. Poux, S. Y. Istomin, A. Bonnefont, D. M. Antipin, A. Y. Baranchikov, E. E. Levin, A. M. Abakumov, G. Kéranguéven, E. V. Antipov, G. A. Tsirlina and E. R. Savinova, *Electrochim. Acta*, 2016, **187**, 161–172.

252 I. Roche and K. Scott, *J. Appl. Electrochem.*, 2009, **39**, 197–204.

253 F. Cheng, Y. Su, J. Liang, Z. Tao and J. Chen, *Chem. Mater.*, 2010, **22**, 898–905.

254 V. Celorrio, L. Calvillo, G. Granozzi, A. E. Russell and D. J. Fermin, *Top. Catal.*, 2018, **61**, 154–161.

255 T. Hyodo, *J. Electrochem. Soc.*, 1996, **143**, L266.

256 M. Yuasa, N. Yamazoe and K. Shimanoe, *J. Electrochem. Soc.*, 2011, **158**, 411–416.

257 D. Kan, Y. Orikasa, K. Nitta, H. Tanida, R. Kurosaki, T. Nishimura, T. Sasaki, H. Guo, Y. Ozaki, Y. Uchimoto and Y. Shimakawa, *J. Phys. Chem. C*, 2016, **120**, 6006–6010.

258 V. Celorrio, L. J. Morris, M. Cattelan, N. A. Fox and D. J. Fermin, *MRS Commun.*, 2017, **7**, 193–198.

259 X. Liu, C. Chen, Y. Zhao and B. Jia, *J. Nanomater.*, 2013, 1–7.

260 W. Wang, J. Geng, L. Kuai, M. Li and B. Geng, *Chem. - A Eur. J.*, 2016, **22**, 9909–9913.

261 J. H. Lee and J. Y. Ham, *Korean J. Chem. Eng.*, 2006, **23**, 714–719.

262 N. M. Islam, T. Noguchi, Y. Hakuta and H. Hayashi, *Nanosci. Nanotechnol. Lett.*, 2011, **3**, 324–327.

263 D. Rangappa, S. Ohara, M. Umetsu, T. Naka and T. Adschiri, *J. Supercrit. Fluids*, 2008, **44**, 441–445.

264 W. G. Hardin, J. T. Mefford, D. A. Slanac, B. B. Patel, X. Wang, S. Dai, X. Zhao, R. S. Ruoff, K. P. Johnston and K. J. Stevenson, *Chem. Mater.*, 2014, **26**, 3368–3376.

265 W. G. Hardin, D. A. Slanac, X. Wang, S. Dai, K. P. Johnston and K. J. Stevenson, *J. Phys. Chem. Lett.*, 2013, **4**, 1254–1259.

266 W. Zhou and J. Sunarso, *J. Phys. Chem. Lett.*, 2013, **4**, 2982–2988.

267 M. Retuerto, A. G. Pereira, F. J. Pérez-Alonso, M. A. Peña, J. L. G. Fierro, J. A. Alonso, M. T. Fernández-Díaz, L. Pascual and S. Rojas, *Appl. Catal. B Environ.*, 2017, **203**, 363–371.

268 W. J. Yin, B. Weng, J. Ge, Q. Sun, Z. Li and Y. Yan, *Energy Environ. Sci.*, 2019, **12**, 442–462.

269 J. Du, T. Zhang, F. Cheng, W. Chu, Z. Wu and J. Chen, *Inorg. Chem.*, 2014, **53**, 9106–9114.

270 W. L. Wang, Q. Meng, X. Weng and Z. Wu, *Catal. Commun.*, 2016, **84**, 167–170.

271 Y. C. Hou, M. W. Ding, S. K. Liu, S. K. Wu and Y. C. Lin, *RSC Adv.*, 2014, **4**, 5329–5338.

272 C. N. Borca, S. Canulescu, F. Loviat, T. Lippert, D. Grolimund, M. Döbeli, J. Wambach and A. Wokaun, *Appl. Surf. Sci.*, 2007, **254**, 1352–1355.

273 B. T. Sone, E. Manikandan, A. Gurib-Fakim and M. Maaza, *J. Alloys Compd.*, 2015, **650**, 357–362.

274 M. J. Dzara, J. M. Christ, P. Joghee, C. Ngo, C. A. Cadigan, G. Bender, R. M. Richards, R. O'Hayre and S. Pylypenko, *J. Power Sources*, 2018, **375**, 265–276.

275 C. L. Li and Y. C. Lin, *Appl. Catal. B Environ.*, 2011, **107**, 284–293.

276 Y. Zhang, S. Chen, Y. Wang, W. Ding, R. Wu, L. Li, X. Qi and Z. Wei, *J. Power Sources*, 2015, **273**, 62–69.

277 G. Zhang, S. Sun, M. Cai, Y. Zhang, R. Li and X. Sun, *Sci. Rep.*, , DOI:10.1038/srep01526.

278 J. Lü, Y. Zhang, Z. Lü, X. Huang, Z. Wang, X. Zhu and B. Wei, *RSC Adv.*, 2015, **5**, 5858–5862.

279 G. Zhong, S. Xu, L. Liu, C. Z. Zheng, J. Dou, F. Wang, X. Fu, W. Liao and H.

Wang, *ChemElectroChem*, 2020, **7**, 1107–1114.

280 K. N. Jung, J. H. Jung, W. Bin Im, S. Yoon, K. H. Shin and J. W. Lee, *ACS Appl. Mater. Interfaces*, 2013, **5**, 9902–9907.

281 V. Celorrio, L. Calvillo, C. A. M. van den Bosch, G. Granozzi, A. Aguadero, A. E. Russell and D. J. Fermín, *ChemElectroChem*, 2018, **5**, 3044–3051.

282 R. M. Piticescu, P. Vilarnho, L. M. Popescu and R. R. Piticescu, *J. Optoelectron. Adv. Mater.*, 2006, **8**, 543–547.

283 Y. Xue, H. Miao, S. Sun, Q. Wang, S. Li and Z. Liu, *RSC Adv.*, 2017, **7**, 5214–5221.

284 A. Bonakdarpour, M. Lefevre, R. Yang, F. Jaouen, T. Dahn, J. P. Dodelet and J. R. Dahn, *Electrochem. Solid-State Lett.*, 2008, **11**, B105–B108.

285 A. Ashok, A. Kumar, R. R. Bhosale, F. Almomani, S. S. Malik, S. Suslov and F. Tarlochan, *J. Electroanal. Chem.*, 2018, **809**, 22–30.

286 P. K. Shen, C.-Y. Wang, S. P. Jiang, X. Sun and J. Zhang, *Electrochemical Energy: Advanced Materials and Technologies*, CRC Press, 2018.

287 E. Davari and D. G. Ivey, *Sustain. Energy Fuels*, 2018, **2**, 39–67.

288 H. F. Wang, C. Tang and Q. Zhang, *Adv. Funct. Mater.*, 2018, **28**, 1–22.

289 J. Suntivich, K. J. May, H. a Gasteiger, J. B. Goodenough and Y. Shao-horn, *Science (80-.).*, 2011, **334**, 2010–2012.

290 M. Sakthivel, S. Bhandari and J. F. Drillet, *ECS Electrochem. Lett.*, 2015, **4**, A56–A58.

291 S. Egelund, M. Caspersen, A. Nikiforov and P. Møller, *Int. J. Hydrogen Energy*, 2016, **41**, 10152–10160.

292 P. Li, C. Tian, W. Yang, W. Zhao and Z. Lü, *Front. Mater. Sci.*, 2019, **13**, 277–287.

293 K. Bradley, K. Giagloglou, B. E. Hayden, H. Jungius and C. Vian, *Chem. Sci.*, 2019, **10**, 4609–4617.

294 P. Scardi, M. Leoni and K. R. Beyerlein, *Zeitschrift fur Krist.*, 2011, **226**, 924–933.

295 J. Blasco, M. C. Sánchez, J. Pérez-Cacho, J. García, G. Subías and J. Campo, *J. Phys. Chem. Solids*, 2002, **63**, 781–792.

296 G. Pecchi, P. Reyes, R. Zamora, L. E. Cadús and J. L. G. Fierro, *J. Solid State Chem.*, 2008, **181**, 905–912.

297 R. Ran, X. Wu, D. Weng and J. Fan, *J. Alloys Compd.*, 2013, **577**, 288–294.

298 E. Granado, J. A. Sanjurjo, C. Rettori, J. J. Neumeier and S. B. Oseroff, *Phys. Rev. B - Condens. Matter Mater. Phys.*, 2000, **62**, 11304–11307.

299 N. Van Minh, S.-J. Kim and I.-S. Yang, *Phys. B Condens. Matter*, 2003, **327**, 208–210.

300 K. Tabata, Y. Hirano and E. Suzuki, *Appl. Catal. A Gen.*, 1998, **170**, 245–254.

301 C. L. Li and Y. C. Lin, *Catal. React. Eng. Div. - Core Program. Top. 2011 AIChE Annu. Meet.*, 2011, **2**, 836–868.

302 H. Taguchi, A. Sugita, M. Nagao and K. Tabata, *J. Solid State Chem.*, 1995, **119**, 164–168.

303 X. W. Wang, Q. Q. Zhu, X. E. Wang, H. C. Zhang, J. J. Zhang and L. F. Wang, *J. Alloys Compd.*, 2016, **675**, 195–200.

304 J. Sunarso, A. A. J. Torriero, W. Zhou, P. C. Howlett and M. Forsyth, *J. Phys. Chem. C*, 2012, **116**, 5827–5834.

305 Y. Zhao, T. Liu, Q. Shi, Q. Yang, C. Li, C. Zhang and D. Zhang, *Green Energy Environ.*, 2017, **3**, 78–85.

306 H. Zhu, P. Zhang and S. Dai, *ACS Catal.*, 2015, **5**, 6370–6385.

307 Y. Yi, G. Weinberg, M. Prenzel, M. Greiner, S. Heumann, S. Becker and R. Schlögl, *Catal. Today*, 2017, **295**, 32–40.

308 R. Ignatans, G. Mallia, E. A. Ahmad, L. Spillane, K. A. Stoerzinger, Y. Shao-Horn, N. M. Harrison and V. Tileli, *J. Phys. Chem. C*, 2019, **123**, 11621–11627.

309 V. Celorrio, L. Calvillo, E. Dann, G. Granozzi, A. Aguadero, D. Kramer, A. E. Russell and D. J. Fermín, *Catal. Sci. Technol.*, 2016, **6**, 7231–7238.

310 H. Y. Su, Y. Gorlin, I. C. Man, F. Calle-Vallejo, J. K. Norskov, T. F. Jaramillo and J. Rossmeisl, *Phys. Chem. Chem. Phys.*, 2012, **14**, 14010–14022.

311 Z. Chen, D. Higgins, A. Yu, L. Zhang and J. Zhang, *Energy Environ. Sci.*, 2011, **4**, 3167–3192.

312 M. Hamdani, R. N. Singh and P. Chartier, *Int. J. Electrochem. Sci.*, 2010, **5**, 556–577.

313 A. Pendashteh, J. Palma, M. Anderson and R. Marcilla, *Appl. Catal. B Environ.*, 2017, **201**, 241–252.

314 C. Yuan, H. Bin Wu, Y. Xie and X. W. Lou, *Angew. Chemie - Int. Ed.*, 2014, **53**, 1488–1504.

315 Y. Zhang, Y. Wang, J. Huang, C. Han and J. Zang, *Int. J. Hydrogen Energy*, 2020, **45**, 6529–6537.

316 T. Ma, C. Li, X. Chen, F. Cheng and J. Chen, *Inorg. Chem. Front.*, 2017, **4**, 1628–1633.

317 G. Li, K. Zhang, M. A. Mezaal and L. Lei, *Int. J. Electrochem. Sci.*, 2015, **10**, 10554–10564.

318 J. Liu, L. Jiang, T. Zhang, J. Jin, L. Yuan and G. Sun, *Electrochim. Acta*, 2016, **205**, 38–44.

319 J. Duan, S. Chen, S. Dai and S. Z. Qiao, *Adv. Funct. Mater.*, 2014, **24**, 2072–2078.

320 M. Prabu, P. Ramakrishnan and S. Shanmugam, *Electrochem. commun.*, 2014, **41**, 59–63.

321 J. Du, C. Chen, F. Cheng and J. Chen, *Inorg. Chem.*, 2015, **54**, 5467–5474.

322 Z. Sadighi, J. Huang, L. Qin, S. Yao, J. Cui and J. K. Kim, *J. Power Sources*, 2017, **365**, 134–147.

323 H. Yang, H. Wang, S. Ji, V. Linkov and R. Wang, *Int. J. Hydrogen Energy*, 2014, **39**, 3739–3745.

324 Y. Zhan, C. Xu, M. Lu, Z. Liu and J. Y. Lee, *J. Mater. Chem. A*, 2014, **2**, 16217–16223.

325 Z. Zhang, Q. Shu, C. Chen, T. Xiao, Z. Hu, S. Wu and J. Li, *Int. J. Electrochem. Sci.*, 2017, **12**, 6129–6136.

326 S. Enthaler, K. Junge and M. Beller, *Angew. Chemie - Int. Ed.*, 2008, **47**, 3317–3321.

327 Y. Xu, W. Bian, J. Wu, J. H. Tian and R. Yang, *Electrochim. Acta*, 2015, **151**, 276–283.

328 X. Zhao, Y. Fu, J. Wang, Y. Xu, J. H. Tian and R. Yang, *Electrochim. Acta*, 2016, **201**, 172–178.

329 B. M. Li and J. Lu, *Science (80-.).*, 2020, **367**, 979–980.

330 G. L. Li, C. Di Liu, S. M. Chen, C. Hao, G. C. Cheng and Y. Y. Xie, *Int. J. Hydrogen Energy*, 2017, **42**, 4133–4145.

331 S. Yuvaraj, R. K. Selvan and Y. S. Lee, *RSC Adv.*, 2016, **6**, 21448–21474.

332 T. Xiao-Xia, A. Manthiram and J. B. Goodenough, *J. Less-Common Met.*, 1989, **156**, 357–368.

333 Y. Ma, C. W. Tai, R. Younesi, T. Gustafsson, J. Y. Lee and K. Edström, *Chem. Mater.*, 2015, **27**, 7698–7709.

334 P. V. M. Kutty and S. Dasgupta, *Ceram. Int.*, 2013, **39**, 7891–7894.

335 T. Poux, A. Bonnefont, G. Kéranguéven, G. A. Tsirlina and E. R. Savinova, *ChemPhysChem*, 2014, **15**, 2108–2120.

336 K. Sue, M. Aoki, T. Sato, D. Nishio-Hamane, S. I. Kawasaki, Y. Hakuta, Y. Takebayashi, S. Yoda, T. Furuya, T. Sato and T. Hiaki, *Ind. Eng. Chem. Res.*, 2011, **50**, 9625–9631.

337 S. Li, J. Xu, Z. Ma, S. Zhang, X. Wen, X. Yu, J. Yang, Z. F. Ma and X. Yuan, *Chem. Commun.*, 2017, **53**, 8164–8167.

338 D. Alburquenque, L. Troncoso, J. C. Denardin, A. Butera, K. D. Padmasree, J. Ortiz, F. Herrera, J. F. Marco and J. L. Gautier, *J. Alloys Compd.*, 2016, **672**, 307–316.

339 M. Zhang, S. Guo, L. Zheng, G. Zhang, Z. Hao, L. Kang and Z. H. Liu, *Electrochim. Acta*, 2013, **87**, 546–553.

340 A. W. Moses, H. G. G. Flores, J. G. Kim and M. A. Langell, *Appl. Surf. Sci.*, 2007, **253**, 4782–4791.

341 G. Huang, E. He, Z. Wang, H. Fan, J. Shangguan, E. Croiset and Z. Chen, *Ind. Eng. Chem. Res.*, 2015, **54**, 8469–8478.

342 T. Larbi, K. Doll and M. Amlouk, *Spectrochim. Acta - Part A Mol. Biomol. Spectrosc.*, 2019, **216**, 117–124.

343 S. Karmakar, C. D. Mistari, V. Parey, R. Thapa, M. A. More and D. Behera, *J. Phys. D. Appl. Phys.*, , DOI:10.1088/1361-6463/ab523a.

344 Y. Lei, X. Lin and H. Liao, *Sep. Purif. Technol.*, 2018, **192**, 220–229.

345 E. Martin, B. Tartakovsky and O. Savadogo, *Electrochim. Acta*, 2011, **58**, 58–66.

346 J. S. Ko, C. N. Chervin, M. N. Vila, P. A. Desario, J. F. Parker, J. W. Long and D. R. Rolison, *Langmuir*, 2017, **33**, 9390–9397.

347 Z. Ye, Nanyang Technological University, 2018.

348 S. G. Bratsch, *J. Phys. Chem.*

349 R. Zhou, Y. Zheng, M. Jaroniec and S. Z. Qiao, *ACS Catal.*, 2016, **6**, 4720–4728.

350 C. Zhao, M. Yu, Z. Yang, J. Liu, S. Chen, Z. Hong, H. Chen and W. Wang, *Nano Energy*, 2018, **51**, 91–101.

351 H. Wang, R. Liu, Y. Li, X. Lü, Q. Wang, S. Zhao, K. Yuan, Z. Cui, X. Li, S. Xin, R. Zhang, M. Lei and Z. Lin, *Joule*, 2018, **2**, 337–348.

352 A. R. Groves, T. E. Ashton and J. A. Darr, , DOI:10.1021/acscombsci.0c00094.

List of Figures

Figure 6.18: The methanol resistance test of $Ni_{0.75}Mn_{2.25}O_4$ vs a commercial Pt Black sample. Measurements were carried out over 4000 s in O_2 saturated 0.1 M KOH at −0.5 V with a scan speed of 10 mV s^{-1} and a rotation speed of 900 rpm. After 1200 s 10 % volume of methanol was injected into the electrolyte. **(188)**

List of Abbreviations

AB	Acetylene Black
AFC	Alkaline Fuel Cell
AMFC	Alkaline Membrane Fuel Cell
BHT	Batch Heat Treatment
CHFS	Continuous Hydrothermal Flow Synthesis
CJM	Confined Jet Mixer
CV	Cyclic Voltammetry
DMFC	Direct Methanol Fuel Cell
EIS	Electrochemical Impedance Spectroscopy
EDX	Energy Dispersive X-ray
EXAFS	Extended X-ray Absorption Fine Structure
FHT	Flash Heat Treatment
IPA	Isopropyl Alcohol
KCD	Kinetic Current Density
K-L	Koutecky-Levich
LIB	Lithium Ion Battery
LSV	Linear Sweep Voltammetry
MCFC	Molten Carbonate Fuel Cell
OER	Oxygen Evolution Reaction
ORR	Oxygen Reduction Reaction
PAFC	Phosphoric Acid Fuel Cell
PEM	Proton Exchange Membrane
PEMFC	Polymer Electrolyte Membrane Fuel Cell
PGM	Platinum Group Metal
PXRD	Powder X-ray Diffraction

List of Abbreviations

RDE	Rotating Disk Electrode
RHE	Reversible Hydrogen Electrode
RRDE	Rotating Ring Disk Electrode
SEM	Scanning Electron Microscope
SOFC	Solid Oxide Fuel Cell
SSA	Specific Surface Area
TEM	Transmission Electron Microscope
TiBALD	Titanium(IV) bis(ammonium lactate)dihydroxide
TM	Transition Metal
URFC	Unitized Regenerative Fuel Cell
XPS	X-ray Photoelectron Spectroscopy
XRF	X-ray Fluorescence Spectroscopy
ZAB	Zinc Air Battery

List of Tables

Publications

Publications directly related to work presented in this thesis:

- **Groves, A R.**, Ashton, T E. and Darr, J. A.: High Throughput Synthesis and Screening of Oxygen Reduction Catalysts in the *M*TiO_3 (M = Ca, Sr, Ba) Perovskite Phase Diagram[352], *ACS Comb. Sci*. (2020). Doi: 10.1021/acscombsci.0c00094.

Other work:

- Bauer, D., Ashton, T E., **Groves, A R**., Dey, A., Krishnamurthy, S., Matsumi, N. and Darr, J A.: Continuous Hydrothermal Synthesis of Metal Germanates (M2GeO4; M=Co, Mn, Zn) for High-Capacity Negative Electrodes in Li-Ion Batteries, *Energy Technol.* 8 (2020) 1900692. Doi: 10.1002/ente.201900692
- Birrozzi, A., Asenbauer, J., Ashton, T E., **Groves, A R**., Geiger, D., Kaiser, U., Darr, J A. and Bresser, D.: Tailoring the Charge/Discharge Potentials and Electrochemical Performance of SnO2 Lithium-Ion Anodes by Transition Metal co-Doping, *Batteries & Supercaps.* 3 (2020) 284–292. Doi: 10.1002/batt.201900154
- Ashton, T E., Baker P J., Bauer, D., **Groves, A R**., Sotelo-Vazquez, C., Kamiyama, T., Matsukawa, T., Kojima, K M. and Darr, J A.: Multiple diffusion pathways in LixNi0.77Co0.14Al0.09O2 (NCA) Li-ion battery cathodes, *J. Mater. Chem. A*, 8 (2020) 11545–11552. Doi: 10.1039/D0TA03809A
- Xu, Y., Sumboja, A., **Groves, A R**., Ashton, T E., Zong, Y and Darr, J A.: Enhancing bifunctional catalytic activity of cobalt–nickel sulfide spinel nanocatalysts through transition metal doping and its application in secondary zinc–air batteries, *RSC Adv.* 10 (2020) 41871–41882. Doi: 10.1039/d0ra08363a

9. Supplementary Information (SI)

9.1. SI for Chapter 3

Table 9.1: Molar amounts of precursor used in the synthesis of group 2 titanate perovskites. This was dissolved in a Ti sol of 0.075 M. Compositions are nominal.

Product	$Ba(NO_3)_3$	$Sr(NO_3)_3$	$Ca(NO_3)_3$
$BaTiO_3$	0.083	0.000	0.000
$Ba_{0.9}Sr_{0.1}TiO_3$	0.074	0.008	0.000
$Sr_{0.1}Ca_{0.9}TiO_3$	0.000	0.008	0.074
$Ba_{0.8}Sr_{0.2}TiO_3$	0.066	0.017	0.000
$Ba_{0.8}Sr_{0.1}Ca_{0.1}TiO_3$	0.066	0.008	0.008
$Ca_{0.8}Sr_{0.2}TiO_3$	0.000	0.017	0.066
$Ba_{0.7}Sr_{0.3}TiO_3$	0.058	0.025	0.000
$Ba_{0.7}Sr_{0.1}Ca_{0.2}TiO_3$	0.058	0.008	0.017
$Ba_{0.7}Sr_{0.2}Ca_{0.1}TiO_3$	0.058	0.017	0.008
$Ca_{0.7}Sr_{0.3}TiO_3$	0.000	0.025	0.058
$Ba_{0.6}Sr_{0.4}TiO_3$	0.050	0.033	0.000
$Ba_{0.6}Sr_{0.1}Ca_{0.3}TiO_3$	0.050	0.008	0.025
$Ba_{0.6}Sr_{0.2}Ca_{0.2}TiO_3$	0.050	0.017	0.017
$Ba_{0.6}Sr_{0.3}Ca_{0.1}TiO_3$	0.050	0.025	0.008
$Ca_{0.6}Sr_{0.4}TiO_3$	0.000	0.033	0.050
$Ba_{0.5}Sr_{0.5}TiO_3$	0.041	0.041	0.000
$Ba_{0.5}Sr_{0.1}Ca_{0.4}TiO_3$	0.041	0.008	0.033
$Ba_{0.5}Sr_{0.2}Ca_{0.3}TiO_3$	0.041	0.017	Ni0.025
$Ba_{0.5}Sr_{0.3}Ca_{0.2}TiO_3$	0.041	0.025	0.017
$Ba_{0.5}Sr_{0.4}Ca_{0.1}TiO_3$	0.041	0.033	0.008
$Sr_{0.5}Ca_{0.5}TiO_3$	0.000	0.041	0.041
$Ba_{0.4}Sr_{0.6}TiO_3$	0.033	0.050	0.000
$Ba_{0.4}Sr_{0.1}Ca_{0.5}TiO_3$	0.033	0.008	0.041
$Ba_{0.4}Sr_{0.2}Ca_{0.4}TiO_3$	0.033	0.017	0.033
$Ba_{0.4}Sr_{0.3}Ca_{0.3}TiO_3$	0.033	0.025	0.025
$Ba_{0.4}Sr_{0.4}Ca_{0.2}TiO_3$	0.033	0.033	0.017
$Ba_{0.4}Sr_{0.5}Ca_{0.1}TiO_3$	0.033	0.041	0.008
$Sr_{0.6}Ca_{0.4}TiO_3$	0.000	0.050	0.033
$Ba_{0.3}Sr_{0.7}TiO_3$	0.025	0.058	0.000

$Ba_{0.3}Sr_{0.1}Ca_{0.6}TiO_3$	0.025	0.008	0.050
$Ca_{0.5}Ba_{0.5}TiO_3$	0.041	0.000	0.041
$Ca_{0.4}Ba_{0.6}TiO_3$	0.050	0.000	0.033
$Ca_{0.3}Ba_{0.7}TiO_3$	0.058	0.000	0.025
$Ba_{0.3}Sr_{0.2}Ca_{0.5}TiO_3$	0.025	0.017	0.041
$Ba_{0.3}Sr_{0.3}Ca_{0.4}TiO_3$	0.025	0.025	0.033
$Ba_{0.3}Sr_{0.4}Ca_{0.3}TiO_3$	0.025	0.033	0.025
$Ba_{0.3}Sr_{0.5}Ca_{0.2}TiO_3$	0.025	0.041	0.017
$Ba_{0.3}Sr_{0.6}Ca_{0.1}TiO_3$	0.025	0.050	0.008
$Sr_{0.7}Ca_{0.3}TiO_3$	0.000	0.058	0.025
$Ba_{0.2}Sr_{0.8}TiO_3$	0.017	0.066	0.000
$Ba_{0.2}Sr_{0.1}Ca_{0.7}TiO_3$	0.017	0.008	0.058
$Ba_{0.2}Sr_{0.2}Ca_{0.6}TiO_3$	0.017	0.017	0.050
$Ba_{0.2}Sr_{0.3}Ca_{0.5}TiO_3$	0.017	0.025	0.041
$Ba_{0.2}Sr_{0.4}Ca_{0.4}TiO_3$	0.017	0.033	0.033
$Ba_{0.2}Sr_{0.5}Ca_{0.3}TiO_3$	0.017	0.041	0.025
$Ba_{0.2}Sr_{0.6}Ca_{0.2}TiO_3$	0.017	0.050	0.017
$Ba_{0.2}Sr_{0.7}Ca_{0.1}TiO_3$	0.017	0.058	0.008
$Sr_{0.8}Ca_{0.2}TiO_3$	0.000	0.066	0.017
$Ba_{0.1}Sr_{0.9}TiO_3$	0.008	0.074	0.000
$Ba_{0.1}Sr_{0.1}Ca_{0.8}TiO_3$	0.008	0.008	0.066
$Ba_{0.1}Sr_{0.2}Ca_{0.7}TiO_3$	0.008	0.017	0.058
$Ba_{0.1}Sr_{0.3}Ca_{0.6}TiO_3$	0.008	0.025	0.050
$Ba_{0.1}Sr_{0.4}Ca_{0.5}TiO_3$	0.008	0.033	0.041
$Ba_{0.1}Sr_{0.5}Ca_{0.4}TiO_3$	0.008	0.041	0.033
$Ba_{0.1}Sr_{0.6}Ca_{0.3}TiO_3$	0.008	0.050	0.025
$Ba_{0.1}Sr_{0.7}Ca_{0.2}TiO_3$	0.008	0.058	0.017
$Ba_{0.1}Sr_{0.8}Ca_{0.1}TiO_3$	0.008	0.066	0.008
$Sr_{0.9}Ca_{0.1}TiO_3$	0.000	0.074	0.008
$CaTiO_3$	0.000	0.000	0.083
$Ca_{0.9}Ba_{0.1}TiO_3$	0.008	0.000	0.074
$Ca_{0.8}Ba_{0.2}TiO_3$	0.017	0.000	0.066
$Ca_{0.7}Ba_{0.3}TiO_3$	0.025	0.000	0.058
$Ca_{0.6}Ba_{0.4}TiO_3$	0.033	0.000	0.050

$Ca_{0.2}Ba_{0.8}TiO_3$	0.066	0.000	0.017
$Ca_{0.1}Ba_{0.9}TiO_3$	0.074	0.000	0.008
$SrTiO_3$	0.000	0.083	0.000

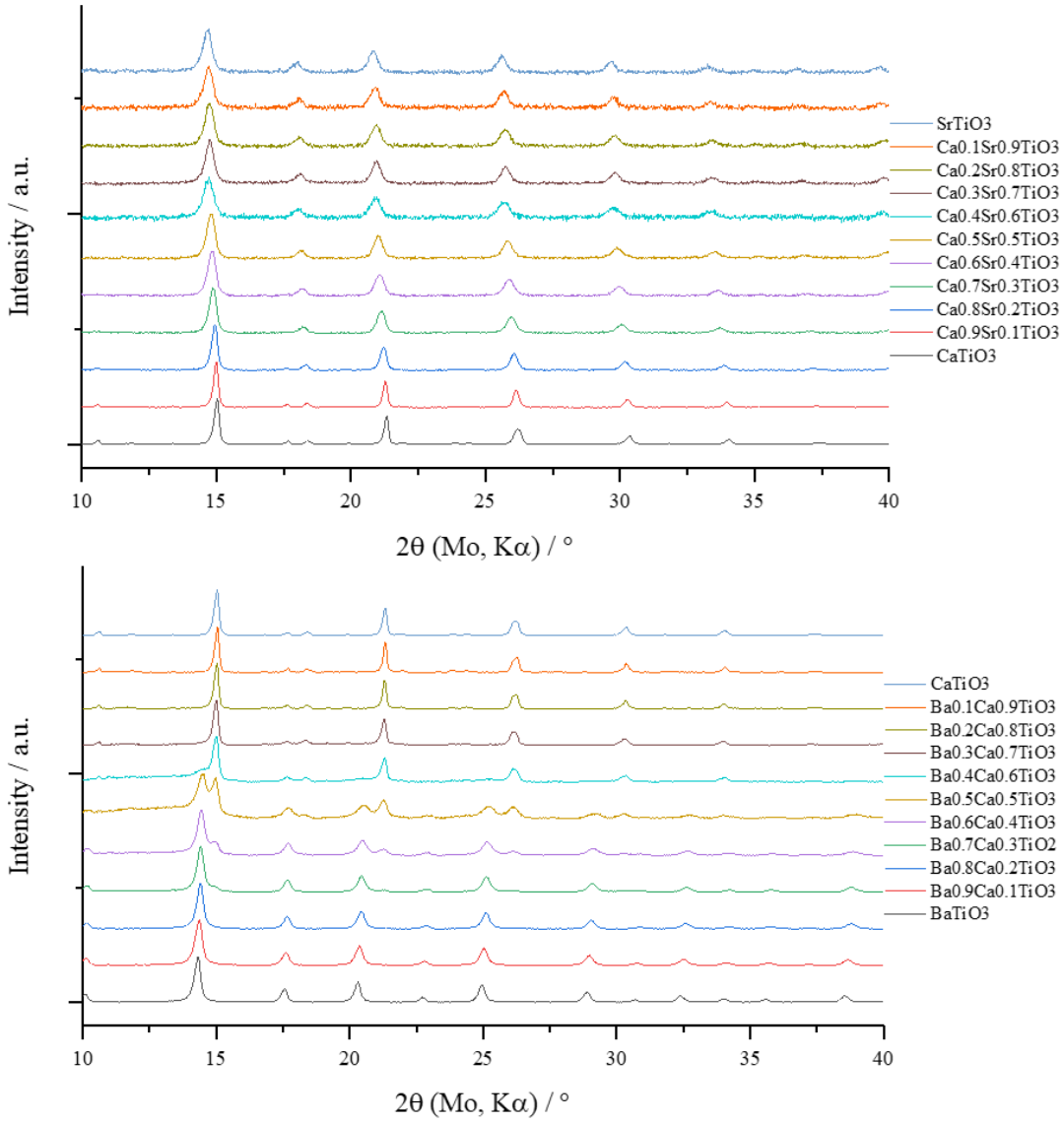

Figure 9.1: Various PXRD patterns for perovskite titanates.

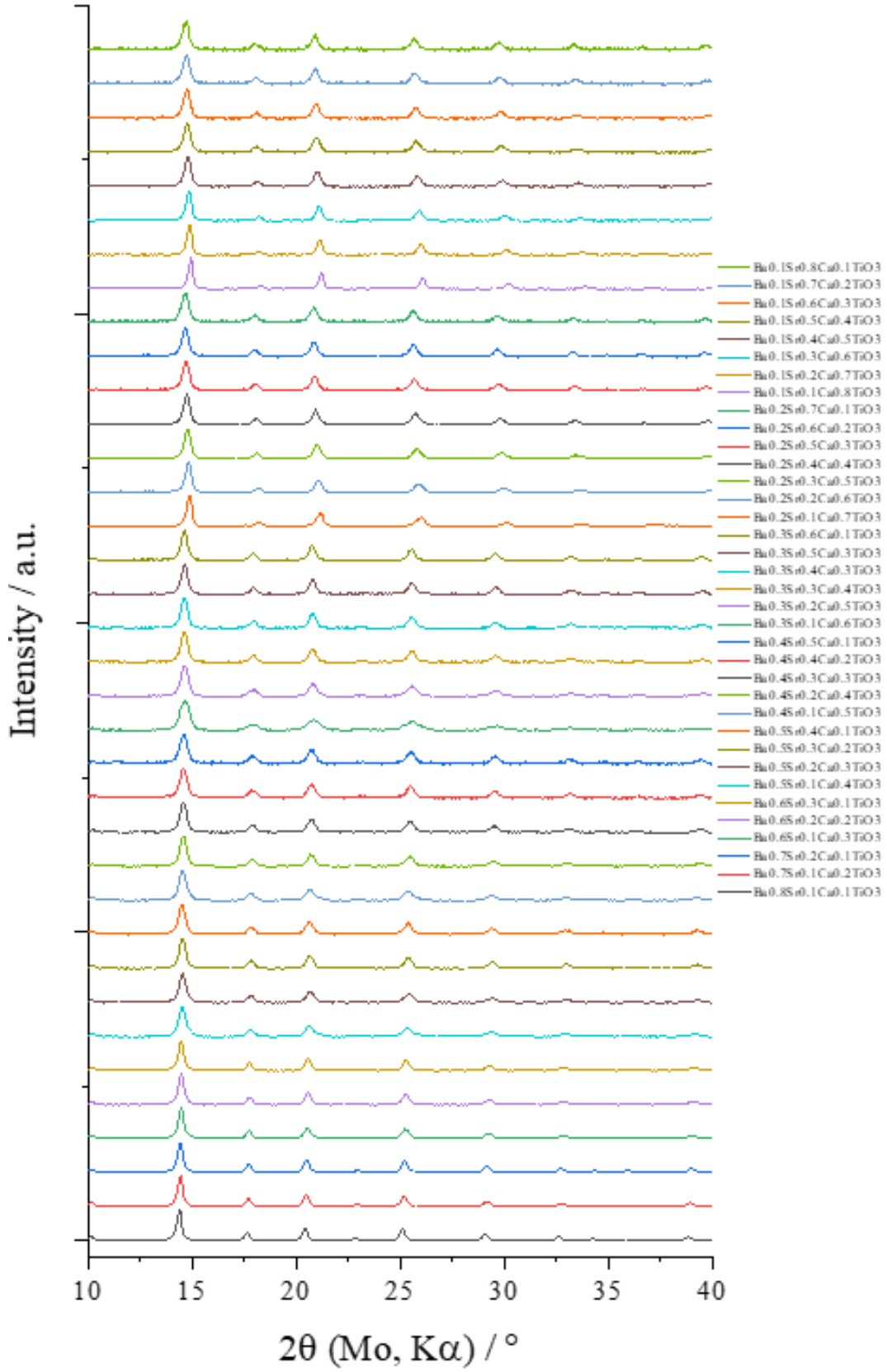

Figure 9.2: Various PXRD patterns for perovskite titanates.

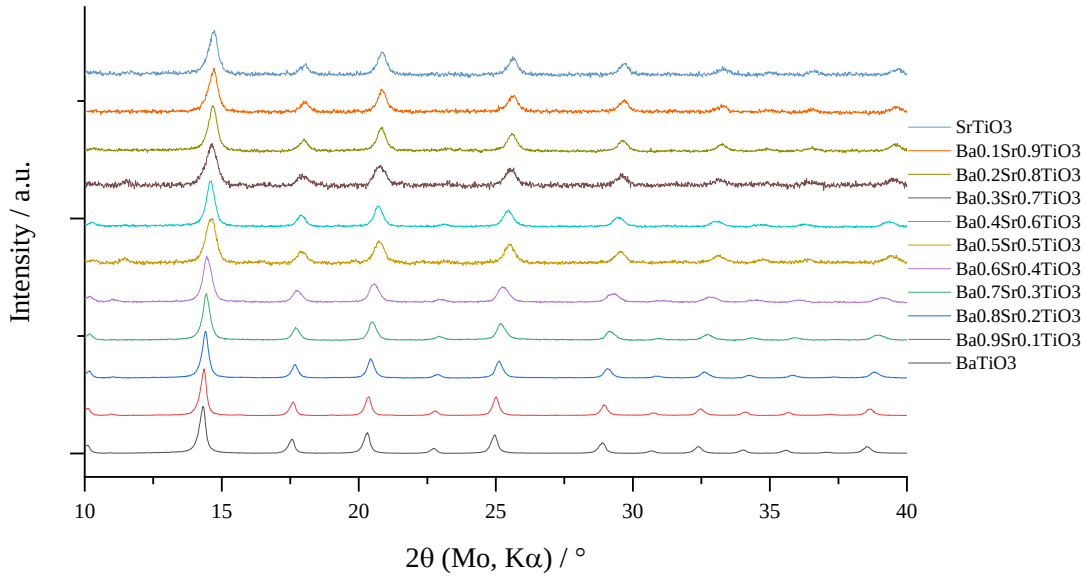

Figure 9.3: Various PXRD patterns for perovskite titanates.

Table 9.2: Ternary data for perovskite titanates in Chapter 3.

Composition	Scherrer Size / nm	SSA / m^2g^{-1}	$E_{0.1\ mA\ cm^{-2}}$ / V	$J_{0.5\ V}$ / mA cm^{-2}
$BaTiO_3$	13.6	72.6	−0.176	−1.454
$Ba_{0.9}Sr_{0.1}TiO_3$	13.6	54.6	−0.288	−0.745
$Sr_{0.1}Ca_{0.9}TiO_3$	13.6	59.6	−0.318	−0.602
$Ba_{0.8}Sr_{0.2}TiO_3$	12.9	63.8	−0.222	−1.491
$Ba_{0.8}Sr_{0.1}Ca_{0.1}TiO_3$	13.0	63.0	−0.282	−0.905
$Ca_{0.8}Sr_{0.2}TiO_3$	11.4	69.7	−0.314	−0.728
$Ba_{0.7}Sr_{0.3}TiO_3$	10.6	68.1	−0.224	−1.421
$Ba_{0.7}Sr_{0.1}Ca_{0.2}TiO_3$	11.7	59.2	−0.274	−1.054
$Ba_{0.7}Sr_{0.2}Ca_{0.1}TiO_3$	11.2	67.4	−0.292	−0.853
$Ca_{0.7}Sr_{0.3}TiO_3$	8.6	75.3	−0.222	−1.338
$Ba_{0.6}Sr_{0.4}TiO_3$	8.8	67.9	−0.268	−1.048
$Ba_{0.6}Sr_{0.1}Ca_{0.3}TiO_3$	10.6	61.3	−0.292	−0.842
$Ba_{0.6}Sr_{0.2}Ca_{0.2}TiO_3$	10.4	76.0	−0.218	−1.375
$Ba_{0.6}Sr_{0.3}Ca_{0.1}TiO_3$	9.0	77.8	−0.254	−1.322
$Ca_{0.6}Sr_{0.4}TiO_3$	8.2	92.2	−0.286	−0.897
$Ba_{0.5}Sr_{0.5}TiO_3$	8.4	98.4	−0.222	−1.285
$Ba_{0.5}Sr_{0.1}Ca_{0.4}TiO_3$	7.8	61.4	−0.256	−1.275
$Ba_{0.5}Sr_{0.2}Ca_{0.3}TiO_3$	7.7	68.5	−0.232	−1.245

$Ba_{0.5}Sr_{0.3}Ca_{0.2}TiO_3$	7.8	90.4	−0.276	−1.048
$Ba_{0.5}Sr_{0.4}Ca_{0.1}TiO_3$	8.4	90.5	−0.302	−0.747
$Sr_{0.5}Ca_{0.5}TiO_3$	8.7	97.3	−0.232	−1.260
$Ba_{0.4}Sr_{0.6}TiO_3$	8.0	78.5	−0.262	−1.220
$Ba_{0.4}Sr_{0.1}Ca_{0.5}TiO_3$	7.7	89.6	−0.278	−1.106
$Ba_{0.4}Sr_{0.2}Ca_{0.4}TiO_3$	7.2	67.8	−0.236	−1.238
$Ba_{0.4}Sr_{0.3}Ca_{0.3}TiO_3$	8.6	80.1	−0.260	−1.266
$Ba_{0.4}Sr_{0.4}Ca_{0.2}TiO_3$	7.6	94.2	−0.278	−1.092
$Ba_{0.4}Sr_{0.5}Ca_{0.1}TiO_3$	7.7	95.5	−0.236	−1.241
$Sr_{0.6}Ca_{0.4}TiO_3$	6.0	115.5	−0.242	−1.137
$Ba_{0.3}Sr_{0.7}TiO_3$	5.3	108.2	−0.264	−1.086
$Ba_{0.3}Sr_{0.1}Ca_{0.6}TiO_3$	4.9	57.6	−0.280	−0.967
$Ba_{0.3}Sr_{0.2}Ca_{0.5}TiO_3$	6.6	75.7	−0.234	−1.224
$Ba_{0.3}Sr_{0.3}Ca_{0.4}TiO_3$	7.9	88.3	−0.250	−1.276
$Ba_{0.3}Sr_{0.4}Ca_{0.3}TiO_3$	7.6	91.3	−0.270	−1.075
$Ba_{0.3}Sr_{0.5}Ca_{0.2}TiO_3$	8.7	98.5	−0.258	−0.996
$Ba_{0.3}Sr_{0.6}Ca_{0.1}TiO_3$	9.3	99.5	−0.248	−1.150
$Sr_{0.7}Ca_{0.3}TiO_3$	7.7	106.7	−0.282	−0.900
$Ba_{0.2}Sr_{0.8}TiO_3$	8.3	103.2	−0.296	−0.882
$Ba_{0.2}Sr_{0.1}Ca_{0.7}TiO_3$	9.0	75.6	−0.246	−1.143
$Ba_{0.2}Sr_{0.2}Ca_{0.6}TiO_3$	9.0	76.8	−0.264	−1.163
$Ba_{0.2}Sr_{0.3}Ca_{0.5}TiO_3$	8.4	91.9	−0.284	−0.960
$Ba_{0.2}Sr_{0.4}Ca_{0.4}TiO_3$	7.2	93.8	−0.246	−1.122
$Ba_{0.2}Sr_{0.5}Ca_{0.3}TiO_3$	8.6	103.2	−0.262	−1.165
$Ba_{0.2}Sr_{0.6}Ca_{0.2}TiO_3$	8.5	113.8	−0.290	−0.852
$Ba_{0.2}Sr_{0.7}Ca_{0.1}TiO_3$	6.4	99.2	−0.248	−1.041
$Sr_{0.8}Ca_{0.2}TiO_3$	7.7	108.2	−0.256	−1.219
$Ba_{0.1}Sr_{0.9}TiO_3$	8.3	108.4	−0.284	−0.907
$Ba_{0.1}Sr_{0.1}Ca_{0.8}TiO_3$	13.1	70.7	−0.246	−1.030
$Ba_{0.1}Sr_{0.2}Ca_{0.7}TiO_3$	13.0	76.7	−0.258	−1.172
$Ba_{0.1}Sr_{0.3}Ca_{0.6}TiO_3$	11.8	94.7	−0.272	−0.847
$Ba_{0.1}Sr_{0.4}Ca_{0.5}TiO_3$	10.2	92.6	−0.262	−0.944
$Ba_{0.1}Sr_{0.5}Ca_{0.4}TiO_3$	7.5	96.2	−0.272	−1.055
$Ba_{0.1}Sr_{0.6}Ca_{0.3}TiO_3$	9.0	103.8	−0.290	−0.854

$Ba_{0.1}Sr_{0.7}Ca_{0.2}TiO_3$	5.7	97.8	−0.254	−0.947
$Ba_{0.1}Sr_{0.8}Ca_{0.1}TiO_3$	8.9	106.5	−0.256	−1.261
$Sr_{0.9}Ca_{0.1}TiO_3$	7.7	112.8	−0.260	−1.061
$CaTiO_3$	13.9	63.0	−0.252	−1.003
$Ca_{0.9}Ba_{0.1}TiO_3$	15.8	78.8	−0.260	−1.198
$Ca_{0.8}Ba_{0.2}TiO_3$	15.4	73.7	−0.284	−0.849
$Ca_{0.7}Ba_{0.3}TiO_3$	12.9	66.7	−0.264	−1.214
$Ca_{0.6}Ba_{0.4}TiO_3$	11.7	68.4	−0.254	−1.014
$Ca_{0.5}Ba_{0.5}TiO_3$	7.0	74.0	−0.258	−1.191
$Ca_{0.4}Ba_{0.6}TiO_3$	9.1	69.8	−0.256	−1.046
$Ca_{0.3}Ba_{0.7}TiO_3$	11.2	67.5	−0.252	−0.997
$Ca_{0.2}Ba_{0.8}TiO_3$	11.7	75.7	−0.256	−1.227
$Ca_{0.1}Ba_{0.9}TiO_3$	11.3	99.6	−0.258	−1.224
$SrTiO_3$	7.4	107.5	−0.260	−0.842

9.2. SI for Chapter 4

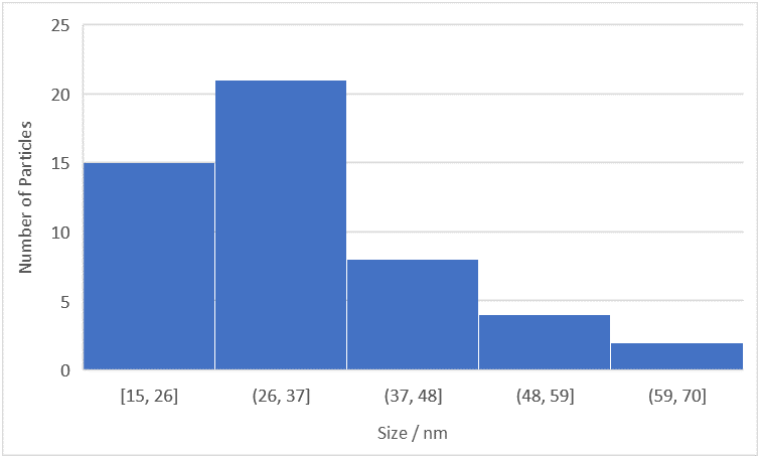

Figure 9.4: Histogram of particle sizes for $LaMnO_3$-BHT.

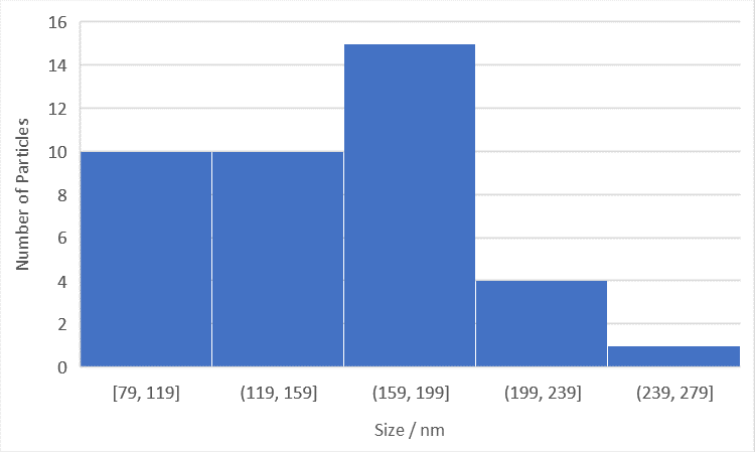

Figure 9.5: Histogram of particle sizes for $YMnO_3$.

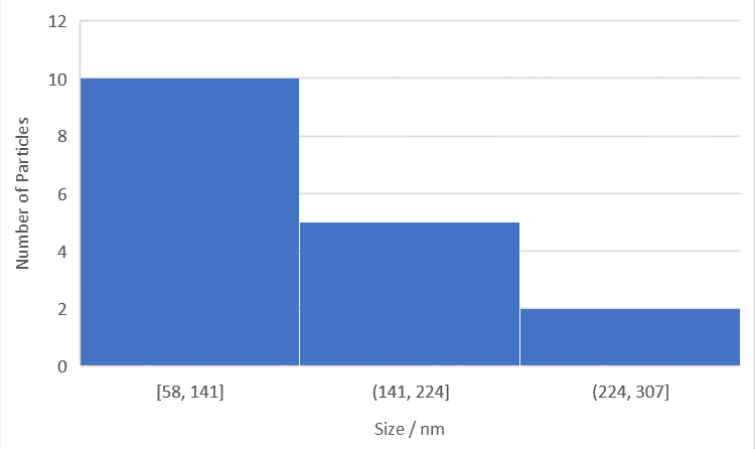

Figure 9.6: Histogram of particle sizes for $SmMnO_3$.

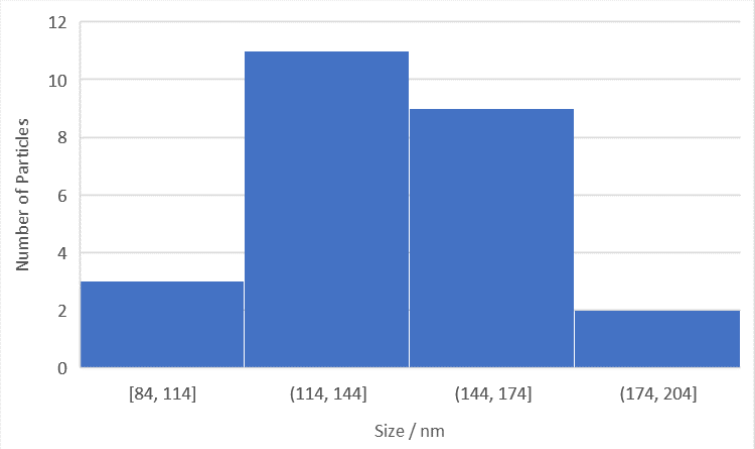

Figure 9.7: Histogram of particle sizes for $CaMnO_3$.

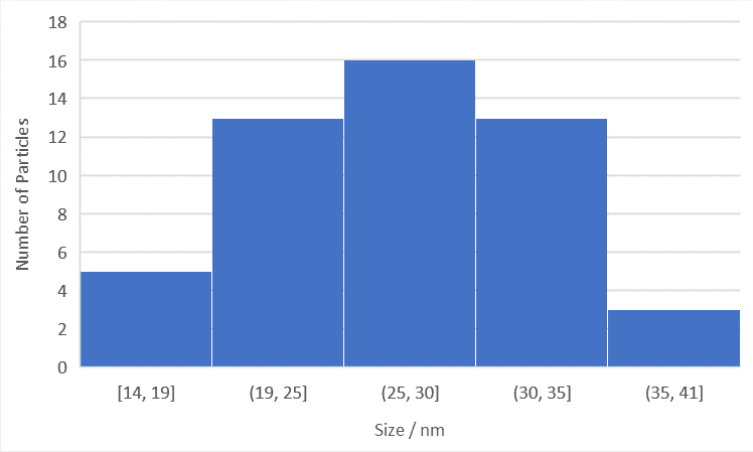

Figure 9.8: Histogram of particle sizes for $LaMnO_3$-FHT.

9.3. SI for Chapter 5

Table 9.3: Synthesis details for Chapter 5.

Sample	$La(NO)_3.6H_2O$ / M	$Ni(NO_3)_2.6H_2O$ / M	$Mn(NO_3)_2.xH_2O$ / M
$La_{1.1}Mn_{0.84}Ni_{0.06}O_3$	0.05	0.0025	0.0475
$La_{1.05}Mn_{0.84}Ni_{0.11}O_3$	0.0475	0.005	0.0475
$LaMn_{0.86}Ni_{0.14}O_3$	0.045	0.0075	0.0475
$La_{0.94}Mn_{0.85}Ni_{0.21}O_3$	0.0425	0.01	0.0475
$La_{0.89}Mn_{0.86}Ni_{0.25}O_3$	0.04	0.0125	0.0475
$La_{0.83}Mn_{0.86}Ni_{0.31}O_3$	0.0375	0.015	0.0475
$La_{1.14}Mn_{0.80}Ni_{0.06}O_3$	0.0525	0.0025	0.045
$La_{0.85}Mn_{0.82}Ni_{0.33}O_3$	0.0375	0.0175	0.045
$La_{1.19}Mn_{0.75}Ni_{0.06}O_3$	0.055	0.0025	0.0425
$La_{1.09}Mn_{0.75}Ni_{0.16}O_3$	0.05	0.0075	0.0425
$La_{1.04}Mn_{0.76}Ni_{0.20}O_3$	0.0475	0.01	0.0425
$La_{0.98}Mn_{0.76}Ni_{0.26}O_3$	0.045	0.0125	0.0425
$La_{0.94}Mn_{0.75}Ni_{0.31}O_3$	0.0425	0.015	0.0425
$La_{0.85}Mn_{0.78}Ni_{0.37}O_3$	0.0375	0.02	0.0425
$La_{1.24}Mn_{0.70}Ni_{0.06}O_3$	0.0575	0.0025	0.04
$La_{1.15}Mn_{0.71}Ni_{0.14}O_3$	0.0525	0.0075	0.04
$La_{0.93}Mn_{0.69}Ni_{0.38}O_3$	0.0425	0.0175	0.04
$La_{0.83}Mn_{0.73}Ni_{0.44}O_3$	0.0375	0.0225	0.04
$La_{1.28}Mn_{0.66}Ni_{0.06}O_3$	0.06	0.0025	0.0375
$La_{1.20}Mn_{0.64}Ni_{0.16}O_3$	0.055	0.0075	0.0375

$La_{1.08}Mn_{0.68}Ni_{0.24}O_3$	0.05	0.0125	0.0375
$La_{1.04}Mn_{0.65}Ni_{0.31}O_3$	0.0475	0.015	0.0375
$La_{0.93}Mn_{0.67}Ni_{0.40}O_3$	0.0425	0.02	0.0375
$La_{0.82}Mn_{0.67}Ni_{0.51}O_3$	0.0375	0.025	0.0375
$La_{1.34}Mn_{0.60}Ni_{0.06}O_3$	0.0625	0.0025	0.035
$La_{1.23}Mn_{0.62}Ni_{0.15}O_3$	0.0575	0.0075	0.035
$La_{1.13}Mn_{0.61}Ni_{0.26}O_3$	0.0525	0.0125	0.035
$La_{1.08}Mn_{0.61}Ni_{0.31}O_3$	0.05	0.015	0.035
$La_{1.03}Mn_{0.62}Ni_{0.35}O_3$	0.0475	0.0175	0.035
$La_{0.96}Mn_{0.63}Ni_{0.41}O_3$	0.0425	0.0225	0.035
$La_{0.82}Mn_{0.610.57}O_3$	0.0375	0.0275	0.035
$La_{1.34}Mn_{0.55}Ni_{0.11}O_3$	0.0625	0.005	0.0325
$La_{1.24}Mn_{0.55}Ni_{0.21}O_3$	0.0575	0.01	0.0325
$La_{1.12}Mn_{0.57}Ni_{0.31}O_3$	0.0525	0.015	0.0325
$La_{1.07}Mn_{0.56}Ni_{0.37}O_3$	0.05	0.0175	0.0325
$La_{0.98}Mn_{0.58}Ni_{0.44}O_3$	0.045	0.0225	0.0325
$La_{0.86}Mn_{0.59}Ni_{0.55}O_3$	0.04	0.0275	0.0325
$La_{1.32}Mn_{0.52}Ni_{0.16}O_3$	0.0625	0.0075	0.03
$La_{1.18}Mn_{0.51}Ni_{0.30}O_3$	0.0575	0.0125	0.03
$La_{1.02}Mn_{0.52}Ni_{0.45}O_3$	0.0475	0.0225	0.03
$La_{0.89}Mn_{0.52}Ni_{0.59}O_3$	0.0425	0.0275	0.03
$La_{1.32}Mn_{0.47}Ni_{0.21}O_3$	0.0625	0.01	0.0275
$La_{1.235}Mn_{0.51}Ni_{0.24}O_3$	0.0575	0.015	0.0275
$La_{1.18}Mn_{0.47}Ni_{0.35}O_3$	0.055	0.0175	0.0275
$La_{1.11}Mn_{0.47}Ni_{0.42}O_3$	0.0525	0.02	0.0275
$La_{1.07}Mn_{0.47}Ni_{0.46}O_3$	0.05	0.0225	0.0275
$La_{0.95}Mn_{0.46}Ni_{0.58}O_3$	0.045	0.0275	0.0275
$La_{1.32}Mn_{0.41}Ni_{0.27}O_3$	0.0625	0.0125	0.025
$LaMn_{0.41}Ni_{0.59}O_3$	0.0475	0.0275	0.025
$La_{1.32}Mn_{0.37}Ni_{0.31}O_3$	0.0625	0.015	0.0225
$La_{1.27}Mn_{0.36}Ni_{0.37}O_3$	0.06	0.0175	0.0225
$La_{1.23}Mn_{0.37}Ni_{0.40}O_3$	0.0575	0.02	0.0225
$La_{1.18}Mn_{0.37}Ni_{0.45}O_3$	0.055	0.0225	0.0225
$La_{1.11}Mn_{0.37}Ni_{0.52}O_3$	0.0525	0.025	0.0225

$La_{1.05}Mn_{0.37}Ni_{0.58}O_3$	0.05	0.0275	0.0225
$La_{0.88}Mn_{0.95}Ni_{0.16}O_3$	0.0400	0.0075	0.0525
$La_{0.87}Mn_{0.93}Ni_{0.20}O_3$	0.0375	0.0100	0.0525
$La_{0.80}Mn_{0.96}Ni_{0.25}O_3$	0.0350	0.0125	0.0525
$La_{0.72}Mn_{0.97}Ni_{0.31}O_3$	0.0325	0.0150	0.0525
$La_{0.73}Mn_{0.91}Ni_{0.36}O_3$	0.0325	0.0175	0.0500
$La_{0.72}Mn_{0.86}Ni_{0.42}O_3$	0.0325	0.0200	0.0475
$La_{0.73}Mn_{0.80}Ni_{0.47}O_3$	0.0325	0.0225	0.0450

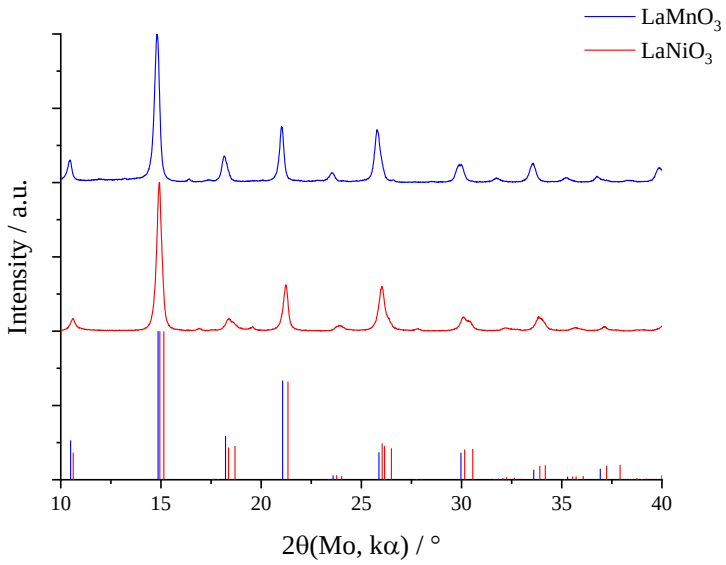

Figure 9.9: PXRD patterns for CHFS $LaMnO_3$ and $LaNiO_3$ made using a flash heat-treatment step.

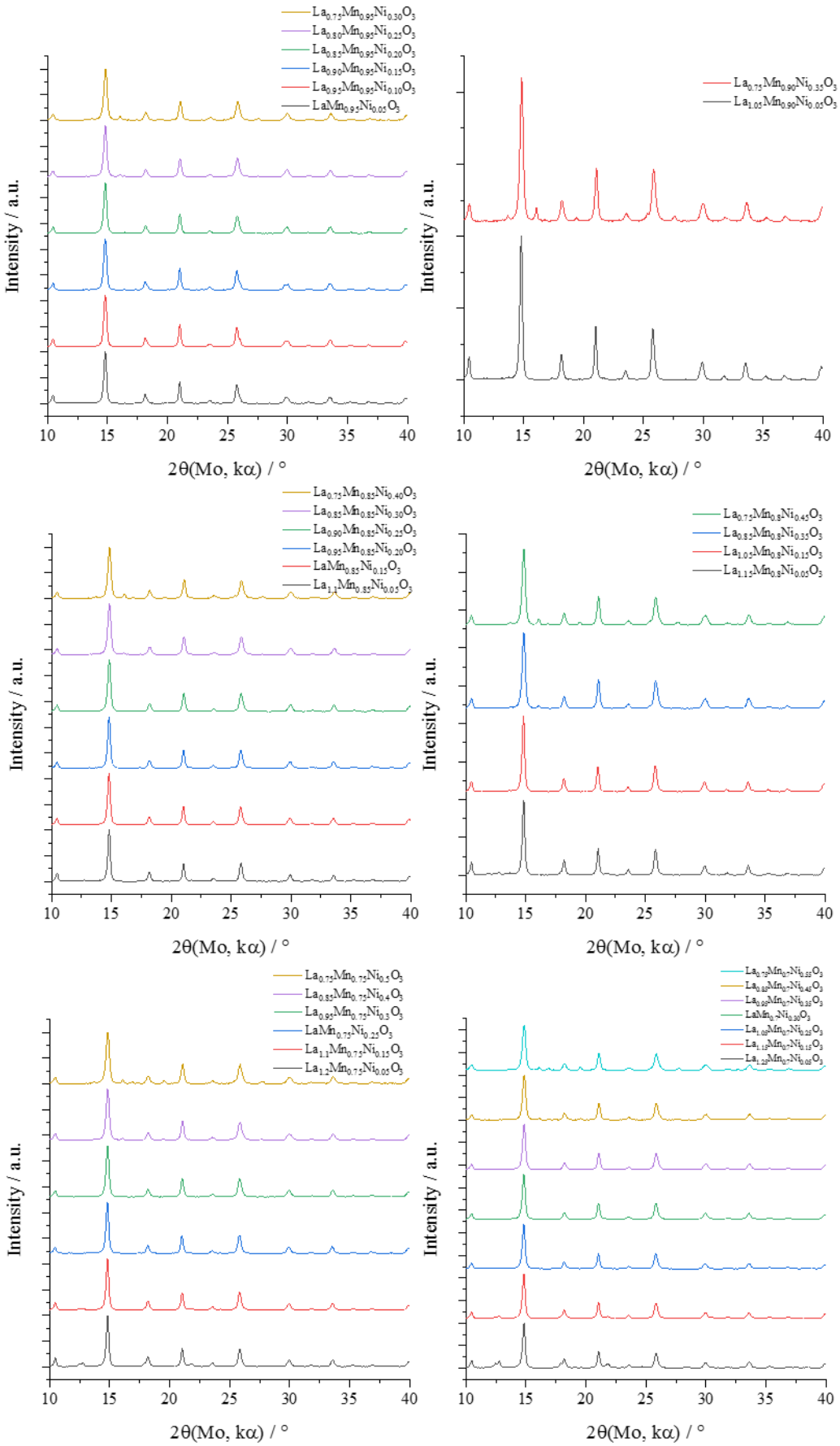

Figure 9.10: PXRD data for $La_xMn_yNi_zO_3$ sorted by Mn concentration.

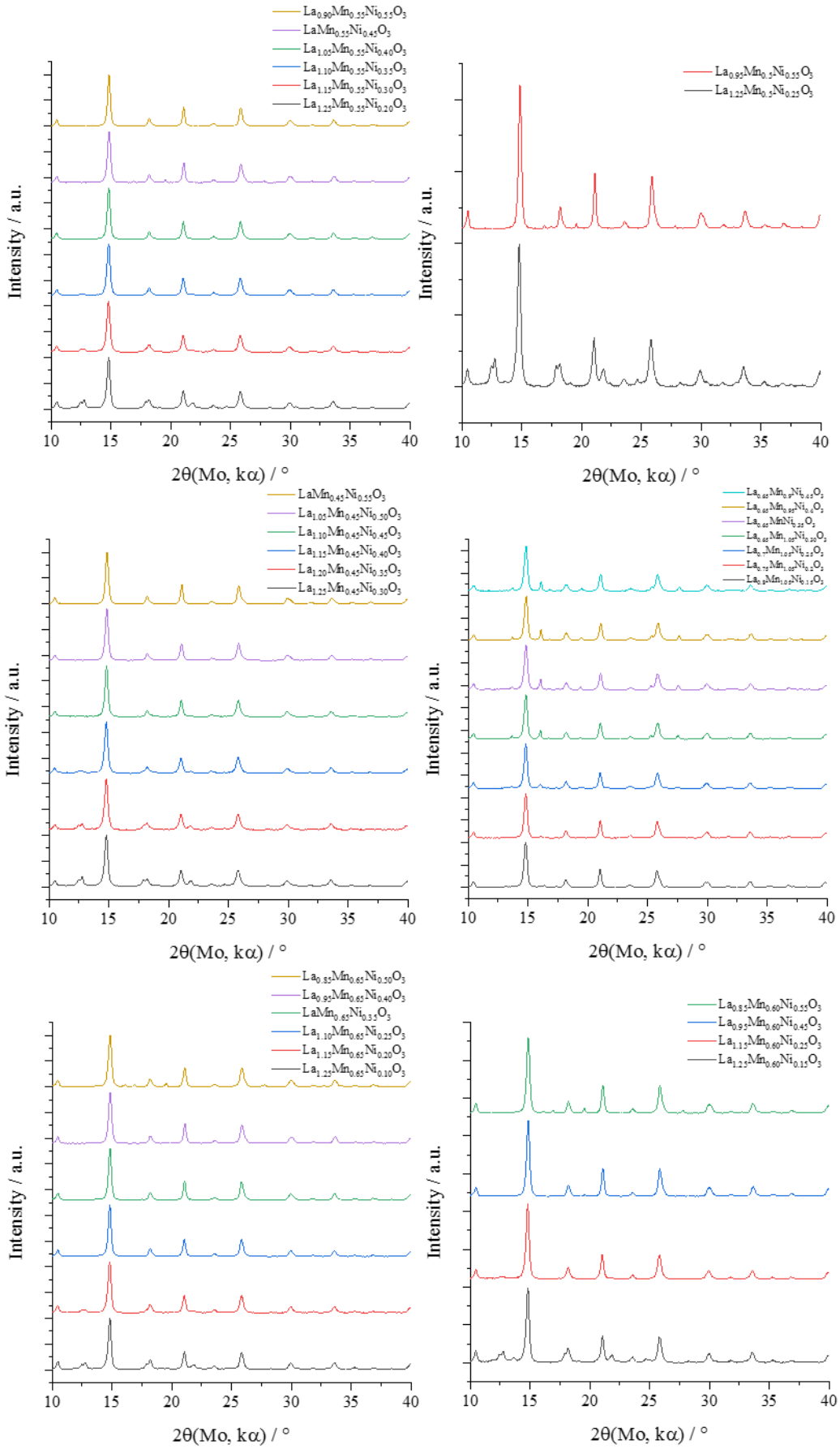

Figure 9.11: PXRD data for $La_xMn_yNi_zO_3$ sorted by Mn concentration.

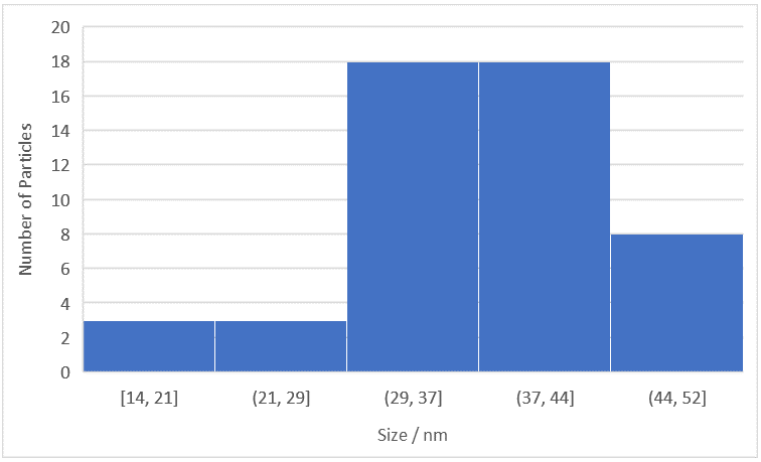

Figure 9.12: Histograms of particle sizes for $La_{1.1}Mn_{0.84}Ni_{0.06}O_3$.

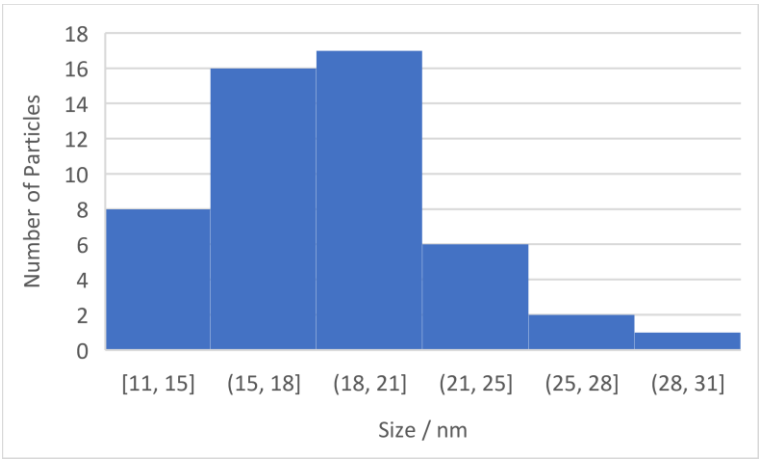

Figure 9.13: Histograms of particle sizes for $La_{0.83}Mn_{0.86}Ni_{0.31}O_3$.

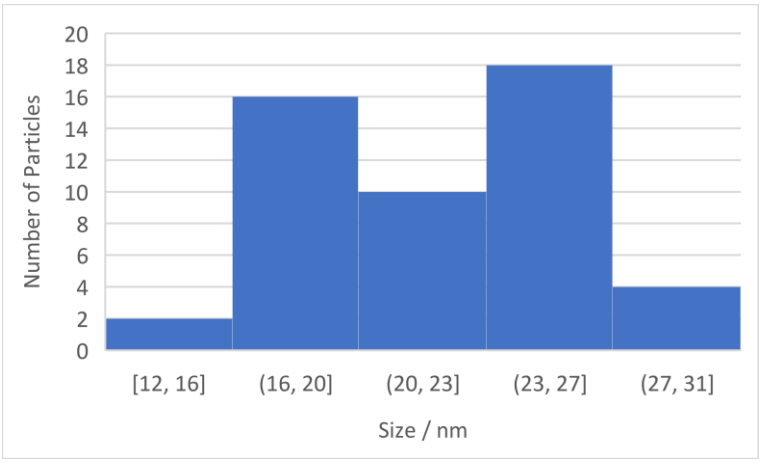

Figure 9.14: Histograms of particle sizes for $La_{1.08}Mn_{0.61}Ni_{0.31}O_3$.

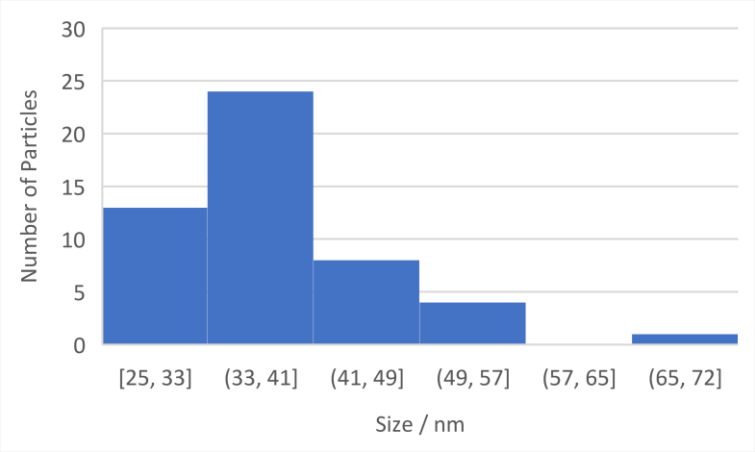

Figure 9.15: Histograms of particle sizes for $La_{1.05}Mn_{0.37}Ni_{0.58}O_3$.

Table 9.4: Ternary data for $La_xMn_yNi_zO_3$ samples in Chapter 5. 1: Scherrer size / nm, 2: BET SSA / $m^2\ g^{-1}$, 3: ORR overpotential / V, 4: OER overpotential / V, 5: Combined overpotential / V, 6: Current density at −0.5 V / mA cm^{-2}, 7: Current density at 0.8 V / mA cm^{-2}, 8: Koutecky-Levich gradient, 9: Koutecky-Levich y-intercept.

Sample	1	2	3	4	5	6	7	8	9
$La_{1.1}Mn_{0.84}Ni_{0.06}O_3$	13.66	21.66	0.31	0.42	0.73	−6.35	1.31	1.99	0.05
$La_{1.05}Mn_{0.84}Ni_{0.11}O_3$	12.81	23.68	0.31	0.44	0.75	−6.40	1.42	2.03	0.05
$LaMn_{0.86}Ni_{0.14}O_3$	12.27	26.81	0.30	0.44	0.74	−6.89	1.58	1.84	0.05
$La_{0.94}Mn_{0.85}Ni_{0.21}O_3$	12.48	31.32	0.30	0.42	0.71	−6.82	2.20	1.84	0.05
$La_{0.89}Mn_{0.86}Ni_{0.25}O_3$	12.01	33.40	0.29	0.41	0.71	−6.93	2.22	1.79	0.05
$La_{0.83}Mn_{0.86}Ni_{0.31}O_3$	11.45	35.54	0.29	0.40	0.69	−7.04	2.26	1.78	0.04
$La_{1.14}Mn_{0.80}Ni_{0.06}O_3$	14.89	22.17	0.31	0.49	0.80	−6.20	0.71	2.01	0.05
$La_{0.85}Mn_{0.82}Ni_{0.33}O_3$	11.51	35.53	0.30	0.42	0.72	−6.59	2.14	1.89	0.05
$La_{1.19}Mn_{0.75}Ni_{0.06}O_3$	11.56	19.72	0.31	0.49	0.80	−6.51	0.70	1.98	0.04
$La_{1.09}Mn_{0.75}Ni_{0.16}O_3$	13.50	22.49	0.31	0.48	0.79	−6.42	0.84	1.96	0.05
$La_{1.04}Mn_{0.76}Ni_{0.20}O_3$	13.43	25.59	0.30	0.45	0.75	−6.78	1.49	1.88	0.04
$La_{0.98}Mn_{0.76}Ni_{0.26}O_3$	12.85	33.15	0.31	0.43	0.74	−6.80	2.05	1.89	0.04
$La_{0.94}Mn_{0.75}Ni_{0.31}O_3$	11.95	34.29	0.29	0.41	0.71	−6.51	2.20	1.80	0.05
$La_{0.85}Mn_{0.78}Ni_{0.37}O_3$	11.78	35.37	0.31	0.42	0.73	−6.47	1.80	1.98	0.05
$La_{1.24}Mn_{0.70}Ni_{0.06}O_3$	15.27	21.51	0.33	0.52	0.85	−6.38	0.58	1.90	0.06
$La_{1.15}Mn_{0.71}Ni_{0.14}O_3$	14.61	20.87	0.31	0.48	0.79	−6.22	0.90	2.04	0.05
$La_{0.93}Mn_{0.69}Ni_{0.38}O_3$	12.01	29.16	0.30	0.42	0.72	−6.85	2.19	1.80	0.05
$La_{0.83}Mn_{0.73}Ni_{0.44}O_3$	11.54	36.87	0.30	0.42	0.73	−6.13	2.25	2.01	0.05
$La_{1.28}Mn_{0.66}Ni_{0.06}O_3$	14.65	20.14	0.33	0.51	0.84	−5.47	0.65	1.77	0.10

$La_{1.20}Mn_{0.64}Ni_{0.16}O_3$	13.87	21.21	0.32	0.48	0.80	−6.49	1.04	2.03	0.05
$La_{1.08}Mn_{0.68}Ni_{0.24}O_3$	13.59	24.89	0.32	0.49	0.81	−5.74	0.79	2.06	0.07
$La_{1.04}Mn_{0.65}Ni_{0.31}O_3$	12.69	28.91	0.30	0.44	0.73	−6.56	1.65	1.80	0.05
$La_{0.93}Mn_{0.67}Ni_{0.40}O_3$	11.72	32.29	0.30	0.42	0.72	−6.98	2.38	1.82	0.04
$La_{0.82}Mn_{0.67}Ni_{0.51}O_3$	10.94	34.12	0.34	0.46	0.80	−5.70	1.29	1.91	0.08
$La_{1.34}Mn_{0.60}Ni_{0.06}O_3$	10.20	24.08	0.34	0.53	0.86	−6.42	0.53	1.95	0.07
$La_{1.23}Mn_{0.62}Ni_{0.15}O_3$	13.61	23.37	0.32	0.49	0.81	−6.47	0.87	2.01	0.06
$La_{1.13}Mn_{0.61}Ni_{0.26}O_3$	12.74	24.92	0.31	0.47	0.78	−6.02	1.08	1.97	0.06
$La_{1.08}Mn_{0.61}Ni_{0.31}O_3$	12.70	25.46	0.30	0.48	0.78	−5.87	0.82	2.01	0.06
$La_{1.03}Mn_{0.62}Ni_{0.35}O_3$	12.67	29.37	0.30	0.45	0.74	−6.96	1.63	2.03	0.03
$La_{0.96}Mn_{0.63}Ni_{0.41}O_3$	11.85	33.80	0.32	0.43	0.75	−6.74	1.92	1.84	0.05
$La_{0.82}Mn_{0.610.57}O_3$	11.13	35.27	0.32	0.45	0.78	−5.97	1.32	1.92	0.07
$La_{1.34}Mn_{0.55}Ni_{0.11}O_3$	12.69	26.78	0.35	0.54	0.89	−5.58	0.41	1.78	0.13
$La_{1.24}Mn_{0.55}Ni_{0.21}O_3$	11.59	25.34	0.33	0.45	0.78	−6.03	1.62	1.94	0.07
$La_{1.12}Mn_{0.57}Ni_{0.31}O_3$	12.97	24.66	0.31	0.47	0.78	−5.82	1.06	2.05	0.06
$La_{1.07}Mn_{0.56}Ni_{0.37}O_3$	12.80	25.25	0.30	0.46	0.76	−6.15	1.41	1.90	0.06
$La_{0.98}Mn_{0.58}Ni_{0.44}O_3$	11.95	31.17	0.30	0.43	0.73	−6.87	2.13	1.78	0.05
$La_{0.86}Mn_{0.59}Ni_{0.55}O_3$	11.26	34.89	0.31	0.44	0.75	−6.82	1.62	1.83	0.05
$La_{1.32}Mn_{0.52}Ni_{0.16}O_3$	12.27	27.73	0.34	0.49	0.83	−7.81	0.93	1.73	0.06
$La_{1.18}Mn_{0.51}Ni_{0.30}O_3$	11.94	24.75	0.34	0.41	0.75	−5.93	1.57	1.80	0.08
$La_{1.02}Mn_{0.52}Ni_{0.45}O_3$	9.26	28.03	0.31	0.46	0.77	−4.87	1.24	1.82	0.12
$La_{0.89}Mn_{0.52}Ni_{0.59}O_3$	11.71	32.54	0.32	0.46	0.78	−6.31	1.26	2.01	0.05
$La_{1.32}Mn_{0.47}Ni_{0.21}O_3$	11.70	28.89	0.34	0.48	0.82	−6.79	1.00	1.79	0.07
$La_{1.235}Mn_{0.51}Ni_{0.24}O_3$	11.36	26.12	0.34	0.44	0.78	−5.54	1.95	1.77	0.10
$La_{1.18}Mn_{0.47}Ni_{0.35}O_3$	11.58	24.29	0.33	0.43	0.76	−6.47	2.22	1.80	0.08
$La_{1.11}Mn_{0.47}Ni_{0.42}O_3$	12.41	22.05	0.33	0.44	0.76	−6.20	1.81	1.86	0.07
$La_{1.07}Mn_{0.47}Ni_{0.46}O_3$	11.41	18.95	0.33	0.44	0.77	−5.14	2.32	1.95	0.11
$La_{0.95}Mn_{0.46}Ni_{0.58}O_3$	11.34	28.39	0.31	0.44	0.75	−6.23	2.06	1.95	0.06
$La_{1.32}Mn_{0.41}Ni_{0.27}O_3$	13.46	28.57	0.37	0.47	0.84	−6.63	1.29	1.77	0.10
$LaMn_{0.41}Ni_{0.59}O_3$	12.52	18.97	0.33	0.43	0.76	−4.89	2.39	1.98	0.11
$La_{1.32}Mn_{0.37}Ni_{0.31}O_3$	11.35	26.49	0.39	0.44	0.83	−5.89	1.92	1.65	0.13
$La_{1.27}Mn_{0.36}Ni_{0.37}O_3$	11.18	19.03	0.39	0.44	0.83	−6.06	1.97	1.54	0.13
$La_{1.23}Mn_{0.37}Ni_{0.40}O_3$	11.38	25.36	0.37	0.41	0.79	−6.31	2.65	1.63	0.11
$La_{1.18}Mn_{0.37}Ni_{0.45}O_3$	12.39	24.82	0.36	0.40	0.76	−6.15	3.37	1.70	0.10

$La_{1.11}Mn_{0.37}Ni_{0.52}O_3$	12.11	20.31	0.37	0.41	0.78	−5.74	2.57	1.54	0.15
$La_{1.05}Mn_{0.37}Ni_{0.58}O_3$	12.41	15.58	0.38	0.41	0.79	−4.06	3.35	1.93	0.19
$La_{0.88}Mn_{0.95}Ni_{0.16}O_3$	11.53	32.36	0.29	0.41	0.70	−6.81	2.51	1.76	0.04
$La_{0.87}Mn_{0.93}Ni_{0.20}O_3$	12.08	32.47	0.30	0.42	0.71	−6.73	2.15	1.86	0.04
$La_{0.80}Mn_{0.96}Ni_{0.25}O_3$	11.87	34.27	0.32	0.44	0.75	−6.70	1.46	1.93	0.03
$La_{0.72}Mn_{0.97}Ni_{0.31}O_3$	11.60	34.59	0.33	0.44	0.77	−6.16	1.70	1.97	0.04
$La_{0.73}Mn_{0.91}Ni_{0.36}O_3$	11.41	35.03	0.34	0.45	0.79	−6.18	1.52	2.04	0.04
$La_{0.72}Mn_{0.86}Ni_{0.42}O_3$	11.38	35.60	0.32	0.44	0.76	−6.46	1.57	1.99	0.03
$La_{0.73}Mn_{0.80}Ni_{0.47}O_3$	11.11	34.11	0.35	0.47	0.82	−4.24	1.04	2.14	0.10

9.4. SI for Chapter 6

Table 9.5: Synthesis details for Chapter 6. All final compositions are molar ratios by XRF.

Sample	$Ni(NO_3)_2.6H_2O$ / M	$Mn(NO_3)_2.xH_2O$ / M	$Fe(NO_3)_2.9H_2O$ / M
$Ni_{0.75}Mn_{2.25}O_4$	0.067	0.267	0.000
$Ni_{0.82}Mn_{2.18}O_4$	0.078	0.244	0.000
$Ni_{0.92}Mn_{2.08}O_4$	0.089	0.222	0.000
$Ni_{1.08}Mn_{1.92}O_4$	0.100	0.200	0.000
$Ni_{1.22}Mn_{1.78}O_4$	0.111	0.178	0.000
$Ni_{1.36}Mn_{1.64}O_4$	0.122	0.156	0.000
$Ni_{1.53}Mn_{1.47}O_4$	0.133	0.133	0.000
$Ni_{1.58}Mn_{1.32}Fe_{0.10}O_4$	0.122	0.107	0.011
$Ni_{1.50}Mn_{1.26}Fe_{0.24}O_4$	0.111	0.107	0.022
$Ni_{1.38}Mn_{1.24}Fe_{0.38}O_4$	0.100	0.107	0.033
$Ni_{1.25}Mn_{1.23}Fe_{0.52}O_4$	0.089	0.107	0.044
$Ni_{1.12}Mn_{1.19}Fe_{0.69}O_4$	0.078	0.107	0.056
$Ni_{0.94}Mn_{1.19}Fe_{0.87}O_4$	0.067	0.107	0.067
$Ni_{0.90}Mn_{1.31}Fe_{0.79}O_4$	0.067	0.124	0.056
$Ni_{0.92}Mn_{1.45}Fe_{0.63}O_4$	0.067	0.142	0.044
$Ni_{0.91}Mn_{1.61}Fe_{0.48}O_4$	0.067	0.160	0.033
$Ni_{0.90}Mn_{1.76}Fe_{0.34}O_4$	0.067	0.178	0.022
$Ni_{0.88}Mn_{1.92}Fe_{0.20}O_4$	0.067	0.196	0.011
$Ni_{0.95}Mn_{1.90}Fe_{0.15}O_4$	0.078	0.178	0.011

$Ni_{1.09}Mn_{1.76}Fe_{0.15}O_4$	0.089	0.160	0.011
$Ni_{1.24}Mn_{1.61}Fe_{0.15}O_4$	0.100	0.142	0.011
$Ni_{1.34}Mn_{1.51}Fe_{0.15}O_4$	0.111	0.124	0.011
$Ni_{1.36}Mn_{1.40}Fe_{0.24}O_4$	0.100	0.124	0.022
$Ni_{1.28}Mn_{1.37}Fe_{0.35}O_4$	0.089	0.124	0.033
$Ni_{1.10}Mn_{1.40}Fe_{0.50}O_4$	0.078	0.124	0.044
$Ni_{1.05}Mn_{1.49}Fe_{0.46}O_4$	0.078	0.142	0.033
$Ni_{1.04}Mn_{1.64}Fe_{0.32}O_4$	0.078	0.160	0.022
$Ni_{1.13}Mn_{1.59}Fe_{0.28}O_4$	0.089	0.142	0.022

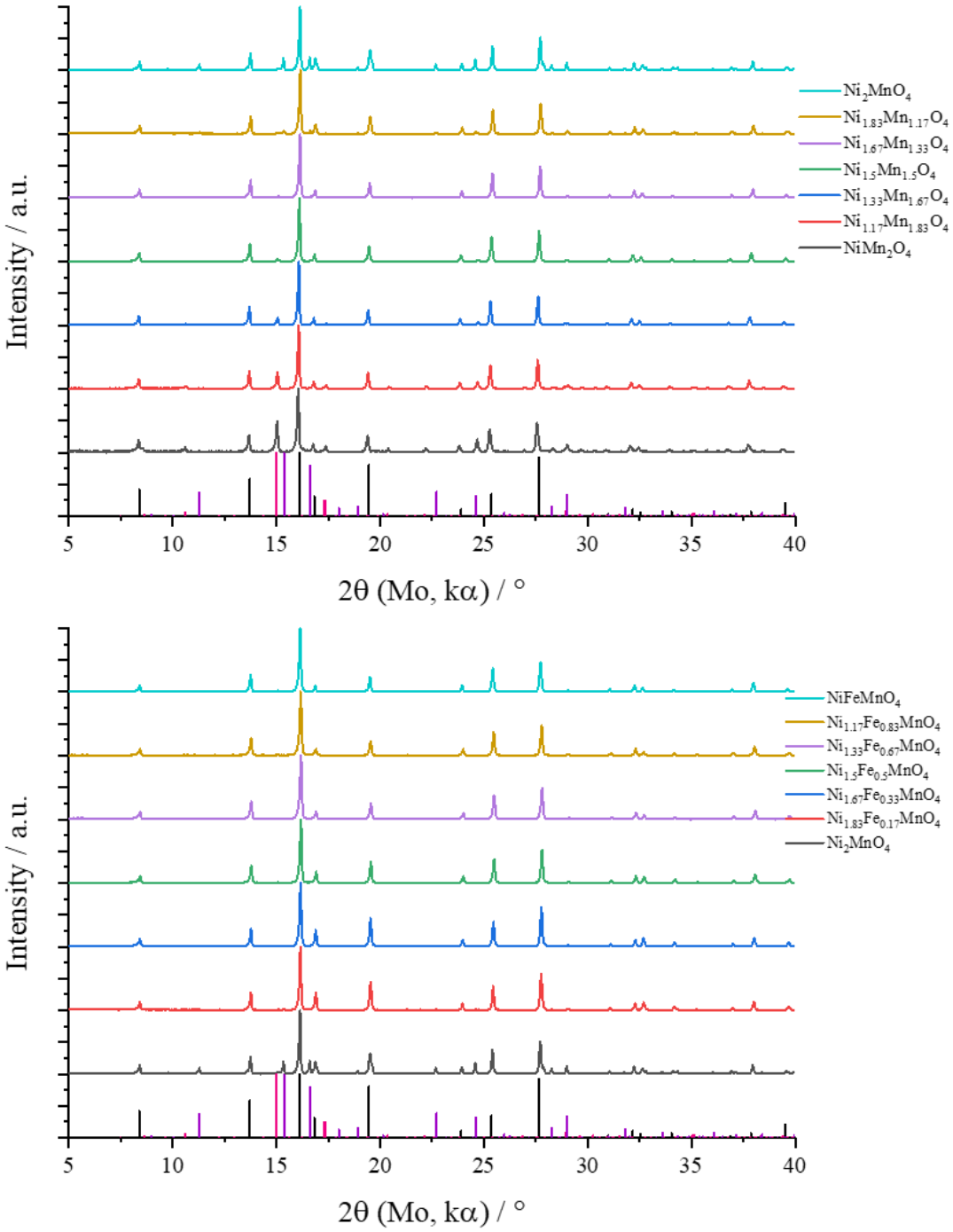

Figure 9.16: PXRD data for the $Ni_xMn_yFe_zO_4$ ternary phase diagram.

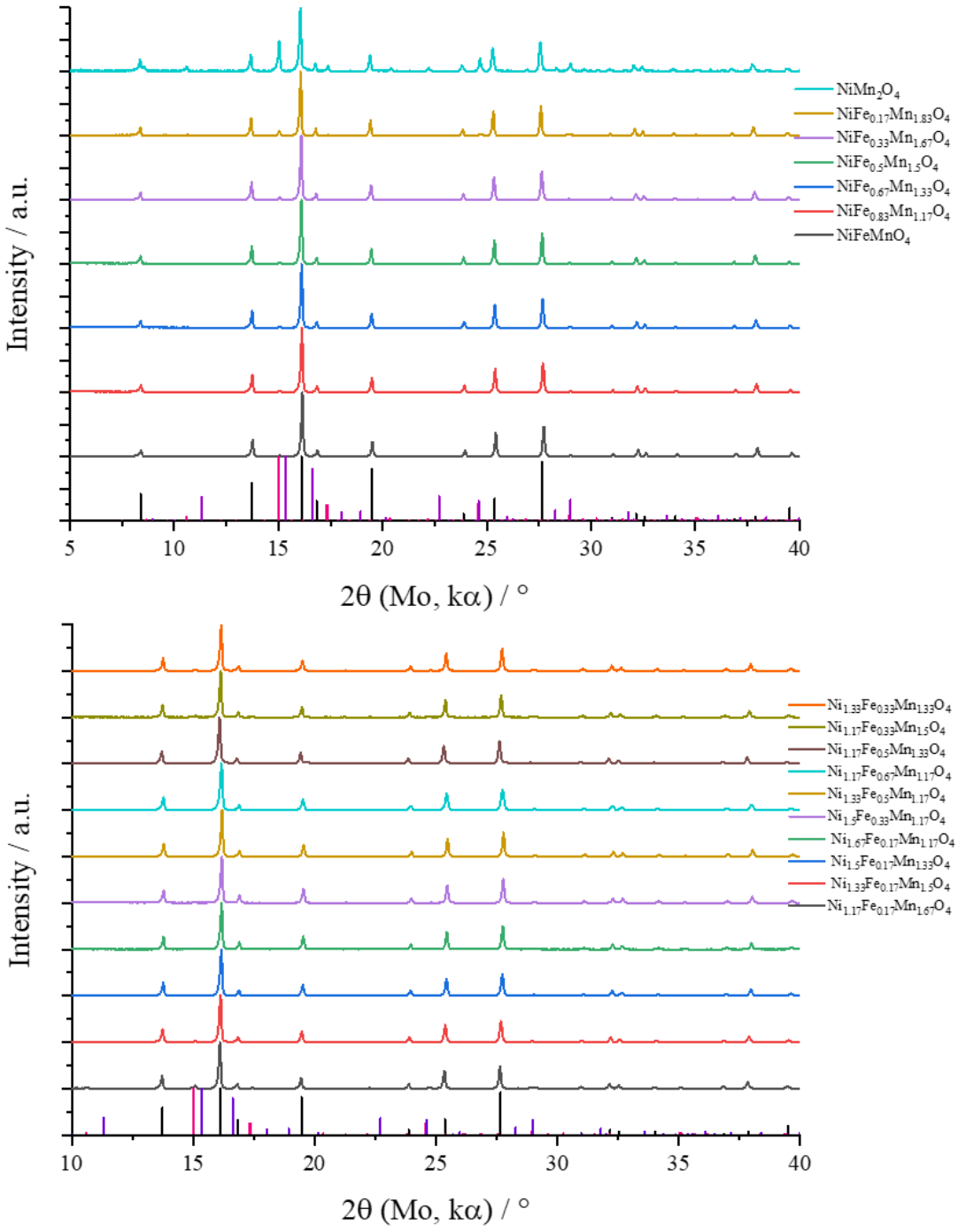

Figure 9.17: PXRD data for the $Ni_xMn_yFe_zO_4$ ternary phase diagram.

Table 9.6: Ternary data for $Ni_xMn_yFe_zO_4$ samples in Chapter 6. All compositions are by XRF. 1: Peak position of the (311) peak. 2: Scherrer size / nm, 3: BET SSA / $m^2\ g^{-1}$, 4: ORR overpotential / V, 5: OER overpotential / V, 6: Combined overpotential / V, 7: Current density at −0.5 V / mA cm^{-2}, 8: Current density at 0.8 V / mA cm^{-2}, 9: Koutecky-Levich gradient, 10: Koutecky-Levich y-intercept.

Sample	1	2	3	4	5	6	7	8	9	10
$Ni_{0.75}Mn_{2.25}O_4$	16.04	35.17	6.39	0.28	0.36	0.64	−5.87	3.86	1.92	0.06

$Ni_{0.82}Mn_{2.18}O_4$	16.07	36.83	6.75	0.30	0.38	0.68	−6.22	3.20	2.03	0.04
$Ni_{0.92}Mn_{2.08}O_4$	16.07	37.04	5.32	0.33	0.38	0.71	−6.48	4.31	2.05	0.03
$Ni_{1.08}Mn_{1.92}O_4$	16.10	35.06	3.61	0.37	0.41	0.78	−5.97	3.49	2.07	0.04
$Ni_{1.22}Mn_{1.78}O_4$	16.13	36.56	2.56	0.41	0.42	0.82	−3.64	3.52	2.11	0.15
$Ni_{1.36}Mn_{1.64}O_4$	16.14	37.37	3.61	0.42	0.42	0.83	−2.98	3.92	2.06	0.21
$Ni_{1.53}Mn_{1.47}O_4$	16.13	39.76	2.33	0.47	0.43	0.89	−2.93	3.73	2.16	0.21
$Ni_{1.58}Mn_{1.32}Fe_{0.10}O_4$	16.15	37.07	2.24	0.47	0.39	0.86	−3.38	4.90	2.30	0.15
$Ni_{1.50}Mn_{1.26}Fe_{0.24}O_4$	16.16	37.07	2.67	0.44	0.35	0.79	−3.39	5.75	2.29	0.15
$Ni_{1.38}Mn_{1.24}Fe_{0.38}O_4$	16.17	35.56	3.63	0.44	0.37	0.81	−3.48	6.68	2.33	0.15
$Ni_{1.25}Mn_{1.23}Fe_{0.52}O_4$	16.17	32.21	4.79	0.42	0.35	0.77	−3.56	6.28	2.26	0.14
$Ni_{1.12}Mn_{1.19}Fe_{0.69}O_4$	16.16	33.67	4.57	0.45	0.38	0.83	−3.17	4.24	2.25	0.18
$Ni_{0.94}Mn_{1.19}Fe_{0.87}O_4$	16.14	34.93	4.53	0.41	0.38	0.79	−3.42	3.66	2.27	0.15
$Ni_{0.90}Mn_{1.31}Fe_{0.79}O_4$	16.12	33.38	4.51	0.42	0.39	0.81	−3.67	3.97	2.29	0.13
$Ni_{0.92}Mn_{1.45}Fe_{0.63}O_4$	16.11	35.24	4.42	0.38	0.37	0.75	−3.45	3.97	2.16	0.16
$Ni_{0.91}Mn_{1.61}Fe_{0.48}O_4$	16.09	35.54	3.88	0.38	0.37	0.75	−3.65	3.63	2.13	0.14
$Ni_{0.90}Mn_{1.76}Fe_{0.34}O_4$	16.08	33.86	4.06	0.36	0.37	0.73	−3.46	3.90	2.12	0.16
$Ni_{0.88}Mn_{1.92}Fe_{0.20}O_4$	16.06	36.65	4.76	0.37	0.37	0.74	−3.68	2.68	2.00	0.15
$Ni_{0.95}Mn_{1.90}Fe_{0.15}O_4$	16.09	37.11	4.48	0.36	0.38	0.73	−4.20	3.50	2.25	0.10
$Ni_{1.09}Mn_{1.76}Fe_{0.15}O_4$	16.11	35.97	2.07	0.36	0.37	0.74	−3.27	3.35	1.96	0.19
$Ni_{1.24}Mn_{1.61}Fe_{0.15}O_4$	16.14	32.88	3.46	0.39	0.37	0.76	−3.33	4.63	2.16	0.17
$Ni_{1.34}Mn_{1.51}Fe_{0.15}O_4$	16.15	35.74	3.29	0.43	0.38	0.81	−3.22	4.53	2.31	0.17
$Ni_{1.36}Mn_{1.40}Fe_{0.24}O_4$	16.16	35.85	2.84	0.41	0.36	0.78	−2.97	6.14	2.34	0.19
$Ni_{1.28}Mn_{1.37}Fe_{0.35}O_4$	16.17	37.21	3.84	0.42	0.37	0.79	−3.02	5.38	2.35	0.19
$Ni_{1.10}Mn_{1.40}Fe_{0.50}O_4$	16.15	30.05	4.82	0.39	0.36	0.75	−3.88	5.80	2.28	0.12
$Ni_{1.05}Mn_{1.49}Fe_{0.46}O_4$	16.07	35.73	3.97	0.41	0.37	0.78	−3.62	5.49	2.18	0.15
$Ni_{1.04}Mn_{1.64}Fe_{0.32}O_4$	16.11	35.38	4.18	0.36	0.36	0.73	−4.94	5.34	2.05	0.08
$Ni_{1.13}Mn_{1.59}Fe_{0.28}O_4$	16.14	36.76	3.97	0.40	0.37	0.77	−3.36	4.24	1.94	0.18